

GEORGIA DOT RESEARCH PROJECT 10-08

FINAL REPORT

**A REMOTE SENSING AND GIS-ENABLED HIGHWAY
ASSET MANAGEMENT SYSTEM**



**OFFICE OF RESEARCH
15 KENNDY DRIVE
FOREST PARK, GA 30297-2534**

1. Report No.: GA-15-1008	2. Government Accession No.:	3. Recipient's Catalog No.:	
4. Title and Subtitle: A Remote Sensing and GIS-Enabled Highway Asset Management System		5. Report Date: April 2016	
		6. Performing Organization Code:	
7. Author(s): Yichang (James) Tsai; Zhaohua Wang		8. Performing Organ. Report No.:	
9. Performing Organization Name and Address: Georgia Institute of Technology 790 Atlantic Drive Atlanta, GA 30332-0355		10. Work Unit No.:	
		11. Contract or Grant No.: RP 10-08	
12. Sponsoring Agency Name and Address: Georgia Department of Transportation Office of Research 15 Kennedy Drive Forest Park, GA 30297-2534		13. Type of Report and Period Covered: Final; June 2010 – February 2015	
		14. Sponsoring Agency Code:	
15. Supplementary Notes: Prepared in cooperation with the U.S. Department of Transportation, Federal Highway Administration.			
16. Abstract: The objective of this project is to validate the use of commercial remote sensing and spatial information (CRS&SI) technologies, including emerging 3D line laser imaging technology, mobile LiDAR, image processing algorithms, and GPS/GIS technologies, to improve the transportation asset data collection, condition assessment, and management. Traffic sign asset and pavement asset were used for validation. For sign asset, an enhanced procedure for sign inventory was proposed; a large-scale case study was conducted on I-285; a preliminary study has been done to evaluate sign retroreflectivity using mobile LiDAR; and a prototype GIS-based sign management system was developed. The research results show that using the automatic image-processing-based sign detection and recognition algorithms and the LiDAR-based sign detection can improve the current time-consuming image-based traffic sign data collection process. For pavement asset, comprehensive validation has been done on network-level rutting measurement and isolated rutting detection; an innovative method was developed to evaluate the performance of an automatic crack detection algorithm; comprehensive lab and field tests have been done to validate the capability of 3D laser data for asphalt pavement crack detection; and a crack propagation study has also been done using the long-term monitoring data. Based on the research results, conclusions were made and recommendations were suggested.			
17. Key Words: 3D Laser; Mobile LiDAR; Cracking; Rutting; Traffic Sign		18. Distribution Statement: No Restriction	
19. Security Classification (of this report): Unclassified	20. Security classification (of this page): Unclassified	21. Number of Pages: 463	22. Price:

Contract Research

GDOT Research Project No. 10-08

Final Report

**A REMOTE SENSING AND GIS-ENABLED HIGHWAY ASSET
MANAGEMENT SYSTEM**

By

Yichang (James) Tsai, Ph.D., P.E.

Zhaohua Wang, Ph.D., P.E.

Georgia Institute of Technology

Contract with

Georgia Department of Transportation

In cooperation with

U.S. Department of Transportation

Federal Highway Administration

April 2016

The contents of this report reflect the views of the author(s) who is (are) responsible for the facts and the accuracy of the data presented herein. The contents do not necessarily reflect the official views or policies of the Georgia Department of Transportation or of the Federal Highway Administration. This report does not constitute a standard, specification, or regulation.

Acknowledgements

The work described in this report was supported by the Georgia Department of Transportation (GDOT) through Research Project 10-08 and the U. S. Department of Transportation Office of the Assistant Secretary for Research and Technology (USDOT/OST-R). We would like to thank the technical advisory committee, including Mr. Butch Wlaschin, Mr. Thomas Van, Mr. Mark Swanlund, and Mr. Mike Moravec from the Federal Highway Administration; Mr. Bouzid Choubane and Mr. Bruce Dietrich from Florida DOT; Ms. Angela Alexander, Mr. Gregory Mayo, and Mr. Eric Pitts from Georgia DOT; Mr. Rick Miller from Kansas DOT; and Dr. Judith B Corley-Lay from North Carolina DOT, for their valuable contributions to this project. The strong support provided by Georgia DOT, including Mr. Buddy Gratton, Mr. Gerald Ross, Mr. Russell McMurry, Mr. David Crim, Ms. Georgene Geary, Ms. Jane Smith, Ms. Meg Pirkle, Mr. Timothy Dale Brantley, Ms. Ernay Robinson, Mr. Jim Leben, Mr. Terry Rutledge, Mr. Ritchie Swindell, Mr. Rick Deaver, Mr. David Jared, Mr. Binh Bui, and Ms. Gretel Sims is highly appreciated. We would like to thank Louisiana DOTD and the city of Nashville for providing us with the testing data. We would like to thank the following state DOTs and companies for their technical support: Connecticut DOT, Florida DOT, Kansas DOT, Louisiana DOTD, Mississippi DOT, Oklahoma DOT, South Carolina DOT, Texas DOT, INO/Pavemetrics, and Trimble Geo3D. We would like to thank the research team members, Dr. James Lai, Dr. Anthony Yezzi, Ms. Yiching Wu, Dr. Vivek Kaul, Dr. Feng Li, Dr. Chengbo Ai, Mr. Zachary Lewis, Mr. Thibaut Dusanter, and Mr. Chenglong Jiang. Mr. Jon Lindsay's editing of this report is also appreciated. Especially, we would like to thank Mr. Caesar Singh, Mr. Vasanth Ganesan, and Mr. Binh Bui for their assistance in managing this project.

Table of Content

Acknowledgements.....	vi
Table of Figures	xvi
Table of Tables	xxvi
Executive Summary	xxx
1. Research Focuses	xxx
2. Research Outcome and Major Findings.....	xxx
3. Recommendations for Future Research and Implementation.....	xxxviii
Chapter 1 Introduction.....	1
1. Background and Research Need	1
2. Introduction to Georgia Tech Sensing Vehicle.....	4
2.1 Introduction to 3D Laser System.....	5
2.2 Introduction to Mobile LiDAR System.....	6
3. Research Focuses	9
4. Report Organization.....	12
Chapter 2 Validation of Traffic Sign Inventory Using Video Log Images and Mobile LiDAR 13	
1. Introduction.....	13
2. Literature Review of Traffic Sign Inventory	13
2.1 Current Practice	14
2.2 Current Studies of Image-based Algorithms	16
2.3 Research Need	22
3. Assessment of Automatic Traffic Sign Inventory Using Video Log Images	23

3.1	Data Preparation	23
3.2	Test Result	25
4.	Assessment of Automatic Traffic Sign Inventory Using mobile LiDAR.....	31
4.1	Determination of Adequate Parameter Values	31
4.2	Test Result	34
5.	An Enhanced Traffic Sign Inventory Procedure.....	39
5.1	Proposed Procedure	39
5.2	Preliminary Assessment	42
6.	Summary and Discussions	44
	References.....	46
Chapter 3 Traffic Sign Inventory and Condition Assessment – A Case Study on I-285 51		
1.	Introduction.....	51
2.	Traffic Sign Characteristics	51
3.	Sensing Data Collection.....	54
4.	Sign Inventory and Condition Assessment.....	54
4.1	Statistics of Inventoried Signs	55
4.2	Three Types of Sign Damages and Causes	58
5.	Summary	61
	References.....	63
Chapter 4 Sign Retroreflectivity Condition Assessment Using Mobile LiDAR – A Feasibility Study		
		65
1.	Introduction.....	65
2.	Literature Review.....	66

2.1	Current Practice	66
2.2	State-of-the-Art Research	68
2.3	Research Need	70
3.	Assessment of the LiDAR-Based Sign Retroreflectivity Condition Assessment Method	70
3.1	Preliminary Results.....	71
3.2	Benefit of LiDAR-based Assessment Method	72
4.	Conclusions and Discussions.....	75
	References.....	76
Chapter 5	A Prototype GIS-Based Sign Management System.....	79
1.	Introduction.....	79
2.	Development of a GIS-Based Sign Inventory Inspection Tool	79
2.1	Data Preparation and Software Environment Set Up.....	79
2.2	Major Functions.....	81
3.	A Case Study on I-285.....	84
4.	Summary	87
Chapter 6	Rut Measurement and Isolated Rut Detection	89
1.	Literature Review.....	89
1.1	Rutting Survey Protocols.....	89
1.2	Rutting Survey Methods.....	91
1.3	Rutting Survey Report Methods.....	92
1.4	Rut Depth Measurement Errors.....	94
2.	Research Need and Objective	95

3.	Assessment of Rut Depth Measurement Accuracy using 3D laser.....	96
3.1	Experimental Test Design	96
3.1.1	Laboratory Test.....	96
3.1.2	Field Test	97
3.2	Data Analyses.....	102
3.2.1	DCT-based Rut Depth Calculation Algorithm	103
3.2.2	3D laser Based Rut Depth Calculation	104
3.2.3	Comparison of Rut Depth Calculation Algorithms	105
3.3	Test Results.....	105
3.3.1	Laboratory Test Results	105
3.3.2	Field Test Results.....	106
3.4	Summary.....	110
4.	Assessment of Rut Depth Measurement Error of Point-based Rut Bar Systems	111
4.1	Research Need	111
4.2	Experimental Test Design	112
4.2.1	Test Data.....	112
4.2.2	Rut Depth Computation	113
4.3	Test Results.....	115
4.4	Summary.....	118
5.	Network-level Rutting Survey	119
5.1	Procedures of Network-level Rutting Survey.....	119
5.1.1	Read XML Files.....	120
5.1.2	Remove Outliers	121

5.1.3	Divide Project into Segments.....	123
5.1.4	Statistical Analyses	124
5.2	Case Study	125
5.2.1	Test Site Selection.....	125
5.2.2	Data Collection	126
5.2.3	Data Analyses and Results.....	127
5.2.4	Computing Consideration	137
5.3	Discussions	142
6.	Isolated Rutting Detection	145
6.1	Research Need	145
6.2	Case Study – I-95	147
6.3	Case Study – SR307	150
6.4	Summary.....	153
7.	Conclusions.....	153
	References.....	155
Chapter 7 A Buffered Distance Method for Quantitatively Evaluating Performance of Crack Detection Algorithms		
		159
1.	Introduction.....	159
2.	A Quantitative Performance Evaluation Method.....	161
2.1	A Proposed Method Using Buffered Hausdorff Distance	161
2.2	Other Method Used for Comparison	165
3.	Experimental Test	167
3.1	Buffered Hausdorff Distance Over Four Other Quantification Methods	167

3.2	Buffer Size Selection	175
3.3	Data Resolution	176
3.4	Crack Width Consideration	178
4.	Applications	179
4.1	Critical Performance Assessment of Pavement Crack Detection Methods..	179
4.2	Parameter Selection of Dynamic Optimization Crack Detection Algorithm	185
5.	Conclusions.....	187
	References.....	188
Chapter 8 Asphalt Pavement Crack Detection Using 3D laser Data.....		191
1.	Introduction.....	191
2.	3D laser Imaging Technology.....	193
3.	Advantages of 3D laser Data	194
3.1	Pavements under Different Lighting Conditions and Low Contrast Conditions	194
3.2	Pavements with Oil Stains.....	199
4.	Evaluation of Automatic Crack Map Generation	202
5.	Evaluation of Crack Width Measurement.....	204
6.	Summary	208
	References.....	210
Chapter 9 Feasibility Study of Crack Deterioration Behavior Using 3D Laser Data....		213
1.	Research Objectives.....	214
2.	Analysis of Crack Growth	215
2.1	Individual Crack Analysis	217

2.1.1	Data Processing.....	217
2.1.2	Data Analysis.....	218
2.2	Clustered Crack Analysis.....	223
2.2.1	Data Processing.....	223
2.2.2	Data Analysis.....	224
3.	Issues of Long-term Monitoring Data.....	230
4.	Summary.....	233
Chapter 10 Conclusions and Recommendations.....		235
1.	Conclusions.....	235
2.	Recommendations.....	241
Appendix I: List of Poor Condition Signs on I-285.....		I-1
Appendix II: List of Overhead Signs on I-285.....		II-1

Table of Figures

Figure 1.1 RS-GAMS Architecture	2
Figure 1.2 Systematic Scheme for the GTSV	4
Figure 1.3 Components of 3D Line Laser System Integrated on the GTSV	5
Figure 1.4 Configuration of 3D Line Laser System on the GTSV	6
Figure 1.5 Mobile LiDAR System Integrated on the Georgia Tech Sensing Vehicle.....	7
Figure 1.6 Configuration of the Mobile LiDAR System and Scanning Mechanism.....	8
Figure 2.1 The PDA Used in GDOT and Field Operation in GDOT	15
Figure 2.2 The Traffic Sign Collection Vehicle in the Field and the Extraction Interface in the office in Phoenix (Moreno & Cook, 2010).....	16
Figure 2.3 Data Collection Routes in Westwego, Louisiana for the Generalized Automatic Traffic Sign Detection Algorithm	24
Figure 2.4 Data Collection Routes in Savannah, Georgia for the Automatic Stop Sign and Speed Limit Sign Recognition	24
Figure 2.5 Examples of two FN Cases Due to Lighting Changes: a) Overexposure; b) Backlighting.....	26
Figure 2.6 Example of an FN Case Due to Discontinuous Boundary	27
Figure 2.7 Examples of Other FN Cases Identified in the Critical Assessment.....	28
Figure 2.8 Sample of FP Cases Identified in the Assessment Test.....	28
Figure 2.9 FN and FP Cases Identified in the Stop Sign Recognition Algorithm.....	30
Figure 2.10 FN and FP Cases Identified in the Speed Limit Sign Recognition	30

Figure 2.11 The Selected Data Collection Sections for Experimental Test	32
Figure 2.12 Example of FN Case with a Traffic Sign with Poor Retroreflectivity on 37th Street	35
Figure 2.13 Example of a FN Case with a Traffic Sign with Insufficient Height on 37th Street	36
Figure 2.14 Example of FN Cases Containing Occluded Signs on (a) I-95 and (b) 37th Street	37
Figure 2.15 Example of FN Cases Containing Overhead Signs on (a) I-95 and (b) 37th Street	38
Figure 2.16 Examples of the Identified FP Cases.....	38
Figure 2.17 Framework of the Enhanced Traffic Sign Inventory.....	40
Figure 3.1 Examples of four categories of poor sign conditions	53
Figure 3.2 Example of overhead sign failure (FHWA 2013)	53
Figure 3.3 Examples of the overhead sign categories defined by GDOT	54
Figure 3.4 Illustration of the coverage of the sensing data collection (including FR – Front Right Camera; FC – Front Center Camera; FL – Front Left Camera; BP – Back Pavement Camera; FR – Front Right LiDAR; FD – Front Down LiDAR; and BU – Back Up LiDAR)	55
Figure 3.5 Distribution of traffic sign classifications on I-285.....	56
Figure 3.6 Distributions of traffic signs in poor condition on I-285 (252 signs).....	57
Figure 3.7 Distributions of traffic signs installed on overhead structure on I-285	57
Figure 3.8 Examples of the damaged signs due to truck gust on median.....	59
Figure 3.9 Examples of the damaged signs due to dual-post.....	60

Figure 3.10 Examples of the damaged signs due to post failure	60
Figure 3.11 Example of a damaged D3-1 street name sign	62
Figure 4.1 The Outlooks and the Schematic Flow of the Systems	69
Figure 4.2 Images of the Type I Stop Sign in the Lab	73
Figure 4.3 Distribution for the Retroreflectivity Measurement	74
Figure 5.1 ArcMap Customize Window	80
Figure 5.2 Sign Query Interface.....	82
Figure 5.3 Sign Summary Interface	83
Figure 5.4 Individual Sign Information Window	84
Figure 5.5 I-285 Sign Data Table	85
Figure 5.6 Query Results	86
Figure 5.7 Individual Sign Info Window	86
Figure 6.1 Configuration of a 5-point Rut Bar System (Wang, 2005)	92
Figure 6.2 Simulated Rutting in Laboratory: (a) Wood Board; (b) Metal Bar	98
Figure 6.3 Laboratory Test Setup: (a) Straightedge Rutting Measurement; (b) 3D laser System Setup in the Laboratory	98
Figure 6.4 Typical Transverse Profiles Measured in the Laboratory	99
Figure 6.5 Field Test: (a) Test Site on Benton Blvd.; (b) Test Site on Towne Center Ct.; (c) 1.8m Straightedge Method; (d) Survey using 3D laser System	100
Figure 6.6 Typical Transverse Profiles: (a) Low Severity Level Rutting; (b) Medium Severity Level Rutting	100
Figure 6.7 Field Test on SR 275: (a) Test Site; (b) Rutting.....	101

Figure 6.8 Labels in (a) Field and in b) 3D Laser Data	102
Figure 6.9 Smoothed Transverse Profiles: (a) DCT Only; (b) DCT plus Stepwise Linear Interpolation	103
Figure 6.10 1.8m Straightedge Method	104
Figure 6.11 Rut Depth Calculation (LCMS, 2010).....	105
Figure 6.12 Correlation of Rut Depth in Two Runs in Laboratory	108
Figure 6.13 Correlation of Rut Depth in Three Runs in Field	109
Figure 6.14 Road Transverse Profiles at Milepoint 3.4m and 6.4m	113
Figure 6.15 Sketch of 3-point Rut Bar Configuration	114
Figure 6.16 Sketch of 5-point Rut Bar Configuration	115
Figure 6.17 Straightedge Method	115
Figure 6.18 Rut Depth Profile along Driving Direction	116
Figure 6.19 Measurement Errors of Point-based Rut Bar Systems along Driving Direction	117
Figure 6.20 Relationships between Mean and Variance of Relative Measurement Errors and Number of Sensors.....	117
Figure 6.21 Example of XML Output File	121
Figure 6.22 Example of Longitudinal Rut Depth Profiles from XML Files	121
Figure 6.23 Causes of Outliers.....	122
Figure 6.24 Examples of Outliers	122
Figure 6.25 Illustration of Representative Rut Depth Mode.....	125
Figure 6.26 Test Site Locations	127

Figure 6.27 Raw Data (SR 275 SB from MP 0.8 to MP 0)	128
Figure 6.28 Raw (Blue) and Filtered Data (Red) (SR275 SB from MP 0.8 to MP 0)....	129
Figure 6.29 Histogram of Filtered Data (SR 275 SB from MP 0.8 to MP 0).....	129
Figure 6.30 Roadway Environment (Benton Blvd.).....	134
Figure 6.31 Raw Data (Benton Blvd.)	134
Figure 6.32 Raw (Blue) and Filtered Data (Red) (Benton Blvd.).....	135
Figure 6.33 Histogram of Rut Depth Measurements (Benton Blvd.).....	135
Figure 6.34 Raw Data (I-95).....	135
Figure 6.35 Raw (Blue) and Filtered Data (Red) (I-95)	136
Figure 6.36 Histogram of Rut Depth Measurements (I-95).....	137
Figure 6.37 Sampling Interval vs. Data Processed per Hour (mi).....	140
Figure 6.38 Sampling Interval vs. Data Processing Speed (mi/hr).....	140
Figure 6.39 Aggregated Rut Depths at 0.1mi Intervals (SR 275 MP0-1 OutWP, Std = 0.5 of 1/8in.).....	141
Figure 6.40 Aggregated Rut Depths at 0.1mi Intervals (Benton Blvd. InWP, Std = 1.6 of 1/8 in.).....	141
Figure 6.41 Issue of Vehicle Wandering	143
Figure 6.42 Issue of Half-lane Rut Depth Calculation	143
Figure 6.43 Lane Marking Detection Results.....	144
Figure 6.44 Issue of Missing Lane Marking.....	145
Figure 6.45 An Isolated Rut in 3D Laser Data	146
Figure 6.46 Location of Test Site on I-95.....	147

Figure 6.47 Raw Longitudinal Rut Depth Profile (Blue) and Filtered Profile (Red)	147
Figure 6.48 Homogeneous Segmentation Results (MinLen = 10ft. and MinDiff = 1/8 in.)	148
Figure 6.49 Detected Isolated Ruts.....	149
Figure 6.50 Isolated Rut Verification in Field (I-95).....	149
Figure 6.51 Test Roadway Section on SR 307	150
Figure 6.52 Raw Longitudinal Rut Depth Profile (Blue) and Filtered profile (Red) (SR 307).....	150
Figure 6.53 Filtered Data (Red) and Homogeneous Segmentation Results (Blue) when MinLen = 10ft. and MinDiff = 1/8 in. (SR 307).....	151
Figure 6.54 Detected Isolated Ruts (SR307)	152
Figure 6.55 Field Verification (SR 307).....	152
Figure 6.56 An Isolated Rut (Spot #2) on SR 307	153
Figure 7.1 Illustration of Hausdorff Distance	162
Figure 7.2 Illustration of Buffered Hausdorff Distance Measure	164
Figure 7.3 Algorithm for Buffered Hausdorff Distance Measure.....	164
Figure 7.4 Overview of Experimental Tests.....	168
Figure 7.5 (a) Original Image; (b) Ground Truth Crack Map; (c) Dynamic Optimization Results (Score: 92.4423); (d) Canny Edge Detection Results (Score: 14.9668); (e) Crack Seed Verification Results (Score: 3.1376); (f) Iterated Clipping Results (Score: 64.0048)	171
Figure 7.6 (a) Original Ground Truth Image (b) Synthetic Ground Truth Image with added noise (c) Test Image 1 (d) Test Image 2 (e) Test Image 3 (f) Test Image 4	174

Figure 7.7 (a) Synthetic Ground Truth Image (b) Test Image 1 (Translation=1 Pixel)
(c) Test Image 2(Translation=2 Pixels) (d) Test Image 3 (Translation= 3 Pixels)..... 175

Figure 7.8 Range Image (Left), Ground Truth Image (Middle), and Dynamic
Optimization Detection Result (Right) for Image Collected on Hwy80 176

Figure 7.9 Ground Truth Image (Left) and Detection Result Image (Right) for Data
Collected on SR275 177

Figure 7.10 Ground Truth Image (Left) and Detection Result Image (Right) for Data
Collected On SR275 178

Figure 7.11 Synthetic Ground Truth Image and Crack Detection Result Image..... 179

Figure 7.12 (a) Original Image (Image 8) (b) Ground Truth Image (c) Canny Edge Image
(d) Statistical Thresholding Image (e) Multi-scale Wavelet Image (f) Dynamic
Optimization Image (g) Crack Seed Image (h) Iterative Clipping Image 183

Figure 7.13 (a) Original Image (Image 1) (b) Ground Truth Image (c) Canny Edge Image
(d) Statistical Thresholding Image (e) Multi-scale Wavelet Image (f) Dynamic
Optimization Image (g) Crack Seed Image (h) Iterative Clipping Image 184

Figure 7.14 (a) Original Range Image; (b) Ground Truth Crack Map; (c) Detected Cracks
at 0.78 (Score: 32.7443); (d) Detected Cracks at 0.84 (Score: 51.6057); (e) Detected
Cracks at 0.90 (Score: 96.3730); (f) Detected Cracks at 0.96 (Score: 38.7939). 186

Figure 8.1 A Gap between Two Solid Wood Boards to Create the Simulated Known
Crack Widths 195

Figure 8.2 Two Lighting Conditions 195

Figure 8.3 Crack Segmentation Results on Simulated Cracks: the One on the Left is Raw
3D Data, and the One on the Right is the Crack-Segmented Results (Tsai, 2010) 196

Figure 8.4 Test Results on Crack with Low-Intensity Contrast: (a) Roadway Image; (b)
3D Laser Data Collected during the Daytime; (c) Drack Segmentation Result (Daytime;

Score = 98.3); (d) 3D Laser Data Collected during the Nighttime; (e) Crack Segmentation Result (Nighttime; Score = 98.0) (Tsai, 2010)	197
Figure 8.5 Examples of Three Lighting Conditions	198
Figure 8.6 3D Laser Data and Corresponding Crack Segmentation Results on the Crack J for Three Lighting Conditions	199
Figure 8.7 Pavement Images with Oil Stain:	201
Figure 8.8 Pavement Images with Oil Stain and Other Noises:	201
Figure 8.9 Crack Detection Procedure.....	203
Figure 8.10 Ground Truth Image (Left) and Result Image (Right) for Sample 1 Collection on SR275.....	204
Figure 8.11 Ground Truth Image (Left) and Result Image (Right) for Sample 2 Collected on SR275.....	204
Figure 8.12 Twelve Locations Selected for Crack Width Measurement.....	206
Figure 8.13 Field Crack Width Measurement for Establishing Ground Truth.....	206
Figure 8.14 Measurement of Transverse Crack Width.....	208
Figure 9.1 Test Site on Pooler Parkway, Pooler near Savannah, Georgia.....	216
Figure 9.2 Labeled Crack.....	218
Figure 9.3 Locations of Labeled Cracks	218
Figure 9.4 Crack Maps of Cracks C1 and C2 at Different Times.....	219
Figure 9.5 Trend of Total Length of Selected Cracks	221
Figure 9.6 Trend of Average Width and Median Width of Selected Cracks.....	222
Figure 9.7 Crack Width Distributions of Selected Cracks.....	223

Figure 9.8 Eastbound and Westbound Subsections Total Crack Length Trends.....	225
Figure 9.9 Assumption of Average Crack Width Analysis	227
Figure 9.10 Eastbound Subsections Average Crack Width Trend	228
Figure 9.11 Westbound Subsections Average Crack Width Trend	230
Figure 9.12 Inconsistent Sampling Area/Region Caused by Vehicle Wandering	231
Figure 9.13 Inconsistent Sampling Area/Region Caused by Incorrect Pavement Marking Detection.....	232
Figure 9.14 Inconsistent Sampling Area/Region Caused by Shift of Data Collection in Longitudinal Direction.....	232

Table of Tables

Table 2.1 The Results for the Generalized Traffic Sign Detection Algorithm.....	25
Table 2.2 The Results for the Stop Sign and Speed Limit Sign Recognition Algorithms	29
Table 2.3 The Parameter Values Applied for the Tests on I-95 and 37th Street	34
Table 2.4 Traffic Sign Detection Results for the Tests on I-95 and 37th Street.....	34
Table 2.5 Preliminary Assessment of the Enhanced Traffic Sign Inventory Procedure ..	43
Table 4.1 Test Results for the 10 Type I Stop Signs on Field	72
Table 4.2 Test Result for the Two Type I Stop Signs in the Lab	73
Table 6.1 Deduct Values for Rutting in GDOT Protocol	90
Table 6.2 Rutting Severity Levels Defined by ODOT and PennDOT	91
Table 6.3 Survey in 2003 (McGhee, 2004).....	92
Table 6.4 Specifications for Scanning Laser Systems	93
Table 6.5 Aggregation Methods for Rutting Survey	93
Table 6.6 Rutting Reporting Methods	94
Table 6.7 COPACES Records in FY 2011 for SR 275 (Overall Project Rating is 80) ..	101
Table 6.8 Manual Survey Results on SR275	102
Table 6.9 Manual Measurement Results on Locations Chosen on SR275	102
Table 6.10 Comparison of Two Algorithms	107
Table 6.11 Laboratory Testing Results.....	107
Table 6.12 Standard Deviation of Rut Depth among 2,000 Profiles	108
Table 6.13 Field Testing Results	109

Table 6.14 Manual vs. Automated Survey Results on SR 275	110
Table 6.15 Characteristics of Outliers and Isolated ruts	123
Table 6.16 Accumulative Vehicle Wandering.....	124
Table 6.17 Selected Test Sites	126
Table 6.18 Reported Indicators (SR 275)	130
Table 6.19 Results for SR 275	131
Table 6.20 Results for SR 275 (Cont'd)	131
Table 6.21 Results for SR 275 (Cont'd)	132
Table 6.22 Results for SR67	133
Table 6.23 Results for SR67 (Cont'd)	133
Table 6.24 Results for SR67 (Cont'd)	134
Table 6.25 Indicators Reported (Benton Blvd. and I-95)	137
Table 6.26 Impact of Sampling Interval on Rutting Condition Assessment Accuracy ..	139
Table 6.27 Sampling Interval vs. Processing Time	140
Table 6.28 Data Storage Need per Inspection for every 100-Lanemile of the Highway Network.....	142
Table 6.29 Homogeneous Segmentation Results (I-95)	148
Table 6.30 Isolated Rutting Detection Results (I-95)	149
Table 6.31 Selected Homogeneous Segmentation Results (SR037)	151
Table 6.32 Isolated Rutting Detection Results (SR307).....	152
Table 7.1 Scoring Measures for GDOT Images	170

Table 7.2 Scoring Measures for Synthetic Image 1	171
Table 7.3 Scoring Measures for Synthetic Image 2	172
Table 7.4 Detection Evaluation Results for Figure 7.9 Using Buffer Hausdorff Distance Measure.....	177
Table 7.5 Detection Evaluation Results for Figure 7.10 Using Buffer Hausdorff Distance Measure.....	178
Table 7.6 Scoring Measure Results from Six Segmentation Methods	182
Table 8.1 Scores for the Controlled Tests.....	196
Table 8.2 Scores for the Second Field Tests.....	199
Table 8.3 Crack Width Measurement Validation Results for 12 Locations.....	207
Table 8.4 Crack Width Measurement Validation Results for Transverse Crack.....	209
Table 9.1 Pooler Parkway Traffic Volume	216
Table 9.2 General Information of Data Collection	216
Table 9.3 Crack Length and Width of Cracks C1 and C2 at Different Times.....	219
Table 9.4 Eastbound Subsections Total Crack Length Regression	225
Table 9.5 Westbound Subsections Total Crack Length Regression	226
Table 9.6 Eastbound Average Crack Width Increasing Ratio Regression	229
Table 9.7 Westbound Average Crack Width Increasing Ratio Regression	230

Executive Summary

The U.S. Department of Transportation Office of the Assistant Secretary for Research and Technology (USDOT/OST-R) and the Georgia Department of Transportation (GDOT) co-sponsored this research project to propose technology that supports the application and validation of commercial remote sensing and spatial information (CRS&SI) technology. GDOT supported the validation of intelligent transportation asset inventory, including traffic signs and asphalt pavement distresses using an intelligent Remote Sensing and GIS-based Asset Management System (RS-GAMS); the USDOT and the Georgia Institute of Technology (Georgia Tech) (through cost sharing) sponsored the integration and calibration of CRS&SI technology, which can be operated non-destructively at highway speed to improve roadway asset management, including traffic signs and pavements.

1. Research Focuses

The following research focuses address GDOT and other transportation agencies' needs regarding the use of CRS&SI technologies to improve the data collection, condition assessment, and management of the two types of transportation assets: signs and pavements.

- **Sign Assets**
 - Develop and validate an enhanced sign inventory procedure using an image-processing-based method and mobile LiDAR
 - Conduct a real-world, large-scale case study of traffic sign inventory and condition assessment
 - Conduct a feasibility study for using mobile LiDAR for sign condition assessment
 - Develop a prototype GIS-based sign management system
- **Pavement Asset**
 - Network-level rut depth measurement using the 3D laser
 - Identify isolated ruts using the 3D laser in support of effective localized treatment

- Develop and validate a quantitative method to scientifically evaluate the performance of different automatic pavement crack detection algorithms
- Validate the asphalt pavement crack detection using the 3D laser
- Analysis of crack propagation using long-term monitoring data

2. Research Outcome and Major Findings

The following conclusions are based on the research focuses for sign asset and pavement asset:

- **Sign Asset - Develop and validate an enhanced sign inventory procedure using an image-processing-based method and mobile LiDAR**

To improve the efficiency of traffic sign data collection, the automatic traffic sign detection and recognition algorithms using video log images and mobile LiDAR were tested using real data acquired from different transportation agencies and the Georgia Tech Sensing Vehicle (GTSV). The results demonstrate the potential for applying these automatic algorithms for establishing a cost-effective sign inventory method.

For the automatic traffic sign detection algorithm that used video log images provided by LaDOTD and the city of Nashville, more than 75% of the traffic signs were correctly detected. For the automatic traffic sign recognition algorithm that used video log images collected by the GTSV, 81% of the stop signs and 96% of the speed limit signs were correctly recognized. For the automatic traffic sign detection algorithm that used mobile LiDAR, more than 94% of the traffic signs were correctly detected based on 17.5 miles of the LiDAR data collected by the GTSV on I-95 near Savannah, Georgia. The LiDAR technology is very promising for sign data collection.

While the current algorithms cannot achieve a satisfactory detection and recognition accuracy for fully automatic data collection purposes, an enhanced procedure was proposed. The procedure enables the incorporation of these developed algorithms and technologies into the manual process method. The efficiency of the proposed procedure can be further enhanced by improving the detection and recognition

algorithms. The ultimate goal of developing full automation can be achieved when the accuracy of the algorithms reaches a satisfactory level. The preliminary assessment results are based on 47 traffic signs on I-95 and demonstrate a 40% improvement over the manual data collection process (i.e. the frame-by-frame manual review).

- **Sign Asset – A real-world, large-scale case study of traffic sign inventory and condition assessment**

A real-world, large-scale case study was conducted on I-285 to practice the enhanced procedure for traffic sign inventory and condition assessment. Other than the data collection productivity, the enhanced procedure greatly reduces the danger to engineers by enabling them to inventory signs without being exposed to roadway hazards, especially on interstate highways and near overhead signs. The case study identified 2,969 signs on I-285. The majority of the installed traffic signs on interstate highways are message signs that convey direction, destination, and service information (2,321 signs, 78.17%). A large percentage of installed traffic signs are mounted on overhead structures on interstate highways (643 signs, 21.66%). There are 252 signs in poor visual condition that require sign maintenance action based on the sign condition assessment.

Visual inspection on the high-resolution video log images reveals the possible reasons for damaged signs. The most frequently occurring sign damage type is surface failure on milepost signs due to truck gusts. The signs are located on concrete lane barriers, on roadsides, or on medians. These signs are damaged by the strong truck gusts that are created by fast-moving trucks. Another sign type suffering frequent damage is made up of exit signs that are damaged due to the instability of their dual posts. They are located at the interstate exits. The inspection shows that the signs are damaged by the unbalanced vibration and twisting of the dual posts. In addition, post failures frequently occur due to direct-crash impacts or soft bases. The only type of overhead sign that is damaged is D3-1 (i.e. street name sign) mounted on bridges. The majority of D3-1 signs are damaged due to surface failure (i.e. color fading and erosion).

Again, this pilot study has demonstrated that the enhanced procedure can save time and money on sign inventory data collection.

- **Sign Asset - Feasibility study of using mobile LiDAR for sign condition assessment**

To validate the use of mobile LiDAR for sign retroreflectivity condition assessment, ten Type I stop signs collected in a community in Savannah, Georgia have been tested to demonstrate the feasibility of the tested LiDAR-based method. The ground truths were established using both nighttime visual inspection and retroreflectometer measurement. The retroreflectivity condition assessment results using the proposed method are consistent with all of the nighttime visual inspection results; they match 90% of the retroreflectometer measurement results in differentiating good and bad sign retroreflectivity conditions. Using the developed mobile LiDAR-based method, a traffic sign retroreflectivity condition assessment can be conducted cost-effectively at highway speed.

- **Sign Asset - Develop a prototype GIS-based sign management system**

A prototype GIS-based sign management system was developed in this study. The objective is to demonstrate the capability of a GIS platform for integrating different data sources, including traffic sign data, video log images, and GIS maps, managing important traffic sign data, and supporting various sign maintenance practices. Though this prototype is not a comprehensive, final product, it is the foundation for the future implementation of a full GIS-based sign management system.

- **Pavement Asset - Network-level rut depth measurement using the 3D laser**

Rutting is one of the important pavement performance measures required by the Highway Performance Monitoring System (HPMS), and every state DOT is required to submit the data to the Federal Highway Administration (FHWA) annually. However, the point-based laser measurement methods (e.g. 3 points) commonly used by state DOTs may not be reliable due to vehicle wandering, variation of rut locations, and rut shapes. Preliminary test results show that 3-point and 5-point rut

bar systems significantly underestimate rut depth, and the average relative measurement errors for 3-point and 5-point rut bar systems are about 63% and 44%. If the number of sensors is more than 25, the relative measurement error drops constantly to a value below 10%. With a 39-point, equally-spaced rut bar system, the relative measurement error is about 8%.

Unlike the traditional manual and rut-bar measurement methods, the 3D laser has virtually 100% coverage in a travel lane width (4,000 range measurements for a pavement 4 meters wide, with a 1 mm resolution in transverse direction). It provides a more accurate and reliable method for measuring rut depth than the traditional rut-bar method. According to laboratory and field tests (field tests were conducted on several roadway sections selected in Pooler, Georgia), the 3D laser can provide rut depth measurements with satisfactory accuracy. The measurement error is within $\pm 3\text{mm}$ and satisfies the accuracy requirements of many state transportation agencies. It is capable of performing project-level and network-level rutting condition assessment.

Besides providing the information needed for network-level rutting condition assessment, the integrated 3D laser provides much denser rutting data. In cooperation with GDOT liaison engineers, case studies were performed on several state and non-state routes using the integrated 3D laser. A systematic approach was developed to aggregate the raw, continuous rut depth measurements on each pavement segment and to generate different statistical indicators that can provide added value to engineers of state DOTs. The 3D laser can provide more useful network-level rutting data and better support for network-level maintenance decision-making than can GDOT's past rutting survey results. GDOT liaison engineers suggested that the 60th percentile rut depth might be a good rutting indicator on each pavement segment. Again, the developed technology can help GDOT meet MAP-21 performance measure requirements on interstate highways.

- **Pavement Asset - Identify isolated ruts using the 3D laser in support of effective localized treatment**

The accurate and dense rutting information acquired by the 3D laser provides an opportunity to further identify isolated ruts, which has never been done in the past due to the lack of continuous and accurate rutting measurements in the longitudinal direction. The identification of isolated ruts can better support effective, low-cost localized pavement treatments and the efficient use of the currently stringent pavement preservation funds. After discussing these issues with GDOT liaison engineers, four sets of criteria were proposed to define an isolated rut: rut depth requirement, rut length requirement, rut division criterion, and rut termini determination criterion. Case studies on two selected roadway sections show the developed approach is applicable to and promising for use in transportation agencies' pavement preservation practices.

- **Pavement Asset - Develop and validate a quantitative method to scientifically evaluate the performance of different automatic pavement crack detection algorithms**

Pavement distress segmentation is identified as a crucial step for automatic distress detection and classification. Researchers have developed many segmentation algorithms, but it is difficult to compare the performance of different algorithms efficiently without an accurate quantitative method. Also, it is hard for a transportation agency to perform a quality check when automatic pavement crack detection is applied to its data collection. To address these issues, a novel quantification method based on the buffered Hausdorff distance was developed to evaluate the performance of distress segmentation algorithms.

The proposed method was compared with four other common quantification methods (Mean Square Error (MSE), Statistical Correlation (SC), Receiving Operating Characteristic (ROC), and Hausdorff distance) on both real data (raw downward pavement images acquired from GDOT) and synthetic data. It was found that the proposed buffered Hausdorff scoring measure accurately reflected the

observed performance of the segmentation techniques and outperformed the other three quantification methods. Both MSE and SC are not sensitive to the relative proximity of the crack pixels between the segmented image and the ground truth image. The Hausdorff distance measure is very sensitive to outliers and is heavily influenced by isolated noise pixels that are far away from crack pixels. Thus, it does not accurately reflect the overall performance of a segmentation method. ROC is a useful scoring measure, but it suffers due to the fact that across a certain boundary, all crack pixels are either detected as true defects or false alarms. The proposed buffered Hausdorff distance measure gave evaluation results consistent with the visual performance inspection of different segmentation techniques. It also achieved good score separation to distinguish between the performance of different methods.

Two potential applications of the proposed buffered Hausdorff distance measure were also explored, including the selection of proper distress segmentation algorithms and the optimization of algorithm parameter settings. Because the distress classifier definitions vary among states and regions, the testing of segmentation precision is of critical importance in assessing the reliability of pavement distress segmentation algorithms. The proposed method provides a solution for transportation agencies to quantitatively evaluate and choose the proper pavement distress segmentation algorithm based on their own survey requirements and actual performance of the crack detection/segmentation algorithm. Also, the proposed method provides an opportunity to optimize the parameter setting for each segmentation algorithm, since it gives sortable scoring measures for the algorithm performance under each parameter setting. Therefore, the proposed method is expected to help transportation agencies determine their automated pavement distress survey strategies.

- **Pavement Asset - Validate the asphalt pavement crack detection using the 3D laser**

The 3D laser is insensitive to different lighting conditions, low-intensity contrast, and pavement oil marks, unlike the traditional line scan camera. Laboratory tests on fabricated crack samples show consistent detection results in the daytime and

nighttime. Cracks with widths greater than 2 mm can be detected easily. However, a hairline crack with a width of approximately 1 mm is hard to detect due to the current resolution of the integrated 3D laser. Field tests on Georgia SR 80 were conducted under three different lighting conditions, daytime with shadow, daytime without shadow, and nighttime. The crack detection results show very good consistency and the average difference of performance scores is less than 2%. Though low-intensity contrast is a challenge for the traditional line scan camera for crack detection, the test result shows no difficulty for the integrated 3D laser as long as the crack is distinct when surface depth changes. Similarly, oil stains can be effectively removed from a possible crack that is falsely detected because of indistinguishable depth change.

To validate the crack width measurement accuracy, 12 spots on two longitudinal cracks were selected on SR 275 near Savannah, Georgia with manually measured crack width as the ground truth. Cracks with widths greater than 2 mm can be detected correctly. However, cracks equal to and less than 1 mm cannot be detected correctly. Compared to the manually measured results, crack widths were captured well by the automatic method. The maximum absolute difference of crack width was 1mm, and the average absolute difference was 0.4 mm. This result shows a promising potential to measure crack width for further crack classification tasks. While the 3D-line-laser-provided software can effectively detect the longitudinal crack widths, the transverse crack width cannot be reliably detected because the current data resolution in the driving direction is about 5 mm. Thus, the alignment angles of laser line to cracks affect the accuracy of crack width measurements. Improvement is needed in this area.

- **Pavement Asset - Feasibility Study of Crack Deterioration Behavior Using 3D Laser Data**

A feasibility study of asphalt pavement crack deterioration behavior was performed using long-term monitoring 3D laser data that has been collected since 2011 on a one-mile test site on Pooler Parkway near Savannah, Georgia. First, the crack growth in length and width for two selected individual cracks was analyzed; second, the crack

growth of clustered cracks in 0.1-mile subsections was studied. These two studies demonstrated the use of long-term monitoring 3D laser data to explore the detailed crack deterioration behavior at the levels of individual cracks and clustered cracks, which can be used to support a) fundamental study of pavement mechanics and deterioration behavior, b) validation of current pavement design methods and development of new design concepts and methods, c) determination of adequate treatment methods and timing, d) development of accurate and reliable pavement deterioration models, and e) development of cost-effective pavement maintenance programming, for example an intelligent crack sealing planning.

3. Recommendations for Future Research and Implementation

The following suggest the future research and implementation:

- The large-scale case study on I-285 traffic sign inventory and condition assessment shows that the proposed enhanced sign inventory procedure using video log images and mobile LiDAR is very promising and can greatly reduce the effort of manual sign data collection especially on interstate highways. It is suggested that, using the proposed and validated method, a comprehensive sign inventory could be done for the entire 2,500-survey-mile interstate highways in Georgia (note: a special research study, RP 15-11, has been awarded by GDOT to implement the sign inventory on all interstate highways)
- Sign retroreflectivity condition assessment is of great concern in GDOT and other state agencies. The current preliminary study on engineer grade STOP signs show that mobile LiDAR could be a promising alternative to the time-consuming manual method for sign retroreflectivity condition assessment. Further tests on more engineer grade STOP signs with different retroreflectivity conditions are still needed. Also, tests on other types of traffic signs, e.g. speed limit signs, warning signs, etc., with different sheeting materials are needed to study the sensitivity of the proposed method on different colors and sheeting materials.

- The currently developed prototype of the GIS-based sign management system has demonstrated the capability to integrate different spatial and non-spatial data sources, such as GIS maps, roadway images, and sign data, and improve sign management and maintenance practice. Next, a pilot study is suggested to further materialize the functionalities by using a large-scale dataset and introducing the GDOT's practice on sign management and maintenance.
- The comprehensive validation of network-level rutting measurement and isolated rutting detection shows that the 3D laser technology can be used to conduct the statewide rutting data collection. In considering the difficulty for measuring rut depth on interstate highways, especially on the high-traffic-volume highways like I-285, it is suggested to firstly conduct rutting data collection for the entire 2,500-centerline-mile interstate highways. The collected data can be used for two purpose. First, the data can be fed into COPACES database. Thus, the current manual rutting data collection on interstate highway can be replaced by the automatic method. Second, the full-coverage rutting data can further be used to identify isolated spots where rutting is a problem and local treatment can be done.
- The validated crack detection using 3D laser data shows that this technology is capable of collecting cracking data. Along with the validation of crack classification that is under development in an on-going research project (RS-GAMS Phase 2), the results can be fed into COPACES, which is very useful for high-traffic-volume interstate highways. After the validation of crack classification is done, it is suggested to conduct a cracking survey for the entire interstate highways in Georgia.
- Lateral wandering of data collection vehicle causes the variation of captured pavement surface area. To mitigate the impact of this issue, more robust algorithms are needed for pavement marking detection, even in the case when a pavement marking is missed. Furthermore, a mechanism is needed to facilitate a vehicle driver to conveniently maintain the vehicle in the middle of a lane while sensing data is being collected.

- The evaluation of crack width increasing rate was based on an assumption that all fine cracks are newly developed cracks without further checking if they were actually new cracks or not. This assumption could create some data variation because the tight, old cracks could, also, be excluded from the analysis. Thus, developing a crack registration method to spatially align cracks that are collected at different timestamps is recommended; then, the behavior of crack width changing can be studied for spatially registered individual cracks or clustered cracks.
- The current 3D laser technology is capable of collecting project-level and network-level pavement distress data for purpose of pavement management and maintenance. However, studying detailed pavement crack deterioration behavior requires higher resolution of 3D laser data to detect finer cracks. The 3D laser system used in this study has a resolution of 5 mm at longitudinal direction, which limits the capability to detect and measure the width of fine transverse cracks. Thus, there is still a need to enhance the resolution of 3D laser system. Fortunately, some manufacturers started to develop the new 3D laser system with 1 mm resolutions.
- In current study, length-weighted average and median (50th percentile) crack widths are used to analyze the crack-width-related crack propagation. To provide more informative statistics that can be more relevant to pavement maintenance, rehabilitation, and reconstruction (MR&R), other factors, e.g. 75th, 90th, or 95th percentiles, can be used to represent the overall crack width. Further discussion with pavement engineers and experts will be needed.

Chapter 1 Introduction

1. Background and Research Need

The U.S. Department of Transportation (USDOT) and the Georgia Department of Transportation (GDOT) co-sponsored this research project to propose technology that supports the application and validation of commercial remote sensing and spatial information (CRS&SI) technology. GDOT supported the validation of intelligent transportation asset inventory, including traffic signs and asphalt pavement distresses, using an intelligent Remote Sensing and GIS-based Asset Management System (RS-GAMS), while USDOT and the Georgia Institute of Technology (Georgia Tech) shared the cost and sponsored the integration and calibration of CRS&SI technology, which can be operated non-destructively at highway speed.

Figure 1.1 illustrates four major components included in the architecture of the proposed RS-GAMS. The four major components are 1) the sensing system; 2) data processing and collection; 3) data integration and management; and 4) decision support. With the advance of sensing technology, many advanced sensors, including 2D imaging, 3D lasers, 3D LiDAR, and unmanned air vehicles (UAV), as shown in the first component in Figure 1.1, are available for use in transportation and asset management. However, there is an urgent need to develop a cost-effective means to process this overwhelming amount of data, as shown in the second component in Figure 1.1. For example, engineers are interested in sign information and crack information (e.g. crack width, length, position, etc.) rather than raw images and laser points. As part of the comprehensive transportation asset management system, CRS&SI technologies play an important role in collecting various transportation asset data, including traffic signs, pavement surface conditions, roadway characteristics, etc., that critically support data-driven decision-making. GIS is an excellent platform with which to integrate different data sources and provide convenient spatial data management functionalities. In the past, manual processing has been the major means of data collection; however, it is labor-intensive, time-consuming, subjective, and inaccurate. As a result, the subsequent decision-making lacks reliability. With the advancement of CRS&SI technologies, the data collection process can be dramatically improved with regard to its speed, comprehensiveness, accuracy, and reliability. However, the application of a new

technology always lags behind its development due to the end users' concern about its usability and the risk resulting from the failure of significant investment. This technology gap can only be bridged by comprehensive testing and validation. This research project addresses this issue and aims to validate the applications of image processing and mobile light detection and ranging (LiDAR) technology for collecting traffic sign data; the project also addresses using 3D line laser imaging technology (3D laser) for assessing pavement surface distresses, including rutting and cracking. This research project (RS-GAMS Phase 1) only focuses on validating the improvement of condition assessment and management by using the state-of-the-practice CRS&SI technologies on traffic signs and asphalt pavement surface distresses, as shown by the light grey blocks in Figure 1.1. The dark grey blocks in Figure 1.1 are tasks for an on-going project sponsored by USDOT and GODT (RS-GAMS Phase 2; RP 12-10).

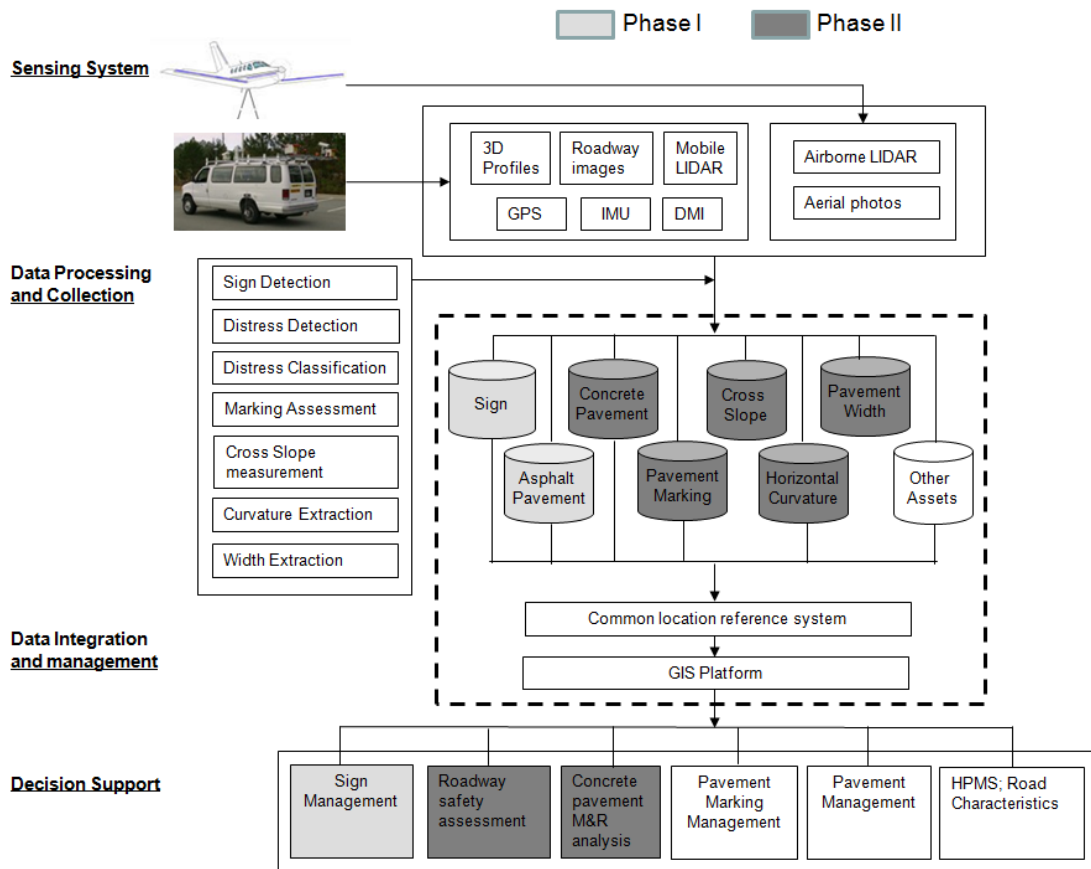


Figure 1.1 RS-GAMS Architecture

The challenges and research needs for inventory, condition assessment, and management of these two types of assets are discussed below.

- **Traffic Sign Asset**

Roadway traffic signs are important for roadway safety and traffic regulation. It is crucial for transportation agencies to maintain an inventory of signs in compliance with the revised Manual on Uniform Traffic Control Devices (MUTCD) that was published in 2012.

However, sign inventory data collection is time-consuming and costly, even when using the currently available video-log-based method. This is because tremendous effort is needed to extract sign data, which is done one image at a time; this process has hindered the advancement of traffic sign inventory using roadway video log images. There is a need to develop a technology with an enhanced procedure to batch-process millions of roadway images instead of reviewing them frame by frame. Sign retroreflectivity condition is a major concern to highway agencies. The traditional measurement method is very time-consuming and costly because a state highway agency needs to survey its millions of signs. Thus, this project also explores the possibility of evaluating a sign's retroreflectivity condition at highway speed using mobile LiDAR.

- **Asphalt Pavement Asset**

In the past, numerous automatic pavement distress detection algorithms have been developed by using 2D images acquired from line scan cameras. However, accurately and reliably detecting pavement distresses remains a challenge because of the inability to detect distresses under various lighting conditions (such as contrasts) and roadway environments. A high-resolution, downward, 3D laser technology operated at highway speed has been recently developed and is commercially available. Because the 3D laser captures the range (depth) change instead of lighting reflectance intensity on pavement surfaces, it can better address the important lighting challenges encountered in the past, and it can improve the existing automatic pavement distress detection methods. Scientific validation is needed to evaluate the 3D laser's capabilities to detect pavement distresses of different roadway environments (e.g. lighting, shadows, etc.) and different pavement conditions (e.g. severities ranging from fine to large cracks). Rutting is one of the important pavement performance measures specified in the Highway Performance Monitoring System (HPMS) and must be annually

submitted to FHWA by state DOTs. The capability to reliably and accurately detect and measure rutting using the 3D laser is also validated in this study. The validation of the 3D laser will be indispensable for transportation agencies as they consider applying it to pavement distress detection activities.

2. Introduction to Georgia Tech Sensing Vehicle

To validate the pavement and roadway asset data collection using CRS&SI technologies, a sensing vehicle, the Georgia Tech Sensing Vehicle (GTSV), was developed by integrating the state-of-the-practice sensing systems. Figure 1.2 shows the systematic diagram of the GTSV. This integrated system incorporates two primary sub-systems, including 3D laser and mobile LiDAR that collect the pavement distress data and the roadside appurtenance data. The mobile LiDAR also collects the precise GPS coordinates for the positioning purpose of the sensing vehicle. The additional power sub-system is used to supply uninterruptible power for both of the data collection sub-systems. To support the comprehensive validation tasks, both the supporting frames and the configurations of each individual sensor (e.g. height, orientation, etc.) can be flexibly adjusted for different configurations. The following introduce these two sub-systems in more detail.

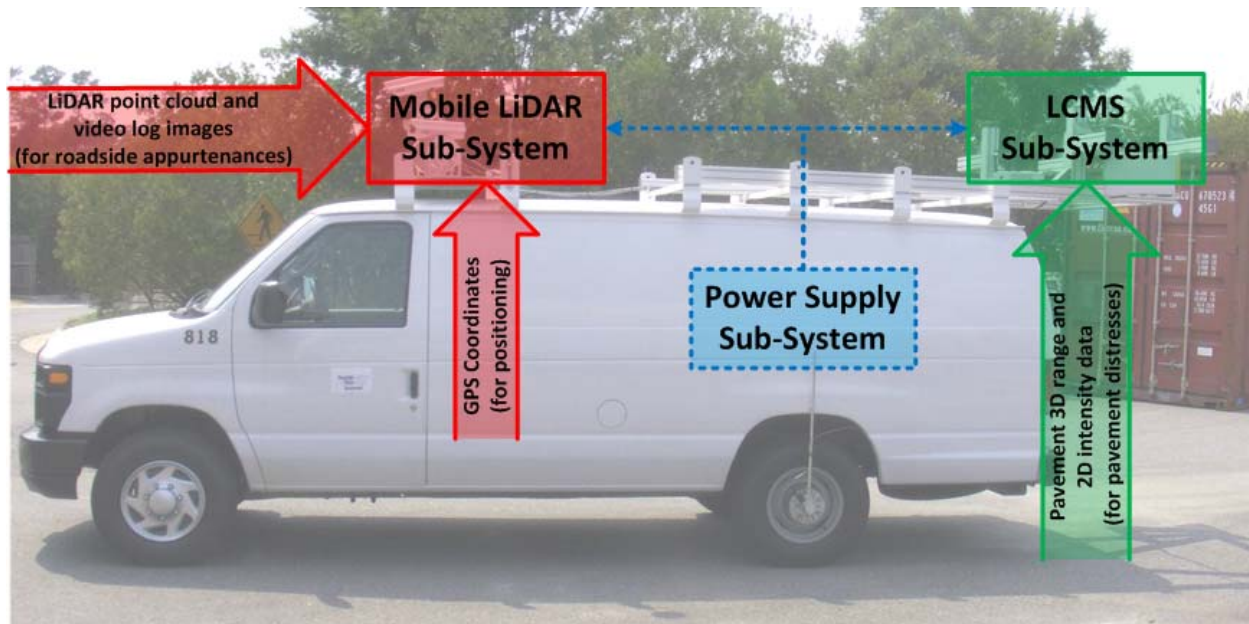


Figure 1.2 Systematic Scheme for the GTSV

2.1 Introduction to 3D Laser System

The integrated 3D laser system is developed by INO, a leading company headquartered in Canada, and marketed by the Pavemetrics System Inc. The 3D laser consists of three primary components, including the imaging component, the distance measuring component, and the data processing component. The imaging component is used to capture the pavement texture data using external infrared laser illumination and the spatial high intensity camera. This component consists of two separate laser sensors to cover a full-lane width. Each laser sensor includes a dedicated infrared laser illumination and a high-intensity area scanning camera. The distance measuring component provides a data-capturing signal by using a Distance Measurement Instrument (DMI), which is user-customizable. The data processing component computes the captured data into 3D range results using a high performance workstation. Figure 1.3 illustrates the 3D laser on the GTSV.

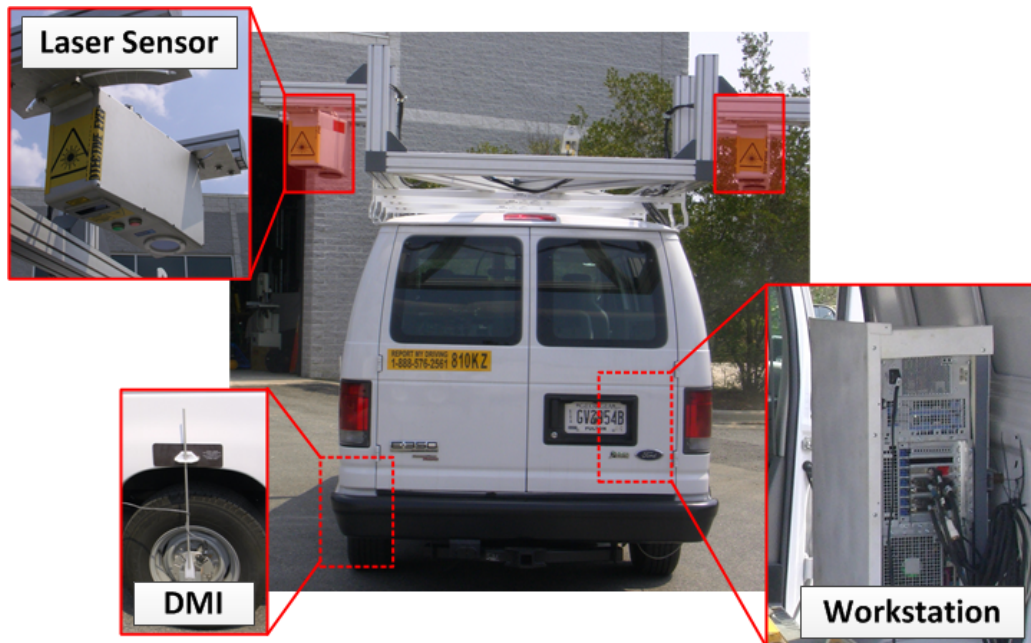


Figure 1.3 Components of 3D Line Laser System Integrated on the GTSV

As shown in the rear view of Figure 1.4, the two laser sensors are installed on each side of the roof at the back of the GTSV. The Field Of View (FOV) of the two sensors covers a full-lane width, i.e. 4 m. To avoid overlooking transverse cracks in the pavement, both sensors are

configured at approximately 15 degrees clockwise to the transverse direction, as shown in the top view of Figure 1.4. During data collection, each laser sensor uses a high-powered laser line projector with a customized filter to generate a fine infrared laser line illuminating a strip of the pavement. The corresponding spatial high intensity camera captures the deformed laser line on the pavement. From the captured image, range measurements are extracted.

The following describes the resolutions in x (transversal direction), y (longitudinal direction), and z (elevation) directions for the integrated 3D laser system. With a two-sensor setup, the 3D line laser produces 4,160 3D data points per profile (2,080 pixels per sensor) covering a 4 m pavement width. Therefore, the resolution in x direction is less than 1mm (4 m / 4,160 points). The resolution is 0.5 mm in z direction. The highest resolution in y direction depends on the shuttle speed of the high intensity camera and driving speed. At a speed of 100 km/h, the minimum interval of transverse profiles is about 5 mm because the shuttle speed of the current system is 5,600 Hz. To acquire smaller interval, the driving speed has to be reduced.

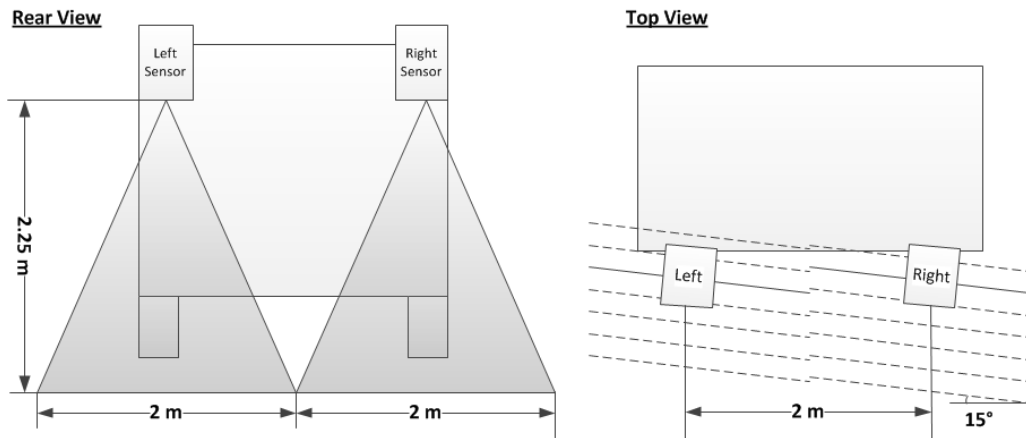


Figure 1.4 Configuration of 3D Line Laser System on the GTSV

2.2 Introduction to Mobile LiDAR System

A mobile LiDAR system for data acquisition on a mobile platform, e.g. vehicle, train, etc., has been developed by Trimble Inc. and is integrated on the GTSV. The selected mobile LiDAR system has high accuracy and good re-configuration flexibility. The LiDAR systems in previous studies are either the airborne LiDAR system with x - y accuracy of meter level or a stationary terrestrial LiDAR system that is not mobile. The mobile LiDAR system integrated on the GTSV can be operated at highway speed with an accuracy of sub-10 cm in x , y and z directions.

The mobile LiDAR system integrated on GTSV consists of three primary components, including the LiDAR sensor, the precise positioning system, and the imaging system. The LiDAR sensor is used to acquire the point cloud of the target, e.g. a traffic sign. Each point includes the accurate distance from the sensor to the target, the relative angle of the laser beam with respect to the LiDAR sensor, and the corresponding reflectance intensity. The precise positioning system is used to acquire accurate GPS coordinates and poses for the LiDAR sensor. Thus, the GPS coordinates for each point from the LiDAR sensor can be derived. To acquire the precise GPS coordinates, the positioning system is composed of a GPS, an Inertial Measurement Unit (IMU), and a DMI. As most of the LiDAR sensors can only acquire point cloud data without any color information, the imaging system is typically integrated with the LiDAR sensor to provide corresponding color images. Figure 1.5 illustrates the mobile LiDAR system integrated on GTSV.

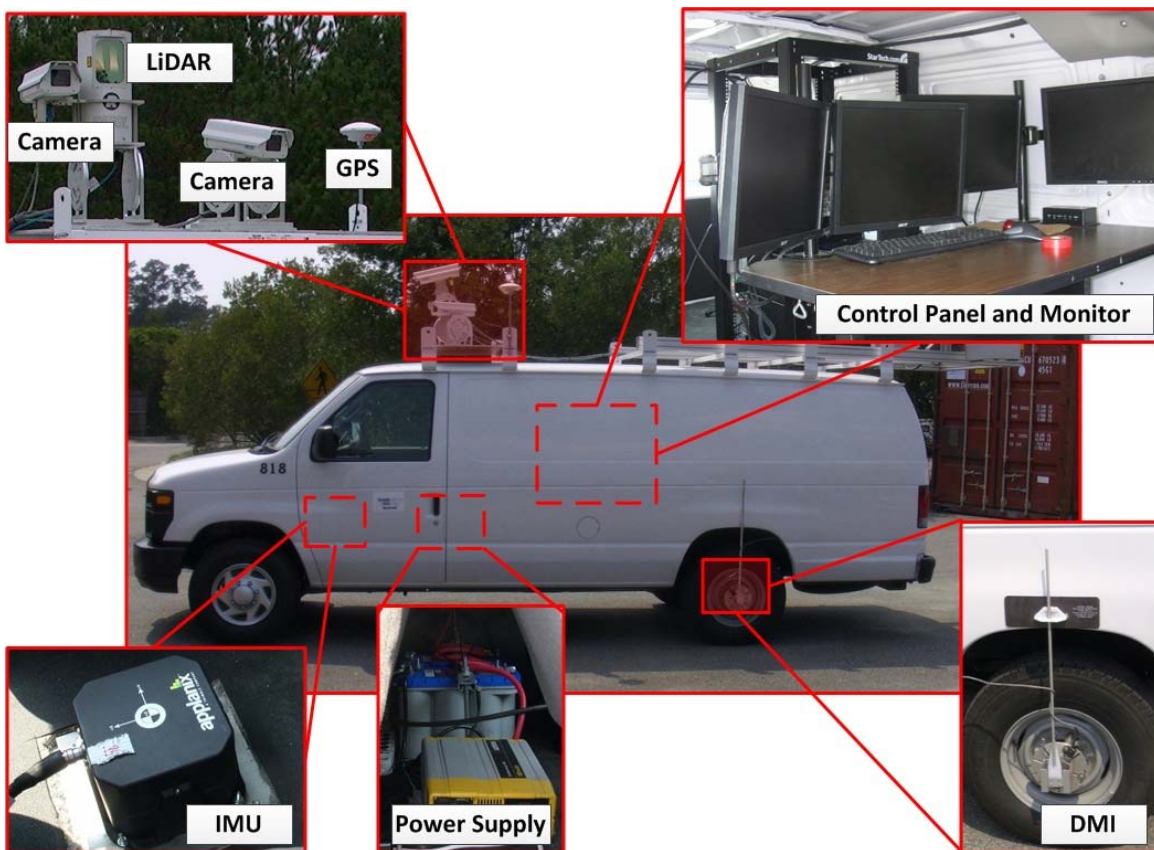


Figure 1.5 Mobile LiDAR System Integrated on the Georgia Tech Sensing Vehicle

LiDAR sensors can be configured with different orientations for different targets. In this project, the purpose of introducing the mobile LiDAR system is to identify the feasibility of this technology for traffic sign asset data collection, including traffic sign inventory and condition assessment. Therefore, the LiDAR system is vertically oriented on the sensing vehicle and has a parallel line scanning pattern. Figure 1.6 shows this configuration and the scanning mechanism. This system can produce 10,000 laser points per second. As the vehicle moves in the longitudinal direction, the scanning line of the LiDAR system is aligned perpendicularly to the ground. The scanning range is $\pm 40^\circ$ to the horizontal direction, which produces an 80° fan covering the roadside. Currently, the frequency of the LiDAR system is configured at 100 Hz and 100 points within each scan, while the LiDAR heading angle is configured at 20° . Figure 1.6 shows the data acquisition. For example, if a standard 48 in. \times 60 in. speed limit sign is mounted on the roadside with a lateral offset of 12 ft. (3.6 m) to the edge of the road, the current configuration will be able to acquire a point cloud containing approximately 12×8 points at 60 mph (100 km/h). As previously mentioned, the configuration can be adjusted to accommodate different data collection scenarios.

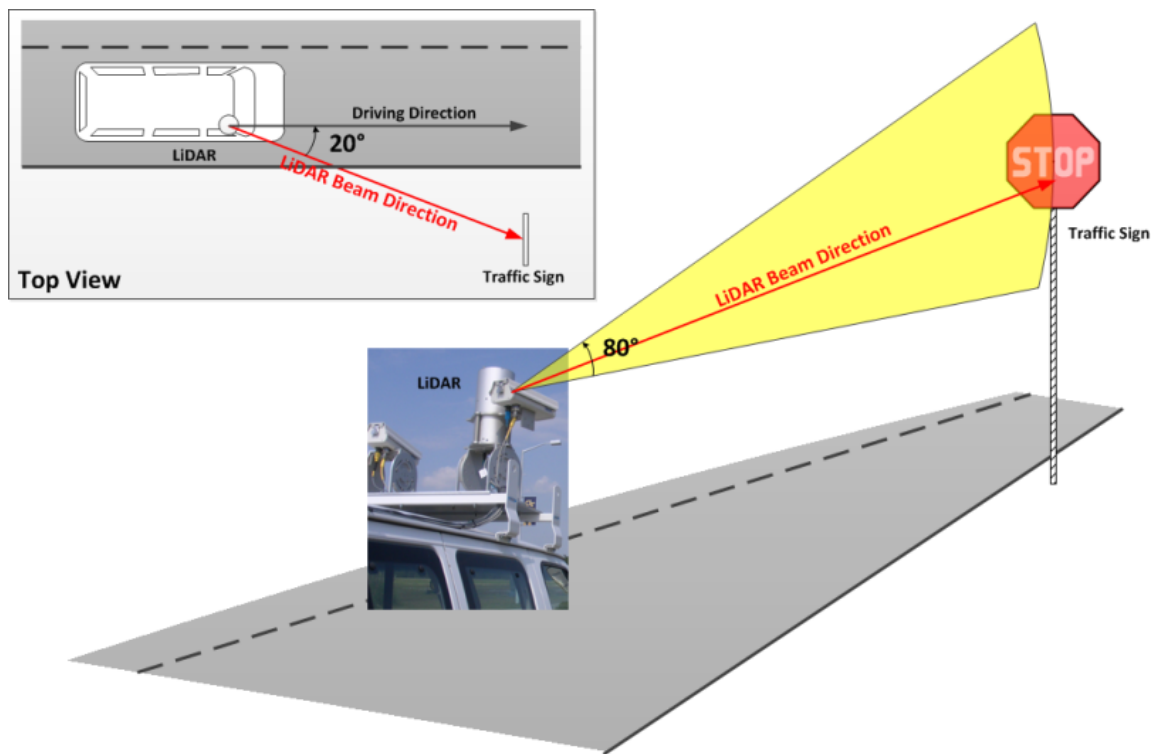


Figure 1.6 Configuration of the Mobile LiDAR System and Scanning Mechanism

3. Research Focuses

The following research focuses address GDOT and other transportation agencies' needs regarding the use of CRS&SI technologies to improve the data collection, condition assessment, and management of the two types of transportation assets: sign asset and pavement asset.

- **Sign Asset - Develop and validate an enhanced sign inventory procedure using an image-processing-based method and mobile LiDAR**

Although video-log-based sign inventory can help reduce roadway hazards and improve safety during field data collection, the sign data collection procedure still remains a challenge because it is time-consuming for engineers to visually review (frame by frame) the large volume of images collected. Thus, there is an urgent need to enhance the efficiency of sign data collection using image data. With the advancement of image processing algorithms and mobile LiDAR, it is possible to speed up this process by incorporating them into a well-designed data collection procedure. In this study, an enhanced sign inventory procedure was developed; image-processing algorithms and mobile LiDAR were incorporated to improve the data collection efficiency.

- **Sign Asset – A real-world large-scale case study on traffic sign inventory and condition assessment**

To practice the enhanced sign inventory procedure using video log images and mobile LiDAR, a real-world, large-scale case study was conducted on I-285. Video log images and mobile LiDAR were collected using the GTSV. All the signs, including both roadside signs and overhead signs, were collected. A visual condition assessment was also conducted based on GDOT's current practice.

- **Sign Asset - Feasibility study of using mobile LiDAR for sign retroreflectivity condition assessment**

Sign condition is mainly indicated by its retroreflectivity. The assessment methods suggested by the new MUTCD are labor-intensive and time-consuming. Thus, in this study, the feasibility of using mobile LiDAR for sign condition assessment was investigated. The basic

research steps are as follows: 1) measure its retro-reflectivity using a retroreflectometer and assess its condition based on MUTCD defined criteria; 2) collect the mobile LiDAR data for a sign and calculate its representative retro-intensity; and 3) correlate the measured retro-reflectivity and retro-intensity. A relationship between these two types of measurements was first established.

- **Sign Asset - Develop a prototype GIS-based sign management system**

GIS is widely used for managing spatially-referenced roadway assets. In this study, a prototype GIS-based sign management system was developed to integrate different data sources, such as collected traffic signs, roadway images, road maps, and satellite images. A set of management tools was implemented to perform spatial query, attribute query, and data reporting.

- **Pavement Asset - Network-level rut depth measurement using the 3D laser**

Through laboratory tests and field tests, three major aspects were investigated and validated: 1) Accuracy of the rut depth measurement with known objects using the integrated 3D laser. This is the foundation for performing two validations (Items 2 and 3 that follow). 2) Assessment of the traditionally used rut-bar measurement errors. A rut-bar system uses 3 to 37 distinct laser sensors to measure pavement rutting. 3) Assessment of the capability of network-level rut depth measurement using a 3D laser. To perform this study, large-scale field tests were conducted.

- **Pavement Asset - Identify isolated ruts using the 3D laser in support of effective localized treatment**

Isolated ruts are important pavement distresses that affect pavement structural integrity and driving safety. In the past, this type of distress has been hard to detect due to the lack of continuous pavement rutting measurements. Using 3D laser data in this study, a systematic approach was developed to identify the isolated ruts and to measure their maximum depth, length, area, and volume. This information could be useful for a transportation agency to determine effective treatment methods and to assess roadway safety.

- **Pavement Asset - Develop and validate a quantitative method to scientifically evaluate the performance of different automatic pavement crack detection algorithms**

Automatic pavement crack detection algorithms have been widely studied in the past. However, the performance of these crack detection algorithms has not been scientifically validated. To address this problem, a quantitative method, the buffered Hausdorff distance based scoring method, was developed and validated in this study.

- **Pavement Asset - Validate the asphalt pavement crack detection using the 3D laser**

This study validated the capability of asphalt pavement crack detection using the 3D laser under different lighting conditions and in low-light intensity contrasts. Since the lighting condition has been the major issue in previous automatic pavement crack detection methods using line scan cameras, different lighting conditions were investigated and validated in laboratory tests and field tests. In the laboratory tests, cracks with different widths were simulated to validate the performance and capability of the current 3D laser for crack detection. Since crack width is a major factor for rating pavement surface condition, this study further validated the crack width measurement accuracy using the data acquired from the 3D laser and comparing the calculated results with the manually measured ground truth.

- **Pavement Asset - Feasibility Study of Crack Deterioration Behavior Using 3D Laser Data**

This study analyzed the asphalt pavement crack deterioration behavior using long-term monitoring 3D laser data. The research results could be used to support a) fundamental study of pavement mechanics and deterioration behavior, b) validation of current pavement design methods and development of new design concepts and methods, c) determination of adequate treatment methods and timing, d) development of accurate and reliable pavement deterioration models, and e) development of cost-effective pavement maintenance programming, for example an intelligent crack sealing planning.

4. Report Organization

This report summarizes the results of the research project co-sponsored by USDOT and GDOT. Though the results of validating data collection have been incorporated into the report for USDOT in consideration of completeness, the feasibility study of crack deterioration behavior and the large-scale case studies on sign data collection on Interstate 285 (I-285) were exclusively contained in this report for GDOT.

This report is organized into ten chapters. Chapter 1 summarizes the research background, need, and approaches. Chapter 2 presents validation results for automatic traffic detection and recognition using image processing technology and mobile LiDAR. Chapter 3 presents a large-scale case study of sign data collection and condition assessment on I-285. Chapter 4 presents the preliminary study on using mobile LiDAR to assess traffic sign retroreflectivity conditions. Chapter 5 introduces a prototype GIS-based sign management system. Chapter 6 presents the validation results for pavement rut depth measurement at the network level and isolated rut detection using the 3D laser. Chapter 7 presents a method to quantitatively evaluate the performance of different automatic pavement crack detection algorithms. Chapter 8 presents the validation results for crack detection using the 3D laser. Chapter 9 presents the feasibility study of crack deterioration behavior using long-term monitoring data. Chapter 10 summarizes the conclusions and makes recommendations for future research.

Chapter 2 Validation of Traffic Sign Inventory Using Video Log Images and Mobile LiDAR

1. Introduction

Traffic signs provide vital guidance to road users regarding traffic regulation, adequate road hazard warnings, destination and other geographic information, and temporary road conditions. State DOTs like GDOT invest very heavily in traffic signs. To better manage traffic signs, “a coordinated program of policies and procedures which ensure that the highway agency provides a sign system that meets the need of the user most cost-effectively within available budget and constraints” is required (McGee & Paniati, 1998).

As one of the most important elements of a traffic sign management system, traffic sign inventory provides the fundamental database for the traffic sign management system. It is a collection of data containing essential traffic sign information, including locations and attributes (e.g. types, dimension, post, etc.). Advancements in the development of information technology (IT) and emerging sensing devices, including GPS/GIS, computer vision, and LiDAR have promoted the technologies to such a level that the intelligent traffic sign inventory has now become possible.

This chapter assesses existing automatic traffic sign inventory methods. A literature review was first conducted to identify the state-of-the-practice and state-of-the-art research. Three automatic traffic sign detection and recognition methods using video log images and an automatic traffic sign detection method using LiDAR were critically assessed. Finally, based on the results of critical assessment, an enhanced automatic traffic sign inventory procedure is proposed to adapt the existing automatic methods and maximize their utilization in the current practice of state DOTs.

2. Literature Review of Traffic Sign Inventory

A comprehensive and reliable traffic sign inventory is indispensable for providing state DOTs with the fundamental information they need to manage their sign assets and support their subsequent maintenance decision-making.

2.1 Current Practice

Based on a literature review, the current traffic sign inventory method carried out by state DOTs is, primarily, a manual process that includes a field engineer's physically collecting a sign's attributes in the field. Only a few transportation agencies use a semi-automatic method to collect sign attributes. The semi-automatic method uses an automatic traffic sign data collection system, which is comprised of a data acquisition vehicle and a manual process to extract traffic sign attributes from video log images. This subsection uses GDOT and the city of Phoenix, Arizona, to illustrate the current inventory processes.

2.1.1 Sign Data Collection Process in GDOT

GDOT plans to use personal digital assistants (PDAs), as shown in Figure 2.1(a), barcode scanners, and GPS devices to inventory newly installed signs. This method was for inventorying only newly installed signs but not for the existing signs because of the need for tremendous amounts of labor. Some state DOTs also use digital cameras (Rasdorf et al., 2009). Figure 2.1(b) shows the process of traffic sign inventory using a PDA.

STEP 1: The field engineer approaches the traffic sign and attaches a barcode sticker to the sign.

STEP 2: The field engineer scans the barcode to create a traffic sign entry in the PDA. The MUTCD code and dimensions are manually input using the PDA program. The corresponding GPS coordinates can be automatically acquired using the PDA under the same entry.

STEP 3: The field engineer then captures a digital photograph using the PDA. The image is automatically linked with the corresponding traffic sign entry. This is a general step for state DOTs.

STEP 4: At the end of the data collection day, the field engineer downloads the data from the PDA to a computer with geo-database and GIS software to render the traffic sign locations and their corresponding attributes.

Several state DOTs use a similar practice, including the West Virginia DOT (WVDOT) (Paoly & Staud, 2010), the Louisiana Department of Transportation and Development (LaDOTD) (Wolshon, 2003), etc. Although GDOT's plans to use PDAs provides a means for traffic sign inventory, the process is time-consuming and unsafe due to two major drawbacks: 1) The field

engineer is required to physically approach traffic signs to collect the data. Many traffic signs, e.g. traffic signs are close to the roadside or on medians or they can be overhead traffic signs so inventorying them can be time-consuming and dangerous. 2) Extensive amounts of travel time are needed to travel from sign to sign. Research conducted by LaDOTD identified the average data collection time for a traffic sign as 43 minutes (Wolshon, 2003). Thus, it is difficult to use this method to inventory all the existing signs.



Figure 2.1 The PDA Used in GDOT and Field Operation in GDOT

2.1.2 Sign Data Collection Process in City of Phoenix, Arizona

The city of Phoenix, Arizona, began its comprehensive sign inventory in 2010, covering more than 28,000 traffic signs along 215 miles of arterial street corridors (Moreno & Cook, 2010). An integrated sensing vehicle is used to collect the traffic sign data; it is equipped with two video cameras and highly accurate GPS devices, as shown in Figure 2.2(a). The steps for using the system are as follows:

STEP 1: The data collection vehicle collects video log images and GPS coordinates.

STEP 2: The collected data is downloaded to a computer with geo-database and GIS software when the data collection is finished.

STEP 3: The operator reviews the collected image frame by frame and manually types in the traffic sign attributes, as shown in Figure 2.2(b). The manual inputs are updated to the geo-database.

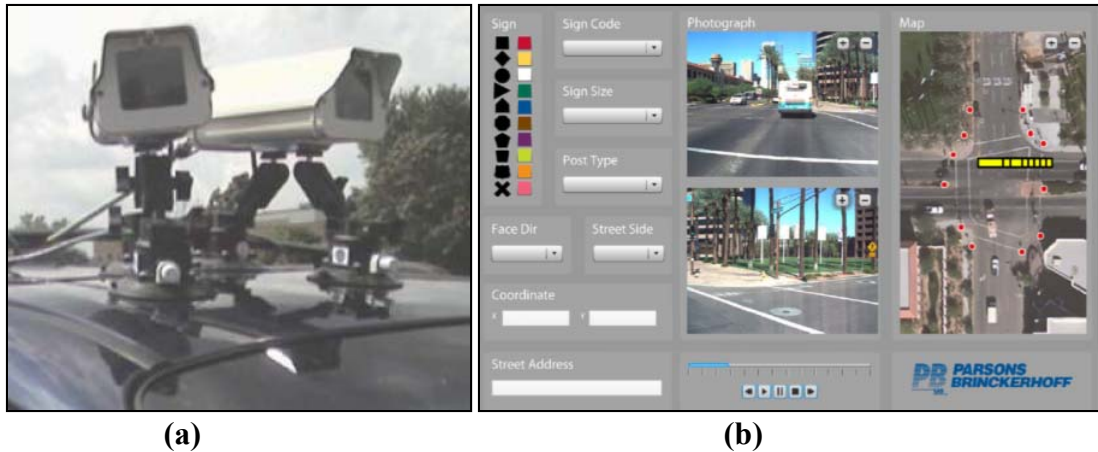


Figure 2.2 The Traffic Sign Collection Vehicle in the Field and the Extraction Interface in the office in Phoenix (Moreno & Cook, 2010)

Although the field data collection is achieved in an automatic fashion in less than 25 man hours, the data extraction is still manually conducted and takes more than 400 man hours. Though the data can be collected effectively and safely, the data extraction is still time-consuming and tedious. Very few transportation agencies use this process for traffic sign inventory because limited human resources hinder the huge effort required for manual data extraction.

In summary, there are several issues in the current practice for traffic sign inventory, including: 1) the majority of state DOTs are still using manual processes, which are time-consuming and dangerous; 2) only a few state DOTs or other transportation agencies are using the semi-automatic process in which the traffic sign data acquisition is automated but the manual traffic sign attribute extraction remains time-consuming and tedious. Consequently, there is a need to develop an automatic traffic sign inventory method that can not only enhance the existing semi-automatic process, but also reliably and efficiently extract the traffic sign attributes automatically.

2.2 Current Studies of Image-based Algorithms

As the semi-automatic process poses a more effective and safer data collection approach for traffic sign inventory, many state DOTs have started to collect video log images of roadways for traffic sign inventory. However, very few agencies are actually using the collected images for traffic sign inventory because the manual data extraction process is time-consuming and tedious. Thus, many image-based algorithms have been proposed to support the automatic process for

traffic sign inventory. Based on a thorough literature review, automatic traffic sign detection and recognition are the two primary focuses of recent research.

2.2.1 Automatic Traffic Sign Detection

From the literature, automatic traffic sign detection is defined as a process of detecting the regions of interest (ROIs) in video log images in which traffic signs may exist. All of the existing traffic sign detection algorithms have been developed using the distinct sign features defined in the MUTCD, including color and shape. There are three primary approaches for traffic sign detection: 1) color segmentation; 2) shape detection; and 3) the combination of color segmentation and shape detection.

- **Color segmentation**

Color segmentation is used to differentiate the unique traffic sign colors from the background in the video log images. Red, green, and blue (RGB) components are used for simple traffic sign color segmentation (Benallal & Meunier, 2003; Wu & Tsai, 2006). Lighting variation is one of the main problems. Other researchers introduced the color spaces that are more immune to lighting changes. The hue, saturation, and intensity (HSI) space is the most common space (de la Escalera, et al., 2003, 2004; Maldonado-Bascon, et al., 2007), whereas the LUV (Kang, et al., 1994) and YUV spaces (Miura, et al., 2000) have also been used. Nguwi and Kouzani (2008) segmented the input image in the HSI color space and successfully located traffic signs. Then, the classification module determined the type of detected traffic signs using a series of one-to-one architectural multilayer perceptron neural network (NN). Both the HSI and YUV color spaces were incorporated by Shadeed et al. (2003) to achieve better segmentation results. As the standard color space cannot always guarantee perfect color segmentation, several more complex color classifications have been proposed. Thus, a hierarchical region-growing technique was explored by Rehrmann and Priese (1997), and a database for the color pixel classification was presented by Priese et al. (1994, 1995). Tsai et al. (2009) proposed a color space extension method based on the probability of a certain pixel belonging to different MUTCD colors. Although these methods are comprehensive, they are computationally intensive. More importantly, the lighting

condition of the collected video log images can severely distort a traffic sign's color, which can lead to incorrect color segmentation results.

- **Shape detection**

Shape detection is used to differentiate a traffic sign's unique shape from other objects in the video log image. For traffic sign detection, several methods have been developed based on shape detection. For instance, Barnes et al. (2008) proposed a traffic sign detection algorithm using an a posteriori probability approach based on the locality and gradient information. Overett et al. (2009) used a fast histogram of oriented gradient features for pedestrian and traffic sign detection, which is suitable for use within typical boosting frameworks. A geometric model of the image gradient orientation was implemented by Balaroussi and Tarel (2009) to detect triangular signs. Milepost signs were detected by Marmo and Lombardi (2007) using optical flow analysis to identify the rectangular signs and then by searching gray-level discontinuity on the image and using the Hough transform for detection. To look for circular and triangular signs, edge orientations were used by Paclik et al. (2000). Barnes et al. (2008) implemented an algorithm based on fast radial symmetry, where patterns of edge orientations are exploited to detect triangular, square, and octagonal traffic signs. However, gradient-based feature detection is, by nature, sensitive to noise, and many shape detectors are slow in computing overly large images. It is also observed that most of the algorithms are designed for several specific shapes of traffic signs, rather than all of the ten shapes defined in the MUTCD. In addition, the cases of traffic sign occlusion are not well addressed.

- **Color segmentation and Shape Detection**

Recent works have used both color segmentation and shape detection to improve the detection rates (i.e. reduce the false negative (FN)) and, more importantly, reduce the false detections rates (i.e. false positive (FP)), which are frequent in the algorithms presented above. For instance, de la Escalera et al. (2003) selected the ROIs using the hue and saturation components, and then employed a genetic algorithm (GA) to the perimeter of the regions for the detection step. Ren et al. (2009) first converted RGB into HSI. Then, traffic signs candidates with special shapes were detected using the Hough transform. However, the Hough transform is computationally complex. Traffic sign detection based on histogram

thresholding in the HSI space and the support vector machine (SVM) was proposed by Maldonado-Bascon et al. (2007). The HSI color space is first used to segment the red, blue, and yellow regions, and the image's achromatic decomposition is used to detect the white traffic signs. Then, traffic sign detection is accomplished by shape classification using linear SVMs, and final recognition is performed by employing Gaussian kernel SVMs. However, the algorithm is not robust to changing illumination. De la Escalera et al. (2004) added a step before the use of thresholds on HSI color values in which nonlinear transformation is employed over hue and saturation to enhance the desired colors in the image (i.e. red and blue) using two lookup tables for every color being sought. By combining the color and shape feature of traffic sign, the performance of the algorithms improved in terms of FN and FP.

A generalized approach that can work for a broad set of traffic sign types is hard to find in literature. In the work of de la Escalera et al. (1997, 2003, 2004), Gil-Jiménez et al. (2005, 2007) and Maldonado-Bascon et al. (2007), a generalized traffic sign detection method was proposed for the European traffic sign system using pictograms and a priori knowledge of the shapes and colors of traffic signs. The model, using only a red circle, a blue circle, and a blue rectangle, detected 176 types of traffic signs. In the work of Tsai et al. (2009), a generalized traffic sign detection method was developed for the MUTCD traffic sign system by which more than 670 types of traffic signs containing ten MUTCD colors and more than ten MUTCD shapes can be detected.

In summary, review of the literature shows that there some automatic traffic sign detection algorithms have been developed. However, to develop a generalized traffic sign detection algorithm for the more than 670 types of traffic signs specified in the MUTCD is technically challenging. Though some effort has been made by de la Escalera et al., Gil-Jiménez et al., and Tsai et al., three major challenges still remain: 1) the lighting changes in the video log images; 2) the discontinuous traffic sign boundaries in the video log images; and 3) the excessive number of FP cases. More importantly, thorough review of the literature shows that there is not a systematic procedure to incorporate these developed algorithms into the current practices of state DOTs to practically improve the productivity of the image-based traffic sign inventory.

2.2.2 Automatic Traffic Sign Recognition

From the literature, automatic traffic sign recognition is defined as a process to determine the MUTCD code for the detected traffic signs. Through an automated process, the detected traffic signs can be uniquely defined by assigning the MUTCD code based on the shape, the color, and the pictogram of a sign. The automatic recognition algorithms evaluate detected ROIs. Current literature identifies two primary approaches for traffic sign recognition, correlation and pictogram pattern recognition, which are explained below:

- **Correlation**

The initial approaches for traffic sign recognition primarily involve correlation methods on a pixel level. Piccioli et al. (1996) introduced a simple pixel-to-pixel correlation method using the normalized (50×50) template and the detection candidates. A similar method was adapted by Miura et al. (2000), who introduced a second threshold to reveal the distinction between the best recognized traffic sign from the rest. A fast, simulated annealing algorithm was developed by Betke and Makris (1995) for automatic traffic sign recognition. The normalized correlation coefficient was used as a measure of the match between a hypothesized object and traffic signs. The system presented by Miura et al. (2000) identified traffic signs by a normalized correlation-based pattern matching technique using a traffic sign image database. Barnes et al. (2008) adapted the fast, radial symmetry detector to eliminate almost all non-sign pixels from the image and then applied normalized cross correlation to recognize the traffic signs. However, this method is suitable only for circular signs. Recent work by Paclik et al. (2006) improved the performance over standard cross correlation with a trainable similarity measures. Because of its simplicity, a correlation matching method can achieve traffic sign recognition for a large number of types. However, this technique can only perform well when the template images can be aligned well with the testing images, which is rarely the case due to the background clutter and geometrical distortion. In addition, it is a challenge to differentiate traffic signs with slight differences, e.g. warning signs with different texts.

- **Pictogram pattern recognition**

Because the icon and text on a traffic sign display unique information of different types, pictogram pattern recognition approaches have been developed in recent years. A simple multi-layer NN using back-propagation (BP) (de la Escalera, et al., 1997; Nguwi & Kouzani, 2008) was first introduced for recognition. Many improvements in NN have been adapted to address different issues in the traffic sign recognition. To improve the flexibility of the NN for accepting new patterns of traffic signs, the adaptive resonance NN was used instead of the BP method (Chiung-Yao, et al., 2003; de la Escalera, et al., 2003, 2004). To prevent the NN training from being trapped in local minima and to introduce the concept of similarity probability, the radial basis function (RBF) was used as the activation function instead of the typical sigmoid function (King Hann, et al., 2009; Yong-Jian, et al., 1994). To avoid the impact of background clutter and geometrical distortion, some techniques have been introduced to pre-process an image to produce the new input vector in other domains, e.g. Gabor wavelet transform (Douville, 2000). Sharing similar capability as NN but providing guaranteed global minima in the training process for classification and a less complex computation, the SVM technique became popular in traffic sign recognition. Gomez-Moreno et al. extensively used SVMs for traffic sign shape and color identification for detection and pictogram recognition (Gomez-Moreno, et al., 2010; Maldonado-Bascon, et al., 2007, Wang, et al., 2010) using several Gaussian kernel SVMs. A different Laplace kernel classifier was also used for traffic sign recognitions (Paclík, et al., 2000). In addition, the boosting method was transferred from the field of face recognition to the field traffic sign recognition. Ada-Boost using Haar features is the commonly used approach (Baro, et al., 2009; Hu & Tsai, 2011; Ruta, et al., 2010), while other features, such as the Gabor wavelet feature (Koncar, et al., 2007), etc., were also studied. However, due to their computational complexity, it is not feasible to apply pictogram pattern recognition algorithms to recognize all types of traffic signs.

In summary, although several individual traffic sign recognition algorithms have been developed, many of them can only recognize limited types of traffic signs. In addition, many traffic signs share similar pictograms with slight differences that cannot be recognized well. There is no literature that demonstrates good performance on a large group of traffic signs, e.g.

the complete warning sign group, which contains more than 200 types, many of which share similar pictograms.

2.3 Research Need

The traffic sign inventory methods currently used by state DOTs are primarily manual processes. These methods are unsafe, labor-intensive, and time-consuming. Some transportation agencies are using a semi-automatic method that uses video log images. Nevertheless, these methods require excessive manual data extraction, which might not be practical for state DOTs. To minimize the manual effort in traffic sign inventory, there have also been some attempts to develop algorithms for automatic traffic sign detection and recognition. However, there are three primary challenges preventing these algorithms from practical use:

- It is still a challenge to inventory all types of the traffic signs defined in the MUTCD.
- All the existing algorithms use the unique features of traffic signs displayed in video log images. However, the performance of the algorithms is not robust to some of general challenges in the outdoor video log images that distort the unique features of traffic signs, e.g. lighting conditions, occlusion conditions, etc.
- Most importantly, all the previous studies have focused on development or improvement of various algorithms' performance. A systematic procedure to seamlessly adapt the existing algorithms in the existing traffic sign inventory process to minimize the manual effort is lacking.

Before making an effort to improve the performance of the existing image-based methods and proposing new LiDAR-based methods, there is a need to comprehensively assess the performance of these methods to better understand the performance of existing algorithms. The objective of this study is to critically assess the representative algorithms by demonstrating the results using actual data, summarizing the technical challenges, and recommending the utilization of the algorithms. Also, a new, enhanced procedure can be proposed by flexibly adapting the existing automatic methods or the future improved methods into the current practices of state DOTs. Thus, the superiority of these automatic methods can be fully developed to improve the productivity of state DOTs.

3. Assessment of Automatic Traffic Sign Inventory Using Video Log Images

This subsection presents the critical assessment of the existing automatic traffic sign detection and recognition methods using video log images, including three image-based traffic sign detection and recognition algorithms. The selected algorithms are as follows:

- Generalized traffic sign detection method developed by Tsai et al. (2009). This method is the only one that has the capability to detect more than 670 types of MUTCD-defined traffic signs with different colors and shapes.
- Specific stop sign and speed limit sign recognition method developed by Tsai and Wu (Tsai & Wu, 2002; Wu & Tsai, 2006). Stop signs and speed limit signs are two of the most important traffic signs. Moreover, the reliable stop sign and speed limit sign recognition provides prompt and reliable applications for state DOTs; even the recognition methods of other types of traffic sign are still under development.

3.1 Data Preparation

The objective for this data preparation is to comprehensively evaluate the performance of the automatic traffic sign detection and recognition algorithms using video log images. Two datasets are separately prepared to assess the performance of the generalized traffic sign detection for all types of traffic signs, and the performance of specific traffic sign recognition algorithms for stop signs and speed limit signs.

The dataset for the generalized traffic sign detection algorithm was retrieved from the roadway video log image dataset provided by LaDOTD. The selected section was on Louisiana SR 541, covering 4.1 miles of the industrial area in Westwego, Louisiana, and contained 2,100 images. In this dataset, 64 traffic signs with different types were manually extracted as the ground truth. Figure 2.3 shows the data collection location. An additional dataset for the generalized traffic sign detection algorithm was retrieved from the roadway data collection in 2009-2010 by Roadware Company in Nashville, Tennessee. The selected section covered 5.0 miles of suburban area in Nashville and contained 1,320 images. In this dataset, 112 traffic signs of different types were extracted for ground truth.



Figure 2.3 Data Collection Routes in Westwego, Louisiana for the Generalized Automatic Traffic Sign Detection Algorithm

The dataset for the specific traffic sign recognition was collected using the GTSV. The video log images were purposely collected on the streets that cover several blocks of residential area that contained a sufficient sample of stop signs and speed limit signs. The selected test roadway section was in the area of 37th street in downtown Savannah, Georgia, covering 8 miles of residential area. To populate the samples, two runs of data collection were conducted in different directions within the area. Figure 2.4 shows the direction of the two runs. In this dataset, 53 stop signs and 28 speed limit signs were manually extracted as the ground truth.



Figure 2.4 Data Collection Routes in Savannah, Georgia for the Automatic Stop Sign and Speed Limit Sign Recognition

3.2 Test Result

3.2.1 Generalized Traffic Sign Detection

The generalized traffic sign detection algorithm was developed to automatically detect all types of traffic signs on the roadways. In this test, two datasets containing the video log images collected by state DOT and city transportation agencies were tested to demonstrate the performance. FN and FP are used to quantitatively measure the performance, where FN measures the reliability of the algorithm, and FP measures the productivity of the algorithm. An FN case is counted if the algorithm does not detect a traffic sign in the image, while an FP case is counted if the algorithm mistakenly detects another object for a traffic sign. Table 2.1 shows the result of the two selected datasets. For the dataset from LaDOTD, 76.6% of the traffic signs were correctly detected, while 117 FP cases were identified. For the dataset from Nashville, 75.9% traffic signs were correctly detected, while 196 FP cases were identified.

Table 2.1 The Results for the Generalized Traffic Sign Detection Algorithm

LaDOTD		Nashville	
Distance	4.1 miles	Distance	5.0 miles
# of Signs	64	# of Signs	112
FN	15	FN	27
FP	117	FP	196

As demonstrated, the current algorithm can correctly detect more than 75% of the traffic signs (49 out of 64 for LaDOTD and 85 out of 112 for Nashville). Although the manual extract process is still needed, much effort in manually digitizing the traffic sign in the images can be saved. However, there remain some FN cases, and the FP cases are excessive in the current algorithm, which can be further improved. The detailed analysis is presented below:

FN Case Analysis

- **Lighting Changes:** Some FN cases are produced due to the lighting changes in the video log images because the colors captured from the camera are distorted when the lighting changes. Figure 2.5 shows two FN cases due to overexposure and backlighting. In these cases, most of the region in the whole image is mistakenly segmented as achromatic colors, i.e. white and black, which makes it difficult for the algorithm to differentiate the traffic sign region and the

background region. These cases can potentially be eliminated during the data collection by appropriately adjusting the camera settings, e.g. shutter speed and exposure time. However, due to the constant changes in driving directions and unpredictable weather conditions, many adjustments are hard to apply in time. An improvement in the color segmentation can potentially reduce the FN cases due to the lighting changes during the data processing. LiDAR technology can also be applied to reduce the FN cases caused by lighting changes.

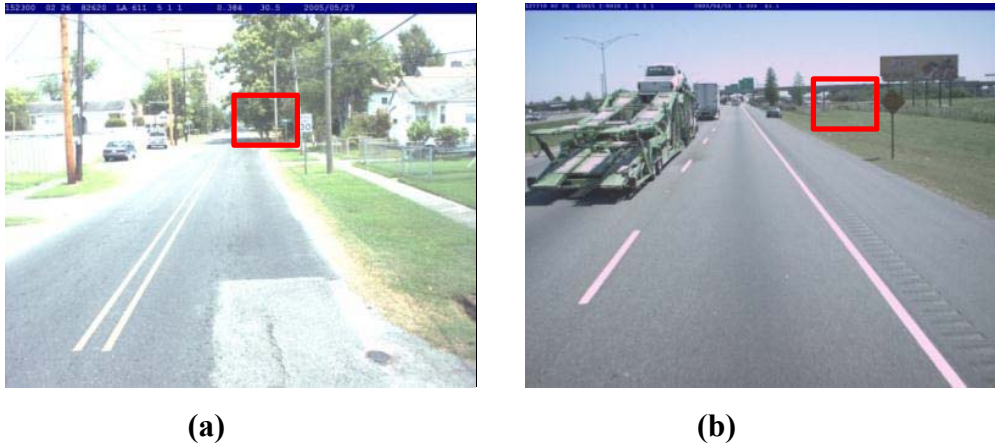


Figure 2.5 Examples of two FN Cases Due to Lighting Changes: a) Overexposure; b) Backlighting

- **Discontinuous Boundary:** Some FN cases are produced due to the discontinuous traffic sign boundaries captured in a video log image because the discontinuous boundary cannot be estimated as a closed traffic sign shape using the detected edges. The discontinuity is typically produced by partial occlusion, casting shadows over the traffic signs, multiple traffic signs on the same post with adjacent boundaries, etc. Figure 2.6 shows an FN case that is due to occlusion by tree branches. These cases can potentially be minimized by applying some active contour-based methods.



Figure 2.6 Example of an FN Case Due to Discontinuous Boundary

- **Other cases:** There are several other FN cases identified in the critical assessment, including the object marker signs, the railroad crossing signs, and the traffic signs with poor conditions due to severe color deterioration.
 - For the object marker signs as shown in Figure 2.7(a), the yellow-black pattern of this type of sign provides challenges to the current algorithm because the algorithm requires identification of the boundary of a sign to detect the shape. These cases can be potentially minimized by applying a shape-merging algorithm to combine the individual stripes into a vertical rectangular shape.
 - For the railroad crossing signs as shown in Figure 2.7(b), the crossing shape of this type of sign provides challenges to the current algorithm that is based on convex shape approximation with limited number of vertices. These cases can be potentially minimized by applying the non-convex shape approximation algorithm.
 - For the traffic signs with poor conditions as show in Figure 2.7(c), the severe color deterioration completely altered the color profiles of the traffic sign. The algorithm cannot correctly segment the traffic sign and distinguish it from the background. Although severely deteriorated, many such traffic signs still have a good retroreflectivity. Thus, LiDAR technology can be used to reduce such FN cases.
- FP Case Analysis

As presented in the literature review, the color feature and shape features are used in the current algorithm. However, these two features are not sufficient for traffic signs, as there are many other objects sharing characteristics similar to the traffic signs in terms of color and shape. Many of these objects are detected as FP cases in the test, including mailboxes, advertisement posters, drums, guardrails, vehicle bodies, windows, etc. Figure 2.8 shows

examples of these FP cases. Because the retroreflectivity feature is another unique feature that can be introduced to differentiate the actual traffic signs, LiDAR technology is expected to be an effective tool to eliminate these identified FP cases.

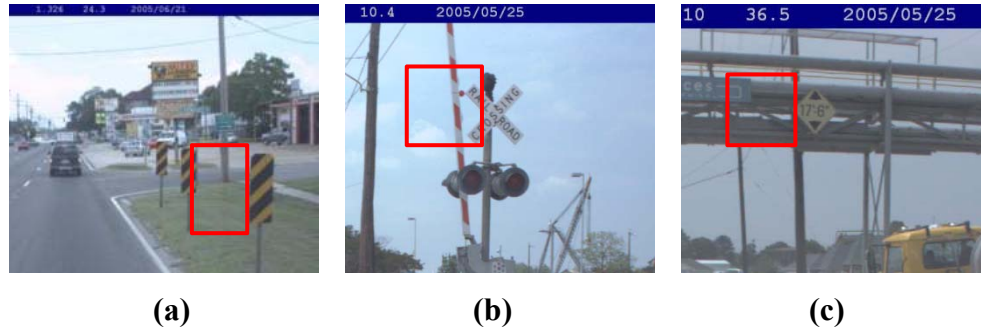


Figure 2.7 Examples of Other FN Cases Identified in the Critical Assessment



Figure 2.8 Sample of FP Cases Identified in the Assessment Test

In summary, the test of the assessment using the generalized traffic sign detection algorithm shows that more than 75% of the traffic signs are correctly detected, which can save much effort in manually digitizing sign regions. Improvement in eliminating the FN cases from the current algorithm using video log images lies in three directions, including: 1) providing a better camera configuration and improving the color segmentation for achromatic colors; 2) improving the current shape approximation method; and 3) developing a shape-merging algorithm. The retroreflectivity feature from the LiDAR sensor is recommended to supplement the current algorithm improvement. In addition, the retroreflectivity feature is also recommended to be

introduced to minimize the FP cases, most of which are non-reflective objects. Section 4 presents such an automatic method using mobile LiDAR.

3.2.2 Specific Traffic Sign Recognition

Specific traffic sign recognition algorithms are developed to recognize specific types of traffic signs, e.g. stop signs, speed limit signs, etc. In this test, stop signs and speed limit signs were used to assess the performance of the algorithms. Table 2.2 shows the results using the data collected on 37th Street in Savannah, Georgia. For the stop sign recognition, 81% of the stop signs were correctly recognized, and only 11 FP cases were identified. For the speed limit sign recognition, 96% of speed limit signs were correctly recognized, and only 1 FP case was identified.

Table 2.2 The Results for the Stop Sign and Speed Limit Sign Recognition Algorithms

37th ST , Savannah	
Distance	8.0 miles
# of Stop Sign	53
# of Speed Limit	28
FN (Stop Sign)	10
FN (Speed Limit)	1
FP (Stop Sign)	11
FP (Speed Limit)	1

It is identified that the recognition algorithms perform well for recognizing both stop signs and speed limit signs in the test data. However, there are still some FN cases and FP cases identified in the test.

For the stop sign recognition, the FN cases were produced due to casting shadows. All of the unrecognized stop signs were in the shade of the trees in the residential area, where strong shadows were cast over the traffic signs. Such casting shadows produce two impacts on the recognition, including 1) distortion of the red color into black color, as shown in Figure 2.9(a), and 2) production of inhomogeneous color in the sign regions, as shown in Figure 2.9(b). All the FP cases are from a vehicle brake light, which shares the same red color feature as the stop sign, as shown in Figure 2.9(c)

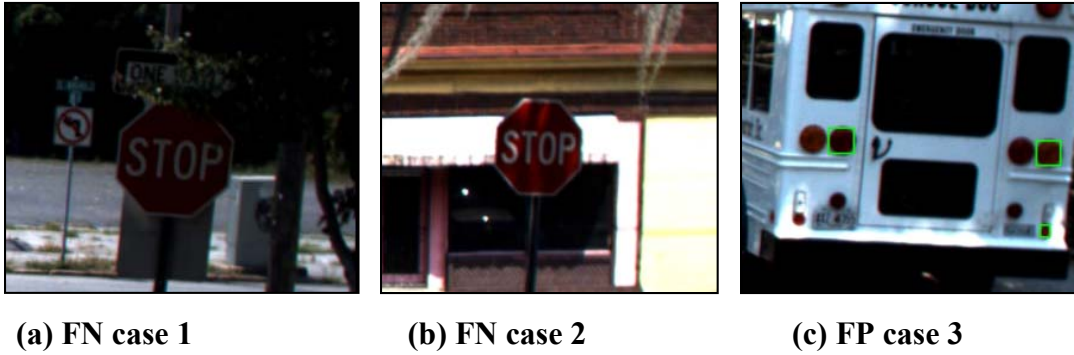


Figure 2.9 FN and FP Cases Identified in the Stop Sign Recognition Algorithm

For the speed limit sign recognition, the FN was produced due to occlusion by a branch. In this case, the digit "5" was connected with the leaves nearby, which introduced the problem for the color segmentation of the white and black colors, as shown in Figure 2.10(a). The only FP was produced because of the similar pictogram the objects shared with the traffic sign, i.e. the warning sign containing speed digit, as shown in Figure 2.10(b).

In summary, the test in the assessment using two specific traffic sign recognition algorithms shows that 81% of the stop signs were correctly recognized with only 11 FP cases, and 96% of the speed limit signs were correctly recognized with only 1 FP case. The results show that it is feasible to apply the current recognition algorithm for the specific traffic signs, e.g. stop signs and speed limit signs. However, there is still a need to further improve the current performance. Besides, as identified in the literature review, there is a need to extend the current algorithms to recognize other important types of traffic signs, e.g. warning signs. Hence, the manual input effort of the MUTCD code can be further reduced.

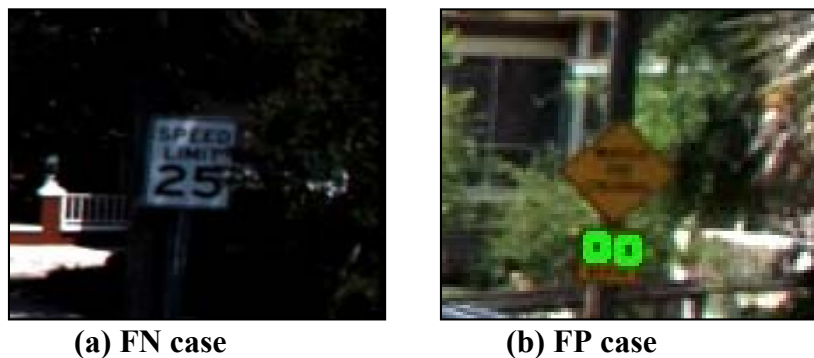


Figure 2.10 FN and FP Cases Identified in the Speed Limit Sign Recognition Algorithm

4. Assessment of Automatic Traffic Sign Inventory Using mobile LiDAR

This section is to assess the automatic traffic sign detection methods using LiDAR point cloud. Although there are very few systems using mobile LiDAR technologies to inventory traffic sign (Laflamme, 2006), most of these methods are proprietary and lack validation. The method in this assessment, by Ai and Tsai (2012), introduces the LiDAR-based method in automatic traffic sign inventory in detail and quantitatively studied the feasibility of this emerging technology.

The objective of the experimental test is to assess the performance of the presented automatic traffic sign detection method using 3D LiDAR point cloud data. Actual data collected on I-95 and 37th Street are used to critically assess the performance of the presented method in terms of detection rates and the FN and the FP. The adequate parameter values for a good detection rate are also suggested.

The dataset collected on I-95 covers 17.5 miles of roadway containing 127 traffic signs with different attributes. The data was collected on the outer lane of the three-lane road at the speed of 60 mph (100 km/h). The dataset collected on 37th Street covers 2.9 miles of roadway containing 115 traffic signs with different attributes. The data was collected at the speed of 30 mph (50 km/h). Both of the datasets were collected using the same LiDAR heading angle of 20° and scanning frequency of 100 Hz. The ground truth was manually extracted using the video log images that were synchronized with the LiDAR data. Figure 2.11 shows the map of the road sections for the data collection.

4.1 Determination of Adequate Parameter Values

The key of the LiDAR-based sign inventory method is to determine the adequate parameter values that are related to the basic traffic sign characteristics, including retroreflectivity, elevation, lateral offset and hit count. The initial parameter values can be set based on the MUTCD standard defining the traffic sign characteristics. To further adapt the traffic sign characteristics to different roadways, the first 10 traffic signs on different roadway types to calibrate the parameter values have been selected. Once these parameter values are calibrated, they can be applied to the same types of roadway. The following rules are used to determine the adequate parameter values:



Figure 2.11 The Selected Data Collection Sections for Experimental Test

- Retro-intensity

The retro-intensity is an important attribute in the LiDAR point cloud data. It is defined as the ratio of the energy returned from the object to the energy emitted from the LiDAR sensor. Since most of the traffic signs are designed to be retroreflective, most of the traffic signs have a relatively high retro-intensity value in the LiDAR point cloud data compared to other objects. A higher retro-intensity indicates a better object reflectance. The retro-intensity value selected for I-95 should be greater than that for 37th Street. It indicates that the traffic sign retroreflectivity condition on the major arterials is generally better than the local roads. On one hand, the retro-intensity value should be kept low enough to prevent FN (i.e. missing signs). On the other hand, a higher retro-intensity value is used to be selective on sign detection for minimizing the FP (i.e. false detection). From the observation of the selected 10 traffic signs for calibration, the minimum retro-intensity values of 0.73 are identified for I-95 and 0.67 for 37th Street. Therefore, values of 0.7 and 0.65 are used for I-95 and 37th Street, respectively.

- Elevation

Elevation is defined as the offset of the LiDAR point to the ground in the z direction. The elevation value selected for I-95 should be slightly smaller than that for 37th Street. It is consistent with the traffic sign installation standard defined in the MUTCD. For example,

although the traffic sign should be typically mounted at a minimum of 7 ft. (2.1 m), many secondary signs can be mounted at a minimum of 5ft. (1.5m) on freeways or expressways. Therefore, values of 4ft. (1.2m) and 6ft. (1.8m) are used for I-95 and for 37th Street, respectively. It is also suggested that the elevation value should not be smaller than 3 ft. (0.9m) to avoid the false detection of vehicle license plates and temporary traffic control drums.

- Lateral Offset

Lateral offset is defined as the offset of the LiDAR point to the data collection trajectory in the x-y direction. The lateral offset value selected for I-95 should be greater than that for 37th Street. It is consistent with the traffic sign installation standards defined in the MUTCD and the observation in the calibration set. Based on the MUTCD, a traffic sign should be mounted at a minimum of 12ft. (3.6m) lateral offset on freeways or expressways, but it should be a minimum of 2ft. (0.6m) lateral offset in residential areas. However, as observed in the calibration set, many specific service signs on the freeway or expressway are mounted as far as 48ft. off the road, while some of the traffic signs are mounted as far as 12ft. (3.6m) off the road when the region is not confined. Therefore, values of 60ft. (18.3m) and 20ft. (6.1m) are used for I-95 and 37th Street respectively.

- Hit Count

Hit count is defined as the number of LiDAR points that hit the cluster, which corresponds to the dimension of the traffic sign, the scanning frequency of the LiDAR sensor, the vehicle driving speed, and the distance between the traffic sign and the LiDAR sensor. The hit count value selected for I-95 should be smaller than that for 37th Street. LiDAR point cloud data is collected using consecutive scanning lines crossing the roadside objects. When the scanning frequency is fixed (i.e. 100 Hz), the distance between the consecutive scanning lines is determined by the driving speed, and the distance between the consecutive points within the same line is determined by the distance between the LiDAR sensor and the object. Therefore, a traffic sign with the same dimension contains fewer hit points on I-95 than on 37th Street because the vehicle speed for data collection is greater, while the distance from the LiDAR to the traffic sign is also larger on I-95 than on 37th Street. By exploring the smallest signs

collected in the datasets on I-95 (i.e. milepost sign) and on 37th, Street (i.e. no-parking sign) and based on the data collection speeds, values of 10 and 20 are used for I-95 and for 37th Street, respectively.

The rules for determining adequate parameter values for the presented detection method are based on the characteristics of traffic signs defined in the MUTCD and the calibration from a fraction of the testing datasets. In this test, the first 10 traffic signs are used for the calibration. However, state DOTs can define their fractions for better parameter values. Table 2.3 presents the selected parameter values used for the experimental test in this study.

Table 2.3 The Parameter Values Applied for the Tests on I-95 and 37th Street

I-95		37 th Street	
Retro-Intensity	0.70	Retro-Intensity	0.65
Min Elevation (ft.)	4	Min Elevation (ft.)	6
Max Lateral Distance (ft.)	60	Max Lateral Distance (ft.)	20
Min Hit Count	10	Min Hit Count	20

4.2 Test Result

With the determined parameter values, the datasets collected on I-95 and 37th Street were tested using the presented method. Table 2.4 shows the automatic detection results.

Table 2.4 Traffic Sign Detection Results for the Tests on I-95 and 37th Street

I-95		37 th Street	
Distance	17.5 miles	Distance	2.9 miles
# of Signs Tested	117	# of Signs Tested	105
Detection Rate	94.0%	Detection Rate	91.4%
False Negative	7	False Negative	9
False Positive	6	False Positive	7

For the data collected on I-95, the detection rate is 94.0% with only 6 FP cases. For the data collected on 37th Street, the detection rate is 91.4% with only 7 FP cases. The results have demonstrated that the presented method using 3D LiDAR point cloud data is promising for providing an alternative for traffic sign inventory.

A detailed analyses of the FN cases and FP cases was conducted. There are four types of FN cases: traffic signs with poor retroreflectivity condition, traffic signs with insufficient height, occluded traffic signs, and overhead traffic signs.

- Traffic sign with poor retroreflectivity condition.

Several such FN cases were identified on 37th Street, where the retroreflectivity condition of the traffic signs is relatively poor. In contrast, this FN case was not identified on I-95, where the traffic signs are maintained in a timely manner. Figure 2.12 shows an example of a FN case containing a traffic sign with poor retroreflectivity condition on 37th Street. It can be observed in the video log image that the no-parking sign has severely deteriorated. In the corresponding LiDAR point cloud data, the retro-intensity values of the points within the no-parking sign region are much smaller than the set parameter value of minimum retro-intensity as 0.65. Therefore, the traffic sign region will not be detected from the background. Further investigation finds that the average of the retro-intensity values in the traffic sign regions is approximately 0.45. By further reducing the parameter value of retro-intensity to below 0.45, this traffic sign can be correctly detected. However, many FP cases are detected using such a small retro-intensity parameter value.



Figure 2.12 Example of FN Case with a Traffic Sign with Poor Retroreflectivity on 37th Street

- Traffic sign with insufficient height.

Several such FN cases were identified on 37th Street, where some of the traffic signs failed to meet the height requirements defined in the MUTCD. In contrast, this FN case was not identified on I-95, where the traffic signs have better compliance. Figure 2.13 shows an example of a FN case containing a traffic sign with insufficient height on 37th Street. The height of the traffic sign measured 5.1 ft. (1.6m), which is smaller than the set parameter

value of minimum elevation as 6ft. (1.8m). Therefore, the traffic sign region was rejected. By further reducing the parameter value of elevation to below 5ft. (1.5m), this traffic sign can be correctly detected. However, several additional FP cases were detected, such as the reflective stickers on the mailbox, etc.



Figure 2.13 Example of a FN Case with a Traffic Sign with Insufficient Height on 37th Street

- Occluded traffic sign

One of the drawbacks of the LiDAR point cloud data collection is that only the object in the line of sight of the LiDAR sensor can be collected. Therefore, when the heading of the LiDAR sensor is configured at a fixed angle (e.g. 20° in this study), the line of sight is fixed. If the object closer to the LiDAR sensor is collected, the occluded object will not be detected. Figure 2.14(a) shows an example of a FN case containing an occluded traffic sign on I-95. The merge sign is occluded by the temporary work zone warning sign. Although in the video log image the merge sign is still visible, it cannot be detected using LiDAR point cloud data due to the occlusion. Similar cases are identified on the local road, where traffic signs are occluded by the tree branches, as shown in Figure 2.14(b).

- Overhead traffic sign

The coverage of the LiDAR data along the road is dependent on the path of the data collection vehicle and the heading angle of the LiDAR sensor (e.g. 20° in this study). For the purpose of traffic sign inventory, the LiDAR sensor is typically scanning vertically to the

roadside, and the data collection vehicle is driving on the outer lane of the road. Under such a configuration, it is likely that many overhead signs are not detected. In contrast, the overhead signs can still be collected in the video log images. Figure 2.15 shows examples of such FN cases on I-95 and 37th Street.

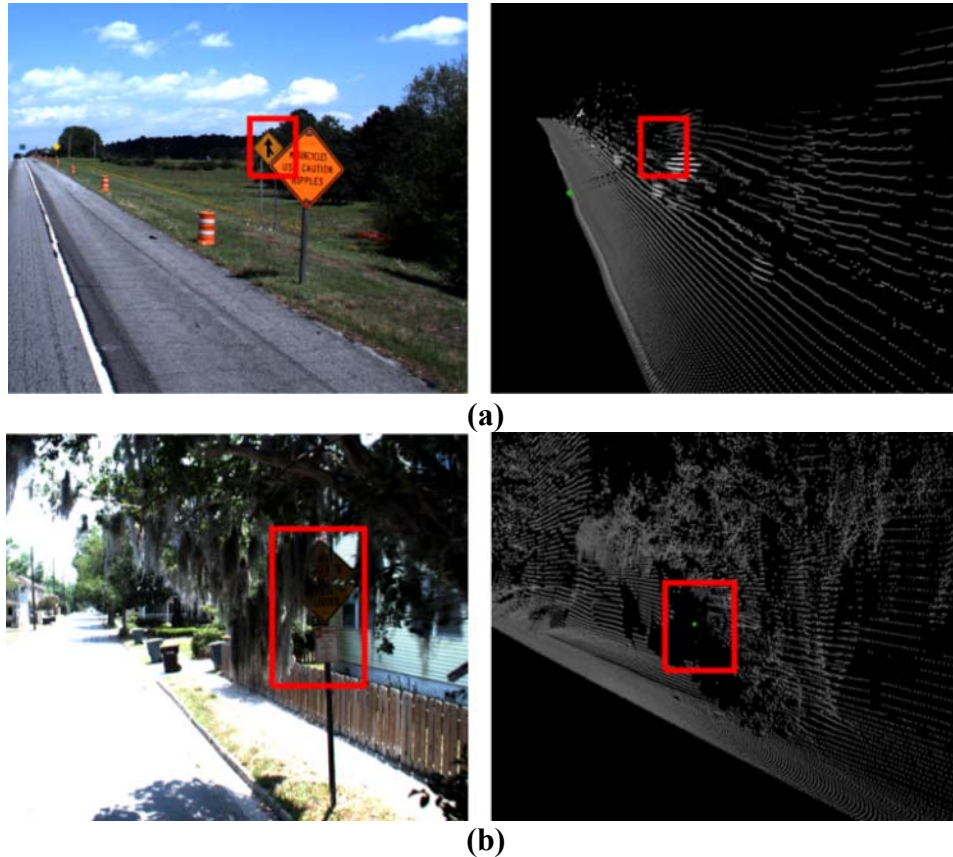
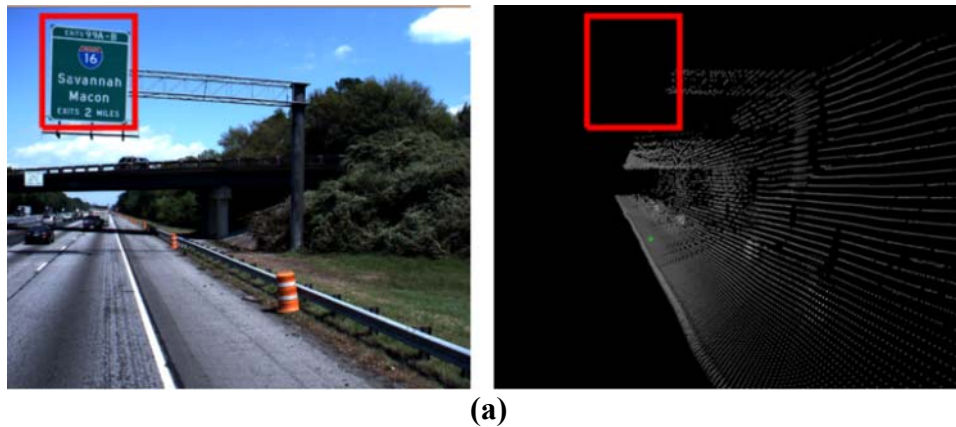
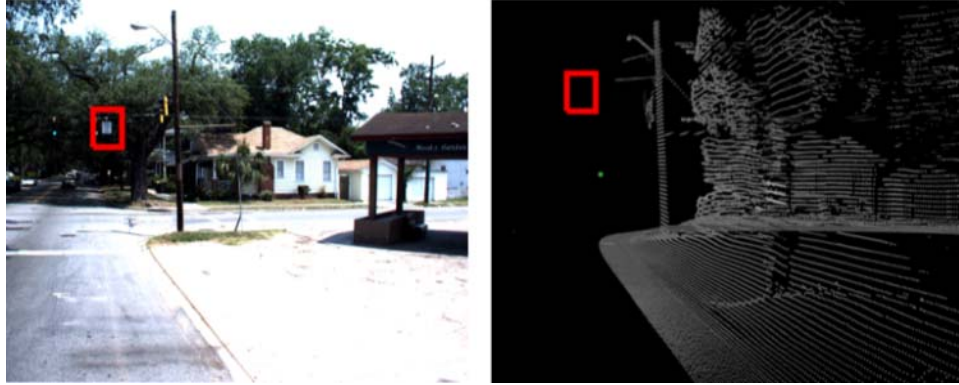


Figure 2.14 Example of FN Cases Containing Occluded Signs on (a) I-95 and (b) 37th Street



(a)



(b)

Figure 2.15 Example of FN Cases Containing Overhead Signs on (a) I-95 and (b) 37th Street

There are three types of FP cases in which objects with high retroreflectivity are mistakenly detected as traffic signs. Although the constraint of traffic sign elevation effectively rejects many of the objects with high retroreflectivity, such as vehicle license plate, temporary traffic control drums, etc., there are still several types of FP cases that are difficult to eliminate, including reflective commercial signs, changeable message boards, gates with reflective strips, etc. Figure 2.16 shows the examples of the identified FP cases. It is observed that although these FP cases are mistakenly detected using 3D LiDAR point cloud data, they can be easily eliminated using the 2D video log images.



(a)

(b)

(c)

Figure 2.16 Examples of the Identified FP Cases

In summary, the results from the data collection on I-95 and 37th Street have demonstrated the presented method using 3D LiDAR point cloud data is promising for providing an alternative for traffic sign inventory. The suggested rules for determining the adequate parameter values show its effectiveness for the presented method. The FN and FP cases were critically assessed to assist

in exploring the potential improvements. Two of the identified FN cases can be further eliminated by adjusting the parameter values, e.g. the traffic signs with poor retroreflectivity condition and insufficient height, while the other two identified FN cases can be further eliminated by changing the LiDAR configuration, changing the data collection path, or integrating the presented method with the image-based method. The integration of the presented method with the image-based method can also help to eliminate the identified FP cases.

5. An Enhanced Traffic Sign Inventory Procedure

In the previous sections of this chapter, several state-of-the-art automatic traffic sign inventory methods have been critically assessed. The assessed methods demonstrated their potential for supporting automatic traffic sign inventory. However, those automatic methods cannot be directly applied in the current practice due to the nontrivial FN and FP cases. To address this issue, this section proposes an enhanced traffic sign inventory procedure to adapt the existing automatic methods and improve the current practice of state DOTs.

5.1 Proposed Procedure

The objective of the enhanced traffic sign inventory procedure is to improve the efficiency of the manual video-log-image-based sign inventory process by incorporating the existing automatic methods. The proposed sign inventory procedure should fully utilize the strength of the automatic methods and still employ the manual process to overcome the FN and FP problems stemming from the automatic ones. With the advancement of automatic methods, the efficiency of the proposed procedure should also be improved accordingly. Though the ultimate goal is to eliminate the need of the manual process, the framework can be utilized immediately in state DOTs' practices. Figure 2.17 shows the complete processes of the traffic sign inventory including the proposed enhanced procedures. There are three primary paths to implement the traffic sign inventory using the collected raw traffic sign data, including:

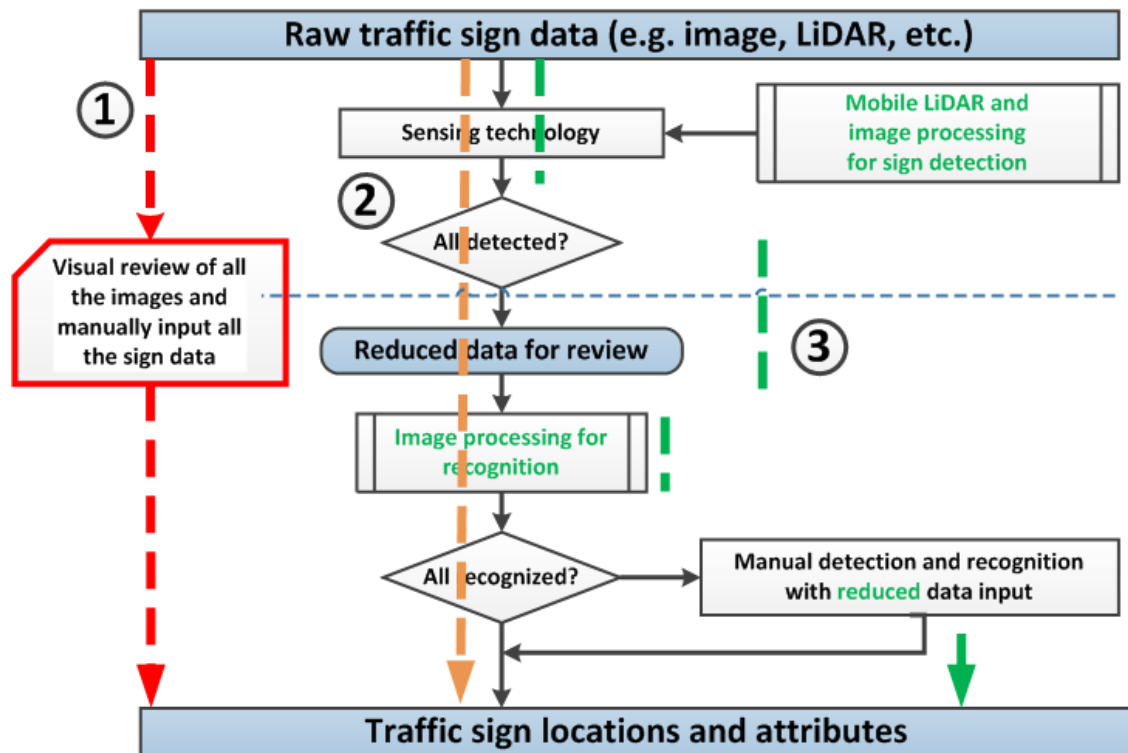


Figure 2.17 Framework of the Enhanced Traffic Sign Inventory

- **PATH 1: Manual Process (Current practice)**

The manual process is typically used in the current operation for traffic sign inventory and condition assessment. The operator needs to manually review all the collected raw data, e.g. video log images, etc. The traffic sign locations are manually digitized on the image, and the traffic sign attributes are manually input into the inventory database. In addition, as the retroreflectivity condition cannot be visually inspected using video log images, a separate field trip for traffic sign condition assessment is still needed.

- **PATH 2: Fully Automatic Process (Final goal)**

This is a fully automated process that rigorously requires the automatic algorithms for detection, recognition, and condition assessment with high accuracy. This is the ultimate goal of the research and application. However, as presented above for the critical assessment, the existing algorithms are not yet reliable enough to achieve the goal.

- **PATH 3: Semi-Automatic Process (Enhanced Procedure)**

The semi-automatic process contains the proposed enhanced procedure that can not only incorporate the current practice of manual process, but with the support of the existing algorithms, it can improve the traffic sign inventory productivity. Three sub-processes are proposed, including:

- STEP 3.1: Traffic sign detection

The raw traffic sign data is first processed using the enhanced image-based and LiDAR-based traffic sign detection algorithms. Although not all the traffic signs can be detected using the existing algorithms, based on the assessment, more than 75% of the traffic signs in the image and more than 94% of the traffic signs in the LiDAR point cloud can correctly be extracted. The integration of the image-based algorithm and the LiDAR-based algorithm can further reduce the number of undetected traffic signs (FNs) and the incorrectly detected cases (FPs). The remaining effort for manual input is twofold: 1) to manually extract the undetected traffic signs; 2) to manually remove the incorrectly detected cases. This means that the majority of the manual digitization effort for traffic sign extraction can be saved. In addition, as the removal of the incorrectly detected cases requires less effort compared to the effort for the extraction of undetected traffic signs, the efficiency of the whole detection process can be improved, although the excessive FP cases are identified using the existing algorithms.

- STEP 3.2: Traffic sign recognition

The raw traffic sign data is then processed using image-based traffic sign recognition algorithms. Although at the current stage only certain types of traffic sign can be recognized using the existing algorithms, at least more than 81% of the stop signs and 96% of the speed limit signs can be correctly recognized. Because the regulatory signs contribute a large population of all the traffic signs on the road, much effort of manual input for MUTCD codes can be saved. The remaining effort for manual input includes the MUTCD codes for other traffic sign types and the revision of the wrong MUTCD code.

The enhanced procedure presented in PATH 3 for traffic sign inventory is not limited by the performance of any individual algorithm. As the performance of the algorithms improves in the future, the enhanced methodology demonstrates a better reliability and efficiency toward full automation. The less involvement of the algorithms in the inventory and condition assessment process, the more enhanced methodology steps back to the existing manual process. The application of the automatic algorithms can be flexibly determined by state DOTs based on their needs, data availability, financial situation, etc. Thus, the proposed enhanced methodology can be flexibly applied to the existing practices in state DOTs.

5.2 Preliminary Assessment

The objective of the preliminary assessment is to quantify the benefit of the proposed enhanced procedure compared to the traditional manual method. The benefit was measured by the average processing time for each traffic sign in the testing section to achieve a full inventory. The testing route was selected on I-95 southbound between MP 100 and MP 105 containing 47 traffic signs with different shapes, colors, and conditions. With the help of GDOT engineers, an additional survey using the manual process was conducted on a 2.5 mile roadway in a non-disclosed location and contained fewer than 100 traffic signs with different shapes, colors, and conditions.

In this preliminary assessment test, the image-enhanced procedure, LiDAR-enhanced procedure, the in-office manual process, and the in-field process were compared. The algorithms and applications implemented by the Georgia Tech research team and the Trimble® Trident software were used for the preliminary assessment.

- **Image-enhanced procedure**

This corresponds to PATH 3 and was presented above. It requires the automatic traffic sign detection and recognition algorithms using video log images and the manual input. The video log images are first processed frame by frame using the algorithms as presented above. The operator then reviews the images frame by frame. The necessary typing-in and revision of the inventory information is manually input; otherwise, the image quickly skips to the next frame.

- **LiDAR-enhanced procedure**

This also corresponds to PATH 3. It requires the automatic traffic sign detection algorithm using mobile LiDAR and manual input. The LiDAR point cloud is first processed using the algorithm as presented above. The operator then reviews the LiDAR point cloud and the corresponding video log image. The necessary typing-in and revision of the inventory information is manually input; otherwise, the image quickly skips to the next frame.

- **Manual Process (In-office)**

This corresponds to PATH 1. It requires the operator to manually review all the collected video log images frame by frame. On each image containing a traffic sign, the operator pauses and manually inputs the corresponding attribute information. All of the manual process is finished in office after the video log images are collected.

- **Manual Process (In-filed)**

This process does not use any video log image. It requires the operator to physically approach each traffic sign to be inventoried and manually input the corresponding inventory information. In this preliminary assessment, the information was input by GDOT using PDAs. All of the manual process is finished in the field.

Table 2.5 Preliminary Assessment of the Enhanced Traffic Sign Inventory Procedure

	Image-Enhanced Procedure	LiDAR-Enhanced Procedure	Manual Process (In-office)	Manual Process (In-field)
Processing Time (sec/sign)	148	74	244	288

Table 2.5 shows the compared results between the enhanced procedure and the manual process. From the assessment result, it is observed that the enhanced procedures using either image or LiDAR-based automatic methods for traffic sign inventory is more efficient than the manual process, either in the office or in the field. The enhanced procedure using mobile LiDAR

demonstrates approximately a 65% improvement of the processing time over the in-office manual process, and 75% over the in-filed manual process. In addition, the enhanced procedure using image-based automatic methods is slightly slower than the one using mobile LiDAR due to the large resolution of the input video log images (i.e. 2,448×2,048). Nevertheless, it still improves by approximately 40% the processing time over the in-office manual process and by 50% over the in-filed manual process. Currently, the automatic methods using video log images and mobile LiDAR have been separately tested and have yet to be integrated. Therefore, there is still good potential to further improve the processing time over the current result once the algorithms are integrated.

It is also identified that for the in-office manual process, the navigation of the images and the digitization of the traffic sign polygon is the most time-consuming process, while for the in-field manual process, the traveling and stopping among different traffic signs is the most time-consuming process. In the enhanced procedure, such processing time can be saved.

Through the preliminary assessment results presented in Table 2.5, the enhanced procedures demonstrate a certain level of improvement over the traditional manual process. Further assessment using larger and more diverse datasets should produce increased benefits with the enhanced procedure. In addition, further improvement of the processing time is expected after the integration of the automatic methods using video log images and the one using mobile LiDAR.

6. Summary and Discussions

The objective of the critical assessment on the representative algorithms developed for traffic sign inventory is to demonstrate the results with actual data, to identify the challenges, and to recommend for the utilization of the algorithms supporting the current practice in state DOTs.

In this chapter, both the automatic traffic sign detection and recognition algorithms using video log images and mobile LiDAR are critically assessed using actual data acquired from different transportation agencies and collected using the GTSV. The results have demonstrated the potential of applying these automatic algorithms in existing operational procedures for state DOTs to provide a reliable, efficient inventory method.

- For the automatic traffic sign detection algorithm using video log images, more than 75% of the traffic signs were correctly detected using the video log images acquired from LaDOTD and the city of Nashville.
- For the automatic traffic sign recognition algorithm using video log images, 81% of the stop signs and 96% of the speed limit signs were correctly recognized using the video log images collected by the GTSV.
- For the automatic traffic sign detection algorithm using mobile LiDAR, more than 94% of the traffic signs were correctly detected using the LiDAR data collected by the GTSV.

However, several technical challenges are also identified from the assessed representative algorithms, including the following:

- For the automatic traffic sign detection algorithm using video log images, there are still approximately 25% of the traffic signs that cannot be detected due to the lighting changes, discontinuous boundaries, and several other cases. In addition, there are excessive FP cases identified in the assessment results. At this stage, it is still challenging to achieve fully automatic traffic sign detection due to the identified FN and FP cases. Manual review of the complete dataset is still required to identify the undetected FN cases and to remove the excessive FP cases.
- For the automatic traffic sign recognition algorithm using video log images, there are still several FN cases existing for both stop signs and speed limit signs due the lighting issues. More importantly, as only limited types of traffic signs can be automatically recognized, manual review of the complete dataset is still required to identify the MUTCD codes for other traffic sign types.
- For the automatic traffic sign detection algorithm using mobile LiDAR, there are still several FN cases due to the poor retroreflectivity, occlusion, non-compliant traffic signs, and overhead signs. In addition, several FP cases are identified, as they share retroreflectivity similar to traffic signs. Further integrating with the image-based algorithms could potentially reduce the FN and FP cases. However, at the current stage, manual review of the complete dataset is still required to identify the undetected FN cases and to remove the FP cases.

In summary, although there is potential to apply the assessed representative algorithms to the existing traffic sign inventory operation procedures, the identified FN and FP cases still require manual review of the complete dataset. Therefore, on one hand, there is a need to further improve the performance of the individual algorithms. On the other hand, to promptly overcome these challenges and maximize the utilization of the existing automatic methods in the current practice of state DOTs, a new enhanced traffic sign inventory procedure is proposed in Section 5 of this chapter. The existing automatic methods or the future improved ones can be flexibly incorporated into the procedure. The preliminary assessment has demonstrated a good improvement (more than 40%) over the traditional manual process in terms of processing time. The further integration of the automatic methods using video log images and the mobile LiDAR shows more improvement of the processing time for traffic sign inventory.

References

- Ai, C., and Tsai, Y. (2012). "Critical Assessment of Automatic Traffic Sign Detection Using Three-Dimensional LiDAR Point Cloud Data." *TRB 91st Annual Meeting*, Washington DC.
- Barnes, N., Zelinsky, A., and Fletcher, L. S. (2008). "Real-Time Speed Sign Detection Using the Radial Symmetry Detector." *IEEE Transactions on Intelligent Transportation Systems*, 9(2), 322-332.
- Baro, X., Escalera, S., Vitria, J., Pujol, O., and Radeva, P. (2009). "Traffic Sign Recognition Using Evolutionary Adaboost Detection and Forest-ECOC Classification." *IEEE Transactions on Intelligent Transportation Systems*, 10(1), 113-126.
- Belaroussi, R., and Tarel, J. P. (2009). "Angle Vertex and Bisector Geometric Model for Triangularroad Sign Detection." *Proc., Workshop on Applications of Computer Vision (WACV)*, 1-7.
- Benallal, M., and Meunier, J. (2003). "Real-Time Color Segmentation of Road Signs." *Proc., Canadian Conference on Electrical and Computer Engineering (CCECE)*, 1823-1826.
- Betke, M., and Makris, N. C. (1995). "Fast Object Recognition in Noisy Images Using Simulated Annealing." *Proc., Fifth International Conference on Computer Vision*, 523-530.

- Chiung-Yao, F., Sei-Wang, C., and Chiou-Shann, F. (2003). "Road-Sign Detection and Tracking." *IEEE Transactions on Vehicular Technology*, 52(5), 1329-1341.
- de la Escalera, A., Moreno, L. E., Salichs, M. A., and Armingol, J. M. (1997). "Road Traffic Sign Detection and Classification." *IEEE Transactions on Industrial Electronics*, 44(6), 848-859.
- de la Escalera, A., Armingol, J. M., and Mata, M. (2003). "Traffic Sign Recognition and Analysis for Intelligent Vehicles." *Image and Vision Computing*, 21(3), 247-258.
- de la Escalera, A., Armingol, J. M., Pastor, J. M., and Rodriguez, F. J. (2004). "Visual Sign Information Extraction and Identification by Deformable Models for Intelligent Vehicles." *IEEE Transactions on Intelligent Transportation Systems*, 5(2), 57-68.
- Douville, P. (2000). "Real-Time Classification of Traffic Signs." *Real-Time Imaging*, 6(3), 185-193.
- Gomez-Moreno, H., Maldonado-Bascon, S., Gil-Jimenez, P., and Lafuente-Arroyo, S. (2010). "Goal Evaluation of Segmentation Algorithms for Traffic Sign Recognition." *IEEE Transactions on Intelligent Transportation Systems*, 11(4), 917-930.
- Hu, Z., and Tsai, Y. (2011). "Generalized Image Recognition Algorithm for Sign Inventory." *Journal of Computing in Civil Engineering*, 25(2), 149-158.
- Kang, D. S., Griswold, N. C., and Kehtarnavaz, N. (1994). "An Invariant Traffic Sign Recognition System Based on Sequential Color Processing and Geometrical Transformation." *Proc., IEEE Southwest Symposium on Image Analysis and Interpretation*, 88-93.
- King Hann, L., Li-Minn, A., and Kah Phooi, S. (2008). "New Hybrid Technique for Traffic Sign Recognition." *Proc., International Symposium on Intelligent Signal Processing and Communications Systems (ISPACS)*, 1-4.

- Koncar, A., Janßen, H., and Halgamuge, S. (2007). "Gabor Wavelet Similarity Maps for Optimising Hierarchical Road Sign Classifiers." *Pattern Recognition Letters*, 28(2), 260-267.
- Laflamme, C., Kingston, T., and McCuaig, R. (2006). "Automated Mobile Mapping for Asset Managers." *Shaping the Change XXIII FIG Congress*, Munich, Germany.
- Maldonado-Bascon, S., Lafuente-Arroyo, S., Gil-Jimenez, P., Gomez-Moreno, H., and Lopez-Ferreras, F. (2007). "Road-Sign Detection and Recognition Based on Support Vector Machines." *IEEE Transactions on Intelligent Transportation Systems*, 8(2), 264-278.
- Marmo, R., and Lombardi, L. (2007). "Milepost Sign Detection." *Proc., International Workshop on Computer Architecture for Machine Perception and Sensing (CAMPS)*, 93-98.
- McGee, H. W., and Paniati, J. F. (1998). "An Implementation Guide for Minimum Retroreflectivity Requirements for Traffic Signs." U.S. Department of Transportation, Federal Highway Administration, Washington, D.C.
- Miura, J., Kanda, T., and Shirai, Y. (2000). "An Active Vision System for Real-Time Traffic Sign Recognition." *Proc., IEEE Intelligent Transportation Systems*, 52-57.
- Moreno, O., and Cook, R. T. (2010). "Presentation: Phoenix Sign Inventory and Replacement." Parsons Brinckerhoff Inc.
- Nguwi, Y., and Kouzani, A. (2008). "Detection and Classification of Road Signs in Natural Environments." *Neural Computing & Applications*, 17(3), 265-289.
- Overett, G., Petersson, L., Andersson, L., and Pettersson, N. (2009). "Boosting a heterogeneous pool of fast HOG features for pedestrian and sign detection." *Proc., IEEE Intelligent Vehicles Symposium*, 584-590.
- Paclik, P., Novovicova, J., and Duin, R. P. W. (2006). "Building Road-Sign Classifiers Using a Trainable Similarity Measure." *IEEE Transactions on Intelligent Transportation Systems*, 7(3), 309-321.

- Paclík, P., Novovicová, J., Pudil, P., and Somol, P. (2000). "Road Sign Classification Using Laplace Kernel Classifier." *Pattern Recognition Letters*, 21(13-14), 1165-1173.
- Paoly, D., and Staud, A. B. (2010). "Use of MobileGIS for Sign Inventories." *Proc., AASHTO GIS for Transportation*.
- Piccioli, G., De Micheli, E., Parodi, P., and Campani, M. (1996). "Robust Method for Road Sign Detection and Recognition." *Image and Vision Computing*, 14(3), 209-223.
- Priese, L., Klieber, J., Lakmann, R., Rehrmann, V., and Schian, R. (1994). "New Results on Traffic Sign Recognition." *Proc., Intelligent Vehicles Symposium*, 249-254.
- Priese, L., Lakmann, R., and Rehrmann, V. (1995). "Ideogram Identification in a Realtime Traffic Sign Recognition System." *Proc., Intelligent Vehicles Symposium*, 310-314.
- Rasdorf, W., Hummer, J. E., Harris, E. A., and Sitzabee, W. E. (2009). "IT Issues for the Management of High-Quantity, Low-Cost Assets." *Journal of computing in Civil Engineering*, 23(2), 91-99.
- Rehrmann, V., and Priese, L. (1997). "Fast and Robust Segmentation of Natural Color Scenes." *Proc., Asian Conference on Computer Vision (ACCV)*, Springer, Berlin/Heidelberg, 598-606.
- Ren, F., Huang, J., Jiang, R., and Klette, R. (2009). "General Traffic Sign Recognition by Feature Matching." *Proc., 24th International Conference on Image and Vision Computing New Zealand (IVCNZ)*, 409-414.
- Ruta, A., Yongmin, L., and Xiaohui, L. (2010). "Robust Class Similarity Measure for Traffic Sign Recognition." *IEEE Transactions on Intelligent Transportation Systems*, 11(4), 846-855.
- Shadeed, W. G., Abu-Al-Nadi, D. I., and Mismar, M. J. (2003). "Road Traffic Sign Detection in Color Images." *Proc., 10th IEEE International Conference on Electronics, Circuits and Systems (ICECS)*, 890-893, Vol.892.

- Tsai, Y., and Wu, J. (2002). "Shape- and Texture-Based 1-D Image Processing Algorithm for Real-Time Stop Sign Road Inventory Data Collection." *Intelligent Transportation Systems Journal*, 7(3/4), 213-234.
- Tsai, Y., Kim, P., and Wang, Z. (2009). "Generalized Traffic Sign Detection Model for Developing a Sign Inventory." *Journal of Computing in Civil Engineering*, 23(5), 266-276.
- Wang, K. C. P., Hou, Z., and Gong, W. (2010). "Automated Road Sign Inventory System Based on Stereo Vision and Tracking." *Computer-Aided Civil and Infrastructure Engineering*, 25(6), 468-477.
- Wolshon, B. (2003). "Louisiana Traffic Sign Inventory and Management System Report-381." Louisiana Transportation Research Center, Baton Rouge.
- Wu, J., and Tsai, Y. (2006). "Enhanced Roadway Inventory Using a 2-D Sign Video Image Recognition Algorithm." *Computer-Aided Civil and Infrastructure Engineering*, 21(5), 369-382.
- Yong-Jian, Z., Ritter, W., and Janssen, R. (1994). "An Adaptive System for Traffic Sign Recognition." *Proc., Intelligent Vehicles Symposium*, 165-170.

Chapter 3 Traffic Sign Inventory and Condition Assessment – A Case Study on I-285

1. Introduction

Previous chapters validated the performance of automatic sign inventory using video log images and mobile LiDAR. Although the performance of these methods remains to be improved to full automation, tremendous amounts of manual effort can be saved by incorporating these methods in an enhanced sign inventory procedure. More importantly, safety can be significantly improved with less or no exposure to roadway hazards. In this chapter, a large-scale case study was conducted to inventory all signs and assess their conditions on I-285. The following list the major objectives:

- To conduct a detailed sign inventory and condition assessment on I-285 using the enhanced, computer-aided sign data collection procedures;
- To develop a detailed analysis of traffic sign characteristics, including sign location, classification (i.e. MUTCD code) and condition;
- To identify the spatial distribution of the overhead traffic signs. They are particularly of interest to state DOTs because the structural failure of these overhead signs could lead to severe roadway hazards;
- To study the types of sign damages and their causes using calibrated high resolution video log images. They are particularly of interest for state DOTs because this information on damage types and causes could be used to minimize the sign damage by improving the stability of a sign post, treating the ground base of a sign post, etc.

2. Traffic Sign Characteristics

This section defines the main traffic sign characteristics that were collected in this study. Traffic sign data collection includes two primary steps: inventory and condition assessment. An inventory collects sign locations and attributes, e.g. classification of traffic signs, while condition assessment determines the performance adequacy of inventoried signs by identifying damaged signs. Sign location, classification, and condition are the key characteristics that must be collected.

Sign Location: Traffic sign location is defined by three GPS coordinates (i.e. longitude, latitude, and elevation) that uniquely define the spatial position. Extracting the location for each individual sign is the most important step for traffic sign inventory. In this study, WGS84 geodetic GPS coordinates are used to represent the traffic sign location, which can be flexibly converted to a linear referencing system that is used in GDOT.

Sign Classification: Traffic signs are classified by different traffic sign functions, and sign classification leads to different designs, e.g. RX-X as regulatory signs, WX-X as warning signs, etc. There are more than 670 traffic signs defined in the MUTCD in three classifications: regulatory signs, warning signs, and message signs. In addition, there could be several sign types that only occur within certain states or regions and are assigned internal MUTCD codes. In this study, the Signs Chapter of the GDOT's Foreman's Academy (2008) is used to define sign classifications and details the general MUTCD codes and the internal MUTCD codes.

Sign Condition: Traffic sign condition is represented by the sign's visual defects and the sign's retroreflectivity. This study used video log images captured during the daytime to identify visual defects. Four categories of poor sign conditions are defined in this study: post failure, dirty, obstructed, and surface failure. Based on the Signs Chapter of the GDOT's Foreman's Academy (2008), the four categories of poor sign conditions correspond to four maintenance actions defined by the Highway Maintenance Management System (HMMS) (Hensing & Rowshan, 2005), including straightening, cleaning, vegetation trimming, and replacing. Figure 3.1 shows several examples signs in poor condition in each category. Appendix I lists all the traffic signs in poor conditions and their locations on I-285.

Overhead Sign: Overhead signs are considered separately from ground-mounted traffic signs. Although overhead signs are only a small portion of the whole sign population, the damage to these signs and/or their corresponding supports, e.g. panel failure or structural failure, etc., may lead to serious roadway hazards, as illustrated in Figure 3.2.

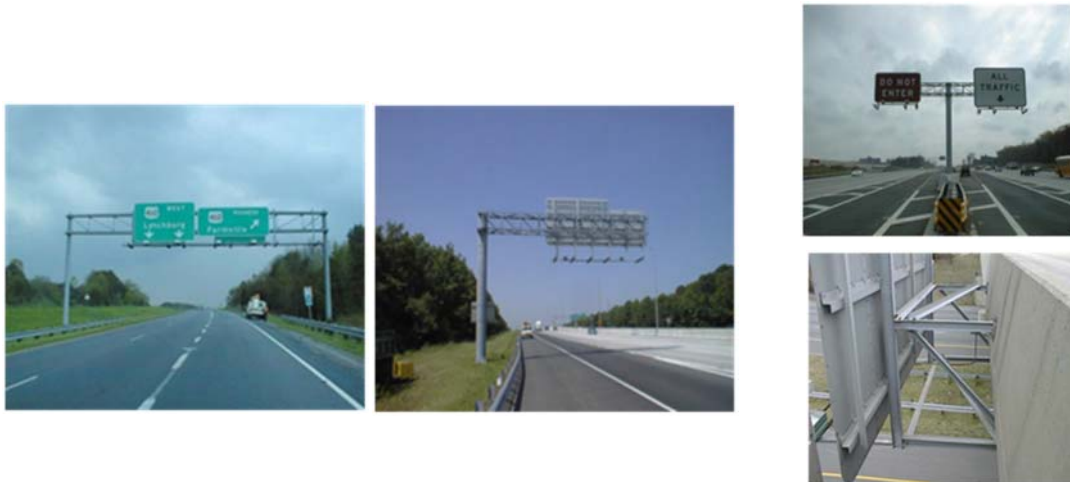


Figure 3.1 Examples of four categories of poor sign conditions



Figure 3.2 Example of overhead sign failure (FHWA 2013)

Therefore, overhead signs are specially categorized and inventoried in detail. According to the different supporting structures for overhead signs defined in the Signs Chapter of the GDOT's Foreman's Academy (2008), three categories are inventoried: Sign-Bridge, Cantilever, and Other Structures. Figure 3.3 illustrates these three categories. Inventorying the detailed categories of overhead signs and identifying the spatial locations of these signs will be beneficial to the subsequent maintenance or more detailed structure inspection. Appendix II lists all the overhead signs and their locations on I-285.



Sign Bridge

Cantilever

Other Overhead

Figure 3.3 Examples of the overhead sign categories defined by GDOT

3. Sensing Data Collection

In this study, data was collected using the GTSV during May 2013. Three sequences of video log images were captured, covering the left and right sides and the center of the roadway. Two sets of LiDAR data were simultaneously acquired, covering the right side and overhead of the road (i.e. the most frequent sign locations). High-resolution video log images (i.e. 5MP) and LiDAR data were calibrated and synchronized so that precise location information could be extracted from either data source. The camera angles and LiDAR scanning orientation were configured to cover all the possible sign locations. Figure 3.4 illustrates the coverage of the sensing data collection. In addition, to minimize the occlusion caused by heavy trucks, the GTSV was maintained in the out-most lane during the data collection session.

4. Sign Inventory and Condition Assessment

Based on the enhanced sign inventory procedure proposed in previous chapters, a semi-automatic method was applied to inventory signs and assess their conditions.

4.1 Statistics of Inventoried Signs

I-285 is an interstate highway loop encircling Atlanta, Georgia, for 63.98 centerline miles. Suburban sprawl has made it one of the most heavily traveled roadways in the United States. In this study, there are 2,969 traffic signs that were inventoried using the proposed approach.

The majority of the identified signs are message signs that make up 78.17% of the total population (2,321 signs). The rest of the population consists of 76 regulatory signs, 333 warning signs, and 239 other signs (internal signs in Georgia). Figure 3.5 shows the distribution of the traffic signs on I-285 based on their classifications.

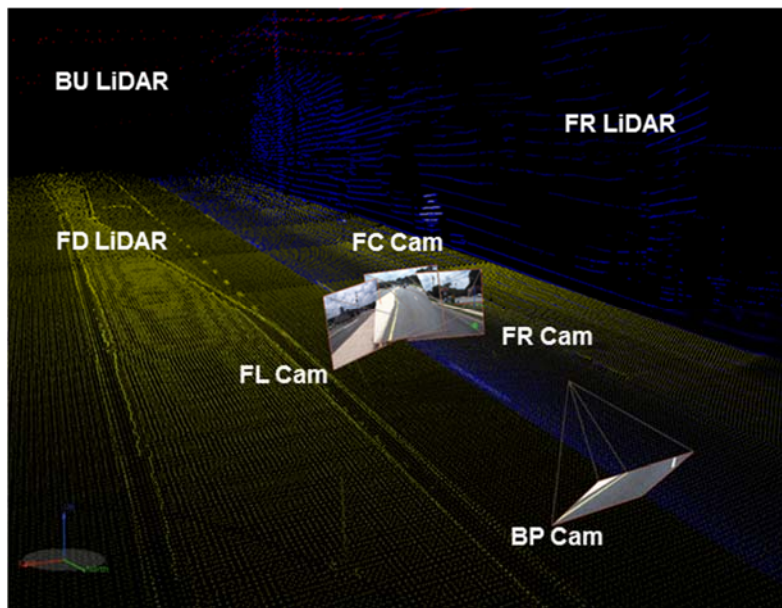


Figure 3.4 Illustration of the coverage of the sensing data collection (including FR – Front Right Camera; FC – Front Center Camera; FL – Front Left Camera; BP – Back Pavement Camera; FR – Front Right LiDAR; FD – Front Down LiDAR; and BU – Back Up LiDAR)

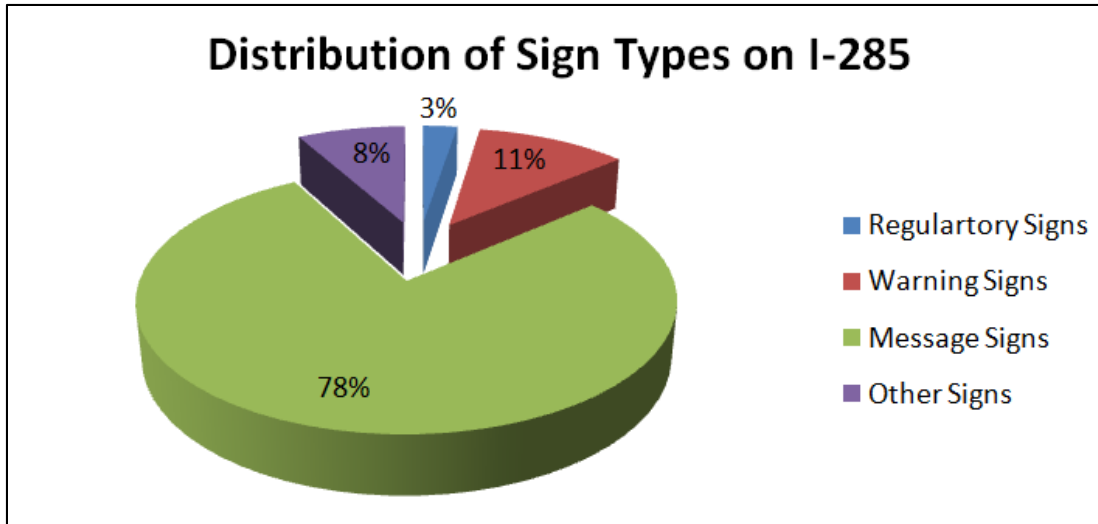


Figure 3.5 Distribution of traffic sign classifications on I-285

Among all the identified signs, about 8.49% (i.e. 252 signs) are in poor condition based on the definitions in the Signs Chapter of the GDOT’s Foreman's Academy (2008). Appendix I lists all the signs in poor conditions and their locations. Surface failure (58.82%) and post failure (28.63%) are the two primary reasons for poor conditions. The rest of the signs are in poor condition due to having an obstruction problem (8.24%) and being dirty (4.31%). Figure 3.6 shows the distribution of the traffic signs in poor conditions on I-285 based on their damages. Three types of sign damages were identified, and their causes are preliminarily studied in this research project through close visual inspection of the high resolution video log images, although further field inspection and in-depth study are recommended to confirm the damages. The possible causes to the three types of sign damages are discussed and summarized in the subsequent sections.

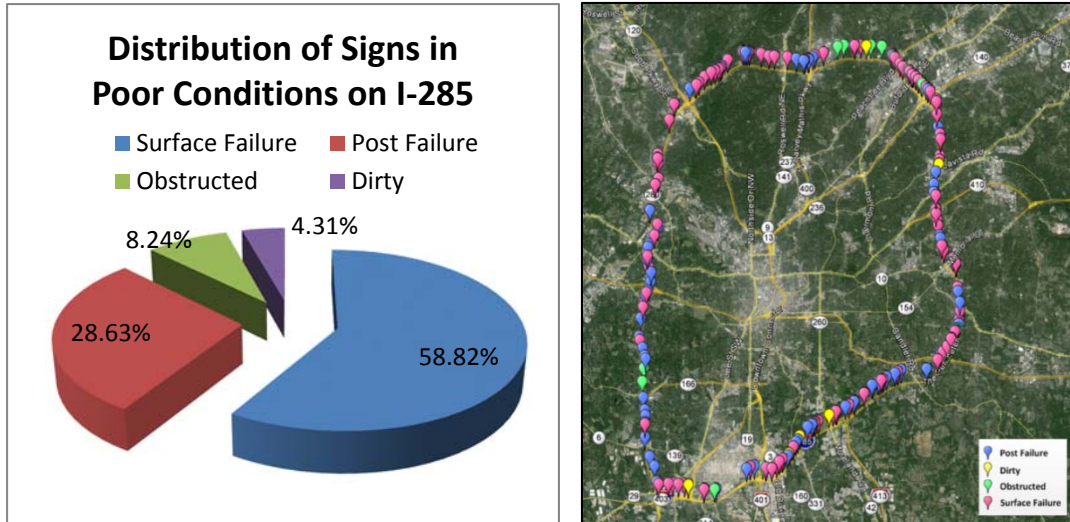


Figure 3.6 Distributions of traffic signs in poor condition on I-285 (252 signs)

Among all the inventoried signs, about 21.66% of the signs (i.e. 643 signs) are installed on overhead structures, including Sign-Bridge, Cantilever, and Other Overhead. Appendix II lists all the overhead signs and their locations. More than 50.23% of the overhead signs are installed on bridges, while 13.06% of the overhead signs are installed on cantilever structures. The rest of the overhead signs (36.70%) are installed either on bridge-mounted structures or butterfly structures, categorized as Other Overhead due to the lack of any other specific definition in the Signs Chapter of the GDOT’s Foreman's Academy (2008). Figure 3.7 shows the distribution of the overhead signs on I-285 based on their base supporting structures.

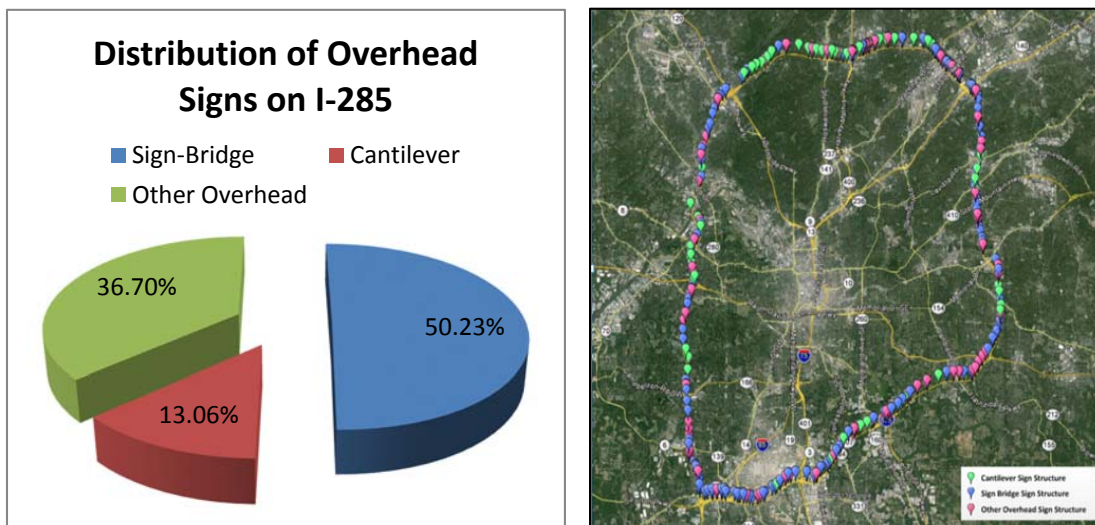


Figure 3.7 Distributions of traffic signs installed on overhead structure on I-285

4.2 Three Types of Sign Damages and Causes

This section studies the three types of sign damages by reviewing high-resolution roadway images. The detailed locations for these signs are available for planning field inspections and maintenance. Through the visual inspection using the high resolution video log images, some of the preliminary damage causes were identified. Three types of damages, truck gust, dual-post support, and post failure, were identified and summarized.

Damage Type 1 – Truck Gust

Of the 252 signs in poor condition, 108 signs are identified as being damaged by truck gusts. This type primarily includes milepost traffic signs that are mounted on concrete medians. The surfaces of the damaged signs are bent or wrapped parallel to the driving directions, as shown in Figure 3.8. From the video log images, it was observed that although the signs are damaged on the median, the median itself doesn't show any evidence of crash or impact. While further investigation is still required to reveal the cause of such sign damage, the preliminary inspection showed that the signs are (probably) damaged by the strong truck gust that is created by fast-moving trucks. While the truck passes by the traffic sign, the frontal area of the sign tends to bear extra gust loads that can potentially bend the sheeting. In addition, it was observed that the majority of the median-mounted traffic signs are not designed with a metal post. Instead, one end of such traffic sign is mounted on a fixed connection attached to the concrete as shown in Figure 3.8, while the whole sign surface stands by the strength of the aluminum sheeting. Such a design may synergize with the truck gusts and facilitate the damage. Adding a square or u-shape sign post may effectively avoid such damage to the median-mounted traffic signs (McGee, 2010).

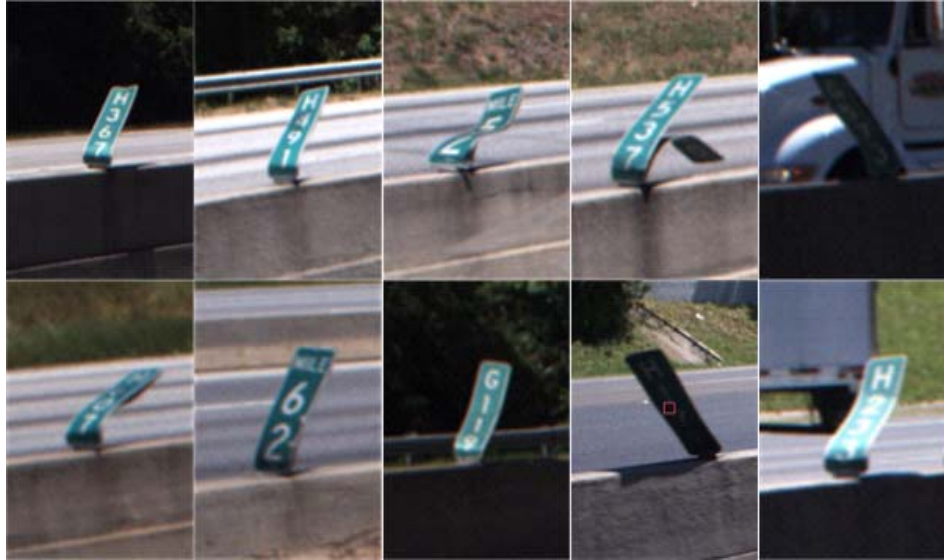


Figure 3.8 Examples of the damaged signs due to truck gust on median

Damage Type 2 – Dual-Post

Of the 252 signs in poor condition, 21 are identified as having dual post damages. This type includes, primarily, the off-ramp signs that are mounted using dual posts to hold multi-panels. The dual posts indicate that the sign is supported by two parallel square or u-shaped sign posts, while the multi-panel indicates that the surface of the sign consists of multiple, elongated sign panels instead of a single panel. It was observed that the surface of the damaged signs shows waviness and unevenness, while the two posts of the damaged signs are no longer parallel to each other. Figure 3.9 shows several examples of such damaged signs. The preliminary inspection showed that such damage is caused by the unbalanced vibration of the dual posts, which shakes the multi-panels so that the surface becomes wavy and uneven. The unbalanced vibration can be produced by the gusts from the passing vehicles and ground support defects. Reinforcing the dual-post using an I-beam steel post with a slip base may effectively avoid such damage (McGee, 2010).



Figure 3.9 Examples of the damaged signs due to dual-post

Damage Type 3 – Post Failure

Of the 252 signs in poor condition, 73 signs are identified as having post failure. This type primarily includes traffic signs with incorrect facing due to the sign post failure. The preliminary inspection showed that the majority of these sign post failures can be caused by direct impact, which deforms the shape of the post, while the rest can be caused by a soft base or poor ground support. Figure 3.10 shows several examples of such damaged signs. Direct replacement will be needed for this damage type to maintain these signs' visibility during the daytime and nighttime. However, if field inspection identifies that the post failure is caused by a soft base, reinforcing the sign post with a slip base may also be required to avoid such damage, especially for large message sign panels (McGee, 2010; Bligh et al., 2001).



Figure 3.10 Examples of the damaged signs due to post failure

5. Summary

This study thoroughly extracted the detailed traffic sign inventory information (including sign location, MUTCD code, and overhead signs) and details sign condition information (visual sign conditions). The enhanced procedure for traffic sign inventory and condition assessment was validated as a means to maximize the utilization of the available sensing data and use computer-aided methods to improve sign inventory productivity. More importantly, this method greatly reduces the danger to engineers by enabling them to take inventory of signs without being exposed to roadway hazards, especially on interstate highways and near overhead signs. The signs on the 63.98 centerline miles on I-285 (128 survey miles) were collected using the enhanced data collection procedure, and their conditions were evaluated based on the Signs Chapter of the GDOT's Foreman's Academy (2008). Detailed statistics were derived to further study the key characteristics of the installed traffic signs.

- On I-285, there are 2,969 signs. The majority of the installed traffic signs on interstate highways are messages signs that convey direction, destination, and service information (2321 signs, 78.17%). Only a limited number of warning signs and regulatory signs are installed to indicate hazardous conditions or regulate drivers' behavior.
- A large percentage of installed traffic signs are mounted on overhead structures on interstate highways (643 signs, 21.66%). These overhead structures hold larger and heavier traffic sign panels that are different from normal sign sheeting. Therefore, the integrity of these signs is critical and requires more frequent inspection and maintenance. They are divided into three categories and inventoried with their location (coordinates), including Sign-bridge (323 signs, 50.23%), Cantilever (84 signs, 13.06%), and Other Overhead, including butterfly and bridge mount (236 signs, 36.70%).
- There are 252 signs in poor condition (255 poor sign condition cases with the four categories of poor sign conditions) that require sign maintenance action based on the sign condition assessment in GDOT Foreman's Manual, including: surface failure (150 cases, 58.82%), post failure (73 cases, 28.63%), obstructed (21 cases, 8.24%), and dirty (11 cases, 4.31%).
- Additional effort was conducted to study the causes of three types of sign damages using the calibrated high-resolution video log images. Through the visual inspection, not only the precise locations of the damaged signs were extracted, but also the damages were

preliminarily assessed. The most frequently occurring sign damage type is surface failure on milepost signs due to truck gusts. They are located on the concrete barriers, on roadsides, or on medians. These signs are damaged by the strong truck gusts that are created by fast-moving trucks. Another sign type suffering frequent damage is made up of exit signs that are damaged due to the instability of their dual posts. They are located at the interstate exits. The inspection shows that the signs are damaged by the unbalanced vibration and twisting of the dual posts. In addition, post failures also frequently occur due to direct crash impact or soft bases. The only type of overhead sign that is damaged is D3-1 (i.e. street name sign) mounted on bridges. The majority of D3-1 signs are damaged due to surface failure (i.e. color fading and erosion). Figure 3.11 shows an example of a damaged D3-1 sign.



Figure 3.11 Example of a damaged D3-1 street name sign

- The coordinates (latitude and longitude) of each sign were collected and visualized on a GIS map. Tables containing mile points were also generated for signs with poor sign condition that require maintenance action and for overhead signs that require frequent monitoring. The image for each sign is also collected to provide visual cues for engineers before they go to the field. GDOT can use this sign data to effectively create a sign maintenance/replacement work plan.

The following are the recommendations for implementing the findings of this study:

- Based on the I-285 study, it has been demonstrated that the proposed enhanced sign data collection procedure is very promising; it is a cost-effective means to collect sign data and assess sign condition, especially on the hazardous interstate highways with heavy traffic. With the successful pilot study on I-285, it is recommended that the signs on all Georgia's

interstate highways (more than 2,500 surveyed miles) be inventoried using the enhanced sign data inventory procedure.

- The overhead signs have high potential risk. With the research outcomes, these signs on I-285 were identified and can be inventoried for routine monitoring to ensure their integrity and safety, and timely maintenance.
- For the signs with poor condition, whose locations were identified in this study, the proper sign maintenance actions can be taken effectively with the derived sign inventory.
- Although the preliminary study of three types of sign damages was conducted, further field inspection and in-depth study are recommended to confirm the causes of the damages and to propose the adequate improvement to minimize the sign damage.

References

- Ai, C. and Tsai, Y. (2012). “Critical Assessment of Automatic Traffic Sign Detection Using Three-Dimensional LiDAR Point Cloud Data.” *Proceedings of the TRB 91st Annual Meeting*, Washington DC.
- Bligh, R. P., Buth, C. E., Menges, W. L., and Butler, B. G. (2001) “Evaluation of Design and Retrofit Concept for Slip-Base Sign Support System.” *Texas Transportation Institute Technical Report TX-01/3911-S*, College Station, TX.
- FHWA (2013). “Guidelines for the Installation, Inspection, Maintenance and Repair of Structural Supports for Highway Signs, Luminaries, and Traffic Signals.” *Federal Highway Association*. Accessed online on Feb. 1, 2014 at <https://www.fhwa.dot.gov/bridge/signinspection.cfm>
- GDOT (2008). “Foremans Academy – Traffic Sign Training in Georgia Department of Transportation”.
- Hensing, D. J., Rowshan, S. (2005). “Roadway Safety Hardware Asset Management Systems Case Studies.” *Technical Report FHWA-HRT-05-073*, Washington DC.
- McGee, H. W. (2010). “Maintenance of Signs and Sign Supports: A Guide for Local Roads Maintenance Personnel.” *Technical Report FHWA-SA-09-025*, Washington DC.

Chapter 4 Sign Retroreflectivity Condition Assessment Using Mobile LiDAR – A Feasibility Study

1. Introduction

Traffic sign retroreflectivity plays a critical role in nighttime driving safety. The new MUTCD requires that the minimum retroreflectivity of traffic signs must be maintained by each state DOT. To do so, state DOTs commonly use manual assessment methods, using either nighttime visual inspection or retroreflectometer measurement. However, these manual methods have limitations. The nighttime visual inspection method is subjective due to the inconsistency of human perception, and the retroreflectometer measurement method is very time-consuming due to the frequent stops for contact measurement. Other management methods, e.g. blanket sign replacement, are also used by state DOTs, but are potentially costly because they may blindly remove many traffic signs in good condition. In recent years, several automatic traffic sign retroreflectivity condition assessment methods using image processing have been proposed. Survey vehicles are equipped with special artificial lighting devices and calibrated video cameras to assess signs' retroreflectivity condition by assessing the intensity response from the cameras to an artificial lighting source. Some of the proposed methods cannot provide results as satisfactorily as the current manual method (Smith & Fletcher, 2001), and other methods are yet to be validated (Retterath & Laumeier, 2008; 2011). The primary challenges for these methods are handling the sensitivity of the image quality due to image saturation, interference from the ambient lighting, and difficulties in acquiring accurate camera parameters. None of these methods have been implemented by state DOTs. Hence, there remains an urgent need for a method that reliably and cost-effectively assesses the traffic sign retroreflectivity condition.

Because of the advancements in emerging light detection and ranging (LiDAR) technology (i.e. improvements in data acquisition frequency and reflectance measurement accuracy), LiDAR systems can acquire point cloud data for individual traffic signs in high resolution and with precise retro-intensity measurement. To develop an automatic traffic sign retroreflectivity condition assessment that can operate at highway speed, this study further investigates the potential to substantially improve traffic sign assessment by exploring the retro-intensity

distribution for the traffic signs associated with LiDAR point clouds. The study presented in this chapter is motivated by the urgent needs of state DOTs and the present-day abilities to meet those needs by utilizing the advancement of the emerging LiDAR and computer vision technologies.

This chapter is organized as follows. This section presents the background and the motivation of the study. Section 2 presents the current traffic sign retroreflectivity condition assessment method in state DOTs and the state-of-the-art research. Section 3 briefly presents the principle of the LiDAR-based traffic sign retroreflectivity condition assessment method and the experimental test to demonstrate the feasibility of the tested method. Section 4 presents conclusions and recommendations.

2. Literature Review

This section presents a literature review of the current practice in state DOTs for traffic sign retroreflectivity condition assessment, including nighttime visual inspection, retroreflectometer measurement, and blanket replacement. In addition, with the advancement of computer vision technologies, some image-based traffic sign retroreflectivity condition methods in previous studies are discussed. This section also presents the state-of-the-art research in detail. Finally, based on the literature review, the identified research needs for this study are presented.

2.1 Current Practice

Traffic sign retroreflectivity is critical for nighttime safety and determining the adequacy of the traffic signs' reflectance during nighttime is one of the most important parts in a state DOT's traffic sign management system to. To address this important issue, FHWA has developed minimum traffic sign retroreflectivity condition standards and mandated all transportation agencies implement a plan for meeting those standards. State DOTs are actively searching for a cost-effective approach for traffic sign retroreflectivity condition assessment by improving their existing methods or adopting new methods suggested by the MUTCD. At present, state DOTs use three primary methods for retroreflectivity condition assessment, including nighttime visual inspection, retroreflectometer measurement, and management methods.

- **Nighttime visual inspection**

Nighttime visual inspection is a manual process that requires an investigator visually assess the traffic sign retroreflectivity condition at night using “trained eyes” (FHWA, 2009). Because it is easy to conduct, most transportation agencies use nighttime visual inspection as their primary method to determine the traffic sign retroreflectivity condition. Although the nighttime visual inspection is widely used by state DOTs, the assessment results can be subjective and inconsistent from one investigator to another. Hawkins and Carlson (2001) conducted a field test using 50 traffic signs removed from the roadside. Sign investigators in the test identified 26 unacceptable signs, but only one traffic sign was considered unacceptable using a retroreflectometer with FHWA standards.

- **Retroreflectometer measurement**

Retroreflectometer measurement is a manual process that requires a field engineer to conduct contact measurements for each traffic sign using a retroreflectometer. The American Society for Testing and Materials (ASTM) has provided a standard measurement procedure using the retroreflectometer, which mimics the traffic sign brightness as seen by a sport utility vehicle (SUV) driver at a distance of 200 meters. A minimum of four measurements for each reflective color of the traffic sign are required. The average of the readings for each reflective color will be compared with the MUTCD standard to determine the retroreflectivity condition. The retroreflectometer can provide a quantitative and consistent measurement to determine the traffic sign retroreflectivity for each measurement point. Several transportation agencies are using this method, including LaDOTD, the Indiana department of Transportation (InDOT), the Virginia Department of Transportation (VDOT), Hillsborough County, Florida, etc. However, as the retroreflectometer measures traffic sign retroreflectivity by contacting the traffic sign surface, the investigator needs to physically approach each traffic sign and conduct the survey. This method is time-consuming and costly. In addition, as the average of multiple measurements (typically using four points) is used to represent the overall retroreflectivity condition for each reflective color, the results can be over- or under-estimated if the traffic sign is non-uniformly deteriorated (Remias et al., 2011).

- **Management Method**

Management methods include expected sign life, blanket replacement, and control signs. These three methods share similar procedures that blindly replace all the traffic signs with similar characteristics, e.g. installation time, sign sheeting and color, etc. In this case, individual retroreflectivity condition assessment is not required. Many transportation agencies are planning to implement this method to save the effort and cost of individual traffic sign condition assessment. For example, the city of Phoenix is performing the blanket replacement method to replace more than 28,000 traffic sign along a major corridor in the city (Moreno & Cook, 2010). However, as the traffic signs are blindly replaced based on limited criteria, this method could potentially replace many traffic signs with good retroreflectivity that do not need to be replaced, which wastes money and resources.

2.2 State-of-the-Art Research

To improve the efficiency of the traffic sign condition assessment process, some methods have been proposed to assess the traffic sign retroreflectivity condition automatically by using video log images. The correlation between the image intensity and the traffic sign retroreflectivity is the key component. However, there are few studies exploring the correlation. Most of the studies are based on empirical results using limited traffic sign samples. Siegmann et al. (2008) systematically developed the fundamentals between the image intensity and the retroreflectivity from a photometrical perspective. Different factors, including camera aperture, camera exposure time, surface materials and colors of traffic sign, the distance from the light source to the surface, and the incident angle, etc., were comprehensively studied. A close form equation between retroreflectivity and the studied factors was derived. The equation was validated using a circular speed limit sign. This equation can be applied to correlations between the image intensity and the retroreflectivity under different camera configurations, e.g. camera aperture, camera exposure time, etc., and different data collection parameters, e.g. distance, incidence angle, etc.

Using correlations established between the image intensity and the retroreflectivity, several image-based traffic sign retroreflectivity condition assessment systems have been developed. A Sign Management and Retroreflectivity Tracking System (SMARTS) van was first developed by FHWA in 1999, as shown in Figure 4.1(a). The pilot test was conducted by Alaska DOT (Smith

& Fletcher, 2001). An external light-emitting diode (LED) was used to provide lighting to a traffic sign with known luminance to mimic a vehicle's headlight, while a single camera was used to collect video log images of the illuminated traffic signs. However, the results from the SMARTS van demonstrated that the image-based results had poor correlations with the retroreflectometer measurement results. Facet Inc. and Mandli[®] Communications Inc. developed a similar system called RetroView. External infrared lighting was used instead of an LED to avoid the impact from the ambient lighting. Two camera systems were used to separately collect low and high levels of intensity (Retterath & Laumeyer, 2008, 2011), as shown Figure 4.1(b). Several pilot tests have been conducted by the Tennessee Department of Transportation (TDOT) and the Texas DOT (TxDOT) using the RetroView system. The results indicate that the system is potentially a cost-effective method for traffic sign condition assessment. In Europe, the VISUAL Inspection of Sign and panEL (VISUALISE) system was developed by Gonzales et al. (2011). The VISUALISE system was tested on 500 traffic signs in Spain, and 91% of the traffic signs were correctly assessed. To avoid ambient lighting, the system was operated during the nighttime. The primary reasons of some erroneous assessments included inclined traffic signs and small traffic signs.



(a) FHWA SMARTS system (b) Mandli/Facet RetroView system

Figure 4.1 The Outlooks and the Schematic Flow of the Systems

Although some prototype systems have been developed, limited validations have been conducted for these systems. NCSU's 2008 nationwide survey of different vendors providing comprehensive roadway appurtenance acquisition reveals that there are no vendors supplying data or services for traffic sign retroreflectivity condition assessment (Findley et al., 2011). No state DOT has adopted any mobile systems for traffic sign retroreflectivity condition assessment.

In summary, in previous studies, there have been a few attempts to develop a mobile, image-based traffic sign retroreflectivity condition assessment method. However, several challenges have been identified for the image-based method, including: 1) based on the study by Siegmann et al. (2008), many parameters, such as the distance and incidence angle from camera to targeted sign, are needed to establish a reliable correlation between the image intensity and retroreflectivity. However, it is difficult to acquire these parameters because they change from one location to another location; 2) the image-based method needs to know the luminance of the external lighting, and to cope with image saturation and ambient lighting effects, which are difficult to achieve. Therefore, there is a need to explore alternative methods to cost-effectively conduct traffic sign retroreflectivity condition assessment.

2.3 Research Need

This sub-section summarizes the findings from the literature review. It is identified that the methods used in the current practice of state DOTs are primarily manual processes. These methods can be subjective, time-consuming, and costly. A management method is also used by state DOTs, i.e. blanket replacement. Although the cost for individual assessment for each traffic sign can be saved, the methods increases costs when it needlessly replaces traffic signs in good conditions. With the FHWA-mandated implementation time of minimum traffic sign retroreflectivity approaching, a reliable and cost-effective traffic sign retroreflectivity condition assessment method is being sought by state DOTs. There are some studies developing image-based automatic traffic sign retroreflectivity condition assessment methods and systems. However, all of these systems are still in the research stage and lack validation. In addition, these methods pose many image-inherent challenges that might affect the reliability of the methods. In summary, there is an urgent need to explore an alternative method for a reliable and cost-effective retroreflectivity condition assessment.

3. Assessment of the LiDAR-Based Sign Retroreflectivity Condition

Assessment Method

Retroreflectivity is the most critical attribute of a traffic sign for nighttime visibility. It is defined as the ratio of the luminance that is redirected from a sign's surface to the luminance originated from the vehicle headlight (ASTM D4956-11a). A LiDAR system collects the retro-intensity

values in a way similar to the measurement of traffic sign retroreflectivity. A retro-intensity value is acquired with each LiDAR point that measures the ratio of the energy redirected from the object to the energy emitted from the LiDAR sensor. Hence, there is a possible correlation between the retro-intensity values and the traffic sign retroreflectivity conditions. Such a correlation can potentially be used to conduct an automatic traffic sign retroreflectivity condition assessment. The principle of the tested LiDAR-based sign retroreflectivity condition assessment method (Tsai & Ai, 2013) is to correlate the LiDAR retro-intensity values with the traffic sign retroreflectivity condition (i.e. retroreflectometer readings, etc.) using the population of the retro-intensity values. Computer vision technology is applied to assist the LiDAR-based method by differentiating traffic sign colors and associate the color information with each of the LiDAR point.

The objective of this experimental test was to demonstrate the feasibility of the LiDAR-based sign retroreflectivity condition assessment method. In the experimental test, the actual retroreflectivity of traffic signs was collected in a community in Savannah, Georgia. Considering the challenges of manually assessing a large number of traffic signs, a small group of 10 Type I stop signs were specifically selected for the experimental test. Different installation years of the traffic signs were considered during the selection to introduce a possible variety of the sign retroreflectivity conditions. The LiDAR point cloud data was acquired using the GTSV that can collect the data at highway speed.

3.1 Preliminary Results

To evaluate the performance of the tested method on the selected traffic signs, both the nighttime visual inspection and the retroreflectometer measurement were conducted for ground truths at the same time as the LiDAR data collection. The outcome of the nighttime visual inspection is a two-level assessment based on the perception of the investigator, i.e. PASS and FAIL. The outcome of the retroreflectometer measurement was a four-point average of the retroreflectivity measurement values using a handheld retroreflectometer in compliance with ASTM standard (E1709-09). Each measurement point was randomly selected at each quadrant of the sign. The average value was compared with the MUTCD standard for the minimum retroreflectivity. If the average was greater than the minimum retroreflectivity requirement, the retroreflectivity condition was identified as PASS; otherwise, it was FAIL. Both of the outcomes were used as

the ground truths to evaluate the performance of the tested method. Given the small number of the tested stop signs, strong conclusions from these results should not be drawn. Table 4.1 shows the assessment results from the tested method and the established ground truths using both the nighttime visual inspection and the retroreflectometer measurement. The threshold value of 0.767 derived from the tested method was used for this test. A traffic sign with a greater median retro-intensity value than 0.767 is considered as the PASS condition, while with a less median value is considered as the FAIL condition.

The assessment results from the tested method are consistent with the nighttime visual inspection results, except one of the results was inconsistent with the retroreflectometer measurement results: Sign 2, as shown in Table 4.1. By retrieving the original four retroreflectometer measurement values for Sign 2, it was found that there is one value that is significantly smaller than the other three, i.e. 10, 7, 9, and 1. Although the four retroreflectometer measurements were taken at each quadrant of the sign, the number of measurements was still not sufficient to indicate the overall retroreflectivity condition of the whole sign due to water damage. The result can be easily impacted when the retroreflectivity of the sign is not uniform.

Table 4.1 Test Results for the 10 Type I Stop Signs on Field

ID	Tested Method Results (≥ 0.767)	Visual Inspection Results	Retroreflectometer Measurement Results (≥ 7)
1	0.763 / FAIL	FAIL	5.3 / FAIL
2	0.776 / PASS	PASS	6.8 / FAIL
3	0.745 / FAIL	FAIL	4.0 / FAIL
4	0.741 / FAIL	FAIL	2.3 / FAIL
5	0.712 / FAIL	FAIL	2.0 / FAIL
6	0.753 / FAIL	FAIL	5.1 / FAIL
7	0.755 / FAIL	FAIL	4.3 / FAIL
8	0.760 / FAIL	FAIL	5.3 / FAIL
9	0.682 / FAIL	FAIL	2.0 / FAIL
10	0.787 / PASS	PASS	19.3 / PASS

3.2 Benefit of LiDAR-based Assessment Method

As presented in previous sub-section, the LiDAR-based method is population based that can realistically reflect the overall retroreflectivity condition of a traffic sign, while the retroreflectometer measurement method is only a sample-based method using only four

measurement points. To further investigate the disparity between the assessment results from the tested method and the retroreflectometer measurement (i.e. sample-based method), an additional Type I stop sign acquired from GDOT was tested in the lab. Figure 4.2(a) shows the nighttime image of the tested stop sign. The sign was non-uniformly deteriorated due to water damage. Several blocks of the sign have much lower retroreflectivity than the rest of the sign.

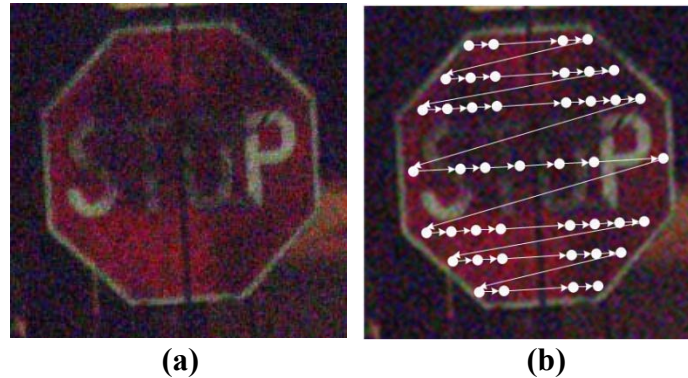


Figure 4.2 Images of the Type I Stop Sign in the Lab

In this in-lab test, more retroreflectometer measurements were acquired for a single sign in the well-controlled lab environment. To obtain a larger number of retroreflectivity measurements, 144 sampling points were measured using a retroreflectometer for the tested stop sign. The measuring pattern is illustrated in Figure 4.2(b), where the offset between the adjacent sampling points was approximately 2 in. Only the samples from the red color were tested. To simulate the four-point measurement using retroreflectometer in practice, one point from each quadrant was randomly selected, and the average of the four retroreflectivity values was used to represent the condition of the tested sign. Four runs of the random selections were conducted for the sign. In addition, the average of retroreflectivity values from all the measurement points was also calculated for each sign to compare with the four-point measurement results. Using the tested method, 322 retro-intensity values were acquired from the LiDAR system for the tested stop sign. We applied the same threshold of retro-intensity value as in the test on field, i.e. 0.767. Table 7.2 shows the results.

Table 4.2 Test Result for the Two Type I Stop Signs in the Lab

Tested Method Results Median (≥ 0.767)	Retroreflectometer Measurement Results				
	Mean (≥ 7)	Run 1	Run 2	Run 3	Run 4
0.744 / FAIL	4.5 / FAIL	10.0 / PASS	2.0 / FAIL	2.5 / FAIL	4.0 / FAIL

From Table 7.2, it is observed that the retroreflectometer measurement results using the average value of all the measurement points are consistent with the results using the tested method. However, the assessment result from Run 1 of the four-point measurement is different from other runs. The average is much higher than the rest of the runs. To further identify the different results, we investigated the distribution of the retroreflectivity from the retroreflectometer measurement.

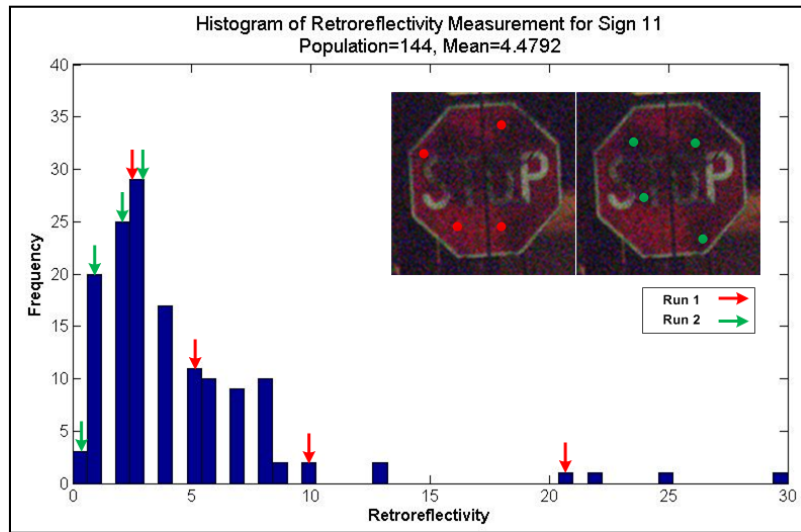


Figure 4.3 Distribution for the Retroreflectivity Measurement

As shown in Figure 4.3, the majority of the retroreflectivity values are below 7, and the average of all the measurement points is 4.5, which indicate a FAIL condition. However, using the four-point measurement, there was a chance to select the points with a large retroreflectivity value, so that the average of the four values overestimated the true condition of the sign. For example, as shown in Figure 4.3, Run 1 (i.e. the red arrows) includes measurement values of 10 and 21, which only appear once or twice among all the 144 measurements. The location of the measurement points (i.e. red dots) for Run 1, as shown in the image, also verifies that the measurements were incidentally conducted where the retroreflectivity condition is good. In contrast, if all the measurement points were used, the average can better reflect the true retroreflectivity condition for the whole traffic sign. Nevertheless, it is not feasible to manually measure more than 100 points for each traffic sign using a retroreflectometer. Therefore, the tested method can serve as a better alternative to reliably reflect the true retroreflectivity

condition for each sign, since the tested method assesses the traffic sign retroreflectivity condition using the whole population of the sign-associated LiDAR points.

At the current stage, the traffic signs are manually extracted and the LiDAR point cloud for each traffic sign color is manually clustered, so no assessment on the time saving was conducted. However, it is expected that the processing time will be dramatically reduced, comparing with the current practices using nighttime inspection or retroreflectometer measurement, when all of the automatic algorithms within the proposed methods are implemented,

4. Conclusions and Discussions

Traffic sign retroreflectivity condition is critical for nighttime driving safety. State DOTs have an urgent need for a cost-effective traffic sign retroreflectivity condition assessment method to meet the requirement from the MUTCD. This study tested a potentially cost-effective method for assessing the traffic sign retroreflectivity condition using mobile LiDAR and computer vision. Ten actual Type I stop signs collected in a community in Savannah, Georgia were tested to demonstrate the feasibility of the proposed method. The ground truths were established using both nighttime visual inspection and retroreflectometer measurement. The retroreflectivity condition assessment results using the proposed method are consistent with all of the nighttime visual inspection results; they match 90% of the retroreflectometer measurement results in differentiating good and bad sign retroreflectivity conditions. Using the developed mobile-LiDAR based method, coupled with the integrated GTSV, it is promising that the traffic sign retroreflectivity condition assessment can be conducted cost-effectively at highway speed.

The following are recommendations for future research:

- Experimental tests using more Type I stop signs is recommended to further validate the performance of the proposed method and the determined adequate retro-intensity threshold value.
- Experimental tests using other types of sheeting and other colors are recommended to further validate the performance of the proposed method.
- The processing time and cost-effectiveness is recommended for study to quantify the benefits for state DOTs using the proposed method.

References

- Benallal, M., and Meunier, J. (2003). "Real-Time Color Segmentation of Road Signs." *Proc., Canadian Conference on Electrical and Computer Engineering (CCECE)*, 1823-1826.
- FHWA (2009). "Manual on Uniform Traffic Control Devices for Streets and Highways 2009 Edition (MUTCD 2009)." Washington D.C.
- Findley, D. J., Cunningham, C. M., and Hummer, J. E. (2011). "Comparison of Mobile and Manual Data Collection for Roadway Components." *Transportation Research Part C: Emerging Technologies*, 19(3), 521-540.
- Gonzalez, A., Garrido, M. A., Llorca, D. F., Gavilan, M., Fernandez, J. P., Alcantarilla, P. F., Parra, I., Herranz, F., Bergasa, L. M., Sotelo, M. A., and Revenga de Toro, P. (2011). "Automatic Traffic Signs and Panels Inspection System Using Computer Vision." *IEEE Transactions on Intelligent Transportation Systems*, 12(2), 485-499.
- Hawkins, H., and Carlson, P. (2001). "Sign Retroreflectivity: Comparing Results of Nighttime Visual Inspections with Application of Minimum Retroreflectivity Values." *Transportation Research Record: Journal of the Transportation Research Board*, No. 1754, 11-20.
- Kang, D. S., Griswold, N. C., and Kehtarnavaz, N. (1994). "An Invariant Traffic Sign Recognition System Based on Sequential Color Processing and Geometrical Transformation." *Proc., IEEE Southwest Symposium on Image Analysis and Interpretation*, 88-93.
- Maldonado-Bascon, S., Lafuente-Arroyo, S., Gil-Jimenez, P., Gomez-Moreno, H., and Lopez-Ferreras, F. (2007). "Road-Sign Detection and Recognition Based on Support Vector Machines." *IEEE Transactions on Intelligent Transportation Systems*, 8(2), 264-278.
- Miura, J., Kanda, T., and Shirai, Y. (2000). "An Active Vision System for Real-Time Traffic Sign Recognition." *Proc., IEEE Intelligent Transportation Systems*, 52-57.
- Moreno, O., and Cook, R. T. (2010). "Presentation: Phoenix Sign Inventory and Replacement." Parsons Brinckerhoff Inc.

- Nguwi, Y.-Y., and Kouzani, A. (2008). "Detection and Classification of Road Signs in Natural Environments." *Neural Computing & Applications*, 17(3), 265-289.
- Remias, S. M., Hubbard, S. M. L., Eric A. Hulme, E. I., Hainen, A. M., Farnsworth, G. D., and Bullock, D. M. (2011). "Bias and Uncertainty in Traffic Sign Retroreflectivity." *Journal of Transportation of ITE*, 1(1), 19.
- Retterath, J. E., and Laumeyer, R. A. (2008). "System for Automated Determination of Retroreflectivity of Road Signs and Other Reflective Objects." Facet Technology Corporation, US Patent.
- Retterath, J. E., and Laumeyer, R. A. (2011). "System for Road Sign Sheeting Classification." Facet Technology Corp., US Patent.
- Shadeed, W. G., Abu-Al-Nadi, D. I., and Mismar, M. J. (2003). "Road Traffic Sign Detection in Color Images." *Proc., 10th IEEE International Conference on Electronics, Circuits and Systems (ICECS)*, 890-893 Vol.892.
- Siegmann, P., Lopez-Sastre, R. J., Gil-Jimenez, P., Lafuente-Arroyo, S., and Maldonado-Bascon, S. (2008). "Fundamentals in Luminance and Retroreflectivity Measurements of Vertical Traffic Signs Using a Color Digital Camera." *IEEE Transactions on Instrumentation and Measurement*, 57(3), 607-615.
- Smith, K., and Fletcher, A. (2001). "Evaluation of the FHWA's Sign Management and RetroReflectivity Tracking System (SMARTS) Van." *Report FHWA-AK-RD-01-01*, Alaska Department of Transportation, Juneau, AK, .
- Tsai, Y., and Ai, C. (2013). "A Sensing Methodology for an Intelligent Traffic Sign Inventory and Condition Assessment Using GPS/GIS, Computer Vision and Mobile LiDAR Technologies." *US Patent 61/806,237*, Georgia Institute of Technology, US.

Chapter 5 A Prototype GIS-Based Sign Management System

1. Introduction

As discussed in Chapter 1, GIS is an excellent platform for integrating different kinds of data sources into an effective transportation asset management system. Spatial data, such as GIS maps, sign locations, roadway image locations, and non-spatial data, such as sign attributes and video log images, can all be integrated on a GIS platform. Through a global coordinate system, e.g. WGS84, the roadway assets can be integrated with base GIS maps and linked through the use of a Linear Reference System (LRS). An integrated GIS-based management system would enable transportation agencies to efficiently manage their roadway assets. In GDOT, a 10-digit RCLINK is used as an LRS to integrate different kinds of data sources, which is composed of 1-digit route type code, a 3-digit county code, a 4-digit route number, and a 2-digit route suffix code. GDOT uses this LRS in its pavement surface condition evaluation, referencing each pavement segment and project by its starting and ending milepoints. Further integration of GIS-based information, such as a comprehensive traffic sign asset management system, will enhance overall roadway management and maintenance.

In this research project, traffic signs are used to demonstrate the application of a prototype GIS-based asset management system. A sign data management tool was developed, utilizing GIS technology, integrating both spatial data (global coordinate system and LRS) and non-spatial data (sign condition, position, type and video image) to benefit the sign management process.

The following section introduces the key functions and the data preparation for a new sign management application. After that, the major workflow was illustrated using a case study on I-285. Finally, the benefits and future potential of this application were discussed.

2. Development of a GIS-Based Sign Inventory Inspection Tool

2.1 Data Preparation and Software Environment Set Up

The application requires data to be collected and stored in a geo-database. And, the ESRI ArcMap 10.1 software environment also needs to be set up for the application to function properly.

- **Data Preparation**

The sign video log image data are collected using the GTSV equipped with multiple high definition cameras, and each image comes with accurate GPS location. The ones with signs are extracted through the process of sign data inventory as introduced in Chapter 2 along with their conditions, positions, and MUTCD codes. Then all the sign information are consolidated into a geo-database file. Each road has its own table in the database, and each row in the database represents a single sign. Except for a one-time loading data at the beginning of the work flow, no additional set up is needed within ArcMap 10.1.

- **ArcMap 10.1 Set Up**

After installation of the application, the user needs to make sure the tool appears on the ArcMap toolbar. To do this in ArcMap, click on “Customize” -> “Customize Mode...”, and the Customize window appears as shown. In categories, select “SignManageTool,” then drag the “Sign tool button” to the toolbar (see Figure 5.1).

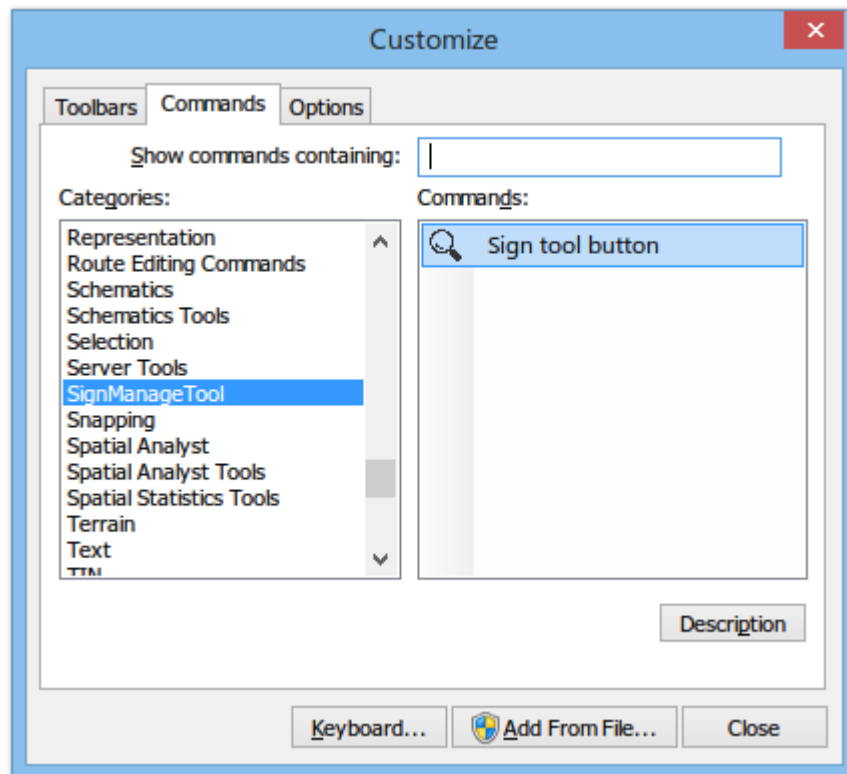


Figure 5.1 ArcMap Customize Window

2.2 Major Functions

The following introduce some major function in the developed GIS-based application.

- **Sign Query**

The tool provides several type of filters that the user can choose from or combine multiple of them (see Figure 5.2). The available filters are as follows:

- 1) Sign conditions: All / Good / Post failure / Obstructed / Surface failure
- 2) Sign positions: All / Normal / Cantilever / Sign-bridge / Other overhead
- 3) Sign types: MUTCD codes and GDOT sign types.

The queried results will show up in the result table with the condition description, position information, RCLINK and milepoint. The user can also double click each column header to sort the results according to the selected field, which would be handy for a large query. The total number of qualified signs will show up in the bottom text box.

- **Sign Statistical Summary**

The tool also provides overall statistics and reporting functionality (see Figure 5.3). For each road, the following statistics would be calculated to give the big picture:

- 1) Total number of signs
- 2) Total number of dirty signs
- 3) Total number of post failure signs
- 4) Total number of obstructed signs
- 5) Total number of cantilever signs
- 6) Total number of sign-bridge signs
- 7) Total number of overhead signs

And three types of charts can be made:

- 1) Distribution of top 10 frequent signs
- 2) Distribution of damage types
- 3) Distribution of overhead positions

Sign Management Tool [Maximize] [Close]

Sign Search | **Summary**

Sign Type

- ACC
- ADOPT
- BUCKLEUP
- CLEANGEOORGIA
- CLICKIT
- D2-1
- D2-2
- D2-3
- D2-4
- D3-1
- D3-2
- D9-13A
- D9-18E
- D10-1

Select All

Route List

I-285

Sign Condition

Dirty

Sign Position

Normal

Load Data (.gdb Folder)

Search

Query Results

	Id	Type	Condition	Position	RCLINK	Mile Point
▶	1898	D10-3	Dirty	Normal Position	1211040700	60.87
	3455	D10-3	Dirty	Normal Position	891040700	9.785
	1157	SLOWERTRAFFIC	Dirty	Normal Position	891040700	2.242
	1956	D10-3	Dirty	Normal Position	891040700	3.644
	353	W8-13	Dirty	Normal Position	891040700	13.343
	406	R7-201A	Dirty Surface-failure	Normal Position	891040700	14.824
	514	W4-1	Dirty	Normal Position	891040700	25.812
	509	R2-1	Dirty	Normal Position	1211040700	53.256
	500	D10-3	Dirty	Normal Position	1211040700	54.311
	490	D10-3	Dirty	Normal Position	631040700	0.585
	2822	I-3	Dirty	Normal Position	891040700	20.402
	2862	W4-1	Dirty Obstructed	Normal Position	891040700	18.712
*						

Total Number: 13

Figure 5.2 Sign Query Interface

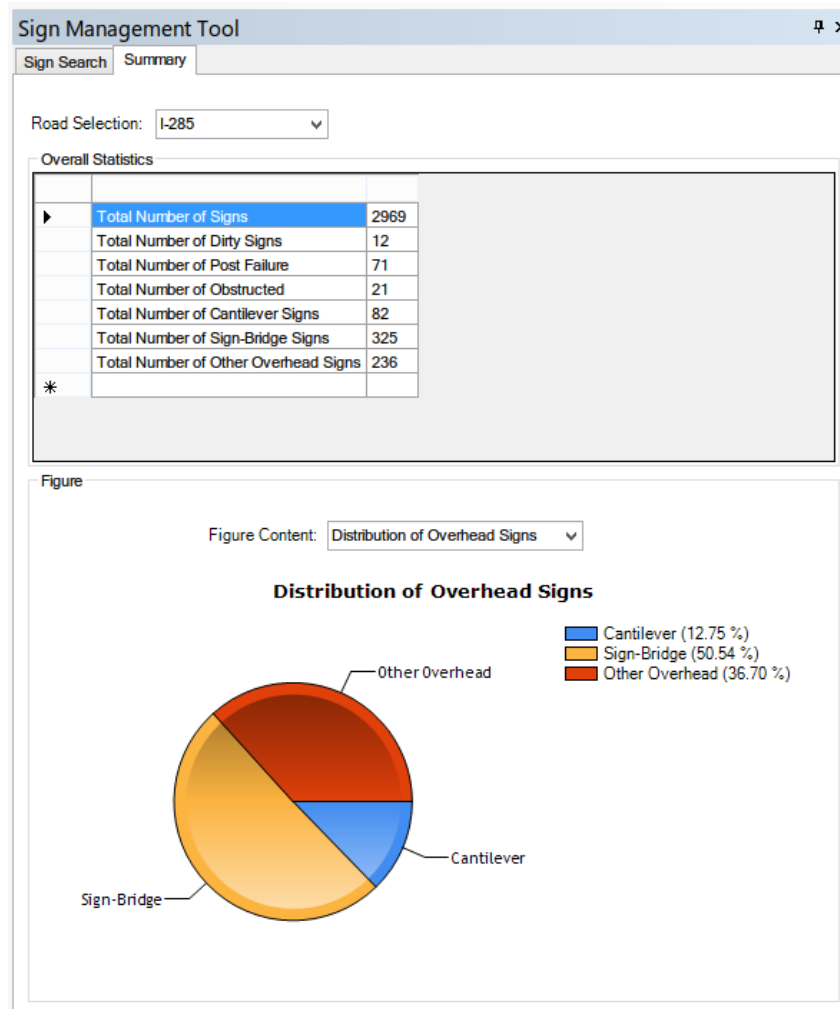


Figure 5.3 Sign Summary Interface

- **Individual Sign Inspection**

After the query function returns all the result sign items, the user could double click on a row to open the individual sign information window. All the data associated with the selected sign would show as a table in the window, along with the video log image. The map would re-center at the selected sign at the meantime, making it easier to locate the sign position (see Figure 5.4).

Sign Information
- □ ×

Sign Information	
Longitude	-84.34831
Latitude	33.91493
Id	2778
RCLINK	1211040700
Milepoint	26.655
MUTCD	E6-2
Damaged_Type	<Null>
Overhead_Type	Sign Bridge

RC1211040700 MP-26.7 MUTCD:E6-2 Sign Bridge



Sign Image

Figure 5.4 Individual Sign Information Window

3. A Case Study on I-285

For the example, sign data from 2,969 signs on I-285 are inventoried in the table, as shown in Figure 5.5:

OBJECTID *	Image_	Orig_ID	Longitude	Latitude	Id	RCLINK	Milepoint	MUTCD	Surface_Fail	Post_Failur	Obstructed
1	1016.jpg	1016	-84.42328	33.913708	232	1211040700	22.252	D2-3	0	0	
2	1019.jpg	1019	-84.4203	33.914854	234	1211040700	22.451	E1-1	0	0	
3	1030.jpg	1030	-84.406811	33.915787	241	1211040700	23.199	E1-1	0	0	
4	1064.jpg	1064	-84.379142	33.91213	259	1211040700	24.836	E1-1	0	0	
5	1086.jpg	1086	-84.365519	33.910153	267	1211040700	25.522	EB-2	0	0	
6	1110.jpg	1110	-84.34831	33.91493	277	1211040700	26.655	EB-2	0	0	
7	1178.jpg	1178	-84.243843	33.779434	187	891040700	14	D3-2	0	0	
8	1179.jpg	1179	-84.244114	33.779724	187	891040700	13.975	D3-2	0	0	
9	1200.jpg	1200	-84.249798	33.799239	178	891040700	12.59	E1-1	0	0	
10	1369.jpg	1369	-84.280021	33.90661	776	891040700	4.348	E1-1	0	0	
11	1396.jpg	1396	-84.288815	33.915129	638	891040700	3.573	EB-2	0	0	
12	1416.jpg	1416	-84.296616	33.919899	538	891040700	3.003	E1-1	0	0	
13	1537.jpg	1537	-84.231057	33.746248	197	891040700	16.563	E1-1	0	0	
14	1548.jpg	1548	-84.232022	33.752654	194	891040700	16.117	D3-1	0	0	
15	1569.jpg	1569	-84.23286	33.769481	189	891040700	14.954	MARTA	0	0	
16	1571.jpg	1571	-84.23365	33.771535	188	891040700	14.805	EB-2A	0	0	
17	1572.jpg	1572	-84.233634	33.771361	188	891040700	14.816	E1-1	0	0	
18	1638.jpg	1638	-84.273548	33.902442	864	891040700	4.821	EB-2	0	0	
19	1796.jpg	1796	-84.37131	33.646861	17	631040700	0.114	EB-2A	0	0	
20	1807.jpg	1807	-84.366865	33.652634	283	1211040700	54.35	D2-2	0	0	
21	191.jpg	191	-84.471905	33.881986	997	671040700	5.455	E1-1	0	0	
22	2055.jpg	2055	-84.357354	33.907137	120	1211040000	6.715	W4-3	0	0	
23	2056.jpg	2056	-84.357305	33.907305	121	1211040000	6.726	W20-1	0	0	
24	2057.jpg	2057	-84.357273	33.907227	120	1211040000	6.722	EB-2	0	0	
25	2058.jpg	2058	-84.357223	33.907216	121	1211040000	6.722	EB-2A	0	0	
26	2059.jpg	2059	-84.356909	33.908065	121	1211040000	6.782	WRK	0	0	
27	2060.jpg	2060	-84.356746	33.909804	124	1211040000	6.899	EB-2	0	0	
28	2061.jpg	2061	-84.356685	33.909795	124	1211040000	6.899	EB-2A	0	0	
29	2064.jpg	2064	-84.356549	33.910121	125	1211040000	6.92	E5-1A	0	0	
30	2065.jpg	2065	-84.35652	33.909775	124	1211040000	6.898	EB-2A	0	0	

Figure 5.5 I-285 Sign Data Table

Assume what is of interest is all D2 and D3 signs. Select the sign types in the checkbox list, and select “All” for condition and “All” for Position. A total of 147 signs are populated into the result table (see Figure 5.6). From the result, it can be seen that the sign with id 3,903 is classified as “Other overhead.” To further check what type of overhead is it, after double clicking on the row, an info window pops out. From the video log picture, it is clear that the sign is attached to a bridge, as shown in Figure 5.7.

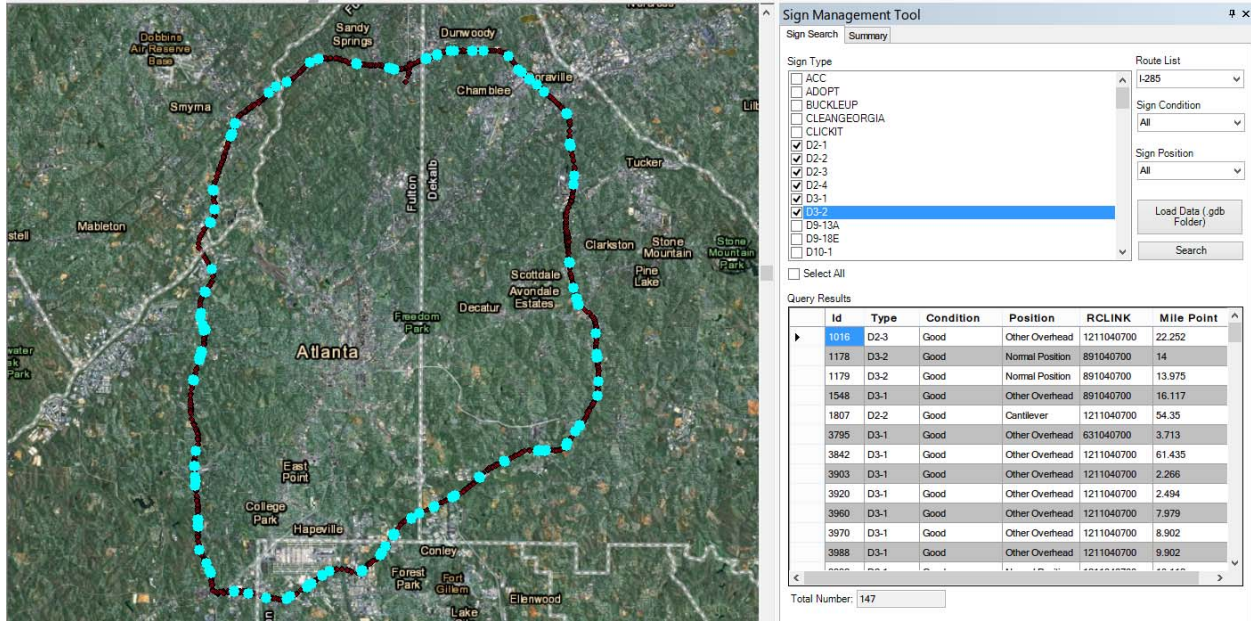


Figure 5.6 Query Results

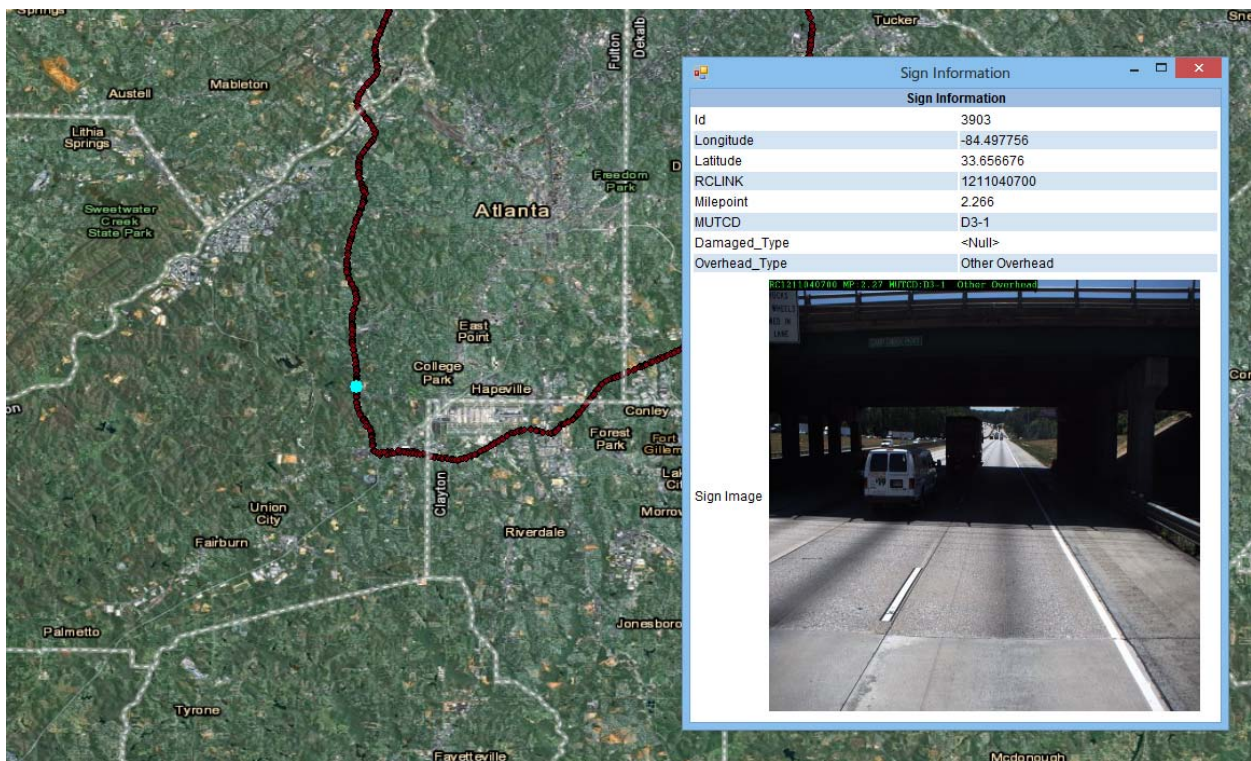


Figure 5.7 Individual Sign Info Window

4. Summary

The sign management tool we developed integrates spatial data with non-spatial data of signs and provides essential functionality for the common tasks in sign management. The underlying GIS data structure further enables effective data management and intuitional visualization. Such a tool would be very useful for the decision-making process in sign management and maintenance. In the future, more functions, such as condition history reporting for signs and condition prediction based on the analysis, are suggested for further implementation.

Chapter 6 Rut Measurement and Isolated Rut Detection

This chapter presents the research results for network-level rut depth measurement and isolated rut identification using the 3D laser technology.

1. Literature Review

Rutting is a well-known asphalt pavement distress that affects pavement structure integrity and driving safety (Kamplade, 1990; Start et al., 1998). It is the permanent longitudinal depression that forms due to traffic loadings in the wheel paths of a road. Rut depth is commonly used to indicate the level of rutting severity.

1.1 Rutting Survey Protocols

Currently, pavement rutting surveys are carried out by transportation agencies for network-level pavement maintenance and rehabilitation. However, different protocols have been adopted by different transportation agencies. The following briefly summarizes the protocols applied in federal and several state Departments of Transportation (DOTs):

- LTPP Rut Depth Measurement (FHWA, 2003)

For Specific Pavement Studies (SPS)-3 only, the maximum rut depth measured with a 1.2-m straightedge is recorded to the nearest millimeter at an interval of 15.25 m for each wheel path. For all other LTPP sections, transverse profiles are measured with a Dipstick® profiler at an interval of 15.25m.

- Georgia Department of Transportation (GDOT) Rut Depth Measurement (GDOT, 2007)

GDOT performs an annual survey of pavement surface condition, including rutting, on its 18,000 centerline miles of state highways. The entire pavement network is divided into segments for the survey purpose. Each segment is typically one mile long. During the survey, a rater first drives over the entire segment to examine the general pavement condition and then identifies the representative 100ft. sample section. A walk-through survey is then performed on each representative sample section.

As one of ten types of predefined pavement distresses, the average rut depth for the left and right wheel path within the 100 ft. sample section is recorded to the nearest 1/8 in. If the rut depth is less than 3/8 in., the rater will estimate it; if the rut depth is 3/8 in. or greater, actual measurement, made by using a straightedge, is required. Rut depth measurement will not be taken from locations where potholes, wide cracks, or loss of section exists. The deduct values for rutting are listed in Table 6.1. According to the treatment criteria in GDOT, a rut is usually treated with surface treatments, such slurry seal, if its depth is less than 1/4 in.; if its depth is between 1/4 in. and 3/8 in., micro seal or level and overlay is applied; if its depth is greater than 3/8 in., mill and inlay are used.

Table 6.1 Deduct Values for Rutting in GDOT Protocol

Depth (1/8 in.)	0	1	2	3	4	5	6	7	8
Deduct	0	2	5	12	16	20	24	24	24

- Oregon Department of Transportation (ODOT) Rut Depth Measurement (ODOT, 2010)

ODOT manually rates its highway network every 0.1 mi, except that the rut depths for both wheel tracks are automatically measured using a 5-point laser system mounted on a class 1 high speed profilometer. The laser system measures rut depth at 6 in. intervals and provides the average rut depth and standard deviation for each wheel track for every 0.1mi. This automated rut depth measurement is conducted separately from the manual crack survey. The rut depth measurements are then categorized into four severity levels: zero (rut depth between 0 and 1/4 in.), low (rut depth between 1/4 in. and 1/2 in.), moderate (rut depth between 1/2in. and 3/4 in.), and high (rut depth equal to or greater than 3/4 in.).

- Pennsylvania Department of Transportation (PennDOT) Rut Depth Measurement (PennDOT, 2010)

PennDOT adopts the ARAN to automatically collect pavement condition data. The evaluation section is typically 0.5 mi long. Within each evaluation section, the rut depth measurements are taken at an interval of no greater than 30ft. Then, each measurement is assigned to one of the three severity levels. They are low (rut depth between 1/4 in. and 1/2

in.), medium (rut depth between 1/2 in. and 1 in.), and high (rut depth equal to or greater than 1 in.). After that, the length for each severity level is recorded and reported for each wheelpath. Table 6.2 summarizes the definitions of rutting severity levels in ODOT and PennDOT.

Table 6.2 Rutting Severity Levels Defined by ODOT and PennDOT

Severity Level	Zero	Low	Medium	High
ODOT	< 1/4 in.	≥ 1/4 in. & < 1/2 in.	≥ 1/2 in. & < 3/4 in.	≥ 3/4 in.
PennDOT	< 1/4 in.	≥ 1/4 in. & < 1/2 in.	≥ 1/2 in. & < 1 in.	≥ 1 in.

1.2 Rutting Survey Methods

Some transportation agencies use manual methods, such as the straightedge method, to measure the rut depth. However, the manual method is time-consuming, labor-intensive, and dangerous, especially on highways with high traffic volume. Thus, automated methods, e.g., the point-based rut bar systems, have been developed to gradually replace the manual method.

A point-based rut bar system utilizes several laser sensors to profile the pavement surface along the driving direction and then uses the collected data to calculate the rut depth along the transversal direction. According to a survey conducted in 2003 (see Table 6.3) (McGhee, 2004), most transportation agencies (46 out of 56 responding transportation agencies from both U.S. and Canada) measured rut depth using point-based rut bar systems. The number of sensors used in current systems varies from 3 to 37. Thirty-two agencies were equally divided over the 3-point and 5-point rut bars; another 14 agencies adopted a rut bar with 7 to 37 sensors. Figure 6.1 shows the configuration of a 5-point rut bar system. Usually, a rut bar system is limited to being no longer than 3.0m for the sake of survey safety. To cover the full-lane width (typically 12ft., or, 3.6 m), the two sides of a rut bar system are mounted with point lasers that are tilted to some angle in the vertical direction as illustrated in Figure 6.1.

Besides point-based rut bar systems, INO in Canada developed a Laser Rut Measurement System (LRMS) to measure the rutting. This system consists of two laser profilers; each covers a 2m width and collects 640 laser points per transverse profile. This device has much higher resolution than the point-based rut bar systems. It can operate at a speed up to 100km/h. Its depth accuracy is +/-1mm. However, this system sheds the laser light onto the road surface at a small angle. The

transverse profile collected is different from the one collected when the laser is shooting straight downward. It may potentially overestimate the rut depth, especially for severe rutting. More recently, Li et al. (2010) from the University of Texas at Austin developed a real-time 3D scanning system for pavement distortion inspection. Similar to the LRMS, the system is built on the triangulation principle. However, the laser line is aimed straight downward. The system specifications are shown in Table 6.4. This system has a higher scan rate than LRMS.

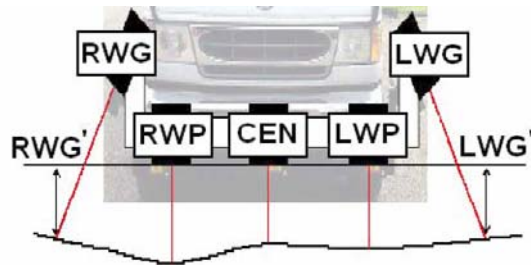


Figure 6.1 Configuration of a 5-point Rut Bar System (Wang, 2005)

Table 6.3 Survey in 2003 (McGhee, 2004)

Automated Survey System	3-point	5-point	7-point to 37-point
Number of Highway Agencies	16	16	14

1.3 Rutting Survey Report Methods

For network-level and project-level rutting surveys, the continuous rut depth measurements are not convenient for engineering use. Instead, different aggregation methods used on the continuous rut depth measurements are applied in different transportation agencies. As shown in Table 6.5, the sampling interval varies among different state transportation agencies. The smallest sampling interval is 6 in., applied in ODOT. The typical aggregation unit is 0.1 mi for state agencies in the U.S. Both the Austroads and the Quebec Ministry of Transportation (MTQ) aggregate the rut depths for every 100 m section. Statistical indicators, including average and maximum rut depth, are reported. PennDOT and Texas DOT (TxDOT) report the linear percentages of different severity levels (zero, low, medium, and high) of rutting within the aggregation unit.

Table 6.4 Specifications for Scanning Laser Systems

	LRMS	Real-time 3D Scanning System
Number of sensors	Two profilers	One projector and two cameras
Sample points	640 points/profile/profiler	1024 points/ profile/camera
Scan width	2m/profiler	1.83m/camera
Transverse resolution	3mm	1.79 mm
Depth resolution	--	2 mm
Depth accuracy	±1mm	--
Maximum scan rate	30 or 150 profiles/s	200 lines/s
Maximum vehicle speed	100km/h	112 km/h
Profile spacing	509 or 102 mm @ 55 km/h	76mm @ 55 km/h

Table 6.5 Aggregation Methods for Rutting Survey

Agency	Method	Aggregation Unit	Sampling Interval	Data Aggregation
AASHTO (2010)	--	10m (network) or 2m (project)	<3m (network) or <0.5m (project)	Average and maximum rut Depth
KDOT (mails with Rick Miller)	3-point	0.1 mi	1 ft.	Average rut Depth for each wheel path
ODOT (2010)	5-point	0.1 mi	6 in.	Average rut depth and standard deviation for each wheel path
PennDOT (2010)	Profiler	0.5 mi	<30 ft.	Length for each severity level for each wheel path
TxDOT	Self-developed device	0.1 mi	1 ft.	Average, maximum, etc.
Australia (Austroads, 2007)	Multi-laser	100 m	≤250 mm	Average of maximum rut depth for each wheel path; standard deviation; wheel path rut bins
MTQ (Grondin et al., 2002)	LRMS	100 m	1 m	Maximum of average rut depth for each wheel path

The aggregated rut depth values are further aggregated into reporting units. Table 6.6 lists the reporting methods used by several transportation agencies. In Kansas DOT (KDOT), the average

and maximum rut depth values within 1 mi are reported. It is also observed that typically used statistics are average, maximum, and standard deviation. The average value is generally used to indicate the overall rutting characteristics. However, maximum and standard deviation values can be used to identify the uniformity of rut distribution.

Although current data aggregation and reporting methods fulfill the need of network-level reporting, they do not develop the information needed to support project-level decision-making, such as determining the location of an isolated rut for qualifying a localized treatment. The severe ruts could be averaged out with the current methods.

Table 6.6 Rutting Reporting Methods

Agency	Report Unit	Aggregation Unit	Data Aggregation
KDOT (mails with Rick Miller)	1 mi	0.1 mi	Average and maximum rut depth for each wheel path
TxDOT	1 mi	0.1 mi	Average, maximum, standard deviation, percentiles of rut depth for each wheel path

1.4 Rut Depth Measurement Errors

For transportation agencies, the network level rutting survey, in which the accuracy of rut depth measurement is most concerned, is an indispensable means to assess the a pavement’s structure and safety performance. Although rut bar systems have been broadly used, researchers and practitioners generally have concerns about the accuracy of rut bar methods, since they only sample a limited number of points along the transverse direction. A number of studies have shown that the point-based rut bar systems could underestimate the rut depth in comparison with the manual method (the straightedge method). Ksaibati (1996) evaluated the rut depths measured by 3-sensor and 5-sensor profilometers and found significant differences between the non-contact and direct-contact measurements. Jameson et al. (1989) and Cenek et al. (1994) both compared the rut depth obtained by the laser Road Surface Tester (RST) to those by the straightedge method and found major differences. Hallett and Robieson (1996) compared the ARRB multi-laser profilometer with the detailed manual survey profiles and found differences, as well.

More recently, the reliability of the derived rut information from point-based rut bar systems has been further challenged. The analysis results echoed the conclusions made by previous researchers. For example, HTC (2001) compared the rut depths from a 30-sensor ROMDAS profilometer with those field measurements using a 1.5m straightedge method and identified a 3mm bias. Mallela and Wang (2006) assessed the actual sampling bias of the profilometers operated in New Zealand (13 to 30 sensors) and concluded that rut depth measurement is underestimated by 2-4mm. Simpson (2001a) determined that the correlation of rut depths measured by a 5-point rut bar and a rod and level elevation survey is approximately 0.4. Also, Simpson (2001b) studied the accuracy and bias of the RoadRecon and Dipstick methods. The coefficient of variance of the rut depth measured by the RoadRecon unit is 11% and 4% for Dipstick.

In summary, 3-point and 5-point rut bar systems have shown poor accuracy. The measurement error is primarily due to the limited sampling points taken by a point-based rut bar system, which cannot capture the real shape of a rut and usually underestimates the rut depth.

2. Research Need and Objective

The following needs are identified for rutting data analyses in transportation agencies' practice:

- There are systematic errors in rut depth measurement using point-based rut bar systems. Since those systems consist of only a limited number of laser points, they usually underestimate the rut depth. It is expected that the 3D laser technology can better measure rut depth because it captures more than 4,000 laser points on each transverse profile. However, there is a need to validate the rut depth measurement accuracy before it can be utilized by transportation agencies. In addition, the measurement error of a point-based rut bar system can be further evaluated by downsampling the captured transverse profiles.
- There is a need to develop a methodology to characterize rutting information using the 3D laser technology in support of the existing pavement management system (e.g. the Georgia Pavement Management System, GPAM). Algorithms or methods are needed to aggregate the detailed rut depth data to support existing pavement data collection practice and support both network-level and project-level treatment decision-making.

- There is a need to develop a method to automatically identify isolated ruts using the 3D laser technology for determining low-cost and localized treatments.

To fulfill the above needs, the following study has been performed and is presented in this chapter:

- To verify the rut depth measurement accuracy using the 3D laser through both the controlled laboratory tests and field tests. For these tests, the 3D continuous transverse profiles were collected and processed using commercial software and a developed rut depth calculation application. The calculated rut depths were then compared to the manually-measured ground truth, and, the rut depth measurement accuracy was quantified.
- To assess the error of point-based rut bar systems using the essentially continuous 3D data as the ground truth. Different severity levels of rutting were analyzed to have a better understanding of the measurement error from point-based systems.
- To evaluate the feasibility of using the 3D laser in network-level rutting survey. To evaluate the feasibility of using the 3D system for detecting isolated ruts.

3. Assessment of Rut Depth Measurement Accuracy using 3D laser

Both laboratory test and field tests have been conducted to evaluate the accuracy of rut depth measurement using the integrated 3D laser system. The laboratory test was performed under a controlled environment to exclude the effect of external factors, such as vehicle vibration. After the laboratory test, field tests at highway speed were also conducted to estimate the measurement error coming from both the instrument and the vehicle vibration. The following introduces the test design and then the test results.

3.1 Experimental Test Design

3.1.1 Laboratory Test

The rutting severity levels are commonly indicated by the ranges of rut depth. In ODOT (ODOT, 2010), rut depth for the low severity rutting is 1/4 in. (6.35mm) to 1/2 in. (12.7mm). Rut depth for the medium severity rutting is 1/2 in. to 3/4 in. (19.1mm). Rut depth for high severity rutting is greater than 3/4 in. To simulate the rutting of different severity levels in the laboratory, a curved wood board and a curved metal bar were used as shown in Figure 6.2 (a) and (b). On the

wood board, 10 profiles were marked with blue tapes. The rut depths of those profiles varied from several millimeters to several centimeters. The curved metal bar was used to simulate a rut of the high severity level. Thus, there were a total of 11 profiles fabricated in the laboratory for testing rut depth measurement.

The ground truth was established by using the straightedge method, and, the data collection procedure followed the standard specified in ASTM E1703 (2010). As shown in Figure 6.2(a), a steel angle bar was used as the straightedge. The rut depth was measured using a vernier caliper with a precision of 0.02mm. During the measurement, the vernier caliper is set to be perpendicular to the steel bar. To identify the maximal distance between the steel bar and the wood board surface, sufficient measurements were made along the steel bar. To reduce the measurement error, the measurement for each profile was repeated 3 times. The average rut depth of these three runs was considered as the ground truth.

To test the 3D laser on the simulated rutting, it was set up in the laboratory as shown in Figure 6.3(b). Because the length of the simulated pavement profiles is less than a half-lane, only one laser profiling unit was installed. The infrared camera was used to observe the invisible laser line as shown in Figure 6.3(b). The measurement procedure for each profile was repeated twice. During each measurement procedure, the wood board or the metal bar was placed under the laser profiling unit and its position was fine-tuned until the laser line was right on the marked profile. After that, 2,000 repetitive data profiles were collected using the 3D laser. For testing the 11 ruts, a total of 44,000 ($=11 \times 2 \times 2,000$) profiles were obtained. Figure 6.4 shows two typical profiles. The rut depth for each profile was calculated using a simulated 1.8m straightedge method, which will be presented in Section 3.2.1.

3.1.2 Field Test

Two roadway sections were selected in Pooler, Georgia. As shown in Figure 6.5(a), a 725m roadway section was chosen on Benton Boulevard. A 45m roadway section was selected on Towne Center Ct., shown in Figure 6.5(b). There were six test transverse profiles marked with paint, which can be seen from the laser intensity data, on the Benton Blvd. test section. On the Towne Center Ct. test section, 4 test profiles were marked. These test profiles are non-uniformly distributed over the test section.

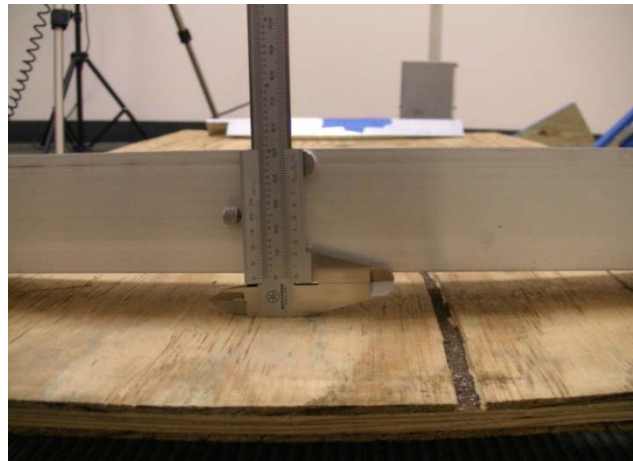


(a)



(b)

Figure 6.2 Simulated Rutting in Laboratory: (a) Wood Board; (b) Metal Bar



(a)



(b)



Figure 6.3 Laboratory Test Setup: (a) Straightedge Rutting Measurement; (b) 3D laser System Setup in the Laboratory

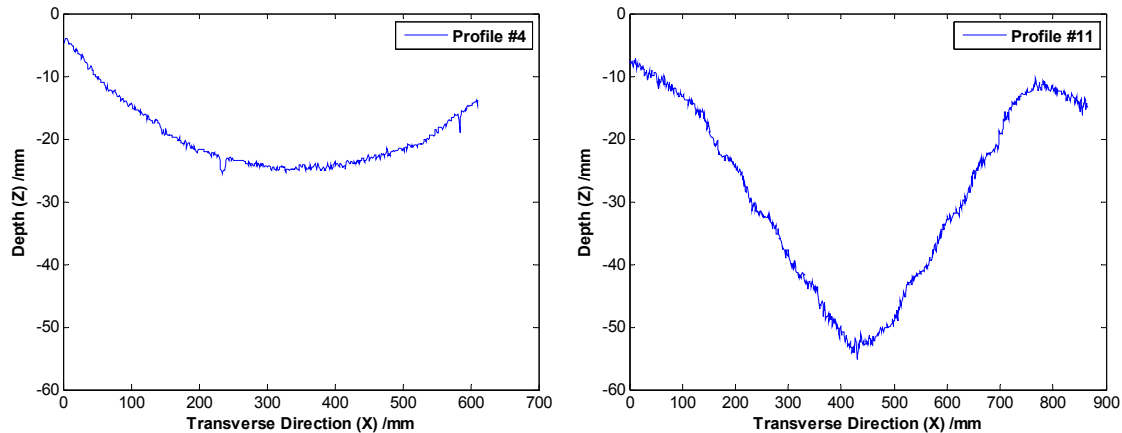


Figure 6.4 Typical Transverse Profiles Measured in the Laboratory

To establish the rut depth ground truth of those 10 test profiles, a 1.8m straightedge method was performed as shown in Figure 6.5(c). The same measurement procedure was followed as that in the laboratory test, which was repeated 3 times for each transverse profile. The average rut depth for each transverse profile was considered as the ground truth.

The 3D laser was mounted on the GTSV as shown in Figure 6.5(d). The sensing vehicle drove on both test sections for three runs and collected 3D continuous transverse profile data. The mean vehicle speeds for the first test section were 37.8mph (mi/hr), 34.4mph, and 32.8mph, respectively; they were 13.5mph, 17.8mph, and 15.3mph for the second test section. Because the road sections were chosen on local roads to facilitate the manual measurement, no highway speed, higher than 60mph, was tested in this study. Figure 6.6 shows two typical transverse profiles obtained by the 3D laser. The measured profiles were then used to calculate the corresponding rut depth.

Another field test was conducted on a GDOT-monitored project on SR 275 near Savannah, Georgia, to assess the rut depth measurement accuracy. Figure 6.7 (a) shows the roadway environment on SR 275. This 2-lane road is 5.53 mi long. The overall PACES rating is 80 in Fiscal Year 2011 (FY2011). Table 6.7 summarizes the PACES ratings for each segment of SR 275. As shown in Table 6.7, only the segment between milepost 0 and milepost 1 has relatively severe rutting, which might have been caused by localized material problems, structural problems, and/or the heavy truck traffic on this section.



(a)



(b)

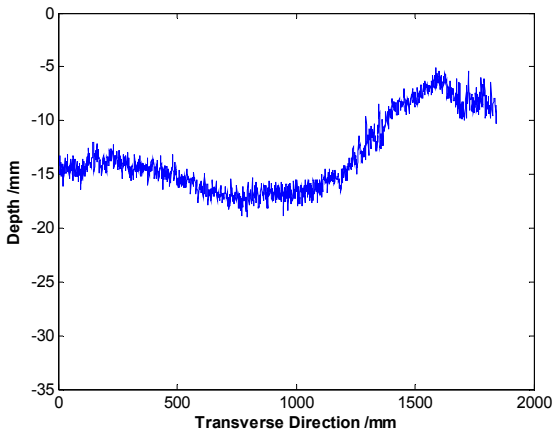


(c)

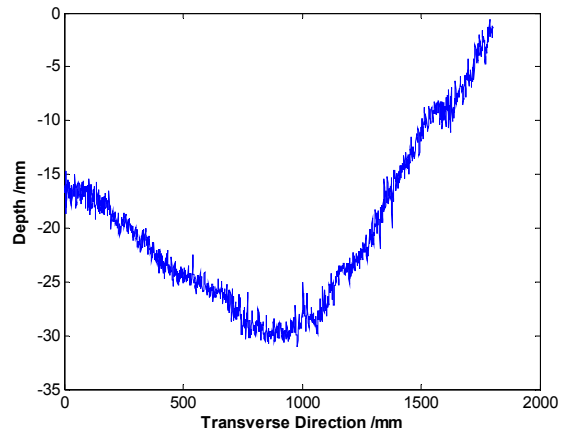


(d)

Figure 6.5 Field Test: (a) Test Site on Benton Blvd.; (b) Test Site on Towne Center Ct.; (c) 1.8m Straightedge Method; (d) Survey using 3D laser System



(a)



(b)

Figure 6.6 Typical Transverse Profiles: (a) Low Severity Level Rutting; (b) Medium Severity Level Rutting

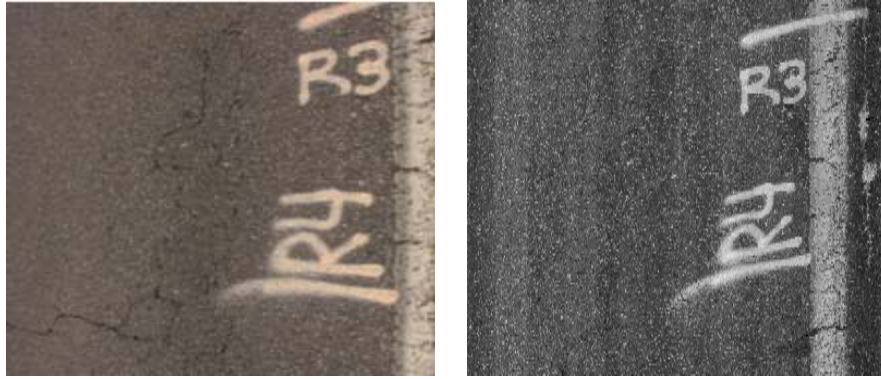


(a) (b)
Figure 6.7 Field Test on SR 275: (a) Test Site; (b) Rutting

Table 6.7 COPACES Records in FY 2011 for SR 275 (Overall Project Rating is 80)

Route No	Segment From-To (mi)	Sample Location (0.1 mi)	Segment Rating	Lane Direct	Rut_Out_WP (1/8 in.)	Rut_In_WP (1/8 in.)
0275	0-1	7	58	NEG.	4	3
0275	1-2	5	80	NEG.	1	1
0275	2-3	4	90	POS.	1	0
0275	3-4	4	74	NEG.	1	0
0275	4-5	6	73	POS.	--	1
0275	5-5.53	4	70	POS.	0	0

A manual survey was carried out by a GDOT liaison engineer. The surveyor first drove over the test site and located a 100ft. sample section that represents the representative pavement condition in each segment (1 mi). Then, a straightedge method was used to measure the rut depth on a randomly selected location within the 100ft. section, which is rounded to the nearest 1/8 in. The manual survey result is presented in Table 3.8. During the manual survey, the locations of the manual survey were also labeled. The labels are visible to the sensing system and can be used as a location reference when the manual survey results and the automated survey results are compared. An example of the labels marked in the field and visualized in the 3D data is given in Figure 6.8.



(a) (b)
Figure 6.8 Labels in (a) Field and in b) 3D Laser Data

Table 6.8 Manual Survey Results on SR275

Segment From-To (mi)	Lane Direct	Rut_In_WP (1/8 in.)	Rut_Out_WP (1/8 in.)
0-1	NEG.	3	3
1-2	NEG.	2	4
2-3	POS.	0	1
3-4	POS.	1	1
4-5	NEG.	1	1

Table 6.9 Manual Measurement Results on Locations Chosen on SR275

Marked Spot	Manual Rut Depth (1/8 in.)	
	In	Out
R1	3	1
R2	3	3
R3	2	4
R4	--	4

3.2 Data Analyses

The simulated straightedge method, which is suggested in the ASTM 1703 Standard (2010) and commonly adopted by researchers (Laurent et al., 1997; Li et al., 2009, 2010), is used for computing the rut depth based on the 3D continuous transverse profiles in this study. Two rut depth calculation algorithms based on the principles of simulated straightedge method have been

applied. One comes with the 3D laser, and the other one has been developed by the Georgia Tech research team. Both algorithms are presented and compared in this section.

3.2.1 DCT-based Rut Depth Calculation Algorithm

From Figure 6.4 and Figure 6.6, it can be seen that the collected profiles are not very smooth. Due to the relatively smooth surface of the simulated ruts in the laboratory, the data variation in Figure 6.4 could come from the noise of the sensing device. The data variation in Figure 6.6 is more severe because it could result from both the device noise and the pavement surface texture. Due to the low frequency of vehicle vibration in comparison with the 3D laser data capturing frequency, the contribution of vehicle vibration to profile data variation can be omitted.

To calculate the rut depth using the collected profiles, the data variation needs to be smoothed out first. For this purpose, a Discrete Cosine Transform (DCT) was employed and the DCT coefficients were selected to preserve 99.9% of the total signal energy. The smoothed profile was shown in Figure 6.9 (a). Due to the significant end effect of a DCT, as seen in Figure 6.9 (a), which will impact the accuracy of rut depth measurement, a stepwise linear interpolation was used at the two ends of the rut profile. The improved and smoothed profile can be seen in Figure 6.9 (b).

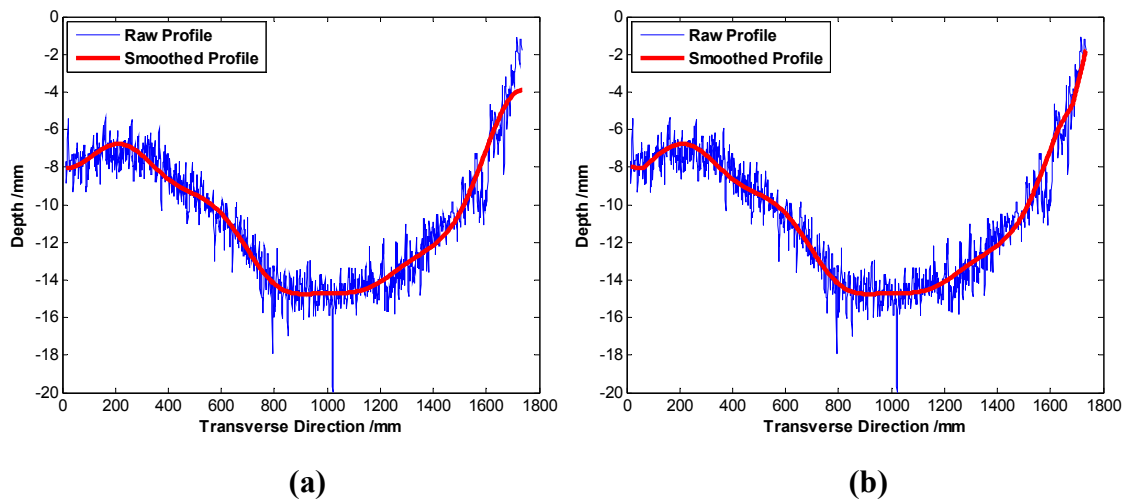


Figure 6.9 Smoothed Transverse Profiles: (a) DCT Only; (b) DCT plus Stepwise Linear Interpolation

After the rut profiles were smoothed, a simulated 1.8m straightedge method was used to calculate the rut depth. The following are the procedures:

- Identify the highest points at both ends of a rut profile that are the standing points of the straightedge;
- Connect the two standing points;
- The maximum distance between the simulated straightedge and the profile is the rut depth, as shown in Figure 6.10.

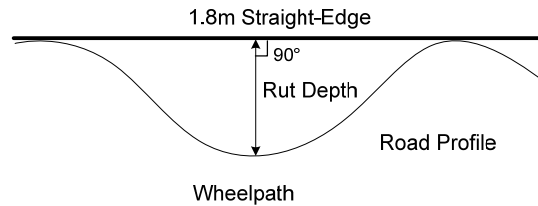


Figure 6.10 1.8m Straightedge Method

3.2.2 3D laser Based Rut Depth Calculation

Another rut depth calculation algorithm is implemented in the tested 3D laser (2010). The algorithm is shown in Figure 6.11. The black curve is a pavement surface transverse profile. The black straight line simulates the straightedge, and the green block simulates the gauge that is used to read the rut depth measurement in the field. The gauge width is adjustable. In this study, 5mm is used. The rut depth computation algorithm is implemented as follows. First, a median filter is used to smooth the raw transverse profile and the smoothed profile is then fit with straight lines. Second, the rut support point pairs, (x_L, z_L) and (x_R, z_R) , are identified and justified. Third, the rutting characteristics (including the rut depth, rut width, rut shape, and rut cross-section area) are measured for both wheelpaths.

- Rut depth is given by: $Depth = \sqrt{(x_B - x_T)^2 + (z_B - z_T)^2}$.
- Rut width is given by: $Width = \sqrt{(x_R - x_L)^2 + (z_R - z_L)^2}$.
- Rut cross-section area is the cross-section area of the detected rut under the straightedge.

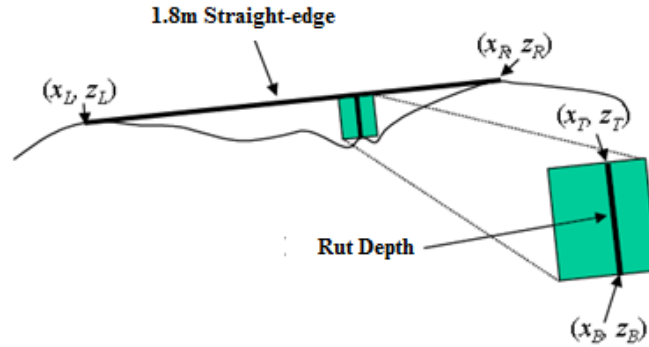


Figure 6.11 Rut Depth Calculation (LCMS, 2010)

3.2.3 Comparison of Rut Depth Calculation Algorithms

The 3D laser provided and DCT-based algorithms are used to process the ten transverse profiles collected from county roads in the field test so that their performance can be compared. The comparison results are tabulated in Table 6.10. According to the comparison results, the absolute difference between the 3D laser provided and DCT-based algorithm is less than 1mm. The average difference is -0.1mm for both run1 and run2. This indicates that both algorithms can provide essentially similar rut depth measurements.

3.3 Test Results

3.3.1 Laboratory Test Results

Table 6.11 shows the rut depth measurement results on the 11 simulated rutting profiles. The average manual measurements vary from 7.9 mm to 43.4 mm covering low to high severity levels. They are considered as the ground truth. Two runs of 3D laser measurements were performed. The difference between these two runs ranges from 0.1mm to 1.3mm, which is comparable to the manual measurement error. The difference between the 3D-line-laser-measured results and the ground truth varies from -0.4 mm to 0.7 mm, which is less than 1mm.

As mentioned above, 2,000 profiles were collected by the 3D laser for each simulated profile in each test run when the locations of the laser profiling unit and the test profile were fixed. These 2,000 profiles can be used to assess the repeatability and the noise level of the 3D laser.

Table 6.12 summarizes the analysis results with regard to the standard deviation of rut depth among 2,000 profiles for each simulated profile in each run. It shows that the standard deviation varies from 0.1mm to 0.3mm, which is satisfactory because the claimed depth measurement accuracy of the 3D laser is 0.5mm. Regarding the measured rut depth between the two runs, the difference is bigger than the variation of 2,000 profiles in each run, since the fine-tune process cannot guarantee that in each run 3D laser takes exactly the marked profile. Figure 6.12 shows the correlation of rut depth measurements between the two runs. In accordance with the standard ASTM C670-03, the average coefficient of variance is about 4.4%, which indicates good measurement repeatability.

3.3.2 Field Test Results

The field test results on the local roads are summarized in Table 6.13. Ten manually marked profiles on the test roadway sections were examined. The manually measured rut depths, which are considered as the ground truth, vary from 6.4mm to 21.1mm. They correspond to the low to high severity level of rutting. Compared to the average of 3D-line-laser-measured results, the difference varies from -1.0mm to 2.3mm, which is apparently higher than the one in the well-controlled laboratory test. Several factors could contribute to this. First, for a profile-based comparison, it is very critical to make sure that the location of each extracted profile from 3D laser data is exactly the same as the manually marked and measured one. In the harsh field testing environment, it is very difficult to make this happen. Second, unlike the well-controlled laboratory test, vehicle wandering is inevitable in a field test, which will impact the rut depth measurement. Besides, from the comparison result, a trend shows that the ground truth is greater than the 3D-line-laser-measured result except the one for profile #3. There is an approximately 1.5mm measurement bias for 3D laser when compared with the ground truth.

From the testing results listed in Table 6.13, the absolute rut depth measurement difference is around 1.6mm, which is the average of “absolute difference to ground truth.” Also, this difference is independent of the rut depth, which indicates that the relative error decreases with the increase of rut depth. For example, though the relative error for profile #10 is around 19%, the one for profile #9, which has the largest rut depth, is just 4%. This will assure the accuracy of rut depth measurement for more severe rutting, which is the most important concern in transportation agencies’ practices.

Table 6.10 Comparison of Two Algorithms

Profile ID	Rut Depth in Run 1 (mm)			Rut Depth in Run 2 (mm)		
	DCT	3D laser	Diff2	DCT	3D laser	Diff2
1	12.1	12.2	-0.1	14.0	14.7	-0.7
2	13.4	13.8	-0.4	14.6	14.7	-0.1
3	10.7	10.4	0.3	10.8	10.0	0.8
4	12.9	12.2	0.7	12.1	12.5	-0.4
5	6.0	6.5	-0.5	6.7	6.9	-0.2
6	7.3	7.5	-0.2	7.2	7.1	0.1
7	5.9	6.1	-0.2	6.0	7.0	-1.0
8	7.2	7.6	-0.4	7.1	7.6	-0.5
9	19.8	20.0	-0.2	20.8	20.0	0.8
10	5.7	5.6	0.1	4.7	4.8	-0.1
Average	--	--	-0.1	--	--	-0.1

Table 6.11 Laboratory Testing Results

Profile #	Severity Level	Rut Depth (mm)					
		Ground Truth	3D laser Measured				Difference to Ground Truth
			1 st Run	2 nd Run	Difference between Runs	Average	
1	Low	8.0	8.3	7.1	1.2	7.7	0.3
2	Low	7.9	8.2	8.0	0.2	8.1	-0.2
3	Low	7.9	6.8	7.6	0.8	7.2	0.7
4	Medium	13.2	13.2	13.1	0.1	13.2	0.0
5	Low	12.3	12.3	11.5	0.8	11.9	0.4
6	Medium	14.2	13.8	14.0	0.2	13.9	0.3
7	Medium	15.5	15.0	14.8	0.2	14.9	0.6
8	Medium	16.2	15.4	16.7	1.3	16.1	0.1
9	Medium	17.5	17.6	17.1	0.5	17.4	0.1
10	Medium	10.0	11.0	9.7	1.3	10.4	-0.4
11	High	43.4	43.2	--	--	43.2	0.2

-- Invalid testing data

Table 6.12 Standard Deviation of Rut Depth among 2,000 Profiles

Profile #		1	2	3	4	5	6	7	8	9	10	11
Std. Dev. (mm)	1 st Run	0.1	0.2	0.2	0.1	0.1	0.2	0.1	0.2	0.1	0.2	0.3
	2 nd Run	0.2	0.1	0.1	0.2	0.2	0.2	0.2	0.2	0.1	0.2	--

-- Invalid testing data

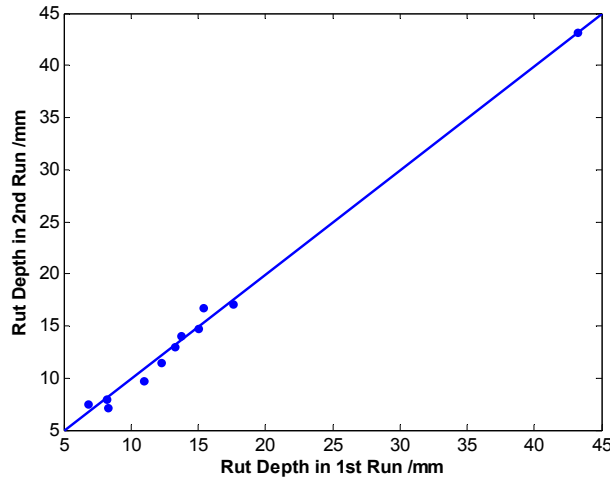


Figure 6.12 Correlation of Rut Depth in Two Runs in Laboratory

In addition, for the network level rutting survey, profile-based rutting data is normally aggregated for every fixed interval, say 10 ft., which will further reduce the random measurement error. In this feasibility study, only profile-based testing was performed. To further validate the accuracy and applicability of using 3D laser for the rutting survey, larger-scale network-level testing is needed.

Figure 6.13 shows the correlation of 3D-line-laser -measured rut depth among 3 runs. The average coefficient of variance is about 5.3%. Although more tests are needed, current results still show good measurement repeatability.

On SR 275, the automated measurements are compared to the manual measurements for four marked spots during the field survey. They are denoted as R1, R2, R3, and R4 in Table 6.14. The rut depths, manually measured in the field using a straightedge method, are used as the ground truth. Then, three runs of automated survey were carried out (at around 47 mph). The rut depth for each spot was calculated using the automated method presented above. The difference of rut

depths measured during different runs is less than 0.8 (of 1/8 in.) for most marked spots. The average coefficient of variance is about 4.6%. This indicates that 3D laser has a high repeatability in measuring the rut depth, which concurs with the previous finding. The average rut depth of the three runs is then compared with the ground truth. The absolute difference between the manual and the automated rut depth measurements is less than 1/8 in. (which is around 3.2mm).

Table 6.13 Field Testing Results

Profile #	Severity Level	Rut Depth (mm)					
		Ground Truth	3D laser Measured				Difference to Ground Truth
			1 st run	2 nd run	3 rd run	Average	
1	Medium	14.5	12.1	14.0	13.5	13.2	1.3
2	Medium	15.8	13.4	14.6	12.8	13.6	2.2
3	Low	9.6	10.7	10.8	10.3	10.6	-1.0
4	Medium	14.2	12.9	12.1	11.3	12.1	2.1
5	Low	8.5	6.0	6.7	7.6	6.8	1.7
6	Low	9.5	7.3	7.2	7.1	7.2	2.3
7	Low	7.8	5.9	6.0	6.6	6.2	1.6
8	Low	9.4	7.2	7.1	7.2	7.2	2.2
9	High	21.1	19.8	20.8	20.3	20.3	0.8
10	Low	6.4	5.7	4.7	5.3	5.2	1.2

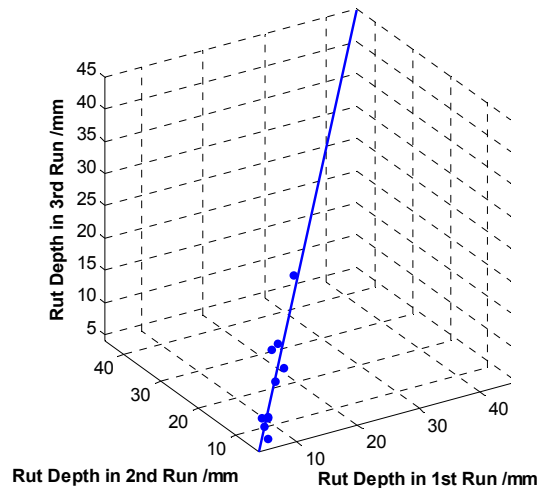


Figure 6.13 Correlation of Rut Depth in Three Runs in Field

Table 6.14 Manual vs. Automated Survey Results on SR 275

Rut Depth (1/8 in.)	Manual		Auto									
Profile #	In	Out	In					Out				
			Run1	Run2	Run3	Avg	Diff	Run1	Run2	Run3	Avg	Diff
R1	3	1	3.4	3.5	3.5	3.5	-0.5	1.5	1.5	1.4	1.5	-0.5
R2	3	3	2.8	2.4	2.7	2.6	0.4	2.1	1.9	2.0	2.0	1.0
R3	2	4	2.8	2.8	--	2.8	-0.8	3.1	3.4	3.4	3.3	0.7
R4	--	4	2.7	2.7	--	2.7	--	2.9	3.1	3.7	3.2	0.8

3.4 Summary

The assessment on the rut depth measurement accuracy using the emerging 3D laser technology is presented above. Eleven laboratory-simulated profiles and 14 field-selected profiles (from two county routes and one GDOT-maintained route) were tested in a well-controlled laboratory environment and in a practical field environment. The ground truth of rut depth for each testing profile was established by using the manual straightedge method. Based on the profiles acquired by 3D laser, the rut depths were calculated by using the simulated straightedge method.

Laboratory test results show that the difference between 3D-line-laser-measured rut depth and the ground truth ranges from -0.4 mm to 0.7 mm, which indicates the high accuracy of the rut depth obtained by 3D laser. In the laboratory, the location of 3D laser, and the simulated profiles are fixed, and 2,000 profiles were obtained in each test run for each simulated profile. The test run was repeated twice. The rut depth standard deviation of every 2,000 profiles ranges from 0.1mm to 0.3mm. This result shows the high repeatability of the laser profiling system. In addition, 4.4% of the average coefficient of variance for two testing runs also shows good repeatability of the rut depth measurement.

Due to the uncontrolled environment, such as vehicle wandering, the results from both field tests are inferior to the ones in the laboratory. However, the -1.0mm to 2.3mm (the measurement error in the second field test is less than 1/8 in., which is equal to the manual measurement accuracy) absolute difference to the ground truth shows sufficient accuracy for the 3D-line-laser-measured rut depth. This measurement error satisfies the rut depth measurement accuracy requirement, which is +/-3mm, from multiple transportation agencies (Alberta DOT, 2002; McGhee, 2004). More importantly, the testing results indicate the difference has no dependence on the rut depth,

which means the relative measurement error would decrease for more severe rutting. In the field test, 3 runs of testing were performed for each marked profile. The average coefficient of variance is about 5.3% and 4.6% for the two field tests, respectively, which indicate a good repeatability of rut depth measurement under the practical field testing environment.

4. Assessment of Rut Depth Measurement Error of Point-based Rut Bar Systems

Using the emerging 3D laser imaging system, the rut depth measurement error of point-based rut bar systems is characterized and quantified in this section. The objective is to use the continuous transverse profile as the ground truth to evaluate the potential rut measurement error for rut bar systems with different sensor configurations. Experimental tests were performed using the continuous transverse profile data that was collected in field.

4.1 Research Need

As reported by a NCHRP report (McGhee, 2004), among 40 state transportation agencies (46 for total transportation agencies in north America), 16 are using 3-point rut bar systems, 13 are using 5-point systems, and 11 are using a rut bar system with sensors varying from 7 to 37. Among these 11 agencies, 5 use a 37-point system. Transportation agencies have concerns about the accuracy of the derived rut information because the rut bar systems cannot measure a continuous pavement transverse profile. The limited number of sensors may not locate exactly on the top of pavement ruts because of the wandering of survey vehicle, varying of lane width, and asymmetry of the transverse profiles. Hence, the rut depth may be underestimated. Besides, the rut bar system cannot cover the full lane because its length is limited to approximately 3m. Previous studies pointed out that 3-point and 5-point rut bar systems are unreliable with regard to rut depth measurement. The inaccurate rut depth measurement generally underestimates the rut depth. This can result in uneconomic treatment planning and safety issues because the deep rut was not repaired in time. Accordingly, there is a need to quantify the measurement errors so that transportation agencies can use the derived information confidently to support their pavement management decision-making.

Several studies have been done to quantify the reliability of the derived rut information using rut bar systems (Mallela and Wang, 2006; Simpson, 2001a; Simpson, 2001b; White et al., 2002).

However, it still remains a challenge to establish the ground truth. Simpson (2001a; 2001b) used transverse profiles, each of which consists of 25 points, collected by the rod and level method as the benchmark. Thirty transverse profiles were collected and analyzed. Data Collection Ltd (DCL) used Transverse Profile Beam (TPB) with a transverse resolution of 3mm to establish reference profiles as ground truth (Mallela and Wang, 2006). Only 64 reference profiles were collected and analyzed. Both static devices to establish the ground truth is time-consuming and labor-consuming and only limited numbers of reference profiles can be obtained.

With the advancement of the emerging line laser technology, the 3D laser can quickly collect the continuous transverse profiles with more than 4,000 points on each of them that cover a single lane. It provides an excellent basis to evaluate the rut depth measurement accuracy of different rut bar systems because the 3D-line-laser -based rut depth measurement accuracy has been validated above.

4.2 Experimental Test Design

The experimental tests were performed to assess the point-based rut-depth measurement error with respect to sensor configuration and rut configuration. For sensor configuration, the rut bar systems with 3 sensors, 5 sensors, and 7 to 39 equally spaced laser sensors were tested. From these tests, the relationship between the rut-depth measurement error and the number of sensors was evaluated. Thus, a recommendation can be made for the minimal number of sensors required to assure that the measurement error falls within the range of an acceptable level. In addition, rut configuration, such as the rut shape, rut depth, and rut location, also affects the measurement error. Therefore, according to the available data, the impact of different rut configurations on rut-depth measurement error was also analyzed. The following subsections will briefly introduce the testing data and the measurement methods of point-based rut bar systems. Then, test results are presented followed by the analyses and discussion of the measurement error.

4.2.1 Test Data

The test data was collected using the 3D laser on an actual 10m asphalt pavement section. There are total 4,000 half-lane transverse profiles, which can be combined to 2,000 full-lane transverse profiles. To avoid the efforts of transforming the original profile data, only half-lane transverse profiles collected by the left 3D laser profiler were used; it was assumed that the right profile is

symmetric to the left one. Thus, the rut depth determined by the left half-lane profile can be used to represent the one of the full lane.

Figure 6.14 shows two typical pavement profiles with U shape (green line) and V shape (red line) that are located at milepoint 3.4m and 6.4m on the tested pavement sections. Intuitively, a U-shape rut has less impact on the rut-depth measurement error brought by a point-based rut bar system because the valley is flat and wide, and the possibility of a sensor located on it is high. In contrast, a V-shape rut has a narrow valley, and it is hard for a sensor to be just located on the top of the valley. So, a V-shape rut has a bigger impact on the measurement error when a point-based rut bar system is used.

4.2.2 Rut Depth Computation

The 3D continuous transverse profiles were processed using the algorithms presented in Section 3.2.2, and the acquired rut depths were used as the ground truth. The rut depth computations for rut bar systems with 3 sensors, 5 sensors, and the others with 7 to 39 equally spaced laser sensors are briefly introduced as follows. In general, the point-based rut depth computation is equivalent to sampling the ground truth profile data with different points and configurations and then calculating the rut depth using the corresponding methods.

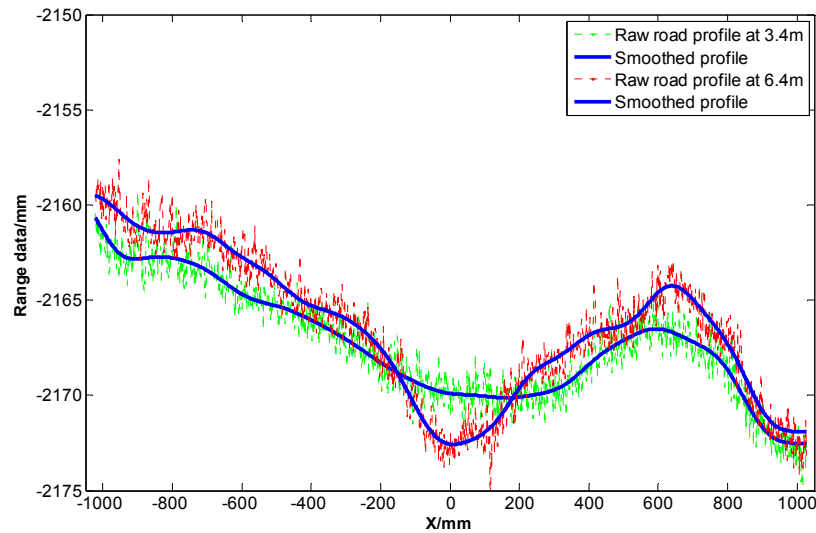


Figure 6.14 Road Transverse Profiles at Milepoint 3.4m and 6.4m

Figure 6.15 illustrates the configuration of a 3-point rut bar system. The 3 sensors are equally spaced at 860mm (Hossain et al., 2002) with the left and right sensors on top of left and right wheel path. Each sensor measures the distance from the reference plane to the corresponding pavement surface, which are D_1 , D_2 , and D_3 for the middle, left, and right sensor. Assuming that the pavement surface in the middle has no rutting, the rut depth in the left and right wheel path can be easily calculated using the distance differences, as shown in Equations (3.1) and (3.2).

$$RD_L = D_2 - D_1 \quad (3.1)$$

$$RD_R = D_3 - D_1 \quad (3.2)$$

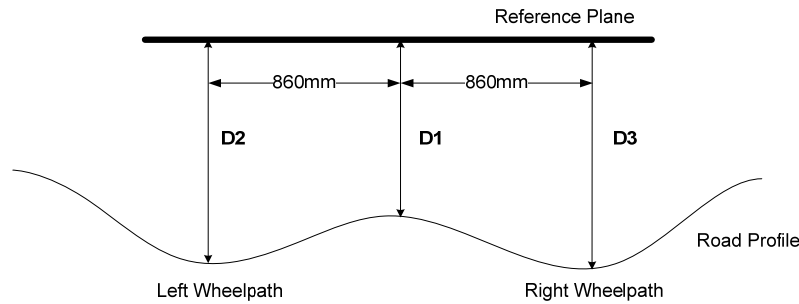


Figure 6.15 Sketch of 3-point Rut Bar Configuration

For the 5-point rut bar system, AASHTO PP 38-00 requires that the minimum spacing between the two outermost sensors be 2,300mm. In our preliminary test, the 5-point rut bar system configuration used by Hossain et al. (2002) was adopted, which is shown in Figure 6.16. The spacing between the sensor on the wheel path and the one on the road centerline is 875mm. The outer sensor is located 546mm from the outside of the wheel path sensor (Hossain et al., 2002). The left and right rut depth can be computed using the left and right 3 sensor-captured distances from the reference plane to the pavement surface, which are shown in Equations (3.3) and (3.4).

$$R_L = D_4 - (D_3 + D_5) / 2 \quad (3.3)$$

$$R_R = D_2 - (D_1 + D_3) / 2 \quad (3.4)$$

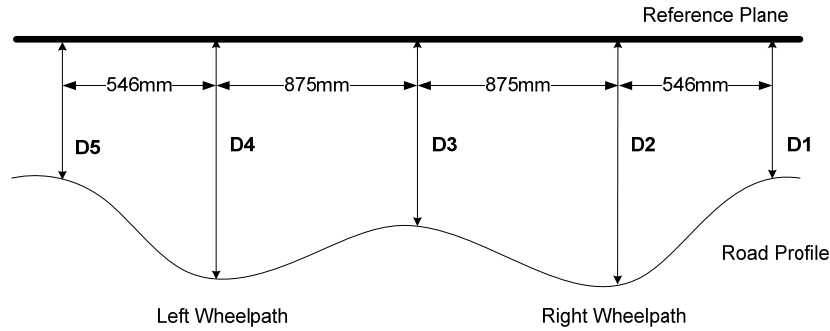


Figure 6.16 Sketch of 5-point Rut Bar Configuration

For other equally-spaced rut bar systems, a 1.8m straightedge method is used to calculate the rut depth. Figure 6.17 illustrates how to calculate straightedge rut depth for a 7-point rut bar system. The red curve represents the road profile obtained by a 7-point rut bar system. Then the straightedge rut depth is calculated as follows: 1) the highest points for both ends of the profile are identified; 2) a straight line is drawn to connect them, which mimics the straightedge; and 3) the maximum perpendicular distance between a laser point and the straightedge is the straightedge rut depth.

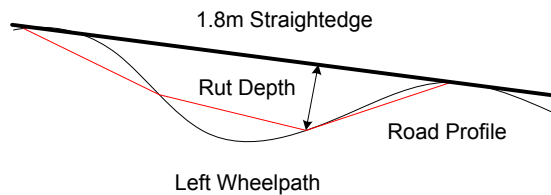


Figure 6.17 Straightedge Method

4.3 Test Results

Figure 6.18 shows the calculated rut depths along the 10m road section that includes 2,000 transverse profiles. Though vehicle wandering is another major source of measurement error of point-based rut bar systems, only the variation of rut locations is considered in the preliminary test; i.e., it is assumed that vehicle travels along the centerline of a lane. Therefore, the measurement error is assumed to be caused only by the rut location variations. In Figure 6.18, the blue line indicates the ground truth pavement rutting profile along the driving direction, which was calculated using the 3D continuous transverse profiles. Rutting that is deeper than 1/4 in. occupies around 62% of the testing road section (pavements with rut depth above the dashed

blue line). Other parts of the road section show no significant rutting. The deepest rutting occurs at about 6.5m with a rut depth of 11mm. In comparison, other rutting profiles along the driving direction are also drawn in Figure 6.18 with different colors. To make the figure readable, only rutting profiles for 3-point, 5-point, 9-point and 39-point rut bar systems are presented. Apparently, with the increasing number of sensors, the rutting profiles get closer and closer to the ground truth.

To further assess the measurement error caused by using point-based rut bar systems with different numbers of sensors, the histograms of measurement errors along the driving direction were analyzed. They are presented in Figure 6.19. The corresponding means of errors for all point-based rut bar systems are reduced with the increasing number of sensors. For 3-point and 5-point rut bar systems, the average measurement errors are about 63% and 44%. When the sensor number increases to 9, the mean error becomes 24%, although the variation of error does not change much. If the number of sensors increases to 39, the average measurement error is lowered to about 8%. The variation of error also decreases.

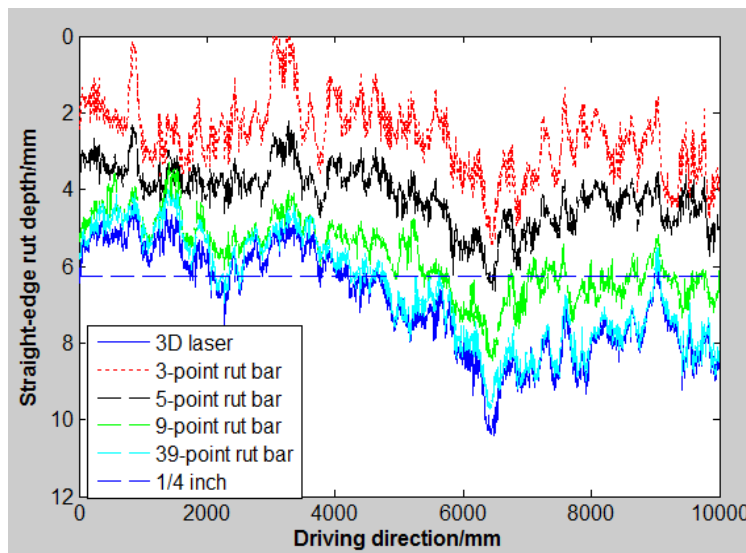


Figure 6.18 Rut Depth Profile along Driving Direction

Figure 6.20 shows the mean and variance of the measurement error vs. number of sensors curve. Though there is some variation from 7 to 21 sensors due to the short testing road section, the overall trend is clear that the measurement error decreases with the increasing number of sensors.

If the number of sensors is larger than 25, both the mean and variance of the error drops constantly. The mean error has a value below 10%.

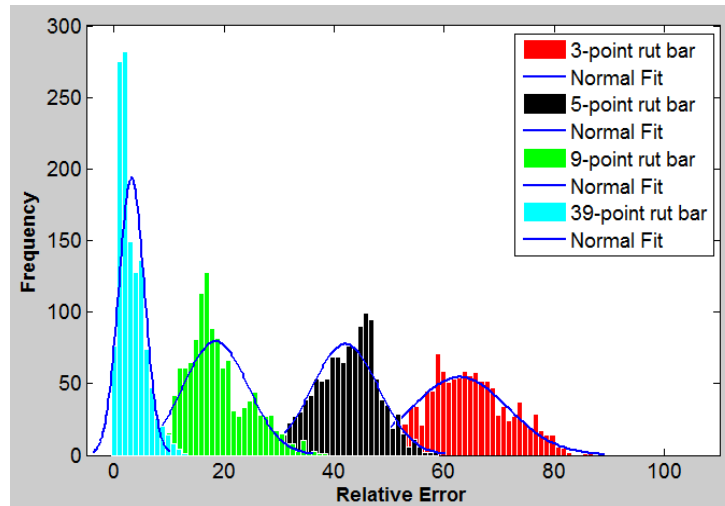


Figure 6.19 Measurement Errors of Point-based Rut Bar Systems along Driving Direction

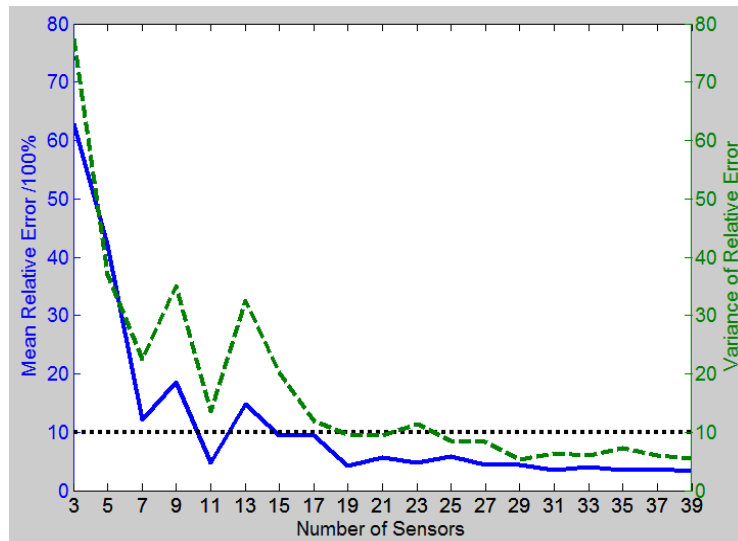


Figure 6.20 Relationships between Mean and Variance of Relative Measurement Errors and Number of Sensors

Without the consideration of vehicle wandering, the variation of measurement error along the driving direction is caused by several factors, such as the number of sensors, sensor locations, rut shape, rut depth, and rut location. As mentioned above, a U-shaped rut could lead to less measurement error for a point-based rut bar system. However, a V-shaped rut might have a

larger error. As an example, the following investigates two transverse profiles that are shown in Figure 6.14. At the milepost 3.4m where the rut shape is U-shaped, the measured rut depths for 3-point, 5-point, 9-point and 39-point rut bar systems are 1.6mm, 3.3mm, 4.7mm, and 5.0mm, respectively. In comparison with the ground truth of 5.5mm, the measurement errors are 78%, 40%, 15%, and 9%. However, at the milepost 6.4m where the rut shape is V-shaped, the measured rut depths are 4.6mm, 6.0mm, 7.9mm, and 9.4mm. Compared with the ground truth of 10.1mm, the measurement errors are 54%, 40%, 22%, and 7%. For 3-point rut bar systems, the errors for the U-shape are larger than the ones for the V-shape because the rut location and sensor location have larger impacts on the error than the rut shape. For the 9-point system, the error for the U-shape is apparently smaller. However, when the number of sensors increases to 39, the error for the V-shape becomes smaller again because, in this case, the rut depth has larger impact (the rut depth for the U-shaped rut is about half of the one for the V-shaped rut). Therefore, the impact factors for rut-depth measurement error are complicated.

4.4 Summary

3D continuous transverse pavement profiles, which were obtained by using the 3D laser, was first used in this study to assess the rut-depth measurement errors caused by using different point-based rut bar systems that had a different number of sensors. The ultimate goal is to establish the optimal rut bar configuration, including number of sensors and sensor spacing, that can fulfill the transportation agencies' needs in their pavement condition surveys and that can accurately support their pavement management and maintenance. The large volume of continuous transverse profiles provides a more accurate and comprehensive ground truth compared with the limited number of ground truth profiles that were used in previous studies. In the preliminary study, the commonly used 3-point and 5-point rut bar systems, as well as the equally-spaced rut bar systems with number of sensors from 7 to 39, were assessed. The testing data uses half-lane, continuous transverse profiles on a 10m road section. Without the consideration of vehicle wandering, variation of rut locations and rut shapes are the major source of measurement error for each type of point-base rut bar system. Testing results show that 3-point and 5-point rut bar systems significantly underestimate the rut depth. The average measurement errors for 3-point and 5-point rut bar systems are about 63% and 44%. With the increasing number of sensors, the measurement error is gradually lowered. With an equally-

spaced 39-point rut bar system, the measurement error is about 8%. If the number of sensors is larger than 25, the measurement error drops constantly to below 10%. From investigation of two transverse profiles with U-shaped and V-shaped ruts, it is concluded that the impact factors for measurement error are complicated. Even without considering vehicle wandering, the number of sensor, sensor locations, rut shape, rut depth, and rut locations could affect the rut depth measurement error.

5. Network-level Rutting Survey

To support the network-level rutting survey, the continuously calculated rut depths from the 3D-line-laser -acquired transverse profiles need to be aggregated and partitioned. A proper statistical factor is needed to represent the condition of each pavement segment. In this section, the procedures to conduct network-level rutting survey using the 3D laser were developed and validated through several case studies, including interstate highways, state routes, and county roads. Then, the determination of an adequate sampling interval and the performance (i.e. processing speed and data storage need) of the method was assessed. The advantages and limitations of the tested method are also discussed.

5.1 Procedures of Network-level Rutting Survey

The major steps for network-level rutting survey using 3D laser include the following:

- Step 1: Collect 3D transverse profile data for each project from the start milepost (MP) to the end MP.
- Step 2: Process the raw data to obtain rut depth measurements for individual transverse profiles. The rutting processing module from Pavemetrics is employed in this step, which is based on the ASTM E1703 standard. The rut information output (including rut depth, rut width, cross-section, and gage width) is stored in an XML file.
- Step 3: Read the XML file to obtain rut depth measurements, which are then aligned to form the longitudinal rut depth profiles for both inside and outside wheelpaths along the driving direction.
- Step 4: Remove outliers, caused by wide transverse cracks and raised pavement markings based on the assumption that the rut depth would not suddenly change.

- Step 5: Divide each project into segments (typically 1mi long) by dividing the data proportionally.
- Step 6: Analyze each segment and report the representative rut depths for both wheelpaths and both driving directions using different statistical factors, such as 60th percentile, average, standard deviation, skewness, and linear percentages of different severity levels of rutting.

5.1.1 Read XML Files

The rutting processing module in 3D laser provides the rutting information (including rut depth, rut width, cross-section, and gauge width) by analyzing individual transverse profiles. It simulates the manual straightedge method and returns the rutting information for both the left and right wheelpaths. The rutting information output is stored in an XML file. Figure 6.21 shows one example of the XML file. The rutting information can be found in the "RutInformation" element, which can include any number of "Rut-Measurement" elements. The number of "RutMeasurement" depends on the length of the road section being processed and the rut calculation interval. Each "RutMeasurement" element contains 6 sub-elements. "Position" gives the position of the measurement with respect to the beginning of the survey point. "Laneside" indicates if the measurement is related to the left or right wheelpath of the lane. "Depth," "Width," "CrossSection," and "Type" are the rut measurement parameters. Ruts are categorized into three types, multiple ruts, simple rut short radius, and simple rut large radius.

A MATLAB program has been developed to extract rutting information from multiple XML files. The extracted rutting information is then aligned to form longitudinal rut depth profiles. One example profile is given in Figure 6.22.

```

- <RutInformation>
  <DataFormat>1.0</DataFormat>
- <Unit>
  <Position>meter</Position>
  <Depth>millimeter</Depth>
  <Width>millimeter</Width>
</Unit>
- <RutMeasurement>
  <Position>105.000</Position>
  <LaneSide>Left</LaneSide>
  <Depth>4.23</Depth>
  <Width>1889.82</Width>
  <CrossSection>5377.44</CrossSection>
  <Type>0</Type>
</RutMeasurement>
- <RutMeasurement>
  <Position>105.000</Position>
  <LaneSide>Right</LaneSide>
  <Depth>2.79</Depth>
  <Width>1256.44</Width>
  <CrossSection>2333.28</CrossSection>
  <Type>0</Type>
</RutMeasurement>

```

Figure 6.21 Example of XML Output File

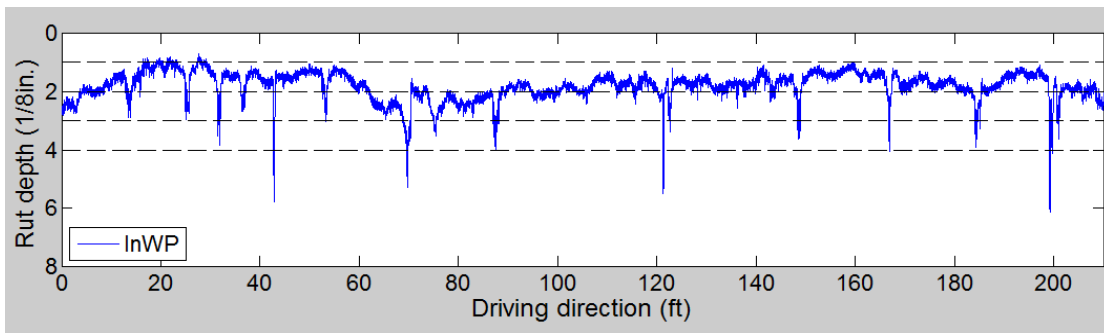
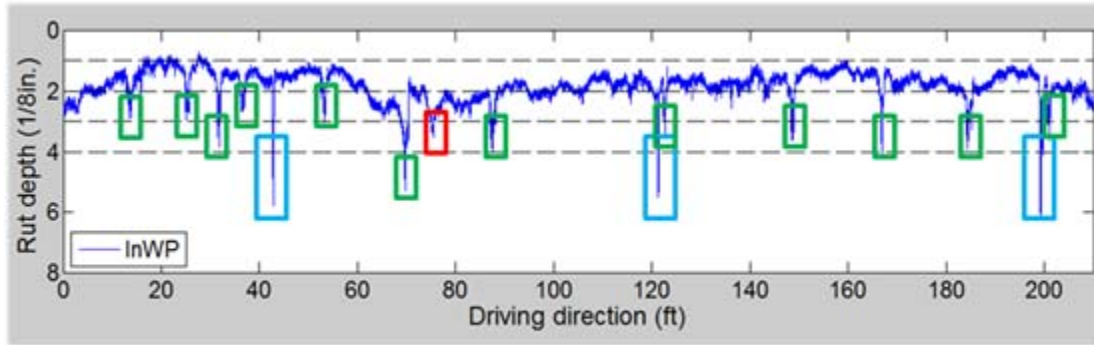


Figure 6.22 Example of Longitudinal Rut Depth Profiles from XML Files

5.1.2 Remove Outliers

Outliers were observed in the longitudinal rut depth profiles. A method is desired to remove outliers and, thereby, clean the data. Figure 6.23 shows the major causal factors of outliers. It is found that outliers are mainly caused by transverse cracking and raised pavement markings. By further examining other data, five types of outliers have been identified according to their causes. They are outliers caused by transverse cracks (especially for cracks wider than 5mm), potholes and patches, raised pavement markings, rail tracks, and other objects (e.g. tree branches on the road). Figure 6.24 shows close-ups of each type of outliers. As seen from the figures, the outliers caused by raised pavement markings are distinct. They are usually 100-125mm wide and 2.5-4 (of 1/8 in.) deep. The outliers caused by a single transverse crack are around 0.8-3 of 1/8 in. deep. The depths of the outliers vary significantly. The outliers caused by rail tracks and potholes usually have very sharp edges. To assure that isolated ruts are preserved when removing outliers, the characteristics of isolated ruts were also explored. One example of a false “outlier event” is

highlighted with a red rectangular. It is observed that the slopes of isolated rut are relative smooth, usually smaller than 0.3 in/ft. The characteristics of those five types of outliers and isolated ruts are summarized in Table 6.15.



■ A single transverse crack
 ■ A raised pavement marker
 ■ An isolated rut

Figure 6.23 Causes of Outliers

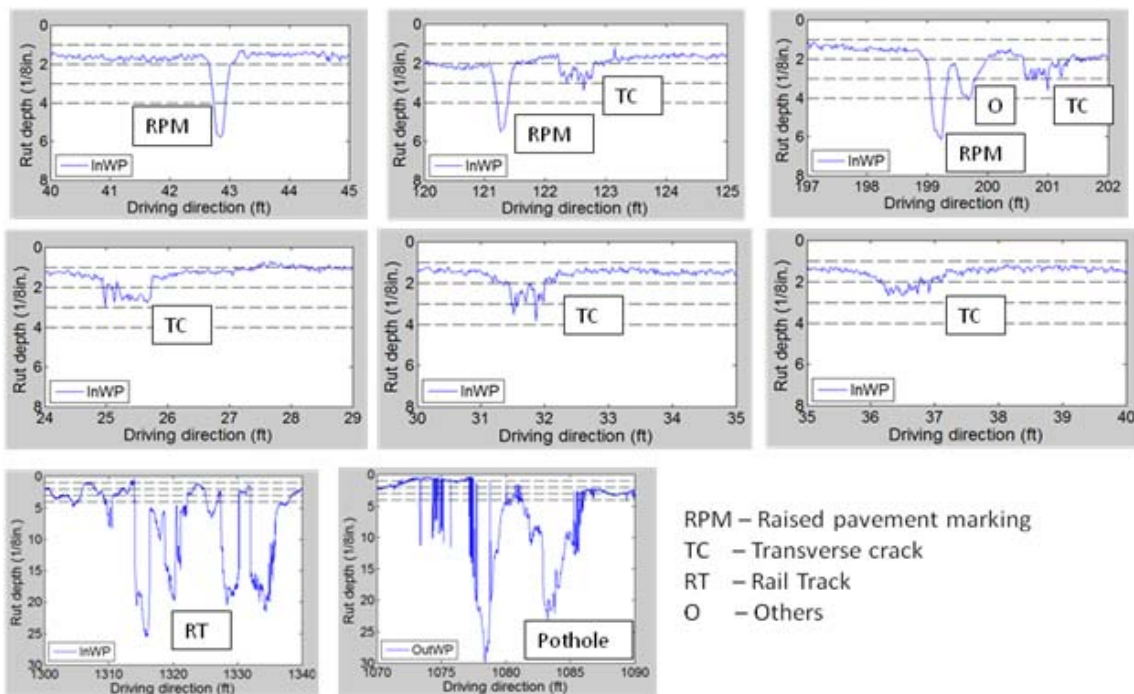


Figure 6.24 Examples of Outliers

Table 6.15 Characteristics of Outliers and Isolated ruts

Outlier Event	Length Range (mm)	Depth Range (1/8in.)	Slope (in/ft.)
Transverse Cracks	25-500	0.8-3	0.3-6.0
Raised Pavement Marker	100-125	2.5-4	1.8-2.7
Rail Tracks	--	20	≥ 2.5
A Pothole	60	1.6	2.0
Another Object	400	5	0.9
Isolated Ruts	≥ 800	≥ 2	≤ 0.3

According to Table 6.15, all outliers have a much sharper slope than the isolated rut. Thus, a thresholding method is used to filter the longitudinal rut depth profile. The key of this filtering is to calculate the slope. Typically, the whole profile is segmented, and then linear regression is applied to calculate the slope for each profile segment. By doing so, the calculated slope value highly depends on the size of the segment. However, it is challenging to determine a proper segment size that is suitable for different types of outliers because the lengths of outliers vary significantly. Therefore, a relatively large segment needs to be used, and a flexible modeling technique is needed to handle various outliers. Through the literature review, it is found that the multivariate adaptive regression splines (MARS) technique, which is a non-parametric regression technique introduced by Friedman (1991), can provide the flexibility. Its concept is to model a given profile with piecewise linear models while maintaining the continuity between these models. More importantly, it can automatically model the profile without prior knowledge of the non-linearity. In this study, MARS is applied to establish piecewise linear models to fit the longitudinal rut depth profile. Based on those linear models, the slopes are calculated.

5.1.3 Divide Project into Segments

With the longitudinal rut depth profile of a project, a procedure is needed to divide it into segments, each of which is typically 1 mi. Sometimes, the first segment or the last segment of a project may be less than 1mi. The longitudinal rut depth profiles are found to be longer than the project, e.g., perhaps, 10.5 mi long instead of 10.3 mi of actual project length. This is because the survey vehicle cannot keep on driving perfectly straight and DMI records the distance that the vehicle actually traveled, which is more than the length of the project. To divide the rut depth profile into segments, an assumption is made that vehicle wandering occurs consistently. So the

profile data is divided into segments proportionally to the segment length. For instance, when dividing the 10.5 mi of data into 11 segments, 10 of which is determined to be 1.019-mi long and the remaining one is 0.31-mi long.

To verify this assumption, the driving behavior of multiple drivers was analyzed. Results are shown in Table 6.16. It is found that the accumulative amount of vehicle wandering varies among drivers, but is fairly consistent for each individual driver. Therefore, it is reasonable to assume that the amount of vehicle wandering for the first mile within the project will be similar to that of any mile within the same project, unless the driver was changed.

Table 6.16 Accumulative Vehicle Wandering

Accumulative Vehicle Wandering (mi per mi)		Driver 1	Driver 2
Southbound	Run1	0.019	0.0088
	Run2	0.020	0.0063
	Run3	0.020	0.0063
Northbound	Run1	0.020	0.0069
	Run2	0.019	0.0063
	Run3	0.019	0.0063

5.1.4 Statistical Analyses

With the filtered rut depth profiles, statistical analyses are conducted. Commonly used statistical indicators, including mean, median, 60th percentile, minimum, maximum, skewness, standard deviation, linear percentages of none, low, medium, and severe rutting, are calculated. The definition of the representative rut depth for a roadway section is that the rut depth can represent the rutting condition of the majority of this section. Based on this definition, the histogram of rut depth measurements within the road section is drawn first and the range, centered at RD_i and from $RD_i - \Delta$ to $RD_i + \Delta$, is identified. The RD_i that contains the maximum number of rut depth measurements is denoted as the representative rut depth mode. The representative rut depth mode is proposed as the new indicator to represent the rutting conditions. Besides, the percentage of rut depths that fall into the range of the representative mode, which is denoted as the maximum percentage, is reported. It equals $\frac{\text{Area}_i}{\text{Total Area}} \times 100\%$. In this study, Δ is set to be 1/16 in. Different

from traditionally used indicators, the newly proposed indicator reflects the true meaning of

representative. It, together with the percentage, indicates the homogeneity of the rutting condition within the analyzed section.

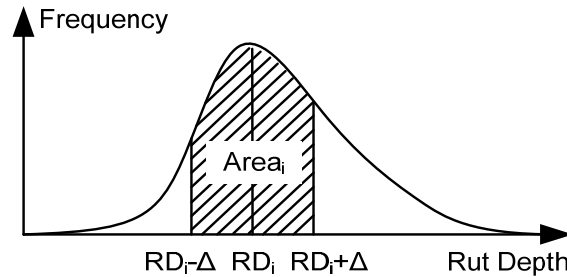


Figure 6.25 Illustration of Representative Rut Depth Mode

5.2 Case Study

Case studies on several state-maintained and non-state-maintained routes were carried out to evaluate the feasibility of improving the network-level rutting survey using the tested method. The test site selection, data collection, and case study results are presented in the following sections.

5.2.1 Test Site Selection

In the process of test site selection, an effort was made to cover different, yet typical, pavement surface types across the state, including OGFC and Superpave, while targeting pavement sections have rutting of different severity levels. After reviewing the treatment criteria in GDOT, four groups of rut depths were identified for investigation. They are none (rut depth shallower than 1/4 in.), low (between 1/4 in. and 1/2 in.), medium (between 1/2 in. and 1 in.), and severe (greater than 1 in.). Also, the selected test site was required to have varying surface conditions (e.g. with little cracking, severe cracking, or potholes), other conditions (e.g. integrity of pavement marking and presence of railroad crossing), and varying traffic volumes. The first two factors are considered because they may impact the rut depth calculation accuracy. The traffic volume is considered because it implies the difficulty to carry out the manual survey and may result in different rutting configurations (e.g. the rut shape).

To locate possible test sites, the annual survey results from GDOT were reviewed. A list of routes was identified based on the fact that the routes exhibited a variety of rut depths and

surface conditions. This list was then narrowed down by performing a preliminary visual investigation and considering the characteristics mentioned above. Finally, I-95, SR 275, SR 67, and Benton Blvd. were selected as primary test sites. Table 6.17 shows the detailed information about those test sites.

SR 275 and SR 67 are two-lane rural roads. The SR 275 has a dead end and only serves a small amount of traffic. After visiting the test site, it was found that this test site has low to medium levels of rutting and few cracks. SR 67 experienced a much higher traffic volume and exhibited medium to severe cracking. I-95 is an interstate highway that connects Florida and Washington, D.C. The short section from MP101 to MP100 was selected as a test section. It is paved with SMA plus OGFC. The daily traffic volume is more than 50,000. This section is still in good condition and exhibits little rutting or few cracks. It has low severity level of raveling. The last test section is Benton Blvd., which is a county road. It was selected a test section because it had very severe rutting (as deep as 2 in.) and severe cracking and potholes.

Table 6.17 Selected Test Sites

Case #	Road	Section (MP)	Surface Type	AADT	Rut Depth (in.)	Surface Condition	Date of Data Collection
1	SR275	0-5	--	1,890	1/8 – 3/4	Few cracks	04/21/2011
2	SR67	9-15	--	7,570	0-1/8	Medium to severe cracking	04/21/2011
3	I-95	101-100	OGFC	>50,000	1/8 – 1/4	Few cracks; low severity level raveling	10/15/2010
4	Benton	--	--	--	1/4 - 2	Severe cracking and potholes	05/10/2011

5.2.2 Data Collection

Once the test sites were finalized, a manual rutting survey was conducted on SR 275 and SR 67 by the GDOT liaison engineers in accordance with GDOT’s protocol. A manual survey was not conducted on I-95 due to the high traffic volume. Then, 3D laser data was collected using the 3D laser at 5mm spacing along the driving direction. Data was collected on SR 275 three times so that the repeatability of the 3D laser can be evaluated. For other test sites, only one run of data was collected.

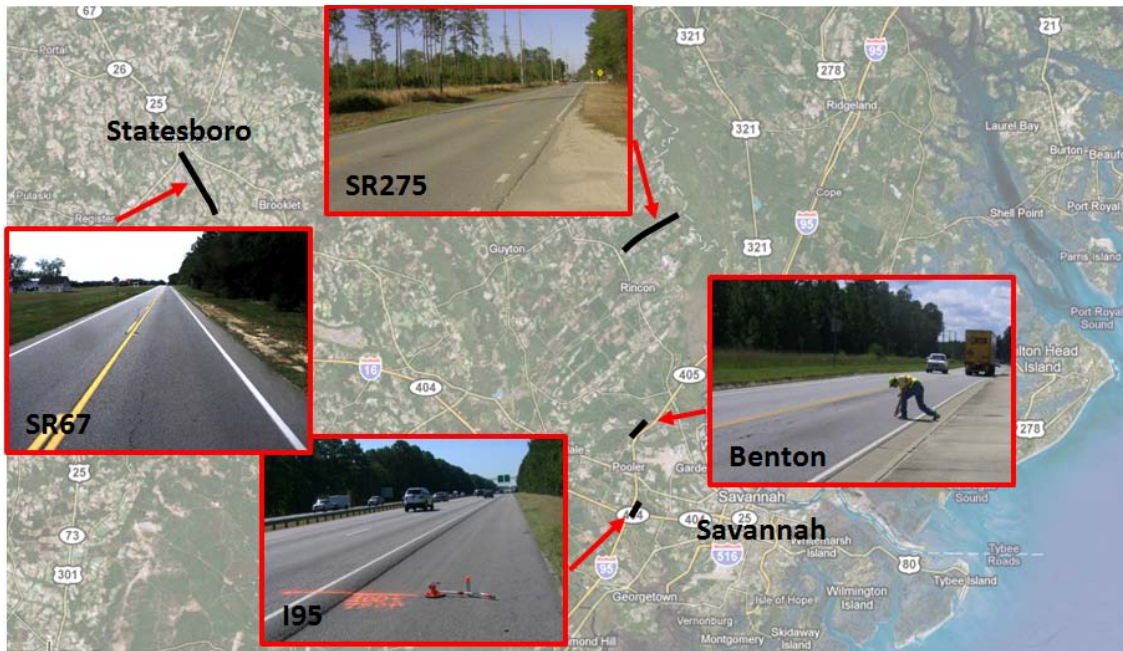


Figure 6.26 Test Site Locations

5.2.3 Data Analyses and Results

The collected 3D laser data was analyzed using the tested method. The analysis results are reported as follows:

Case 1 – SR 275

Figure 6.27 shows the raw data for the outside lane of SR 275, southbound (SB) from MP 0.8 to MP 0. As seen from figures, the rutting condition within this mile is relatively uniform. The maximum rut depth on this route is close to 1/2 in. The representative section identified during the manual survey is highlighted with the green rectangular. For the inside wheelpath, the rutting condition in the selected section can represent the majority of the rutting condition within this mile, whereas a relatively worse 100ft. was selected for the outside wheelpath. Several restrictions have prevented the manual survey from capturing the representative rut depth. First, it is not easy to observe the rutting from the windshield survey. So, the selection of a 100ft. representative section is mainly based on the cracking. Second, the selection of a 100ft. representative section is subjective. Finally, even if a representative section was located correctly, only a limited number of manual measurements were taken in the field.

In the next step, the longitudinal rut depth profiles (shown in Figure 6.27) that have outliers are filtered using the outlier removal algorithm presented above. The red profiles shown in Figure 6.28 are the filtered data. With the filtered data, statistical analyses were conducted. Figure 6.29 shows the histogram of the filtered rutting data. Obviously, the data has some positive skew and does not follow a normal distribution. Statistical indicators, including mean, median, 60th percentile, minimum, maximum, skewness, standard deviation, linear percentages of none, low, medium, and severe rutting, are calculated and presented in Table 6.18.

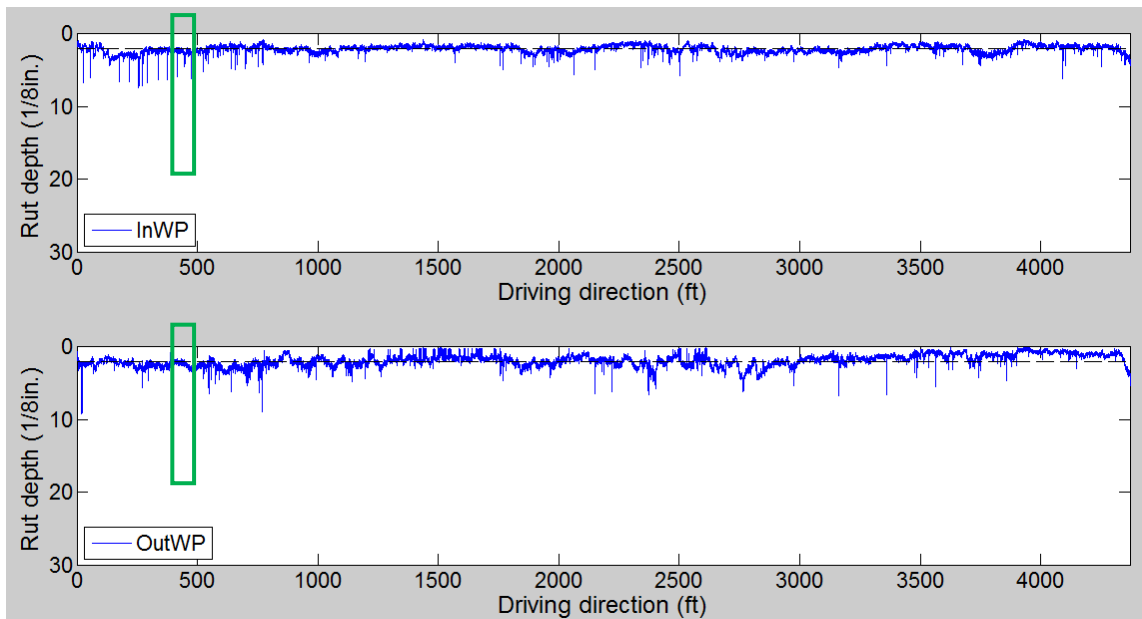


Figure 6.27 Raw Data (SR 275 SB from MP 0.8 to MP 0)

As seen from Table 6.18, the tested method shows high repeatability when reporting most statistics. For instance, the maximum absolute difference among mean rut depths collected from three runs is close to 0. The maximum absolute difference among the linear percentages of different severity levels of rutting is only 2%.

Also, as shown in Table 6.18, the four candidates of representative rut depth, including mean, median, representative mode, and 60th percentile of rut depth, are very close to each other. The maximum percentage is less than 50% for the outside wheelpath, which implies that the rutting condition on the outside wheelpath is less uniform compared to the inside wheelpath. Hence, to advise a treatment that can be properly applied to the majority of this road section, a more conservative indicator, e.g. 60th percentile of rutting, is more appropriate.

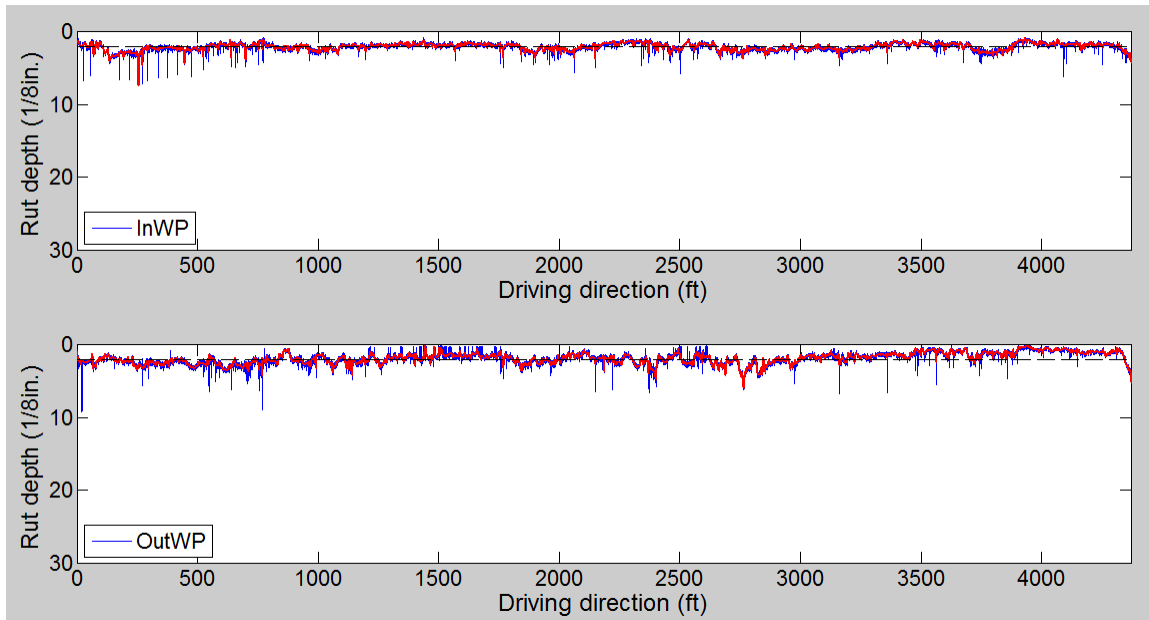


Figure 6.28 Raw (Blue) and Filtered Data (Red) (SR275 SB from MP 0.8 to MP 0)

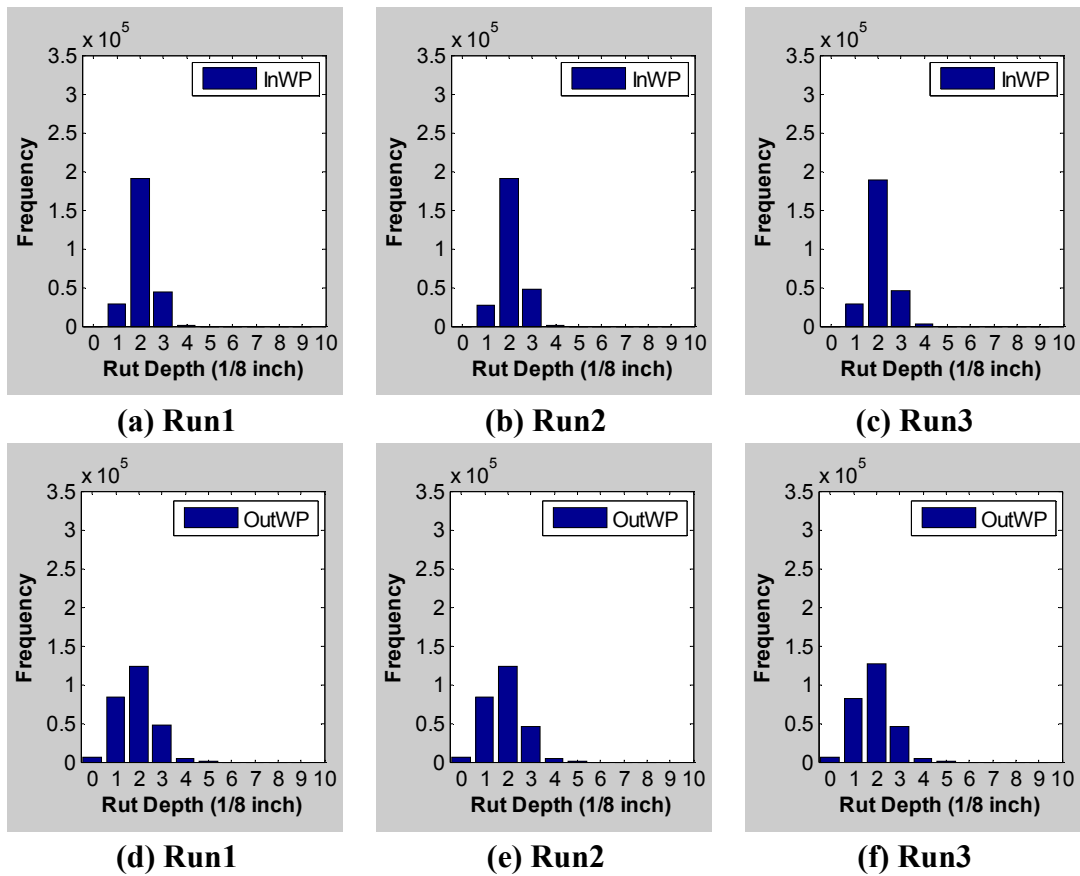


Figure 6.29 Histogram of Filtered Data (SR 275 SB from MP 0.8 to MP 0)

Table 6.18 Reported Indicators (SR 275)

Indicators	InWP Rut Depth (1/8 in.)					OutWP Rut Depth (1/8 in.)				
	Run1	Run2	Run3	Avg	Diff	Run1	Run2	Run3	Avg	Diff
Mean	2.0	2.1	2.1	2.1	0.1	1.8	1.9	1.9	1.9	0.1
Median	2.0	2.0	2.0	2.0	0.0	1.8	1.8	1.8	1.8	0.0
60 th Prct	2.1	2.2	2.1	2.1	0.1	2.0	2.0	2.1	2.0	0.1
Rep Mode	2.0	2.0	2.0	2.0	0.0	1.9	1.9	1.9	1.9	0.0
Max Prct	72%	72%	71%	72%	1%	49%	48%	48%	48%	1%
Min	0.3	0.8	0.4	0.5	0.5	0.2	0.1	0.2	0.2	0.1
Max	7.2	7.4	7.3	7.3	0.2	6.1	6.0	6.0	6.0	0.1
Skewness	0.9	0.9	0.8	0.9	0.1	0.3	0.4	0.4	0.4	0.1
Std	0.5	0.5	0.5	0.5	0.0	0.8	0.8	0.8	0.8	0.0
None	51%	49%	50%	50%	2%	59%	59%	57%	58%	2%
Low	49%	50%	50%	50%	1%	41%	40%	42%	41%	2%
Medium	0%	0%	0%	0%	0%	1%	1%	1%	1%	0%
High	0%	0%	0%	0%	0%	0%	0%	0%	0%	0%

Besides the section from MP 0.8 to MP 0, other sections on SR275 were analyzed similarly, and the analysis results are listed in Table 6.19, Table 6.20, and Table 6.21. As shown in Table 6.19, the statistical indicators, mean, median, 60th percentile of rut depth, and representative mode, provide similar rut depth for road sections with relatively uniform rutting condition and dissimilar values for some other sections. Still, the 60th percentile is suggested by GDOT engineers as the representative rut depth, so that 60% of the road section shows rutting smaller than the representative rut depth and can be maintained using the same treatment.

Case 2 – SR67

Similar analyses have been carried out for data collected from SR 67. The analysis results are summarized in Table 6.22,

Table 6.23, and

Table 6.24. Compared to SR 275, SR 67 has minor rutting issues. The majority of the test section has rutting shallower than 1/4 in. Four statistical indicators, mean, median, 60th percentile of rut

depth, and representative mode, provide similar rut depths for this test section. According to Table 6.22, the automatically measured rut depths are close to the manual measurements. This is mainly due to the fact that the rutting condition within this test section is relatively uniform.

Table 6.19 Results for SR 275

MP	InWP Rut Depth (1/8 in.)						OutWP Rut Depth (1/8 in.)					
	Mean	Median	60 th Prct	Rep Mode	Max Prct	Manual	Mean	Median	60 th Prct	Rep Mode	Max Prct	Manual
5-4	1.1	1.0	1.1	1.1	94%	1	0.9	0.8	0.9	0.9	85%	1
4-3	0.8	0.8	0.8	0.9	99%	-	0.8	0.7	0.8	0.8	94%	-
3-2	1.1	0.8	0.9	0.8	79%	-	0.9	0.8	0.9	0.8	82%	-
2-1	1.6	1.6	1.8	1.0	42%	2	1.6	1.4	1.6	1.2	58%	4
1-0	2.4	2.2	2.4	2.1	60%	3	2.1	2.0	2.2	1.9	48%	3
0-1	2.6	2.6	2.8	2.7	50%	-	1.4	1.3	1.4	1.3	75%	-
1-2	1.8	1.7	2.0	1.3	45%	-	2.3	1.9	2.1	1.2	39%	-
2-3	1.1	0.9	1.0	1.0	72%	0	1.4	0.9	1.1	0.8	67%	1
3-4	0.8	0.8	0.8	0.9	99%	1	0.7	0.6	0.7	0.8	97%	1
4-5	1.0	1.0	1.1	1.1	94%	-	0.9	0.8	0.9	0.8	84%	-

Table 6.20 Results for SR 275 (Cont'd)

	MP	InWP Rut Depth (1/8 in.)				OutWP Rut Depth (1/8 in.)			
		Min	Max	Skewness	Std	Min	Max	Skewness	Std
SB	5-4	0.3	2.8	0.4	0.3	0.2	3.9	1.5	0.4
	4-3	0.3	2.4	0.8	0.2	0.2	6.5	3.5	0.4
	3-2	0.1	4.2	1.7	0.7	0.2	5.1	2.6	0.6
	2-1	0.3	5.8	0.4	0.8	0.0	7.4	1.5	1.0
	1-0	0.0	9.8	2.4	0.9	0.2	13.8	2.6	1.1
NB	0-1	0.0	4.7	-0.2	0.7	0.2	4.7	1.2	0.5
	1-2	0.3	8.5	0.7	0.9	0.2	8.6	1.1	1.4
	2-3	0.1	4.5	1.7	0.7	0.1	9.3	2.6	1.5
	3-4	0.3	2.5	1.4	0.2	0.2	4.1	2.0	0.3
	4-5	0.4	3.5	2.1	0.3	0.2	3.3	1.1	0.4

Case 3 – Benton Blvd SB

Similar analyses have been done to a road section of Benton Blvd. Figure 6.30(a) shows the roadway environment, and Figure 6.30(b) shows a short section with severe rutting and alligator cracking. The 3D laser data collected from Benton Blvd. was processed. The raw rut depth data is presented in Figure 6.31. As seen from the figure, the rutting condition within this mile is less uniform. The rut depth ranges from 1/4 in. to 2 in. Also, the rut depth data is noisy because the severe rutting on this road section is accompanied by alligator cracking, as shown in Figure 6.30(b). After applying the noise removal algorithm, the outliers were removed. The filtered data is shown in Figure 6.32. Then, statistical analysis was carried out. The results are presented in Figure 6.33 and Table 6.25. As shown in the table, the standard deviation of the rut depths in this test section is relative high, greater than 1/8 in. The representative mode is 3.0 and 1.8 for inside and outside wheelpaths. The maximum percentage is only 31% and 39%. This concurs with previous observation that the rutting condition within this section is less uniform.

Case 4 – I-95 SB from MP101-MP100

Figure 6.34 shows the raw data for outside lane of I-95 SB from MP 101 to MP 100. The majority of the inside wheelpath shows low severity level rutting, which is between 1/4 in. and 1/2 in.; the outside wheel path does not have much rutting, and the rut depth is less than 1/4 in. A localized spot between locations 4,500ft. and 5,000ft. has more than 1/2 in. rutting, as shown in Figure 6.34(b), approaching the end of this mile on the inside wheelpath.

Table 6.21 Results for SR 275 (Cont'd)

	MP	InWP Rut Depth (1/8 in.)				OutWP Rut Depth (1/8 in.)			
		None	Low	Medium	High	None	Low	Medium	High
SB	5-4	100%	0%	0%	0%	98%	2%	0%	0%
	4-3	100%	0%	0%	0%	99%	1%	0%	0%
	3-2	85%	15%	0%	0%	95%	5%	0%	0%
	2-1	70%	30%	0%	0%	76%	20%	4%	0%
	1-0	36%	59%	5%	0%	50%	47%	3%	0%
NB	0-1	19%	79%	2%	0%	90%	10%	0%	0%
	1-2	63%	36%	1%	0%	55%	30%	15%	0%
	2-3	87%	12%	1%	0%	84%	9%	7%	0%
	3-4	100%	0%	0%	0%	100%	0%	0%	0%
	4-5	98%	2%	0%	0%	99%	1%	0%	0%

Table 6.22 Results for SR67

MP	InWP Rut Depth (1/8 in.)						OutWP Rut Depth (1/8 in.)					
	Mean	Median	60 th Prct	Rep Mode	Max Prct	Manual	Mean	Median	60th Prct	Rep Mode	Max Prct	Manual
15-14	1.4	1.4	1.5	1.4	75%	1	0.7	0.6	0.7	0.8	96%	1
14-13	1.3	1.3	1.4	1.3	80%	1	0.6	0.5	0.6	0.6	97%	1
13-12	1.0	0.9	1.0	1.0	95%	1	0.4	0.3	0.4	0.7	100%	1
12-11	1.2	1.2	1.3	1.1	85%	1	0.6	0.5	0.6	0.7	96%	1
11-10	1.2	1.1	1.2	1.1	77%	-	0.5	0.4	0.4	0.7	96%	-
10-9	1.4	1.3	1.4	1.3	69%	-	0.6	0.4	0.5	0.7	88%	-
9-10	1.3	1.2	1.3	1.2	75%	1	0.6	0.5	0.6	0.6	89%	1
10-11	1.1	1.1	1.2	1.1	88%	1	0.4	0.3	0.4	0.6	97%	1
11-12	1.4	1.3	1.4	1.4	80%	-	0.5	0.4	0.4	0.7	97%	-
12-13	1.0	1.0	1.1	1.0	86%	-	0.3	0.3	0.3	0.6	100%	-
13-14	1.1	1.1	1.2	1.1	81%	-	0.4	0.3	0.3	0.6	97%	-
14-15	1.0	1.0	1.0	1.0	96%	-	0.3	0.3	0.3	0.6	99%	-

Table 6.23 Results for SR67 (Cont'd)

	MP	InWP Rut Depth (1/8 in.)				OutWP Rut Depth (1/8 in.)			
		Min	Max	Skewness	Std	Min	Max	Skewness	Std
SB	15-14	0.1	3.8	0.0	0.5	0.0	4.9	3.1	0.3
	14-13	0.3	2.7	0.4	0.4	0.1	2.3	0.9	0.3
	13-12	0.3	2.2	0.4	0.3	0.1	1.9	2.0	0.2
	12-11	0.2	4.1	1.3	0.4	0.1	2.6	1.2	0.3
	11-10	0.1	3.8	0.9	0.5	0.1	7.7	8.3	0.5
	10-9	0.0	6.0	1.6	0.6	0.1	9.8	6.3	0.8
NB	9-10	0.0	3.7	1.2	0.5	0.0	5.1	2.3	0.4
	10-11	0.2	2.9	0.7	0.3	0.1	3.9	4.0	0.3
	11-12	0.2	3.9	0.8	0.4	0.0	6.6	6.7	0.5
	12-13	0.3	2.6	0.7	0.3	0.1	1.9	2.3	0.1
	13-14	0.2	3.2	0.8	0.4	0.0	10.1	7.3	0.6
	14-15	0.3	2.3	0.4	0.2	0.1	2.0	3.6	0.1

Table 6.24 Results for SR67 (Cont'd)

	MP	InWP Rut Depth (1/8 in.)				OutWP Rut Depth (1/8 in.)			
		None	Low	Medium	High	None	Low	Medium	High
SB	15-14	91%	9%	0%	0%	99%	1%	0%	0%
	14-13	95%	5%	0%	0%	100%	0%	0%	0%
	13-12	100%	0%	0%	0%	100%	0%	0%	0%
	12-11	98%	2%	0%	0%	100%	0%	0%	0%
	11-10	94%	6%	0%	0%	99%	0%	1%	0%
	10-9	86%	14%	0%	0%	98%	1%	1%	0%
NB	9-10	91%	9%	0%	0%	99%	1%	0%	0%
	10-11	99%	1%	0%	0%	99%	1%	0%	0%
	11-12	93%	7%	0%	0%	98%	1%	1%	0%
	12-13	99%	1%	0%	0%	100%	0%	0%	0%
	13-14	96%	4%	0%	0%	98%	1%	1%	0%
	14-15	100%	0%	0%	0%	100%	0%	0%	0%



(a) (b)
Figure 6.30 Roadway Environment (Benton Blvd.)

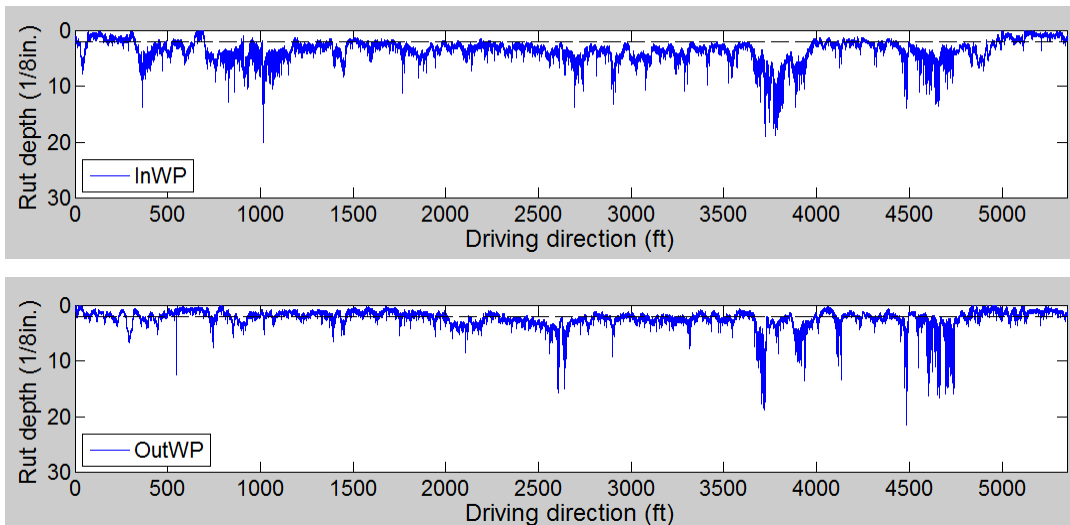


Figure 6.31 Raw Data (Benton Blvd.)

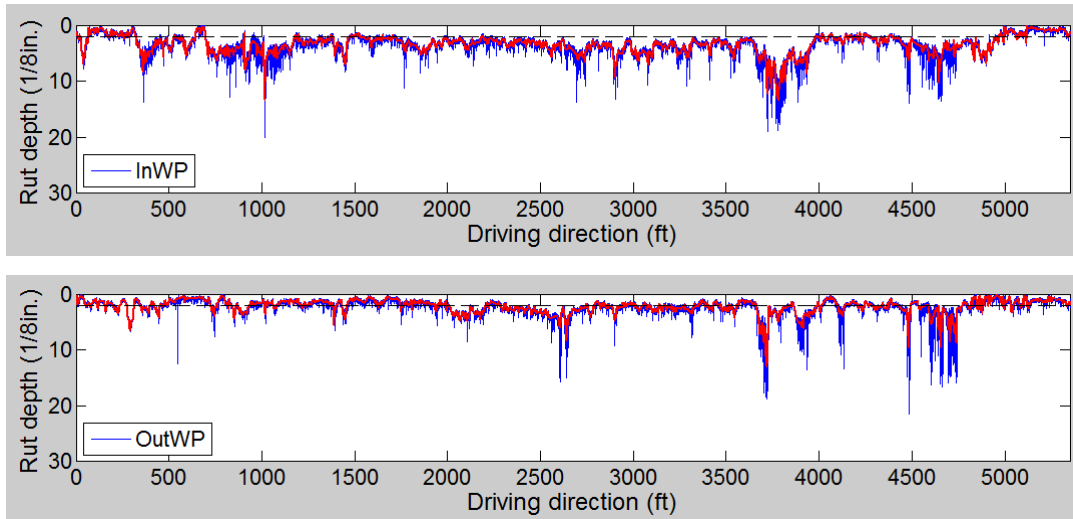


Figure 6.32 Raw (Blue) and Filtered Data (Red) (Benton Blvd.)

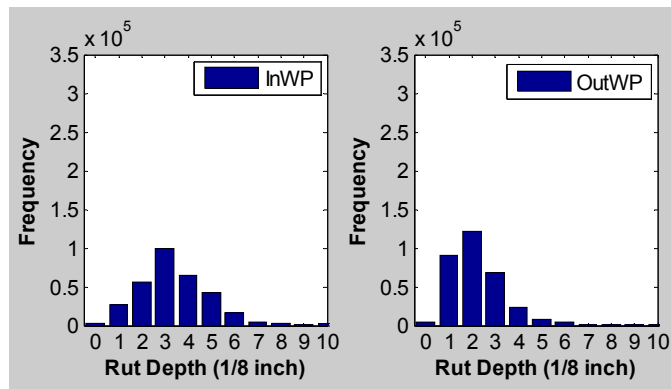


Figure 6.33 Histogram of Rut Depth Measurements (Benton Blvd.)

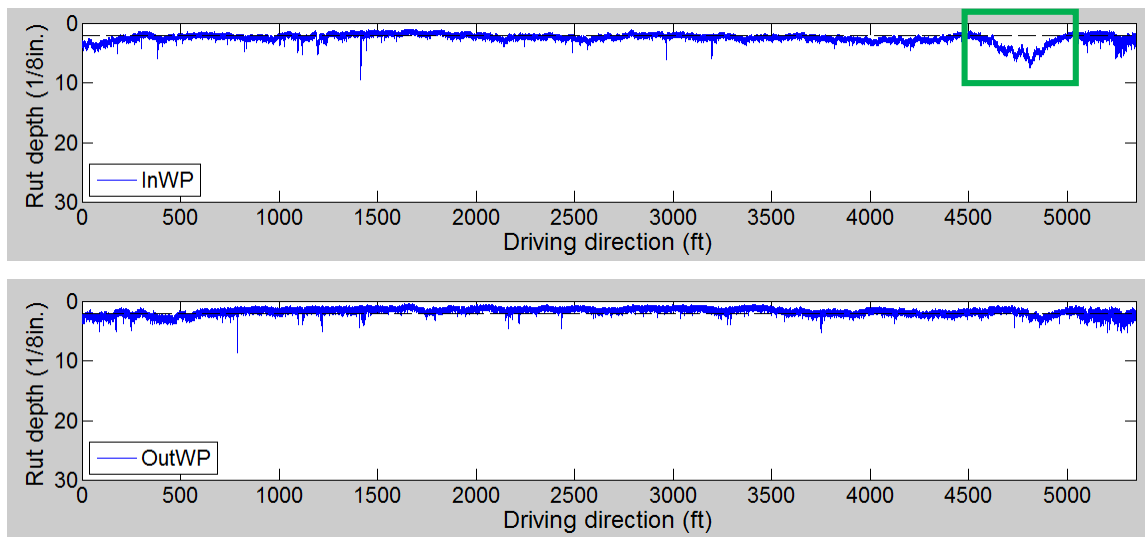


Figure 6.34 Raw Data (I-95)

Figure 6.35 shows the raw data (blue) as well as filtered data (red). The noise removal method removed the outliers and smoothed the profile. The filtered data is then used as the input for statistical analysis. The analysis results are shown in Figure 6.36 and Table 6.25. The maximum percentage is 73% and 76% for the inside and outside wheelpaths, which indicates that the rutting condition is relatively uniform on this road section.

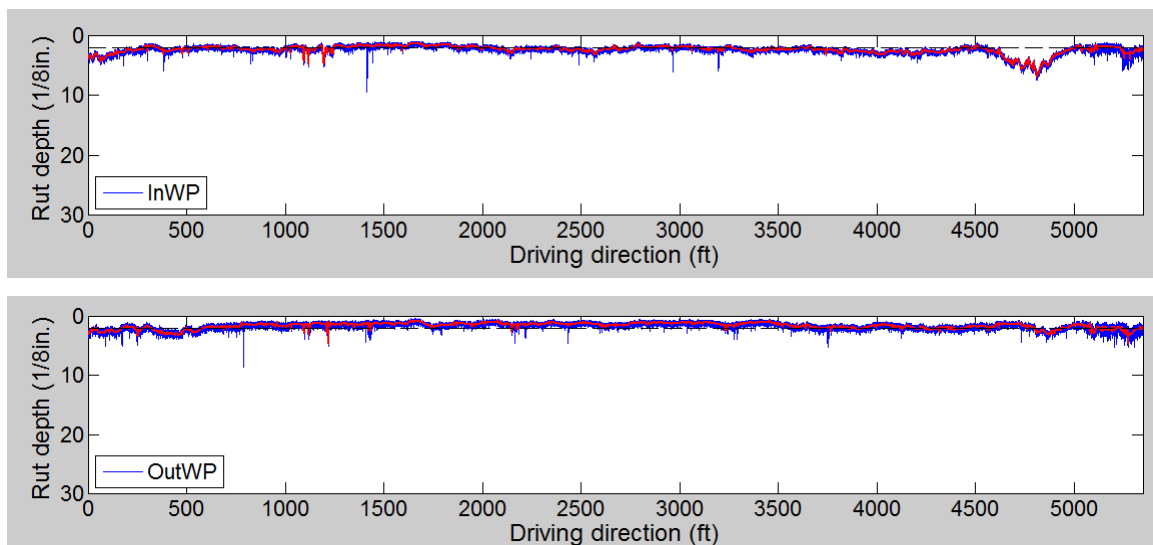


Figure 6.35 Raw (Blue) and Filtered Data (Red) (I-95)

The above case studies on the four selected road sections indicate that

- The tested network-level rutting survey method has good repeatability.
- The tested method can report the representative rut depth, i.e. the 60th percentile, as suggested by engineers from GDOT. The representative rut depth can be directly fed into COPACES, the pavement condition database managed by GDOT, to support pavement management and maintenance.
- The tested method can also report other statistical indicators, e.g. mean, maximum, standard deviation, and linear percentage of none, low, medium, and severe rutting, which are useful in support of the network-level pavement management decision making.

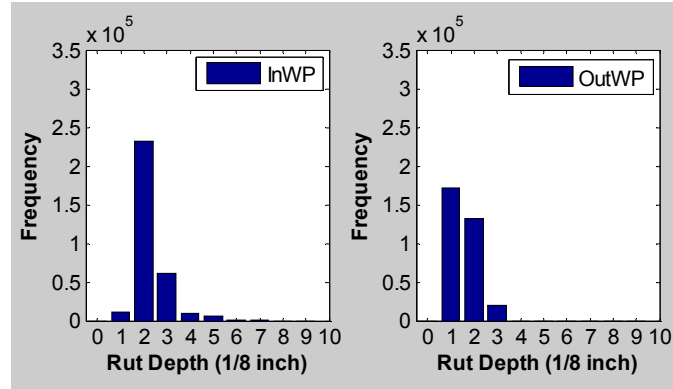


Figure 6.36 Histogram of Rut Depth Measurements (I-95)

Table 6.25 Indicators Reported (Benton Blvd. and I-95)

Indicators	Rut Depth on Benton (1/8 in.)		Rut Depth on I-95 (1/8 in.)	
	InWP	OutWP	InWP	OutWP
Mean	3.4	2.2	2.3	1.6
Median	3.2	2.0	2.2	1.4
60th Prct	3.6	2.3	2.3	1.6
Rep Mode	3.0	1.8	2.1	1.4
Max Prct	31%	39%	73%	76%
Min	0.0	0.2	1.2	0.6
Max	13.4	13.0	6.8	4.7
Skewness	1.2	2.1	2.3	1.0
Std	1.6	1.2	0.7	0.5
None	15%	50%	33%	81%
Low	54%	43%	62%	19%
Medium	29%	7%	4%	0%
High	2%	0%	0%	0%

5.2.4 Computing Consideration

This subsection discusses the determination of an adequate sampling interval and the performance (i.e. processing speed and data storage need) of the tested method. According to literature review, there is little consistency on the sampling interval used by different state transportation agencies. Usually, there is a balance between the sampling interval and the processing time. The smaller the interval, the more accurate the network-level survey results, whereas the longer the processing time. To determine an adequate sampling interval, this subsection evaluates the impact of the sampling interval on the accuracy of network-level rutting

survey and the data processing time. The second part of this subsection assesses the data storage need when using the tested method for network-level rutting survey. The potential means to further reduce the data storage needs are recommended.

Sampling Interval and Network-level Survey Accuracy

To establish the relationship between the sampling interval and the network-level survey accuracy, experimental tests were conducted using the data collected from Benton Blvd. because the rutting on it is less uniform. The less uniform the rutting is, the greater the impact of sampling interval on the survey accuracy is. Four sampling intervals, 5mm, 6 in., 1 ft., and 10ft., are analyzed. The rutting statistics are reported based on the TxDOT's and PennDOT's survey protocols.

The test results are shown in Table 6.26. As seen from the results, all indicators, besides minimum and maximum rut depth, are insensitive to the sampling interval when the report interval is 0.5 mi. If the statistics are reported every 0.1mi, the sampling interval, 10ft. instead of 1ft., makes notable changes on the statistical values. Therefore, an adequate sampling interval partially depends on the report interval. When statistics are reported every 0.1 mi, 1ft. can be the maximum sample interval without compromising the measurement accuracy; while the sampling interval can be increased to 10ft. when we are reporting at 0.5mi intervals.

Sampling Interval and Processing Time

To estimate the relationship between the sampling interval and the processing time (per mile), experimental tests were conducted on a computer with a Windows 7, 64-bit operating system that has i7 CPU@2.67GHz and 12GB RAM. Both road sections on SR 275 and Benton Blvd. are analyzed. For each case, 200 data files are tested. Each data file contains data collected from a 4m-wide and 5m-long section at 5mm intervals. Six sampling intervals, i.e. 5mm, 50mm, 100mm, 150mm, 300mm, and 2.5m, are analyzed. Two of those intervals, i.e. 150mm and 300mm, have been used by multiple state transportation agencies.

Table 6.26 Impact of Sampling Interval on Rutting Condition Assessment Accuracy

State Highway Agency	Indicators	Benton (InWP)				Benton (OutWP)			
		5mm	6in.	1 ft.	10 ft.	5mm	6in.	1 ft.	10 ft.
TxDOT (0.1 mi)	Mean	1.0	1.0	1.1	1.1	3.1	3.1	3.1	3.1
	Min	0.2	0.3	0.3	0.3	0.1	0.2	0.2	0.7
	Max	3.6	3.6	3.6	3.6	6.3	6.3	6.3	6.0
	Std	0.4	0.4	0.4	0.6	1.3	1.3	1.3	1.3
	None	97%	97%	97%	96%	25%	25%	25%	22%
	Low	3%	3%	3%	4%	44%	43%	43%	50%
	Medium	0%	0%	0%	0%	31%	31%	31%	28%
	Severe	0%	0%	0%	0%	0%	0%	0%	0%
PennDOT (0.5 mi)	Mean	1.8	1.8	1.8	1.8	1.9	1.9	1.9	1.9
	Min	0.2	0.3	0.3	0.4	0.2	0.2	0.2	0.4
	Max	4.7	4.7	4.7	4.3	8.6	8.6	8.6	8.4
	Std	0.8	0.8	0.8	0.8	1.4	1.4	1.4	1.5
	None	66%	66%	66%	66%	68%	68%	68%	69%
	Low	33%	33%	33%	33%	20%	20%	21%	21%
	Medium	0%	0%	0%	0%	11%	11%	11%	9%
	Severe	0%	0%	0%	0%	0%	0%	0%	0%

The test results, shown in Table 6.27, Figure 6.37, and Figure 6.38, indicate that the processing time is similar when data from either SR 275 or Benton Blvd. are processed. This means that the processing time is not impacted by the amount of cracking on the pavement surface.

Additionally, the miles of data processed per hour decrease significantly when the sampling interval increases from 5mm to 50mm (2 in.), and, then, go flat gradually when the sampling interval increases from 50mm (2 in.) to 2500mm (100 in.). The time needed to process 1-mile long data become less than 0.1 hr if the sampling interval is 4 in. or greater. There may be some I/O processes, e.g. reading the input and writing the output, inside the algorithm that cannot be saved by increasing the sampling interval. If the sampling interval is 1ft., within one hour, 13 mi of data can be processed and rut depth values can be obtained.

Table 6.27 Sampling Interval vs. Processing Time

Sampling Interval (mm)		5	50	100	150	300	2500
Process Time per Mile (hr)	SR275	0.65	0.12	0.1	0.09	0.08	0.07
	Benton	0.65	0.13	0.1	0.09	0.08	0.07
Processed Data per Hour (mi)	SR275	1.5	8.4	10.5	11.4	12.9	14.7
	Benton	1.5	7.8	10.2	11.4	13.1	14.8

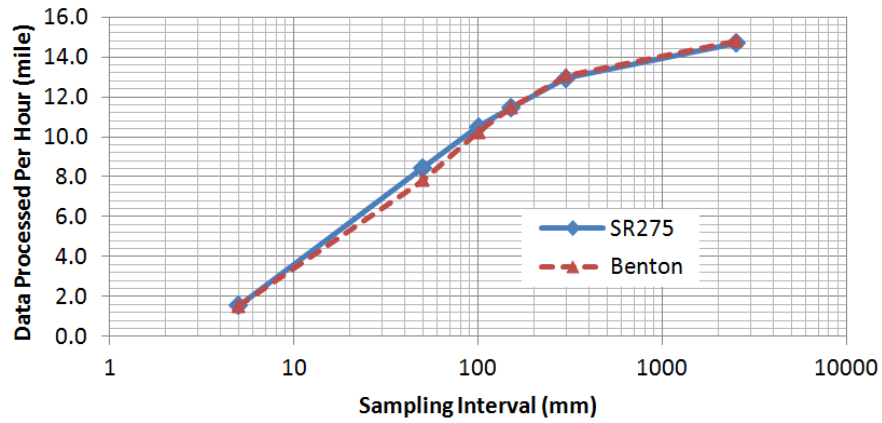


Figure 6.37 Sampling Interval vs. Data Processed per Hour (mi)

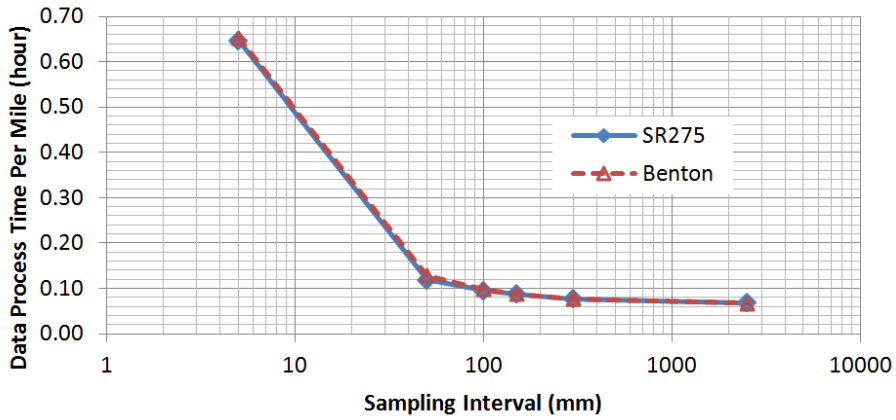


Figure 6.38 Sampling Interval vs. Data Processing Speed (mi/hr)

Aggregation Interval and Network-level Survey Accuracy

According to a literature review of state DOTs' survey practices, most state DOTs use 0.1 mi as the aggregation interval when processing the automatically collected rutting data. This subsection estimates the relationship between the aggregation interval and the network-level rutting survey accuracy. Experimental tests were conducted using the data collected from SR 275 and Benton Blvd. The rutting data was aggregated into 0.1mi and 1 mi, respectively. The results indicate that there is significant variation within the 0.1mi for data collected from Benton Blvd., as shown in Figure 6.40; the rutting condition on SR 275, shown in Figure 6.39, is relatively uniform. It is suggested that when the standard deviation is high, e.g. greater than 2 (of 1/8 in.), the aggregation into 1mi intervals will lose significant details. A smaller aggregation interval is more appropriate for road sections with large variation.

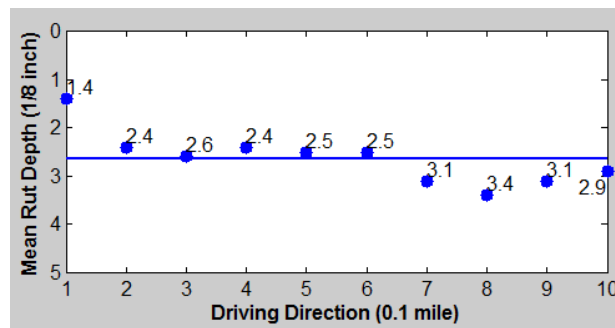


Figure 6.39 Aggregated Rut Depths at 0.1mi Intervals (SR 275 MP0-1 OutWP, Std = 0.5 of 1/8in.)

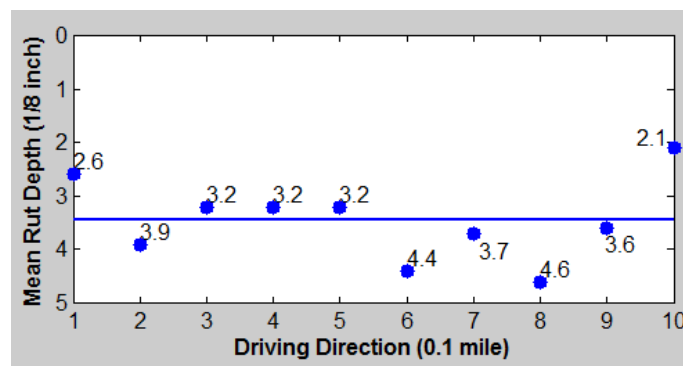


Figure 6.40 Aggregated Rut Depths at 0.1mi Intervals (Benton Blvd. InWP, Std = 1.6 of 1/8 in.)

Data Storage Need

According to Table 6.28, a significant amount of hard disk space to store the raw data, i.e. 3D continuous transverse profiles, is required. If surveying the 18,000 centerline miles of highway maintained by GDOT, at least 33.0TB (=18000mi/100mi*94GB*2lanes) hard disk storage per year is needed. Thus, storing the raw data will demand tremendous amounts of hard disk storage space. This will require extra effort to manage and maintain the huge amount of data. More importantly, the raw data itself provides little information that can directly support pavement management decision making. Therefore, storing all the raw data is not recommended.

The processed results from the raw data are stored in XML files. The storage need for XML files is 4.2 TB for 18,000 lane miles of highway when the sampling interval is 5mm. The data storage need is 13% and 0.6% of the need to store all the raw continuous transverse profiles. The XML files can be read to obtain longitudinal rut depth profiles. The storage need for longitudinal rut depth profiles is further reduced. Assume that each rut depth value requires 4 bytes storage space. Thus, totally, 85.8GB (=18000mi×1600m/mi×1000mm/m / 5mm×2WP×2lanes×4bytes) disk storage is needed per year. This is much less than the space needed to store all the raw data. Up to this point, the data storage need has been reduced by around 99.7%. In the future, this storage need can be further reduced by aggregating and reporting rut depth into bigger intervals.

Table 6.28 Data Storage Need per Inspection for every 100-Lanemile of the Highway Network

Sampling Interval	Raw Data	XML Files	Longitudinal Rut Depth Profiles
5mm	94GB (3MB/5m)	11.9GB (390KB/5m)	250MB (8KB/5m)

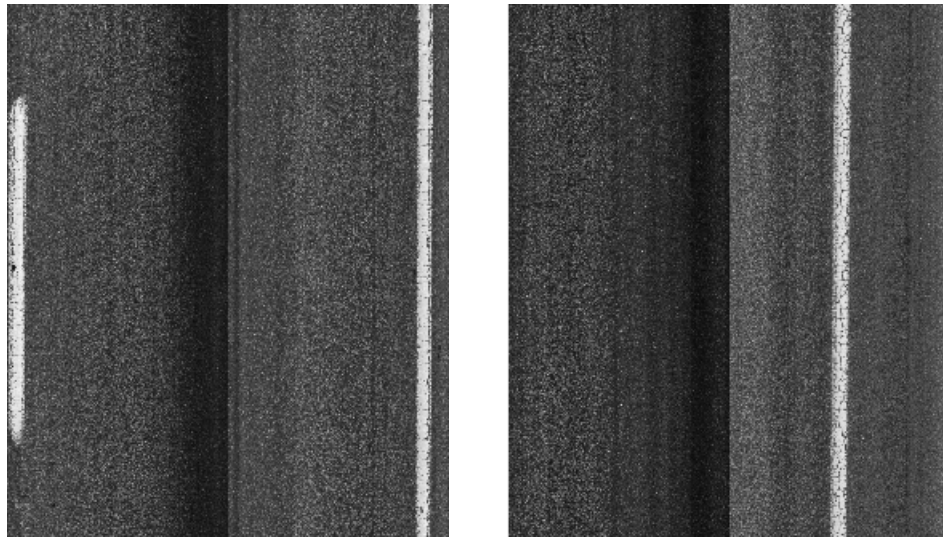
5.3 Discussions

Several issues have been identified during the tests are listed as follows:

- Issues of vehicle wandering

An example is given in Figure 6.41. Figure 6.41 (a) is the 3D laser data collected in a normal driving. Figure 6.41 (b) is the data collected when the vehicle wandered. Because of the vehicle wandering, the left lane marking is missing, and the right lane marking is almost in

the middle of the right sensor data, as shown in Figure 6.41 (b). For the road section in Figure 6.41 (b), both rut depths for the right and left wheelpaths can be underestimated when they are calculated using the half-lane profiles.

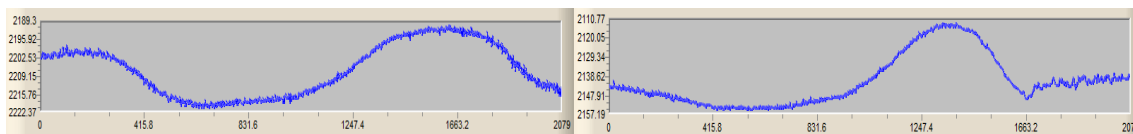


(a) Without vehicle wandering (b) With vehicle wandering

Figure 6.41 Issue of Vehicle Wandering

- Issue of half-lane rut depth calculation

Currently, rut depths are calculated for half-lanes. An assumption is made that the transverse profile is symmetrical to the center line. However, this assumption may not hold and the rut depth for some cases may be underestimated. Figure 6.42 shows such an example. Figure 6.42(a) is the half-lane profile collected by the left sensor and Figure 6.42(b) is the one by the right sensor. If pinning these two half-lane profiles, a full-lane profile can be obtained. As shown in Figure 6.42, the hump in the middle was captured by the left sensor and not the right sensor. Therefore, the rut depth for the right wheelpath can be underestimated if it is calculated using the right half-lane profile only.



(a) Left profile (b) Right profile

Figure 6.42 Issue of Half-lane Rut Depth Calculation

- Issue of lane marking detection

In the 3D laser, the lane marking detection is performed on fixed-length road sections. Each of such road section is 5m long for this study, and only the portion of transverse profile between the lane markings is used for rut depth calculation. Thus, it is crucial to accurately detect lane marking for rut depth calculation. However, current 3D laser software is not robust enough to detect the lane marking correctly for all road sections. An example is shown below.

Figure 6.43 shows the lane marking detection results for three adjacent road sections, S1, S2, and S3. The purple straight lines are the detected lane markings. Compared to S1 and S3, S2's detected lane markings shift to the right significantly. This shift causes abrupt changes of rut depth and rut width. As shown in Figure 6.44, both abrupt changes occur at boundaries between adjacent sections.

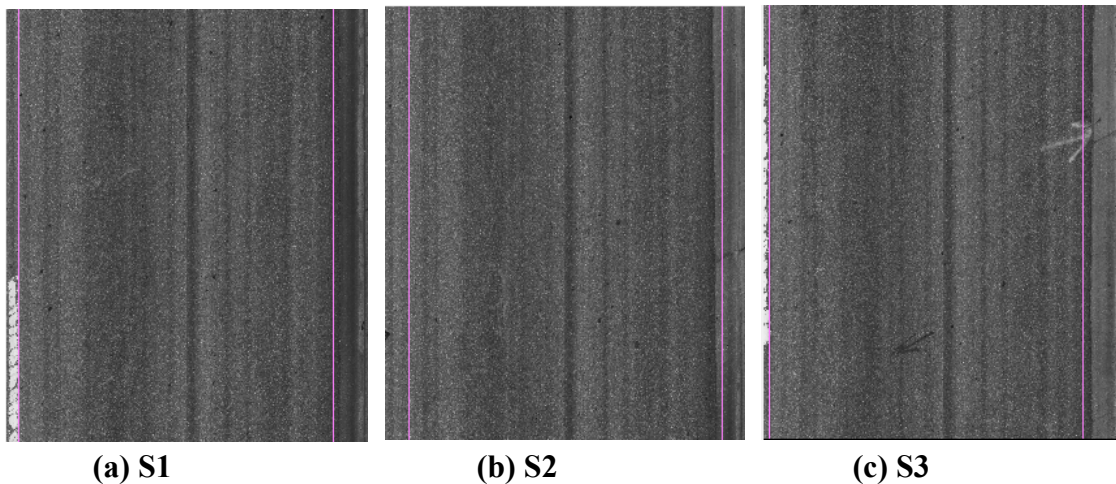


Figure 6.43 Lane Marking Detection Results

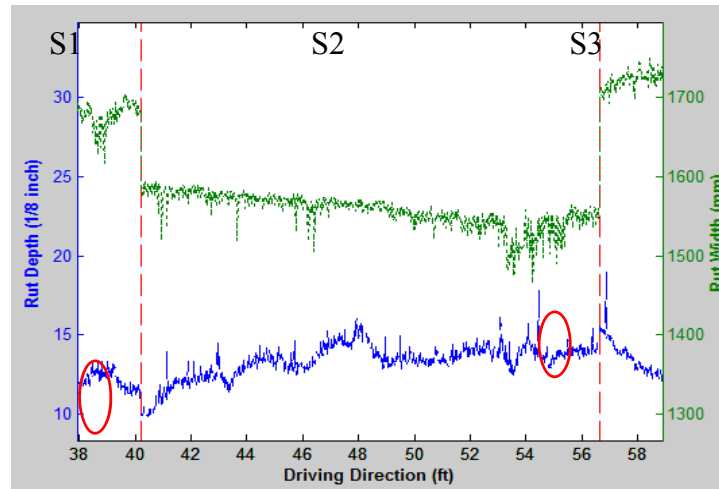


Figure 6.44 Issue of Missing Lane Marking

- Issue of rut depth calculation in the presence of other distresses (e.g. cracking) or objects
 A detailed examination of this issue has been presented in section 5.1.2. It is concluded that the current 3D laser is not able to provide accurate rut depth calculation when rutting is accompanied with transverse cracks (especially for cracks wider than 5mm), potholes and patches, raised pavement markings, rail tracks, and other objects (e.g. tree branches on the road).

6. Isolated Rutting Detection

The benefit of the emerging 3D laser technology is more than improving the network-level rutting measurement accuracy. The detailed information can also be used to further support project-level pavement maintenance, such as the isolated rutting detection. This section presents a method to identify the isolated rutting using the 3D continuous transverse profiles collected by the 3D laser. Pavement engineering knowledge has been extensively incorporated to establish the criteria for identifying isolated ruts. Finally, case studies were performed using the data collected on I-95 and SR 307 near Savannah, Georgia.

6.1 Research Need

Isolated rutting occurs at localized locations, such as spots experiencing high stress/strain conditions or spots with base failure. It reduces serviceability and causes risk for drivers, who may lose control of their vehicles when they maneuver on the uneven road or hydroplane when

water accumulates in wheelpath ruts. More importantly, unlike continuous rutting, isolated rutting is relatively short and unexpected, which makes it even more dangerous. This safety issue urges transportation agencies to treat the deformed, isolated sections in a timely manner to mitigate potential safety problems. To remedy isolated rutting, a low-cost, localized treatment can be applied. It is much more cost-effective than upgrading the entire roadway, which is still in sound condition. In order to apply low-cost, localized treatment, it is imperative to have an efficient method to detect all isolated ruts.

In the past, it was a challenge to detect isolated rutting due to the lack of data acquisition technology and an automatic detection method. Traditionally, transportation agencies survey and record only network-level rutting. The isolated rutting information is not collected in current PMSs because it is time-consuming and difficult to collect manually. To the best of our knowledge, there is no published automated method that detects isolated rutting.

With the advance of 3D laser imaging technology, 3D continuous pavement transverse profiles can be acquired at highway speed and the sensing system can, potentially, be used to detect isolated rutting. Figure 6.45 shows an example of 3D data collected at 100km/hr. Different colors represent different elevations. In the transverse direction, there are 2,080 points covering half of a lane (typically 2m wide). The transverse resolution is 1mm. The spacing between transverse profiles along the driving direction is 5mm. The depth accuracy (in elevation direction) is 0.5mm. This high-resolution provides a unique opportunity to detect isolated rutting.

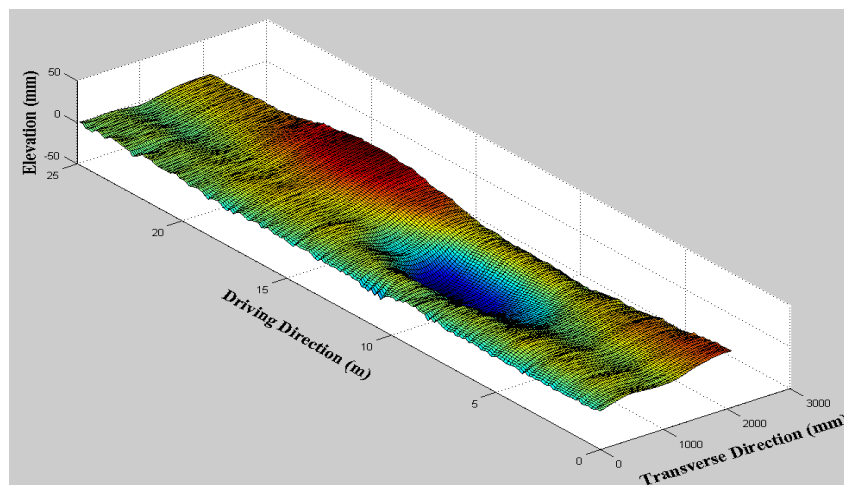


Figure 6.45 An Isolated Rut in 3D Laser Data

6.2 Case Study – I-95

The southbound lane of I-95 from MP 101 to MP 100 near Savannah, Georgia, was selected as a test site to evaluate the tested method. Figure 6.46 shows the location of the test site.

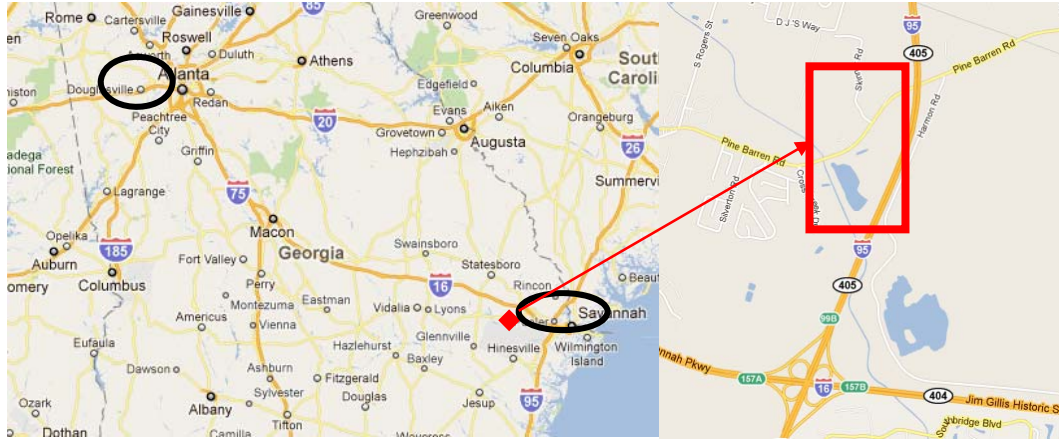


Figure 6.46 Location of Test Site on I-95

Test Results

Figure 6.47 shows the longitudinal rut depth profile for the inside wheelpath, which is the blue line, and the filtered longitudinal rut depth profile, which is the red line. The total length of each profile is 5,350 ft., slightly longer than 5280 ft. (1 mi). This results from the difference between DMI reading and the actual roadway section length. The filtering results show that outliers have been removed.

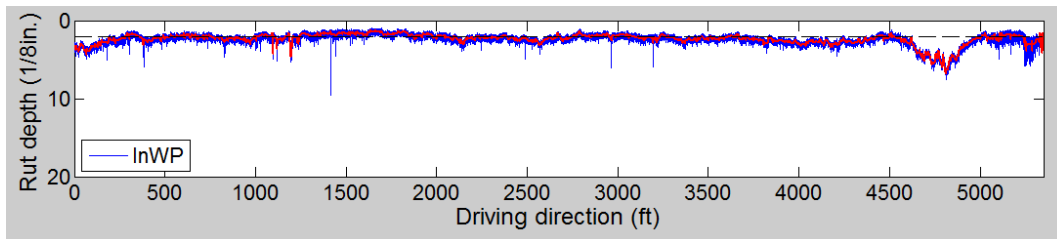


Figure 6.47 Raw Longitudinal Rut Depth Profile (Blue) and Filtered Profile (Red)

Figure 6.48 and Table 6.29 summarizes the homogeneous segmentation results. Each break point on the red profile corresponds to the bound between two adjacent homogeneous segments. The values of those red line segments are the mean rut depths for each homogeneous segment. This homogeneous segmentation results were obtained when setting the minimum segment length, i.e. MinLen, as 10ft., and the minimum mean rut depth difference, MinDiff, as 1/8 in. As seen from

Figure 6.48, the homogeneous segmentation method has successfully captured every point where the pavement rutting condition changes significantly.

Table 6.29 tabulates the homogeneous segmentation results, including the start MP, end MP, length, mean rut depth, and standard deviation. This table can be saved into databases and used to support project-level pavement management.

Figure 6.49 and Table 6.30 show the isolated rut detection results. Two isolated ruts are detected (labeled as 1 and 2 in Figure 6.49). One is 342ft. long (from 1,346ft. to 1688 ft.) and the other one is 32 ft. long (from 1,968ft. to 2,000 ft.). The maximum rut depth is greater than 1/4 in. for both of them. The rut volume for those two isolated ruts is 42 ft³ and 3 ft³, respectively; the rut area is 1,917 ft² and 184 ft².

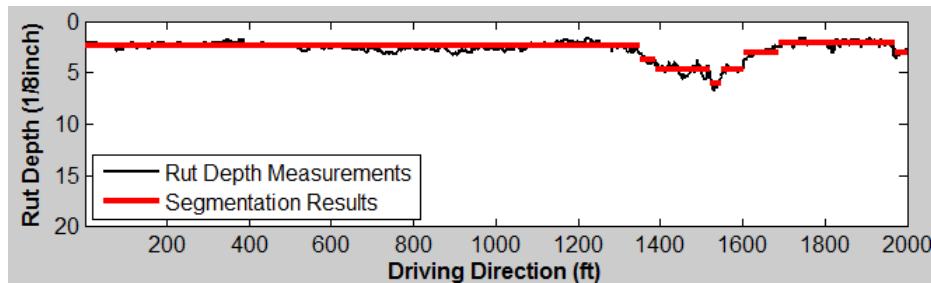


Figure 6.48 Homogeneous Segmentation Results (MinLen = 10ft. and MinDiff = 1/8 in.)

Table 6.29 Homogeneous Segmentation Results (I-95)

Record #	Start MP (ft.)	End MP (ft.)	Length (ft.)	Mean Rut Depth (1/8 in.)	Std (1/8 in.)
1	0	1350	1350	2.4	0.3
2	1350	1390	40	3.7	0.4
3	1390	1522	132	4.7	0.5
4	1522	1550	28	6.1	0.4
5	1550	1602	52	4.7	0.3
6	1602	1688	86	3.1	0.5
7	1688	1970	282	2.0	0.3
8	1970	2000	30	3.0	0.3

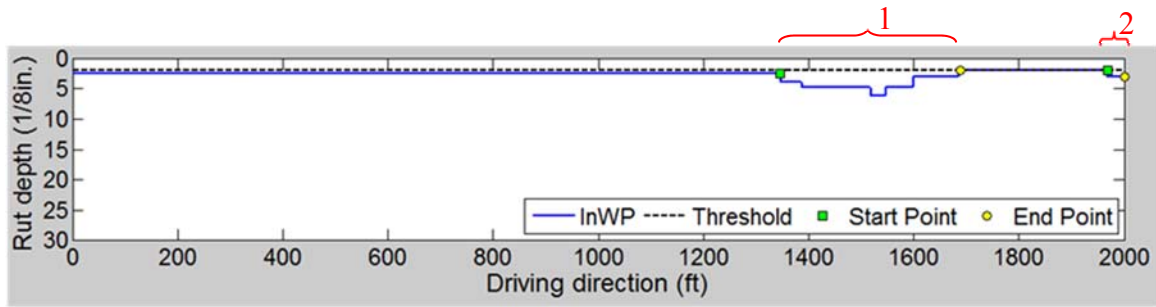


Figure 6.49 Detected Isolated Ruts

Table 6.30 Isolated Rutting Detection Results (I-95)

ID	Start MP (ft.)	End MP (ft.)	Rut Length (ft.)	Max Rut Depth (1/8 in.)	Rut Volume (ft ³)	Rut Area (ft ²)
1	1346	1688	342	6.1	42	1917
2	1968	2000	32	3.1	3	184

Verification in the Field

A windshield survey confirmed that this highway section does not show much rutting, and only a short section is shown in Figure 6.50 (b); approaching the end of this mile on the inside wheel path, it exhibits an isolated rut. This isolated rut could cause the risk of hydroplaning. However, it is tedious and difficult to locate it through the manual survey. In contrast, the method developed in this section is capable of finding spots with high hydroplaning potential automatically for the whole roadway network at highway speed. Therefore, it is very valuable and can dramatically improve existing survey and pavement maintenance practices.



(a) Roadway Environment

(b) Isolated Rut

Figure 6.50 Isolated Rut Verification in Field (I-95)

Table 6.31 Selected Homogeneous Segmentation Results (SR037)

Record #	Start MP (ft.)	End MP (ft.)	Length (ft.)	Mean Rut Depth (1/8 in.)	Std (1/8 in.)
1	0	215	215	1.8	0.4
2	216	235	19	2.9	0.4
3	236	259	23	3.9	0.6
4	260	415	155	2.4	0.6
5	416	427	11	3.9	0.4
6	428	535	107	2.7	0.5
7	536	557	21	3.9	0.5

The homogeneous segmentation results are shown in Figure 6.53 and in Table 3.31. The MinLen is set to be 10ft. and the MinDiff is set to be 1/8 in., as suggested by GDOT engineers. There are 43 homogeneous segments for the longitudinal rut depth profile on the inside wheelpath. The detailed information about the first seven homogeneous segments, such as the start MP, end MP, mean rut depth, and standard deviation, is listed in Table 3.31.

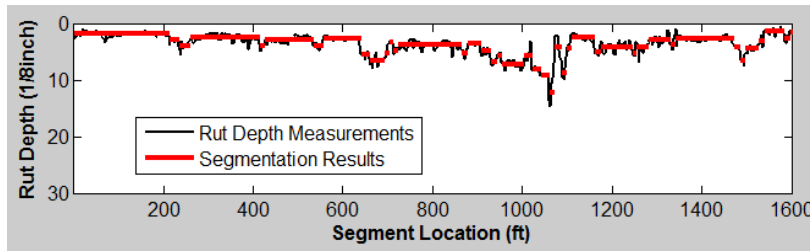


Figure 6.53 Filtered Data (Red) and Homogeneous Segmentation Results (Blue) when MinLen = 10ft. and MinDiff = 1/8 in. (SR 307)

Verification in the Field

The detection results were verified in the field by engineers from GDOT. Figure 6.55 shows the field verification results. Isolated ruts 4 and 6 can be clearly observed in the field since the depth is more than 1/2 in. deep. Some images taken from the field are shown in Figure 6.56. However, it is difficult to locate ruts 1, 2, and 3 in the field. The isolated rut 5 is at the railroad cross-section.

Table 6.32 Isolated Rutting Detection Results (SR307)

ID	Start MP (ft.)	End MP (ft.)	Rut Length (ft.)	Max Rut Depth (1/8 in.)	Rut Volume (ft ³)	Rut Area (ft ²)
1	232	260	28	3.9	3	123
2	414	428	14	3.9	2	69
3	534	558	24	3.9	3	124
4	640	1110	470	12.2	80	2546
5	1160	1284	124	5.2	18	710
6	1470	1542	72	6.6	7	338

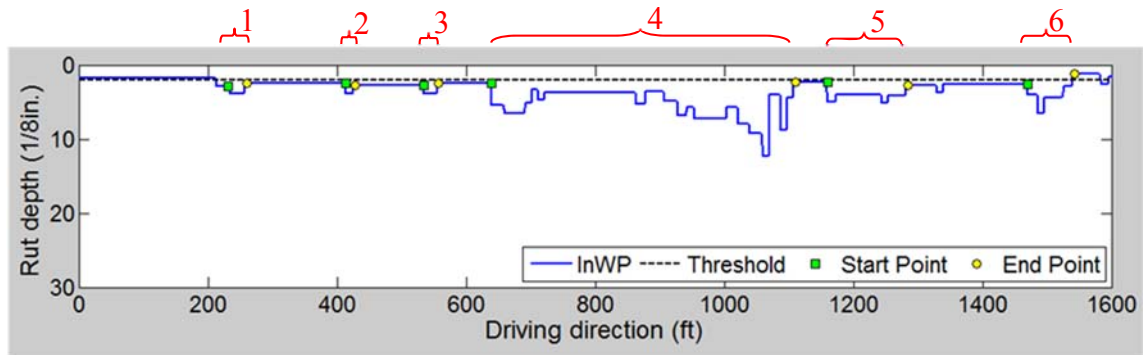


Figure 6.54 Detected Isolated Ruts (SR307)

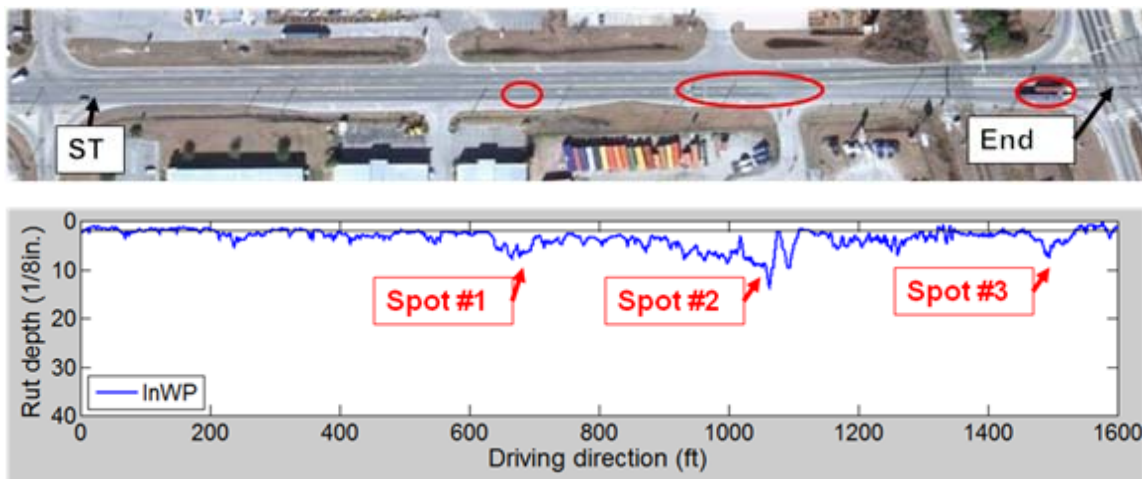


Figure 6.55 Field Verification (SR 307)



Figure 6.56 An Isolated Rut (Spot #2) on SR 307

6.4 Summary

This section has presented another application, detection of isolated rutting. A method was tested to automatically detect isolated rutting using 3D continuous transverse profiles. Besides detecting the isolated rutting, the tested method can also compute the rut termini, maximum rut depth, rut area, and rut volume. A road section from MP 101 to MP 100 on southbound lanes of I-95 was tested. The case study results show that two isolated ruts on the test sites were detected successfully. Additionally, a road section (close to the intersection of SR 307 and SR 21) on SR 307 was tested. Six isolated ruts were detected and verified through field survey. Both case studies demonstrate the feasibility of the tested method.

7. Conclusions

This chapter assessed the rut depth measurement accuracy using emerging 3D laser technology and the feasibility of using the 3D laser for network-level survey and isolated rut detection. The following is a list of the major findings:

- 3D laser has much better rut depth measurement accuracy than manual and rut-bar measurement methods because it has virtually 100% coverage in both transversal and longitudinal (driving) direction. The measurement error is within $\pm 3\text{mm}$ in field and laboratory tests.
- 3D laser was used as the reference to quantify the measurement error of point-based rut bar systems. A comprehensive test has been conducted on multiple sensor configurations. The test results reveal that as the number of sensors increases, the measurement error decreases. The average measurement errors for 3-point and 5-point rut bar systems are about 63% and 44%. With a 39-point equally-spaced rut bar system, the measurement error is about 8%. If

the number of sensors is more than 25, the measurement error drops constantly with a value below 10%.

- A method has been tested to use the advanced 3D laser technology in network-level rutting survey. Case studies on several state-maintained and non-state-maintained routes indicate that the 3D laser system can provide detailed rutting information (e.g. min, max, standard deviation in one mile) besides the mean rut depth and can better support maintenance decision making at the network-level. The 60th percentile rut depth is recommended by engineers as an indicator of the representative rut depth.
- A method has been tested to use the emerging 3D laser technology to detect isolated rutting in support of low-cost, localized treatment. Besides detecting the isolated rutting, the tested method can also compute the rut termini, maximum rut depth, rut area, and rut volume. Case studies demonstrate the feasibility of the tested method.

In the future, the following studies are recommended:

- Parallel processing can be applied to improve the data processing speed. Since the highway network can be broken down into smaller segments, and those segments can be processed independently; parallel processing may be conveniently applied to improve the data processing speed.
- The profile-level data processing needs to be enhanced. Although the current rutting measurement algorithm works well, it has the difficulty to handle the cases like wide transverse cracking, potholes, and rail tracks well. Methods need to be developed to enhance the profile-level data processing and improve the rut depth calculation accuracy.
- A customized application needs to be developed to fit into current network-level data collection practices. The current 3D laser is not application-oriented. It cannot be directly used to fit in with an existing pavement management system. A customization is needed for different transportation agencies' practices.
- A customized application and automatic algorithms need to be developed for isolated rut detection. The detected results can then be added to a PMS database to support localized treatment decision making.

References

- AASHTO. (2010). *AASHTO PP69-10: Standard Practice for Determining Pavement Deformation Parameters and Cross Slope from Collected Transverse Profiles*. American Association of State Highway and Transportation Officials (AASHTO), Washington, D.C.
- ADOT. (2002). *Terms of Reference, Pavement Rut Depth, Roughness, GPS, Calibration, and Verification Sites*, Alberta Department of Transportation, Edmonton, Alberta, Canada.
- ASTM. (2010). *ASTM E1703/E1703M: Standard Test Method for Measuring Rut-Depth of Pavement Surfaces Using a Straightedge*, American Society for Testing and Materials (ASTM), Philadelphia, PA.
- Austrroads. (2007). *AG:AM/T010: Validation of a Multi-Laser Profilometer for Measuring Pavement Rutting (Reference Device Method)*. Austrroads.
- Cenek, P., Patrick, J., McGuire, J., and Robertson, D. (1994). "New Zealand Experience in Comparing Manual and Automatic Pavement Condition Rating Systems." *Proc. of Third International Conference on Managing Pavements*, San Antonio: Transportation Research Board.
- FHWA. (2003). *Distress Identification Manual for the Long-Term Pavement Performance Program*, Federal Highway Administration (FHWA).
- Friedman, J. (1991). "Multivariate Adaptive Regression Splines." *The Annals of Statistics*, 19(1), 1–67.
- Grondin, M., Leroux, D., and Laurent, J. (2002). "Advanced 3D Technology for Rut Measurements: Apparatus on Board of the Quebec Ministry of Transportation Multifunction Vehicle." <http://pms.nevadadot.com/2002presentations/40.pdf>.
- Hallett, J. and Robieson, P. (1996). "Trial of High Speed Data Collection Vehicle: 1996 Validation Report." Beca Carter Hollings & Ferner Ltd., Auckland.

- Hossain, K. V. M., Reigle, J., and Miller, R. (2002). "Comparison of 3-point and 5-point Rut Depth Data Analysis." *Pavement Evaluation 2002 Conference*, Roanoke, Virginia.
- HTC. (2001). "Validation of ROMDAS transverse profile logger." *Internal Report F003/1*, HTC Infrastructure Management Ltd, Auckland.
- Jameson, G.W., Baran, E., and Sheldon, G.W. (1989). "Australian Experience with the Swedish Laser Road Surface Tester." *14th ARRB Conference*. Vermont South, Victoria, Australia.
- Kamplade, J. (1990). "Analysis of Transverse Unevenness with Respect to Traffic Safety." *Surface Characteristics of roadways: International research and technologies*. W. E. Meyer and J.Reichert, eds., American Society for Testing and Materials (ASTM), Philadelphia, PA, 198-210.
- Ksaibati, K. (1996). "Comparison of Rut-Depth Measurements Obtained with Four Different Techniques." *Road and Transport Research*, 5(2), 80-91.
- Laurent, J., M. Talbot, and M. Doucet. (1997). "Road Surface Inspection Using Laser Scanners Adapted for the High Precision 3D Measurements of Large Flat Surfaces." *IEEE Proceedings of the International Conference on Recent Advances in 3-D Digital Imaging and Modeling*, 303-310.
- LCMS Data Processing Library: User Manual (Rev 1.3)*. INO, Pavemetrics Systems inc., Quebec City, Quebec, Canada, 2010, 15.
- Li, Q., M. Yao, X. Yao, W. Yu, and B. Xu. (2009) "A Real-time 3D Scanning System for Pavement Rutting and Pothole Detections." *Proc., Videometrics, Range Imaging, and Applications X, SPIE*, 74470B-74479.
- Li, Q., M. Yao, X. Yao, and B. Xu. (2010). "A Real-time 3D Scanning System for Pavement Distortion Inspection." *Measurement Science and Technology*, 21(1), 015702.
- Mallela, R., and Wang, H. (2006). "Harmonising Automated Rut Depth Measurements - Stage 2." *Land Transport New Zealand Research Report 277*, Data Collection Ltd..

- McGhee, K. (2004). "Automated Pavement Distress Collection Techniques: A Synthesis of Highway Practice." *NCHRP Synthesis 334*, Transportation Research Board, Washington, D.C.
- ODOT . (2010). *Oregon Department of Transportation - Distress Survey Manual*.
http://www.oregon.gov/ODOT/HWY/CONSTRUCTION/docs/pavement/Distress_Survey_Manual.pdf?ga=t Accessed Nov. 07, 2010.
- PennDOT. (2010). *Automated Pavement Condition Survey Field Manual*. Pennsylvania Department of Transportation.
- Simpson, A. (2001). *Measurement of Rutting in Asphalt Pavements*, In Civil Engineering. PhD Thesis, University of Texas at Austin, Austin, TX.
- Simpson, A. (2001). "Characterization of Transverse Profile." *FHWA-RD-01-024*. FHWA, U.S. Department of Transportation.
- Start, M., J. Kim, and W. Berg. (1998). "Potential Safety Cost-Effectiveness of Treating Rutted Pavements." *Transportation Research Record: Journal of the Transportation Research Board*, No. 1629, Transportation Research Board of the National Academies, Washington, D.C., 208-213.
- Wang, H. (2005). *Development of Laser System to Measure Pavement Rutting*. Department of Civil and Environmental Engineering. Tampa, FL, University of South Florida. Master Thesis.
- White, T. D., Haddock, J. E., Hand, A. J. T., and Fang, H. (2002). "Contributions of Pavement Structural Layers to Rutting of Hot Mix Asphalt Pavements", *NCHRP Report 468*, Transportation Research Board, Washington, D.C.

Chapter 7 A Buffered Distance Method for Quantitatively Evaluating Performance of Crack Detection Algorithms

1. Introduction

Automatic pavement distress detection and classification has gained great attention among transportation agencies in the U.S. because current manual pavement condition evaluation is subjective, time-consuming, costly, and unsafe due to the exposure to roadway hazards. Many transportation agencies, including the Texas Department of Transportation (TXDOT), the Florida Department of Transportation (FDOT), the Utah Department of Transportation (UDOT), and the Georgia Department of Transportation (GDOT), have invested resources to find ways to automate their pavement condition evaluation, including pavement distress detection and classification. Segmentation algorithms are the crucial step for automatic pavement distress detection and classification. Image segmentation is the process of differentiating the pavement image pixels containing cracks from the pixels without cracks and then segmenting the pavement image into crack and non-crack pixels. An effective segmentation algorithm is essential for developing a reliable, automatic pavement distress detection and recognition system that performs effectively in different pavement image conditions. Further, the Transportation Research Board Pavement Management Systems Committee (AFD10, 2007) identified a need for establishing fundamental pavement distress elements using automatic image processing, and that need can be addressed by a robust segmentation algorithm. A robust segmentation algorithm that accurately differentiates pavement distress pixels from the pavement pixels without distress can help establish fundamental distress elements that can be standardized and compared among different transportation agencies. These segmented distress elements can be easily classified into the distress types according to the definition of a particular transportation agency. Many image segmentation algorithms have been developed in the past decade, but there is no good method to quantitatively evaluate the performance of these segmentation algorithms. Qualitative assessment of image segmentation results by engineers is time-consuming and inefficient; consequently, there is a critical need to develop an objective and quantitative evaluation criterion that accurately reflects the assessment of a trained visual inspector. This will help the research community focus on the development of better and faster algorithms. We address this issue by

surveying different quantification methods and developing a new, novel quantification method that accurately reflects the assessment of trained engineers.

Nazef et al. (2006) conducted a qualitative evaluation of pavement distress detection algorithms under different lighting conditions, but the performance of segmentation algorithms was not analyzed quantitatively. Others, like Koutsopoulos (1993), Wang (2007a), and Wang (2007b), did a comparison of segmentation algorithms to show the superiority of their particular algorithms, but the evaluations are, again, qualitative. Huang (2006) and Zhou (2006) measured the performance of their algorithms by devising a scoring criterion based on statistical correlation. Mean square error is another metric that is extensively used in image comparison studies. Another metric, called the Mahalanobis distance (Gonzalez and Woods, 2002), has also been described in literature. All the above evaluation methods use the entire image data for image comparison and do not target the crack regions specifically. This can obscure the results because crack pixels are typically only a small percentage of the total number of image pixels, and these scoring measures are not specifically sensitive to crack information. In addition, information about crack locations is not used in these evaluation methods. This may lead to the erroneous conclusion that two segmented crack images having different crack locations are the same simply because they have the same number of crack pixels in an image. Different quantification methods are also used in medical imaging and machine vision. They are briefly discussed to evaluate the possibility of applying them to pavement images. These methods include Receiver Operator Characteristic (ROC) (Tagashira et al., 2008; Song et al., 2007; and Kerekes, 2008) and Hausdorff distance (Beauchemin et al., 1998; Wang, 2002). Hausdorff distance enables the user to measure the distance between objects of different sizes. This can be helpful in the case of cracks, as the number of crack pixels in the ground truth image can be different from the crack pixels in the segmented images. A new quantification method based on buffered Hausdorff distance metric is proposed. The buffered distance metric incorporates the merits of both mean square error and Hausdorff distance metric. The proposed method is compared with four other possible quantification methods (mean square error, statistical correlation, Receiving Operating Characteristic, and Hausdorff distance) to demonstrate its superior capability to distinguish the performance of different segmentation algorithms.

2. A Quantitative Performance Evaluation Method

This section presents the proposed quantification method that is based on buffered Hausdorff distance. Four other quantification methods are also briefly introduced in this section. The scores of different quantification methods are normalized to a common scale of 0 to 100 to facilitate our evaluation. Zero and one hundred represent the worst and the best performance possible for an algorithm, respectively, according to this scoring criterion. The proposed quantification method is presented below.

2.1 A Proposed Method Using Buffered Hausdorff Distance

The proposed buffered distance method incorporates the strengths of both mean square error and Hausdorff distance by modifying the Hausdorff distance metric. The Hausdorff distance is among the most popular distance measures that measures the distance between two curves and is a metric. It has been extensively used in literature (Beauchemin et al., 1998; Wang, 2002). For any two sets of points $A = a_1, a_2, \dots, a_n$ and $B = b_1, b_2, \dots, b_m$,

$$H(A, B) = \max(h(A, B), h(B, A)) \quad (7.1)$$

Where

$$h(A, B) = \max_{a \in A} \min_{b \in B} \|a - b\| \quad (7.2)$$

$h(A, B)$ is the greatest of all the small distances from points of A to B and $h(B, A)$ is the greatest of all the small distances from points of B to A. Figure 7.1 illustrates this distance measurement effectively.

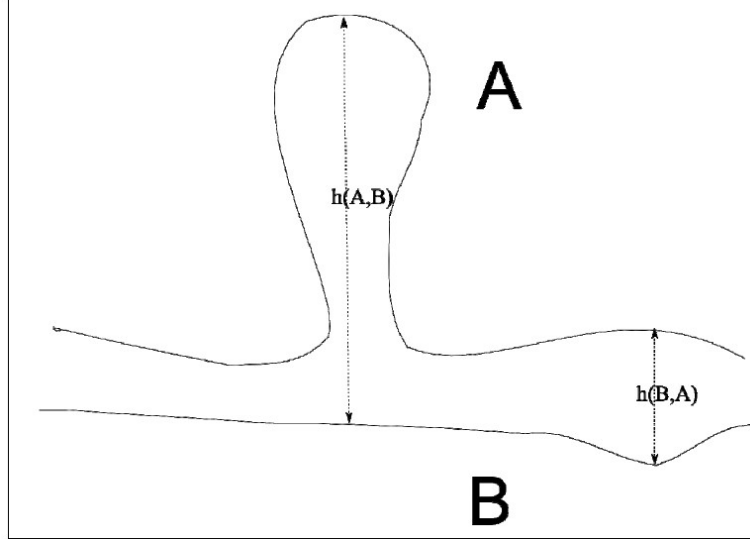


Figure 7.1 Illustration of Hausdorff Distance

The value of Hausdorff distance is large, even if one crack pixel in the segmented image is far from ground truth image crack pixels. Seeing this as a limitation of the Hausdorff distance metric, a new metric was developed that does not suffer from the shortcoming of the Hausdorff distance. The intuitive development of this measure is described next. A better distance measure than the Hausdorff distance is the modified Hausdorff distance given by $MH(A, B)$:

$$MH(A, B) = \max(h_1(A, B), h_1(B, A)) \quad (7.3)$$

Where

$$h_1(A, B) = \frac{1}{m} \sum_{a \in A} \min_{b \in B} \|a - b\| \quad (7.4)$$

Once a crack pixel in the automatically segmented image falls substantially away from the closest pixel in the ground truth image, it no longer makes sense to heavily penalize this distance. Wrong detections beyond a certain distance should be penalized equally. This leads to a new distance measure, the buffered Hausdorff distance measure given by $BH(A, B)$.

$$BH(A, B) = \max(h_2(A, B), h_2(B, A)) \quad (7.5)$$

Where

$$h_2(A, B) = \frac{1}{m} \sum_{a \in A} \underset{L}{sat} \min_{b \in B} \|a - b\| \quad (7.6)$$

Here, $\underset{L}{sat}$ indicates that when the distance of the crack pixel to the closest crack pixel in the other image exceeds a saturation value L , we use a constant value of L for the distance. The pseudo-code of the modified algorithm is given in Figure 7.3. The buffer L was chosen to be 20 for our experiments. Figure 7.2 illustrates the buffered distance measure. The sample values of the buffered distance have a very intuitive meaning, too. The buffered distance can be interpreted as the average Euclidean distance between the crack pixels in the ground truth image and the segmented images. To compare other scoring methods with this buffered distance, a scaled scoring measure was derived and is shown below:

$$\text{Buffered distance score} = 100 - \frac{BH(A, B)}{L} \times 100 \quad (7.7)$$

The buffered distance effectively measures the performance of the segmentation methods and generates a score that corresponds with the qualitative performance of the particular method. In order to establish the merits of the buffered scoring distance, four other scoring measures were used in our experiments. Among the scoring measures, the buffered distance gives the best performance, as will be clear from the results.

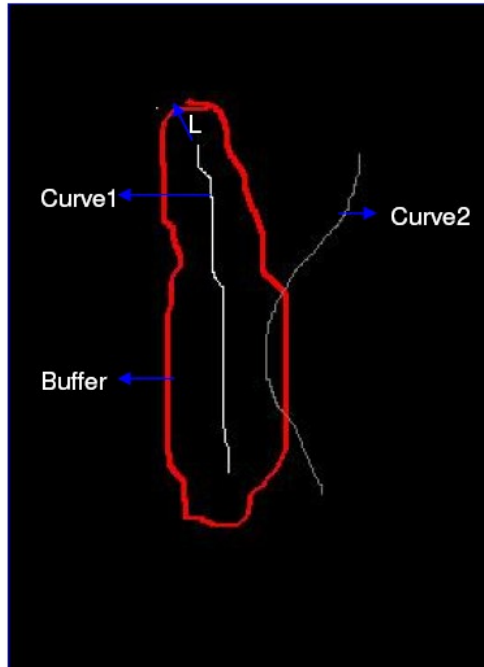


Figure 7.2 Illustration of Buffered Hausdorff Distance Measure

```

for(i=1:S)
Mindist = || (min_{j=1toN} P1(ith row) - M1(jth row)) ||
If Mindist > L
Mindist = L
end
Distance1 = Distance1 + Mindist
end
h(M1,P1) = Distance1/S
for(i=1:N)
Mindist = || (min_{j=1toS} M1(ith row) - P1(jth row)) ||
If Mindist > L
Mindist = L
end
Distance2 = Distance2 + Mindist
end
h(P1,M1) = Distance2/N
MH(M1,P1) = max(h(P1,M1),h(M1,P1))

```

Figure 7.3 Algorithm for Buffered Hausdorff Distance Measure

2.2 Other Method Used for Comparison

To compare the performance of the proposed scoring method, four other scoring methods were used: Mean Square Error, Statistical Correlation, Receiver Operator Characteristic, and Hausdorff distance. These scoring methods are described briefly below.

2.2.1 Mean Square Error Method

Mean Square Error (MSE) is one of the most commonly used performance metrics in the image processing literature, especially in image compression. MSE is the cumulative squared error between the two images, indicated by $I1$ and $I2$, respectively.

$$MSE(I1, I2) = \frac{1}{MN} \sum_{y=1}^M \sum_{x=1}^N [I1(x, y) - I2(x, y)]^2 \quad (7.8)$$

Here, M and N are row and column lengths of the images, respectively, and (x, y) indicate the coordinates of the pixel location in the image. In order to compare MSE performance with other scoring measures, a scaled scoring measure that gives values between 0 and 100 is devised. As segmented images are binary images; the error for each pixel is either 1 or 0. Considering that cracks comprise a small portion of an image, we analyzed 150 different pavement images to compute the maximum crack pixels as a percentage of total pixels. Observations showed that this percentage never exceeded 5%; hence, more than 5% error between two images was considered the worst segmentation performance. Using this fact, a reasonable, scaled scoring measure based on the MSE was derived and is given by the following equation:

$$MSE \text{ score} = 100 - \frac{1}{0.05} MSE(I1, I2) \times 100 \quad (7.9)$$

2.2.2 Statistical Correlation Method

Statistical correlation is another measure used to evaluate performance in the existing literature. It is given by the correlation coefficient between two images.

$$Corr(I1, I2) = \frac{Cov(I1, I2)}{\sqrt{VarI1} \sqrt{VarI2}} \quad (7.10)$$

Where $Cov(I1, I2)$ is the covariance between the two images, and $VarI1$, $VarI2$ are the variances of the two images. As the correlation lies between -1 and 1, the scoring measure for correlation is derived using this information.

$$\text{Corr score} = \frac{\text{Corr}(I1, I2) + 1}{2} \times 100 \quad (7.11)$$

2.2.3 Receiver Operator Characteristic Method

The Receiver Operator Characteristic (ROC) is a highly effective tool for image classification evaluation, and it has been extensively used in medical literature and machine learning (Tagashira et al., 2008; Song et al., 2007; and Kerekes, 2008). In the development of dynamic optimization algorithm (Alekseychuk, 2006), it was used to evaluate the performance of the segmentation algorithm. The ROC represents the dependence of the rate of correct detections and the rate of false detections. The correct detection (CD) rate is defined as the ratio between the number of areas or pixels correctly labeled as defective $N_{detected}$ to the number of truly defective areas N_{true} on the image:

$$CD = \frac{N_{detected}}{N_{true}} \quad (7.12)$$

The false alarm (FA) rate is defined as the ratio between the number of false detection N_{false} to the number of truly defective-free areas $(N_{all} - N_{true})$ (where N_{all} is the total number of areas on the image):

$$FA = \frac{N_{false}}{N_{all} - N_{true}} \quad (7.13)$$

The ROC value is defined based on the ratio between FA and CD:

$$ROC = \frac{FA}{CD} \quad (7.14)$$

For our experiments, correctly detected pixels in the segmented image needed to lie within a square of a 5-pixel width centered on a true crack pixel in the ground truth image. A scoring

measure based on ROC was derived for comparison purposes by taking the maximum value of the ROC to be 0.1. A ROC value above 0.1 would indicate an extremely poorly segmented image, which is not useful for further investigation.

$$\text{ROC score} = 100 - \frac{\text{ROC}}{0.1} \times 100 \quad (7.15)$$

1.1.1.1 2.2.4 Hausdorff Distance Method

The Hausdorff distance $H(A,B)$ between two sets A and B was described in Section 2.1. Using the width of the ground truth image as a scaling factor, a scoring measure for the Hausdorff distance was calculated.

$$\text{Hausdorff score} = 100 - \frac{H(A,B)}{\text{column width}} \times 100 \quad (7.16)$$

3. Experimental Test

3.1 Buffered Hausdorff Distance Over Four Other Quantification Methods

For comparing the capability of the proposed quantification method to other methods, both real data and synthetic data simulating different pavement distress conditions were used. For the actual pavement distress images, GDOT pavement engineers visually marked the cracks (their actual locations) to establish the ground truth. Synthetic images were generated to demonstrate the comparative strength of the buffered distance method over other quantitative scoring methods. Figure 7.4 gives an overview of the experimental data presented in this section.

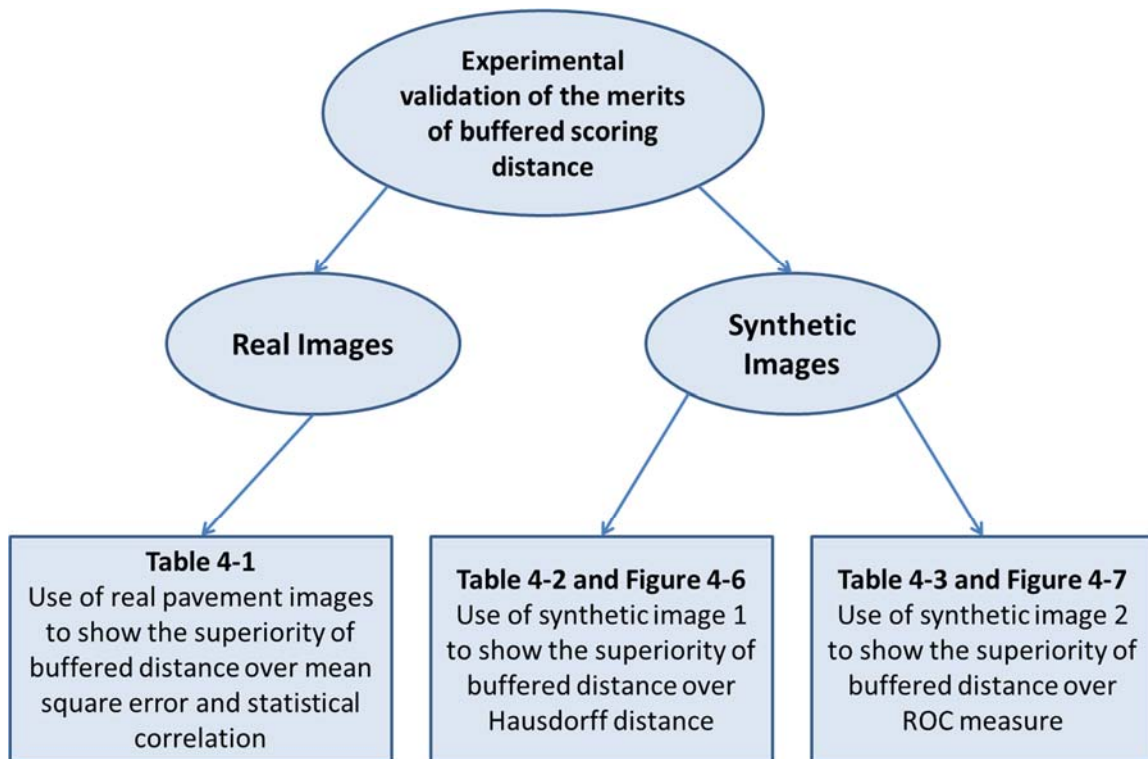


Figure 7.4 Overview of Experimental Tests

Four segmentation algorithms were used to evaluate the capability of different quantification methods for being able to separate the performance of different segmentation methods. These segmentation algorithms include Canny edge detection (Canny, 1986), crack seed verification (Huang & Xu, 2006), the iterated clipping method (Oh et al., 1997), and the dynamic optimization method (Alekseychuk, 2006). Although a large data set of 100 images has been analyzed in our experiments, here we present the results the four segmentation methods on 5 GDOT images. The results obtained from these segmentation algorithms were visually inspected by trained GDOT pavement engineers to assess the comparative performance of the four algorithms. This known performance for each segmentation algorithm was then used to evaluate the capability of different quantification methods. For example, the engineers and authors observed that the dynamic optimization based method gives substantially better performance than the other methods, qualitatively, for all the test images (Tsai et al., 2009). The underlined mean square error score and correlation score values in

Table 7.1 indicate that the dynamic optimization based method is not the best method for some images. Consequently, the results of these two scoring measures do not match the assessment of GDOT engineers. It is also found that the buffered distance score, ROC score, and Hausdorff distance score are consistent with the visual assessment, but the buffered distance score achieves the best score separation to distinguish the performance of different algorithms.

Figure 7.5 uses Image 4 from the five images in Table 7.1 as an example to illustrate the performance of the proposed method. Based on the scoring measurement, we can see that the crack detection performances of the four algorithms are in the following order: (c) dynamic optimization, (f) iterated clipping, (d) Canny edge detection, and (e) crack seed verification. This is consistent with the visual inspection results.

Two synthetic image data sets were generated for illustrating the better performance of buffered distance compared to Hausdorff distance and ROC, and to demonstrate a better score separation achieved by our proposed method. The first synthetic ground truth image, which is shown in Figure 7.6(b), was generated by marking isolated noise pixels, which are located far from the crack pixels, on top of a GDOT ground truth image, as shown in Figure 7.6(a). This synthetic ground truth image was compared to four test images generated by applying the four segmentation algorithms to the raw pavement image. Results in Table 7.2 and images in Figure 7.6 clearly show that though *Test Image1* has the best performance, the Hausdorff distance score and the mean square error actually list it as the worst-performing image. The problem is that Hausdorff distance is very sensitive to isolated noise outliers and does not reflect the overall performance of the segmentation method. The buffered distance measure accurately reflects the performance of test images and also achieves good score separation to distinguish their performance behavior.

Table 7.1 Scoring Measures for GDOT Images

Image	Dynamic Optimization	Canny Edge Detection	Seed Verification	Iterated Clipping
Image 1				
Mean Square Error	<u>95.9941</u>	95.1833	95.4276	96.6716
Correlation	60.3986	49.8636	55.8749	58.7725
ROC measure	99.6927	0	99.614	95.9945
Hausdorff distance	97.6623	80.9665	39.3898	50.9328
Buffered distance	91.6468	24.4089	72.4155	38.8489
Image 2				
Mean Square Error	96.8028	96.1628	96.1355	96.6451
Correlation	61.1738	49.8589	0	54.5732
ROC measure	99.8143	0	0	92.5772
Hausdorff distance	98.1278	41.0895	0	54.9892
Buffered distance	92.7174	15.0362	0	22.2454
Image 3				
Mean Square Error	95.6805	95.0156	95.0714	95.9808
Correlation	<u>58.551</u>	49.846	54.24	59.6205
ROC measure	99.5189	0	99.716	98.4453
Hausdorff distance	96.9521	41.9934	55.3874	42.2313
Buffered distance	91.8955	14.0205	17.5782	66.1937
Image 4				
Mean Square Error	<u>95.5108</u>	94.7141	94.6804	95.5614
Correlation	59.6935	49.9575	50.8001	58.3103
ROC measure	99.6954	2.2489	99.7577	98.2338
Hausdorff distance	98.0013	41.3101	0	40.6776
Buffered distance	92.4423	14.9668	3.1376	64.0048
Image 5				
Mean Square Error	95.4859	94.4584	94.5122	94.5391
Correlation	61.5723	49.9428	53.6835	52.1224
ROC measure	99.7451	0	99.7203	91.3818
Hausdorff distance	97.432	49.3804	31.0443	50.6515
Buffered distance	93.0536	16.1591	19.1754	24.4211

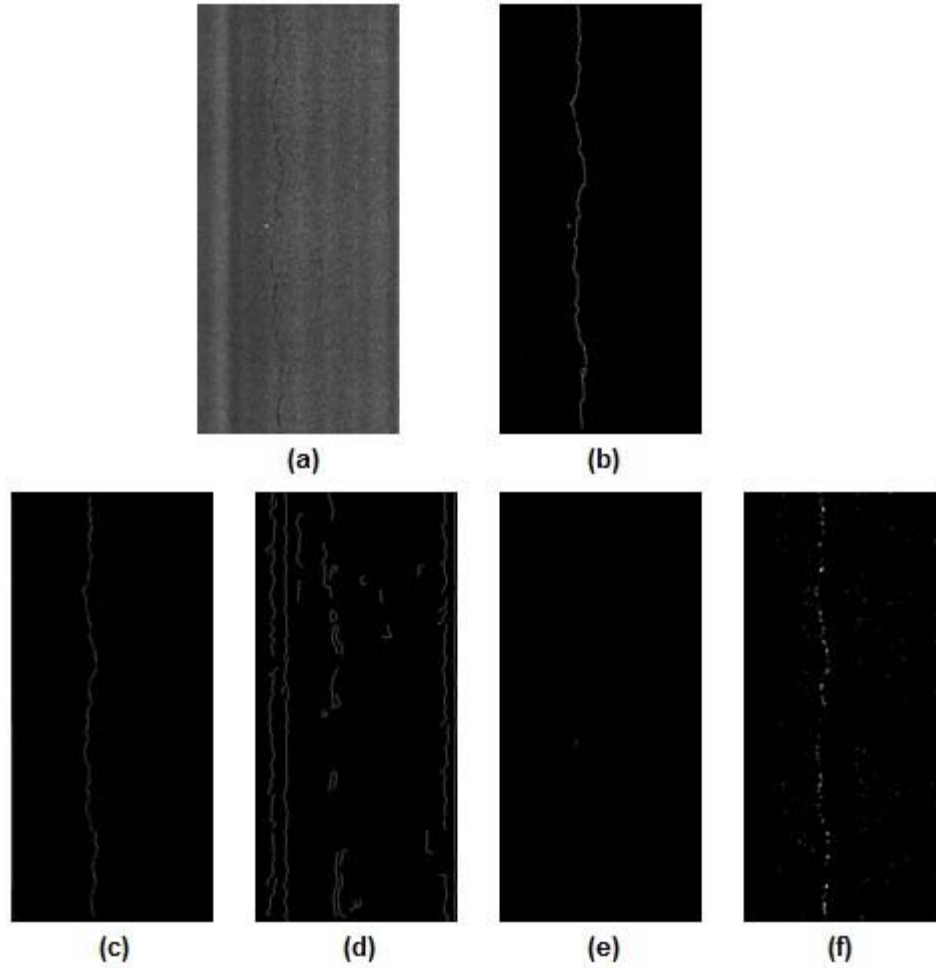


Figure 7.5 (a) Original Image; (b) Ground Truth Crack Map; (c) Dynamic Optimization Results (Score: 92.4423); (d) Canny Edge Detection Results (Score: 14.9668); (e) Crack Seed Verification Results (Score: 3.1376); (f) Iterated Clipping Results (Score: 64.0048)

Table 7.2 Scoring Measures for Synthetic Image 1

	Test Image 1	Test Image 2	Test Image 3	Test Image 4
Mean Square Error	95.2962	94.6596	95.4198	94.8768
Correlation	58.7137	50.0709	56.244	54.9956
ROC measure	99.5161	36.5221	95.5748	98.683
Hausdorff distance	44.7479	64.2952	69.6907	66.9031
Buffered distance	80.9604	22.6031	57.0306	64.022

The second synthetic ground truth image is illustrated in Figure 7.7. This synthetic image has a straight line that runs through the middle of the image. The *Test Images 1, 2, and 3* are

horizontal translations of the ground truth image by 1, 2, and 3 pixels, respectively. Table 7.3 shows the scoring measure results for the 3 images. It is seen that the ROC measure allots the same score of 100, reflecting the best performance, to both *Test Image 1* and *Test Image 2* and a score of 0, reflecting the worst performance, to *Test Image 3*. This observation illustrates that ROC can show very different score value for two similar images. When the horizontal translation exceeds 2 pixels, then all crack pixels in the test image are classified as incorrectly detected. This problem happens around the boundary points where the classification decision changes from true detection to false detection. The buffered distance score still accurately reflects the performance of the test images, as it is not based on a hard decision rule like ROC. The combined results indicate that the buffered distance score is better than the other four scoring methods used in experiments.

Table 7.3 Scoring Measures for Synthetic Image 2

	Test Image 1	Test Image 2	Test Image 3
ROC Measure	100	100	0
Buffered Distance	95	90	85

Based on the results, we examined the strength and weaknesses of each scoring method. Mean Square Error (MSE) takes into account error in the whole image and not just the error in location of crack pixels. Moreover, in its computation, MSE does not take into account the relative proximity of the crack pixels in the ground truth image to the crack pixels in the segmented image. Unless there is an exact overlap between the crack pixels in the ground truth image and the segmented image, the MSE score will be the same for the two, different, automatically segmented images. In other words, the MSE score stays the same irrespective of the relative proximity of the crack pixels in the automatically segmented image to the cracks in the ground truth image. This exact overlap is highly unlikely, considering that marking the ground truth image to such a degree of accuracy can be a tedious exercise. MSE can only be used on images of similar size and cannot selectively focus on the crack pixels in the image. Thus, it is not very useful for comparison of pavement segmentation algorithms. Like MSE, the correlation coefficient also requires exact overlap between crack pixels of the two compared images to get a high performance evaluation score. This coefficient also suffers from the

limitation that it can be applied only to similarly sized objects. Therefore, the non-crack pixels, which are larger in extent in all pavements, affect the correlation severely. Results of ROC are better compared to MSE and correlation scoring measure, but it is seen through results of the second synthetic image data set that qualitatively very similar segmented images can have very different ROC values. This happens due to the fact that ROC uses hard decision rules to classify pixels as false alarms or true defects. Hence, on the boundary of these decision rules, the ROC value can change abruptly, and very similar segmented images can have drastically different ROC values. The Hausdorff distance has the ability to measure the distance between only crack pixels in both the ground truth and segmented image, and, therefore, it can capture the local effectiveness of the segmentation algorithm. However, it is very sensitive to outliers or noise pixels, and Hausdorff score values change drastically even in the presence of one outlier. The buffered distance measure captures the local effectiveness of the segmentation algorithm and is not sensitive to outliers or noise pixels. It also achieves good score separation in the values for different segmentation algorithms, and it is the best of all the methods. The shortcoming of the method is that the buffer value L needs to be chosen heuristically.

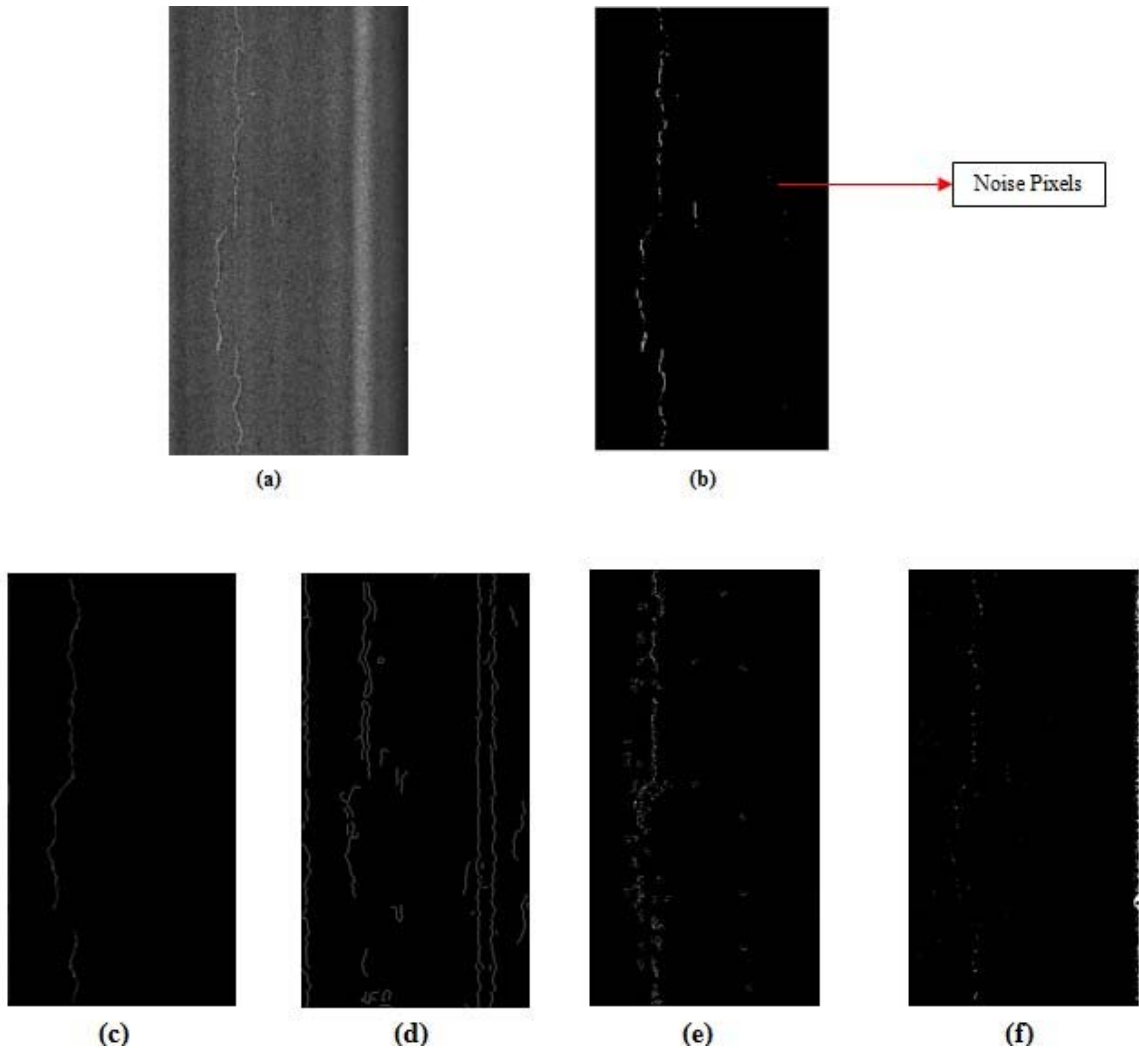


Figure 7.6 (a) Original Ground Truth Image (b) Synthetic Ground Truth Image with added noise (c) Test Image 1 (d) Test Image 2 (e) Test Image 3 (f) Test Image 4

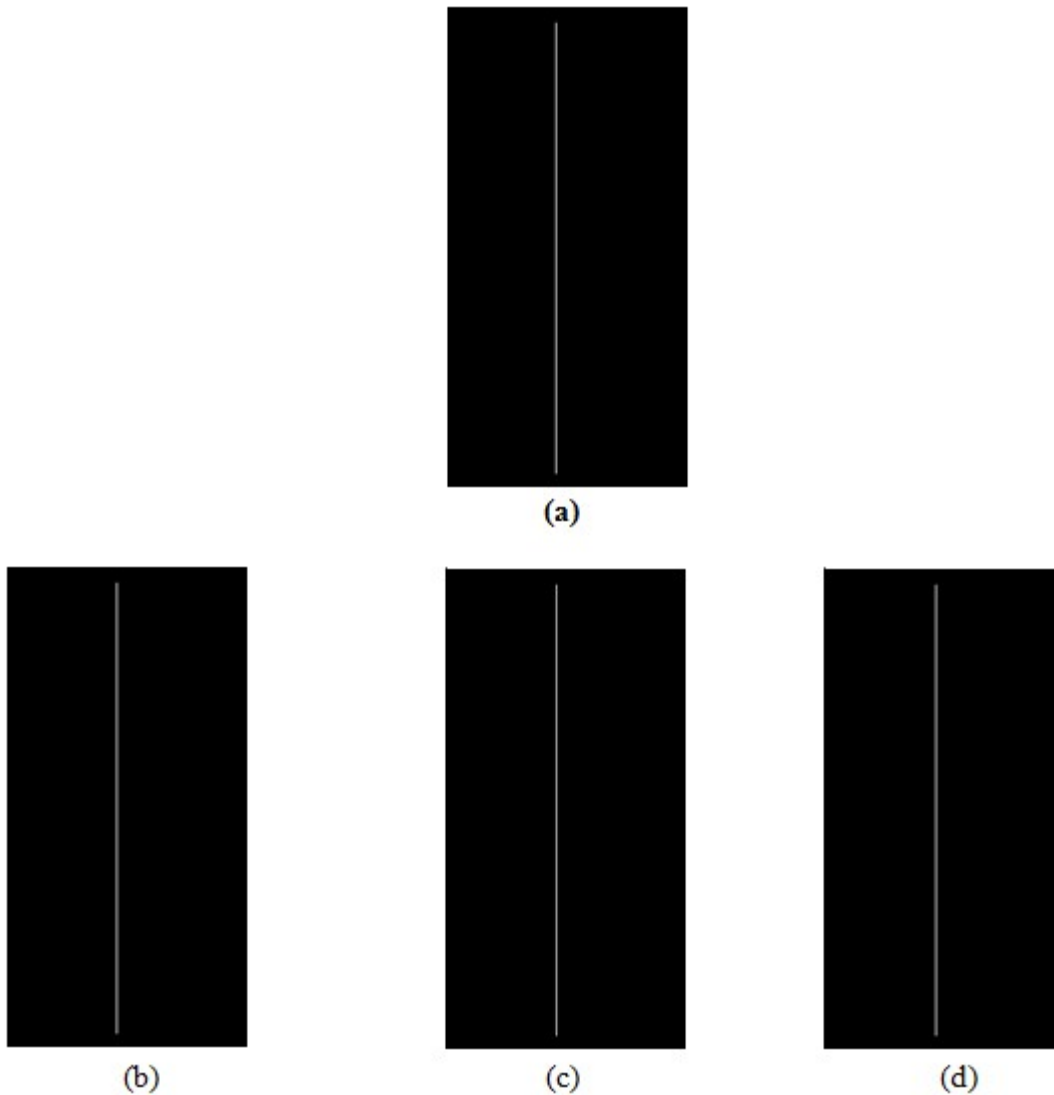


Figure 7.7 (a) Synthetic Ground Truth Image (b) Test Image 1 (Translation=1 Pixel) (c) Test Image 2(Translation=2 Pixels) (d) Test Image 3 (Translation= 3 Pixels)

3.2 Buffer Size Selection

The buffered Hausdorff distance method highly depends on a proper selection of the buffer size. The buffer size will influence the score provided by the method. On one hand, the introduction of a buffer to Hausdorff distance improves the method's robustness for isolated noises; on the other hand, an improper selection of buffer size will reduce the effectiveness of the algorithm.

Figure 7.8 shows a pavement 3D laser data collected on Highway 80, and the image on the left is the raw range data. The images on the middle and right are ground truth cracks map-based on range data and crack detection results using the dynamic optimization method.

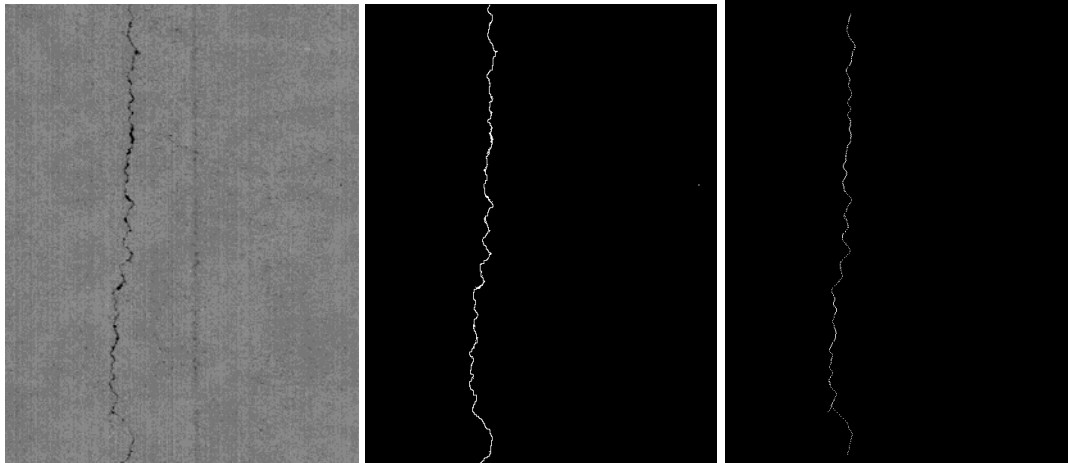


Figure 7.8 Range Image (Left), Ground Truth Image (Middle), and Dynamic Optimization Detection Result (Right) for Image Collected on Hwy80

3.3 Data Resolution

The 3D-line-laser-provided crack detection algorithm was used to test images collected on SR 275. Figure 7.9 shows the binary detection result image and the ground truth image. At the beginning, we used 1mm resolution image, i.e. 4160×5000 , to establish the ground truth and detected results; however, as shown in Table 7.4, the resulting scores are very low. One possible explanation is that the resolution is too high that any tiny difference between the two images can enlarge the error and, therefore, lower the score. So, we resized the two images to 1040×1250 and ran the test again. The results using resized images, as shown in the right columns in both tables below, gave better scores than the originally sized images. Similar results can also be found in the other test on another image collected on SR 275, as shown in Figure 7.10 and Table 7.5.

Again, the key point to utilizing the buffered Hausdorff distance as an effective performance evaluation tool is to choose the proper buffer size that fits best with the objective data set. Based on our preliminary test results, the buffer size of 20 pixels works well for the images with a resolution of about 1,000 pixels.

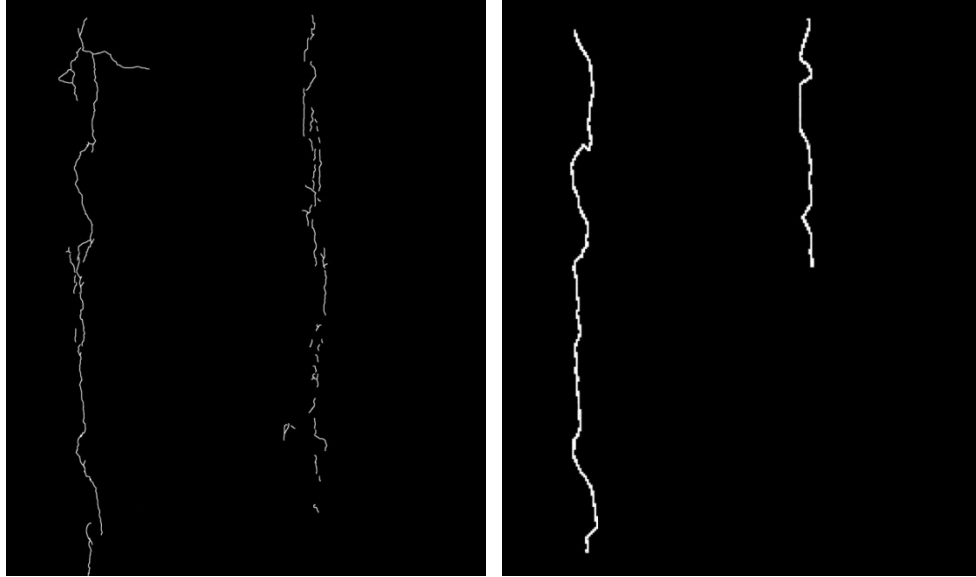


Figure 7.9 Ground Truth Image (Left) and Detection Result Image (Right) for Data Collected on SR275

Table 7.4 Detection Evaluation Results for Figure 7.9 Using Buffer Hausdorff Distance Measure

	Original (4160 x 5000)	Resized (1040 x 1250)
L=10	18.4891	65.0478
L=20	18.8395	69.4417
L=30	19.3536	71.8727
L=50	20.5791	75.4049
L=100	22.5010	80.3330

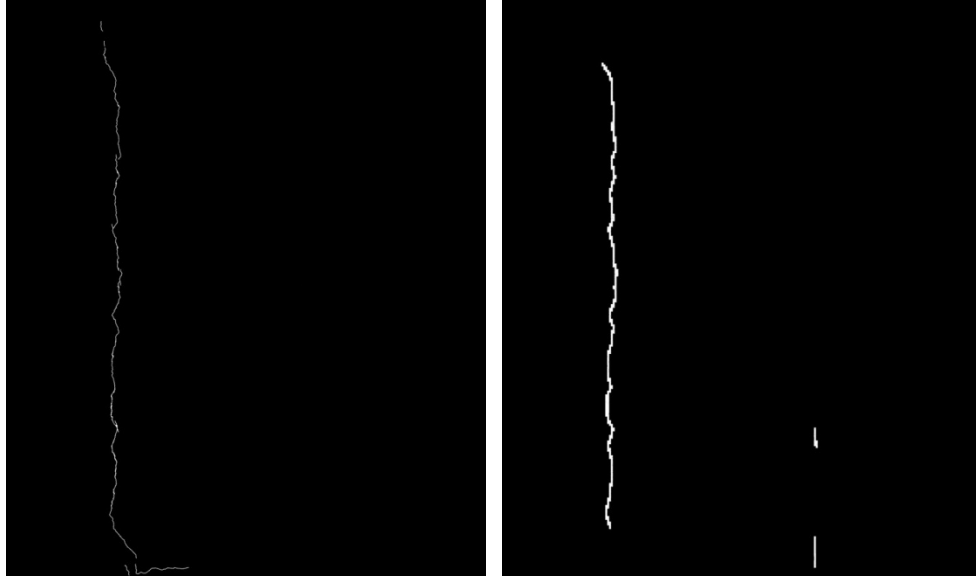


Figure 7.10 Ground Truth Image (Left) and Detection Result Image (Right) for Data Collected On SR275

Table 7.5 Detection Evaluation Results for Figure 7.10 Using Buffer Hausdorff Distance Measure

	Original (4160 x 5000)	Resized (1040 x 1250)
L=10	26.7066	57.8695
L=20	26.9237	74.5179
L=30	27.0371	80.1636
L=50	27.2028	84.6801
L=100	27.5346	88.0676

3.4 Crack Width Consideration

Similar to most of the other performance evaluation methods, the proposed buffered Hausdorff distance method will overlook the width information during its evaluation procedure. A synthetic image is generated to demonstrate this issue.

As shown in Figure 7.11, the synthetic ground truth image on the left contains four simple straight line cracks, and these cracks have incremental widths. It is noticed from the detection results on the right that dynamic optimization can detect cracks in various shapes pretty well, yet the width information of a crack cannot be presented. This should be treated as a detection issue. However, when the proposed buffered method is employed to evaluate this result, it overlooks this issue and still gives a relative good score (over 85 at the buffer size of 20 pixels) for the

detection performance. Therefore, the proposed method does not have a good differentiation for crack width. This will be further studied and improved in future research.

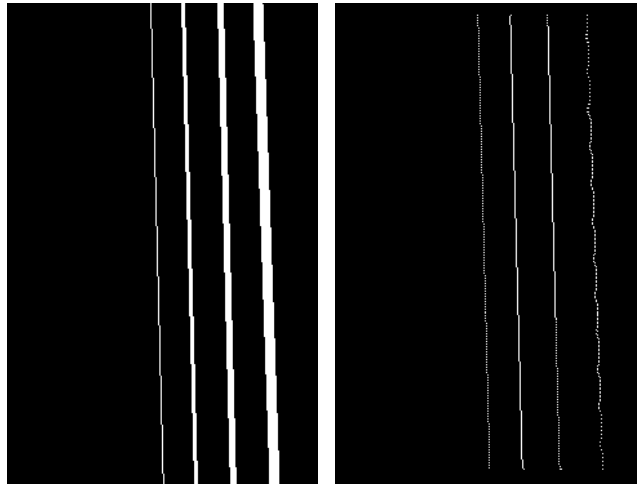


Figure 7.11 Synthetic Ground Truth Image and Crack Detection Result Image

4. Applications

4.1 Critical Performance Assessment of Pavement Crack Detection Methods

Crack detection is the crucial first step of an automated pavement inspection system. Its accuracy and reliability are critical for subsequent distress classification and also for pavement maintenance operations. As mentioned above, the proposed buffered Hausdorff distance measurement can be used as an effective tool for the performance evaluation of crack detection algorithms. In this section, six different automatic crack detection algorithms will be quantitatively and objectively evaluated using the buffered Hausdorff distance method in order to demonstrate its capability. The six segmentation methods include statistical thresholding, Canny edge detection, a multi-scale wavelet method, a crack seed identification method, an iterative clipping method, and a method based on dynamic optimization.

As the purpose is to compare the performance of the algorithms on a diverse image data set, instead of taking a large homogeneous image data set, we selected a data set of 30 images provided by GDOT. Most of the images we selected have a low signal-to-noise ratio, which makes it difficult to segment these images correctly. As a result, we could differentiate the performance of various image segmentation methods effectively. The images selected also had varying crack positions and lighting conditions to ensure objectivity in our evaluation. To

establish a ground truth crack map for performance comparison, GDOT pavement engineers visually identified the cracks, including hairline cracks. An example of an image with the labeled ground truth crack is shown in Figure 7.12 (b) and Figure 7.13 (b).

Table 7.6 presents the results of the 30 images with the scoring measure. We chose the buffered distance L to be 100, which was approximately $1/5^{\text{th}}$ the width of the image. Figure 7.12 shows one test image (Image 8 in Table 7.6) along with a ground truth crack map and the segmented crack maps obtained from six different segmentation methods. Figure 7.13 shows another image (Image 1 in Table 7.6). Image 8 has a distinct crack while Image 1 has a hairline crack, which is not very distinct. The results in Figure 7.13 (Image 1) clearly show the superiority of the dynamic optimization-based method over other methods, especially when segmenting indistinct cracks like hairline cracks. The diagnosis of such cracks is important for state DOTs to perform preventive maintenance. The crack is similar to the dark background in this image, so all the other thresholding methods fail, but the dynamic optimization-based method still performs well.

There are two important characteristics of the algorithms that need to be analyzed: speed and accuracy. Overall, according to Table 7.6, the accuracy of dynamic optimization-based method is consistently better than other methods. The reason for the success of this method is the simultaneous use of both local and global properties of crack indicators. A global score function is maximized by the optimal use of connected pixels with predefined constraints, like minimal crack length and crack width. The statistical thresholding method, on the other hand, uses only local intensity variation at each pixel to classify a pixel as a crack or a non-crack pixel. Therefore, it is able to perform well only when the intensity value difference between crack pixels and background pixels remains the same throughout the image.

This problem is somewhat corrected in the iterated clipping algorithm by dividing images into tiles and segmenting the cracks independently in each tile. As thresholds are iteratively calculated using statistical parameters for each tile, the method gives reasonably good results for images with no shadow effects, high noise, or extremely high variations of pixel intensity values. The Canny edge detection algorithm fails to perform consistently well for all images, as the optimal values of its parameters (edge strength and noise variance) are different

for each image, and the user has to choose these values heuristically. Another problem is that the use of a high noise variance value leads to detection of false edge contours due to the excessive smoothing effects of the Gaussian filter. This makes the algorithm unusable for images with high noise. A standard multi-scale wavelet algorithm is also unsuccessful in detecting cracks across images with varying conditions. The user has to adjust the parameters (numbers of scales, threshold values to separate edges from noise) manually according to the image being processed. The crack seed verification method performs reasonably well for images with uniform lighting conditions, but cracks in images with shadows and variable lighting are not segmented well. This is due to two reasons: the same crack seed verification threshold is used throughout the image, and there is no process in the algorithm to connect crack seeds together optimally.

Table 7.6 Scoring Measure Results from Six Segmentation Methods

Image No.	Ground Truth Image	Dynamic Optimization	Canny Edge Detection	Statistical thresholding	Multiscale Wavelet	Seed Verification	Iterative Clipping
1	100	82.1972	0.06	42.1712	7.4549	32.8086	26.0262
2	100	95.4322	0	33.7171	3.0176	85.9156	27.1151
3	100	97.8158	6.8753	39.9817	3.5542	0	29.9194
4	100	92.4333	10.4488	51.2479	3.319	79.529	52.553
5	100	96.8269	7.6233	8.8029	7.8489	0	35.3812
6	100	84.6843	0	54.3576	79.8406	25.8227	91.191
7	100	92.1084	72.9331	0	73.0214	0	63.2763
8	100	95.5025	46.4897	74.3955	33.4004	84.4648	76.7994
9	100	96.5181	53.2765	47.7759	28.9916	70.6659	57.001
10	100	86.7466	47.891	19.3477	32.4488	68.5483	25.3135
11	100	97.0262	60.4369	71.1571	41.9823	0	24.9242
12	100	98.0994	58.3673	75.7174	29.6138	60.2402	22.9002
13	100	98.0639	51.7698	42.108	28.7498	87.6033	38.9043
14	100	98.3256	81.5556	57.9598	58.2655	94.1165	41.0476
15	100	98.5435	51.1669	0	46.2362	0	21.3327
16	100	98.104	28.3734	0	13.0095	28.8994	82.4285
17	100	98.3791	31.3253	55.1757	11.7903	48.056	76.0915
18	100	98.4885	23.1563	50.4836	9.07	10.925	74.5792
19	100	85.8755	53.3817	52.2418	43.6245	25.3614	62.3795
20	100	87.1256	47.4827	55.9621	42.6735	49.8315	66.1578
21	100	98.7407	29.737	0	13.24	37.0823	49.4361
22	100	98.6107	25.0095	0	11.2718	53.9077	30.0626
23	100	98.5397	26.0818	8.7308	14.2073	11.3578	57.5891
24	100	98.2064	6.035	0	7.0597	0	39.861
25	100	97.8755	13.4397	0	6.7117	2.4976	30.8754
26	100	70.44	9.1421	0	5.6159	2.129	29.1296
27	100	98.6102	1.6972	0	8.3633	0	68.3227
28	100	98.0784	0	61.1267	8.657	23.9357	57.8239
29	100	97.2549	19.2092	89.9646	14.5819	53.723	76.2042
30	100	98.2938	33.3356	50.7301	15.0086	24.3376	45.3196

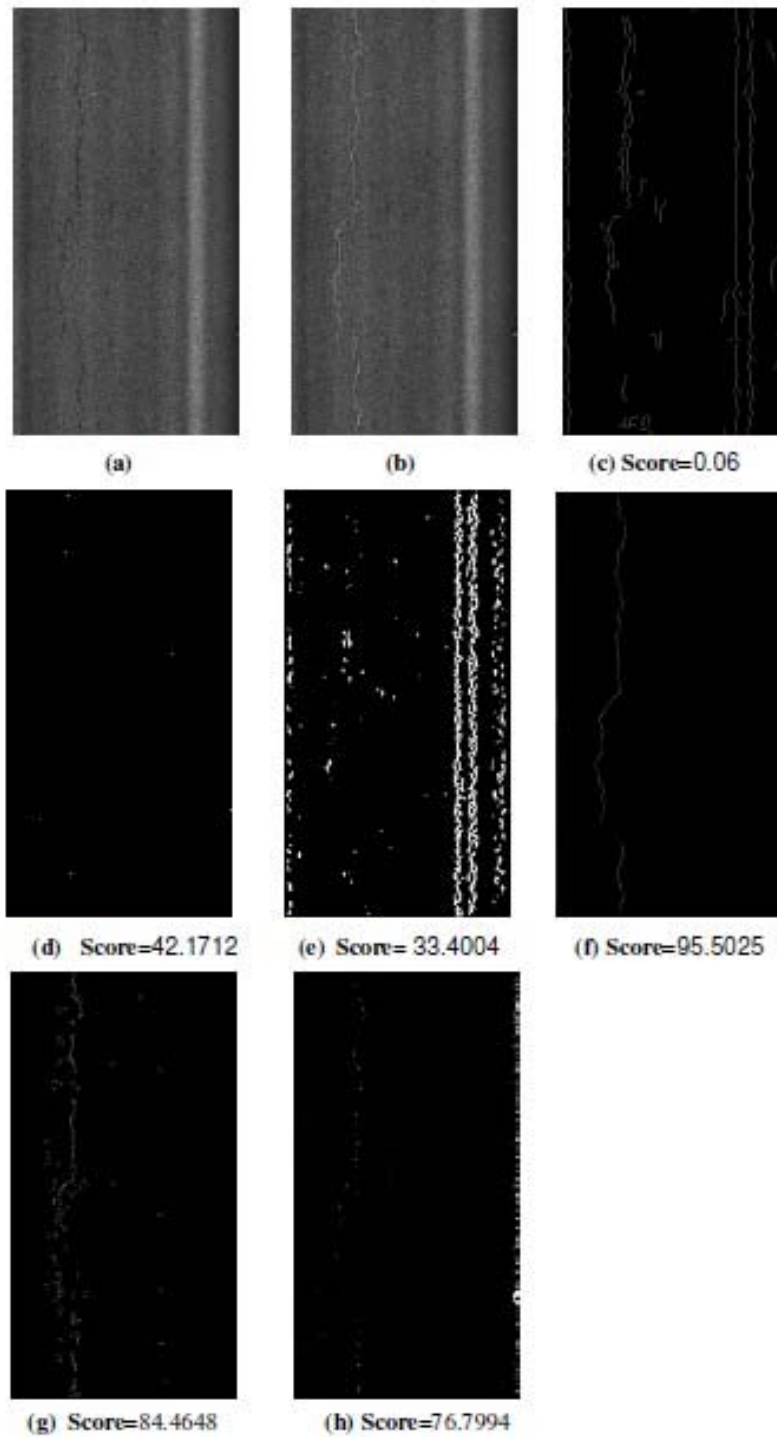


Figure 7.12 (a) Original Image (Image 8) (b) Ground Truth Image (c) Canny Edge Image (d) Statistical Thresholding Image (e) Multi-scale Wavelet Image (f) Dynamic Optimization Image (g) Crack Seed Image (h) Iterative Clipping Image

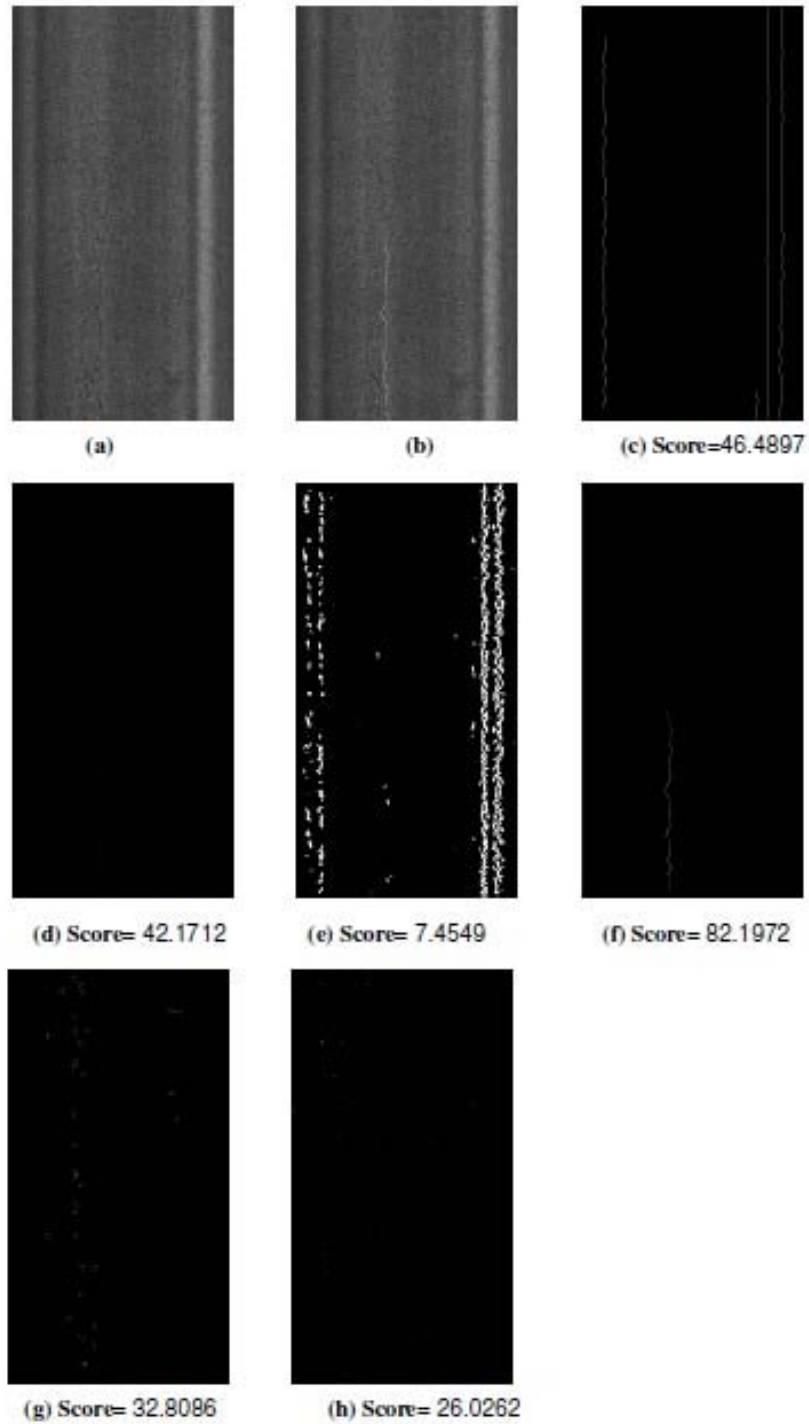


Figure 7.13 (a) Original Image (Image 1) (b) Ground Truth Image (c) Canny Edge Image (d) Statistical Thresholding Image (e) Multi-scale Wavelet Image (f) Dynamic Optimization Image (g) Crack Seed Image (h) Iterative Clipping Image

The downside of the dynamic-optimization based method is its high processing time (101 seconds per image) which makes it unusable for real-time processing. Canny edge detection (1.6 seconds per image), the statistical thresholding method, the iterated clipping method (0.9 seconds per image), and the seed verification method (1.2 seconds per image) are all easy to implement in real time if the code is optimized. The multi-scale wavelet method is, also, slow to implement (50 seconds per image), and the implementation time increases with an increase in the number of scales.

4.2 Parameter Selection of Dynamic Optimization Crack Detection Algorithm

Most crack detection algorithms will need a proper parameter configuration to optimize their performance. However, it is impossible to set a global parameter set, since parameters are usually highly related to the format and characteristics of input data. The proposed buffered Hausdorff distance provides a feasible and objective parameter selection solution for transportation agencies to optimize their crack detection algorithms based on their own data source. In this section, the proposed method will be used to optimize the parameter for dynamic optimization crack detection algorithm.

For the dynamic optimization algorithm, there are several parameters which actually control its performance, including probability interest, SNR interest, maximum and minimum crack width, etc. Among these parameters, the probability interest is the predominant one that determines the algorithm's flexibility for different image conditions, and this is also the parameter we adjusted to optimize the algorithm performance in most times. In this test, an actual pavement range image is selected to conduct a sensitivity test. Under the condition that all the other parameter are fixed, the probability interest increases incrementally, and we evaluate the crack detection results visually and by using the proposed buffered Hausdorff distance method. Figure 7.14 shows the crack detection results under several probability interest values. When the prob-interest value is low, there is much false positive detection. These false alarms are usually caused by the blurred edge on range image (due to slight road elevation, not crack). When the prob-interest value is too high, the algorithm is too strict to detect the entire crack line. Based on the experimental results, the proposed buffered Hausdorff distance has the capability to provide a feasible and objective parameter selection solution for crack detection algorithms, and transportation agencies can use it to optimize their automatic crack detection strategy based on their own data source.

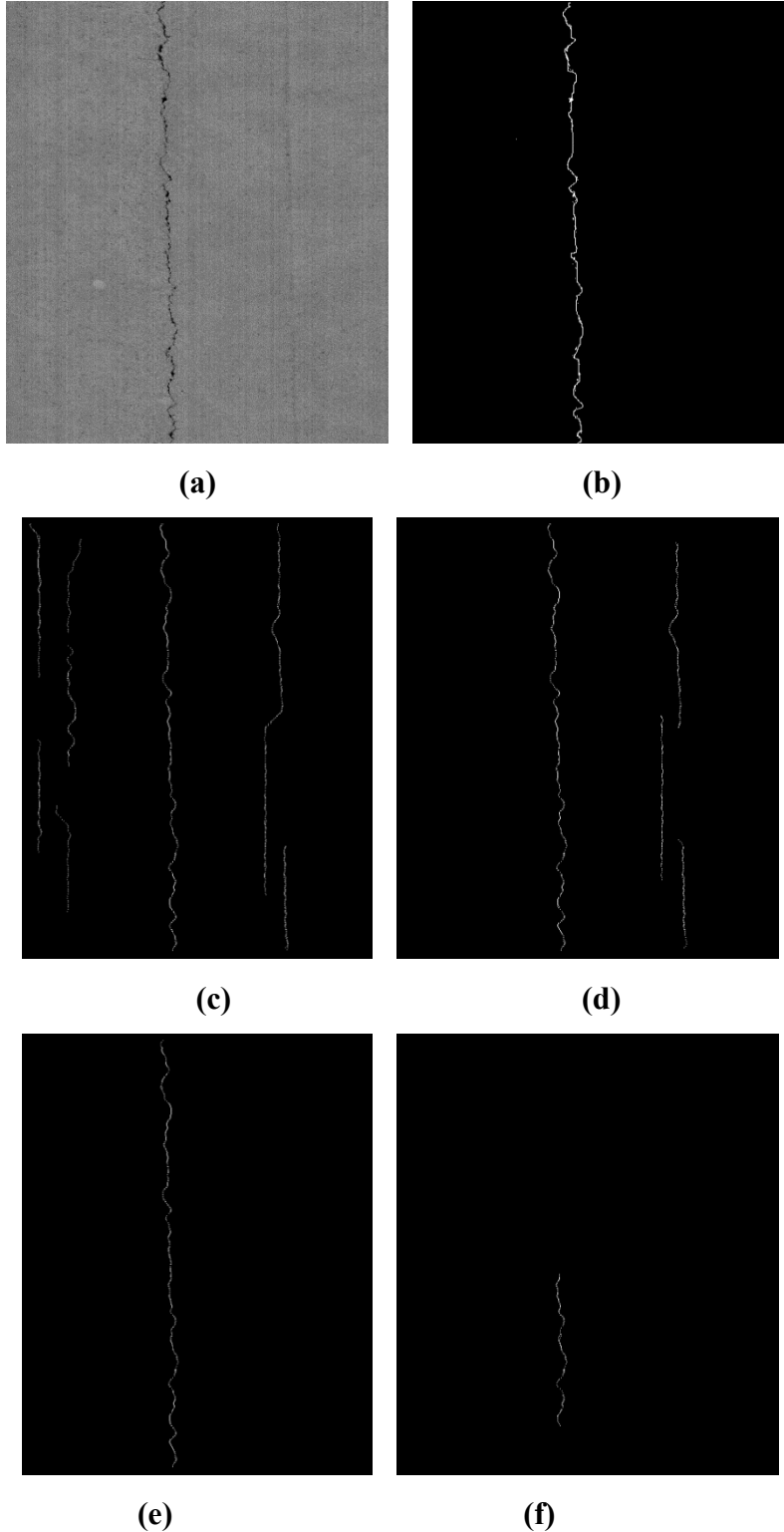


Figure 7.14 (a) Original Range Image; (b) Ground Truth Crack Map; (c) Detected Cracks at 0.78 (Score: 32.7443); (d) Detected Cracks at 0.84 (Score: 51.6057); (e) Detected Cracks at 0.90 (Score: 96.3730); (f) Detected Cracks at 0.96 (Score: 38.7939).

5. Conclusions

Pavement distress segmentation is identified as a crucial step for automatic distress detection and classification. As the distress classifier definitions vary across states and regions, the testing of segmentation precision is of critical importance in assessing the reliability of pavement distress identification algorithms. A robust segmentation algorithm can establish fundamental distress elements that can be standardized and compared among different transportation agencies in the future. Researchers have developed many segmentation algorithms in the past, but it is difficult to compare the performance of different algorithms efficiently without an accurate quantitative method. This hinders the focused development of better segmentation algorithms. Our research is motivated by the need to develop a method to quantitatively evaluate the performance of different pavement distress segmentation algorithms. We developed a novel quantification method based on the buffered Hausdorff distance. In addition, the capability of the proposed method was compared with four other possible quantification methods (mean square error, statistical correlation, receiver operator characteristic (ROC) and Hausdorff distance). Both real and synthetic data were used to validate the capability of our proposed quantification method. The real data sets consisted of raw GDOT images and the resultant images of four segmentation algorithms. These data sets were visually inspected to assess the performance of different algorithms. It is found that the mean square error and statistical correlation do not reflect the assessed performance of different segmentation algorithms. Further, two sets of synthetic images were generated to show the better performance of the buffered distance method compared to the Hausdorff distance and the ROC method and to illustrate the good score separation achieved by the buffered distance method.

The experimental results indicate that the buffered distance scoring measure accurately reflects the observed performance of the segmentation techniques and outperforms the other four quantification methods. It also achieves good score separation to distinguish between the performance of different methods. In addition, the raw value of the buffered distance can be interpreted as the average distance of the crack pixels in two images, and this provides a very valuable insight to researchers. Both mean square error and statistical correlation are not sensitive to the proximity or the distance of the crack pixels in the segmented image to the ground truth image. Hence, unless there is complete overlap of the crack pixels in the segmented

image and the ground truth image, the mean square error scores of two segmented images will be similar. This similarity is even more exaggerated by the fact that both these scoring measures have to use the entire image data in their computation, and a pavement image contains substantially more non-crack pixels than crack pixels. Therefore, the distinction between the performances of segmentation methods is hard to make using these two measures. The Hausdorff distance measure is very sensitive to outliers and is heavily influenced by isolated noise pixels that are far away from crack pixels. Thus, it does not accurately reflect the overall performance of a segmentation method. ROC is a useful scoring measure, but it suffers due to the fact that across a certain boundary all crack pixels are either detected as true defects or false alarms. This hard decision rule can lead to very similar images having extremely different ROC scoring measures. This point was highlighted by a synthetic image data set.

In the future, more segmentation methods can be tested using the buffered distance scoring measure and compared with each other effectively. A standard comparison technique based on our scoring method can be devised and then employed by different transportation agencies to check the relative performance of their pavement distress detection system. A bigger data set that is composed of more complex cracks needs to be tested for the standardization procedure. Currently, the buffer value L for the buffered distance is chosen heuristically. In the future, an automatic technique to find a suitable buffer value L can be designed. In addition, sensitivity analysis that studies the effect of change in buffer value on the buffered distance will be carried out. Finally, the ROC method, which measures useful quantities, like false alarms and correct detection rates, can be used together with buffered distance method to evaluate the performance of the complete pavement distress detection and classification system.

References

- AFD10 (2007). "Delivery of Pavement Distress Data from Automated Systems." *Transportation Research Board*.
- Alekseychuk, O. (2006). "Detection of Crack-Like Indications in Digital Radiography by Global Optimisation of a Probabilistic Estimation Function." BAM-Dissertationsreihe.

- Beauchemin, M., Thomson, K. P. B, Edwards, G. (1998). "Hausdorff Distance Used for the Evaluation of Segmentation Results." *Canadian Journal of Remote Sensing*, 24(1), 3-8.
- Canny, J. (1986). "A Computational Approach to Edge Detection." *IEEE Transactions on Pattern Analysis and Machine Intelligence*, 8(6), 679 – 698.
- Gonzalez, R.C., and Woods, R. E. (2002). *Digital Image Processing*. 2nd Ed., Prentice Hall.
- Huang, Y., and Xu, B. (2006). "Automatic Inspection of Pavement Cracking Distress." *Journal of Electronic Imaging*, 15(1).
- Kerekes, J. (2008). "Receiver Operating Characteristic Curve Confidence Intervals and Regions." *IEEE Geoscience and Remote Sensing Letters*, 5(2), 251-255.
- Koutsopoulos, H. N., Sanhoury, I., Downey, A. B. (1993). "Analysis of Segmentation Algorithms for Pavement Distress Images." *Journal of Transportation Engineering*, 119(6), 868-888.
- Nazef, A., Mraz, A., Gunaratne, M., Choubane, B. (2006). "Experimental Evaluation of a Pavement Imaging System: Florida Department of Transportation's Multipurpose Survey Vehicle." *Transportation Research Record: Journal of the Transportation Research Board*, 1974, 97-106.
- Oh, H., Garrick, N. W., Achenie, L. E. K. (1997). "Segmentation Algorithm Using Iterated Clipping for Processing Noisy Pavement Images." *Imaging Technologies: Techniques and Applications in Civil Engineering: Proceedings of the 2nd International Conference*.
- Song, X., Pogue, B. W., Deghani, H., Jiang, S., Paulsen, K. D., Tosteson, T. D. (2007). "Receiver Operating Characteristic and Location Analysis of Simulated Near-Infrared Tomography Images." *Journal of Biomedical Optics*, 12(5).
- Tagashira, H., Arakawa, K., Yoshimoto, M., Mochizuki, T., Murase, K., Yoshida, H. (2008). "Improvement of Lung Abnormality Detection in Computed Radiography Using Multi-Objective Frequency Processing: Evaluation by Receiver Operating Characteristics (Roc) Analysis." *European Journal of Radiology*, 65(3), 473-477.

- Tsai, Y., Kaul, V., Mersereau, R. (2009). "Critical Assessment of Pavement Distress Segmentation Methods." *ASCE Journal of Transportation Engineering*, 136(11).
- Wang, H., Zhu, N., and Wang, Q. (2007a). "Segmentation of Pavement Cracks Using Differential Box-Counting Approach." *Journal of the Harbin Institute of Technology*, 39(1), 142-144.
- Wang, K. C. P., Li, Q., Gong, W. (2007b). "Wavelet-Based Pavement Distress Image Edge Detection with 'À Trous' Algorithm." *Transportation Research Board Annual Meeting*, National Research Council, Washington, DC.
- Wang, Y. (2002). "Image Matching Based on Robust Hausdorff Distance." *Journal of Computer Aided Design & Computer Graphics*, 14(3), 238-241.
- Zhou, J., Huang, P. S., Chiang, F.-P. (2006). "Wavelet-Based Pavement Distress Detection and Evaluation." *Optical Engineering*, 45(2).

Chapter 8 Asphalt Pavement Crack Detection Using 3D laser Data

1. Introduction

Pavement surface distress measurement is an essential part of a PMS for determining cost-effective maintenance and rehabilitation strategies. Visual surveys conducted by engineers in the field are still the most widely used means to inspect and evaluate pavements, although such evaluations involve high degrees of subjectivity, hazardous exposure, and low production rates. Consequently, automated distress identification is gaining wide popularity among transportation agencies.

For the past two decades, many researchers have been developing pavement distress detection and recognition algorithms using a 2D intensity-based imaging system and improved artificial and laser lighting. However, fully automated pavement distress detection and classification under different lighting and low intensity contrast conditions has remained a challenge. The National Cooperative Highway Research program synthesis document (McGhee, 2004) contains a comprehensive summary of highway practices, research, and development efforts in the automated collection and processing of pavement condition data typically used in network-level pavement management. Over the past decade, the greatest amount of research and development work focused on fully automated methods of distress data segmentation from images. The most widely reported automated method is known as WiseCrax. The vendor, Roadware Group, Inc., has noted several limitations of the WiseCrax technology (McGhee, 2004). First, all digital image analysis is limited by the quality and resolution of the images. WiseCrax can detect cracks approximately 3mm or wider. Second, crack visibility on certain types of pavement surfaces, e.g. chip seal, is not good. To detect this type of crack, human intervention is required. At present, no method has achieved completely satisfactory results. Different pavement distress data acquisition systems are briefly reviewed, and the corresponding issues are summarized below.

Wang (2000) and Wang and Gong (2002) introduced a new automated system that is capable of collecting and analyzing pavement surface distress, primarily cracks, in real-time through the use of a high-resolution digital camera, efficient image processing algorithms, and multi-computer and multi-CPU based parallel computing. In Wang and Gong (2005) and Wang et al. (2008), image processing algorithms are assessed, and a new, low-power, laser-based 2D image

acquisition technique was discussed. The design, implementation, and feasibility issues related to the automated survey system were discussed by Wang (2000; 2004) and Wang and Tee (2002). E1-Korchi et al. (1991) pointed out the importance of lighting in determining the fraction of distress that went undetected. Nazef et al. (2006) comprehensively evaluated pavement distress systems, looking into different factors, including spatial resolution, brightness resolution, optical distortion, and signal-to-noise ratio. Xu (2005), as part of a Texas Department of Transportation (TxDOT) team, used artificial lighting as the ultimate solution for eliminating all shadows in an image and for improving data uniformity across different weather conditions. The TxDOT team designed a Halogen light with a special reflector to accomplish this objective. Hou et al. (2007) assessed the possibility of using 3D pavement stereo images for the automated crack analysis. The preliminary test showed that the accuracy of the system was about 5mm in the vertical direction. Ahmed and Haas (2010) used a low-cost photogrammetric system to reconstruct a detailed model of a pavement surface and demonstrate its capability.

In summary, a 2D intensity-based imaging system has been the main data acquisition system used for the past two decades and is used by most state departments of transportation to collect data. Its intensity-based data acquisition method makes it sensitive to lighting effects. In general, because of the intensity-based data acquisition method, the performance of crack detection algorithms has been severely hampered in the presence of shadows, lighting effects, non-uniform crack widths, and poor intensity contrasts between cracks and the surrounding pavement surfaces. The challenge persists in spite of all the research work that has been carried out to improve image acquisition techniques by minimizing the lighting defects (Kaul et al., 2010). However, it is difficult to achieve consistent crack detection under different ambient lighting conditions when using natural light for illumination (Xu, 2005). Some illumination devices, such as LED lighting, are used to provide constant lighting that prevents the impact of shadows (Xu, 2005; Xu, 2007). However, the beam width of the LED lighting is 0.5 in., which is not thin enough to provide sufficient depth resolution. The shallow cracks and/or thin cracks that have low-intensity contrast with the surrounding pavement are sometimes difficult to detect. Many algorithms are able to perform well only in an image data set that contains images that are not too different from each other. Otherwise, manual inputs are required to adjust the input parameters so that the algorithms can perform reasonably. Although 3D stereovision has been

studied recently, it is not mature enough to be used in practical application. Therefore, full automation of pavement distress detection has remained a challenge, especially for accurate and reliable detection (Kaul et al., 2010).

2. 3D laser Imaging Technology

With the advancement in sensor technology, a 3D line-laser-based pavement surface data acquisition system that can collect high-resolution 3D continuous pavement profiles for constructing pavement surfaces has become commercially available. This 3D laser system is different from the current 2D intensity-based imaging system. First, the 3D laser system is not sensitive to lighting effects when measuring crack ranges (i.e. elevations). Noise, like oil stains and poor intensity contrasts, will not interfere with the segmentation results using the acquired range data. As long as there is a distinguishable elevation difference between a crack and its surrounding background, the segmentation algorithm is able to capture the crack. Consequently, increased attention has been drawn to the development of this 3D laser data acquisition system and its potential application. Researchers from Texas (Li et al., 2010) have developed a research version of the 3D laser system and have demonstrated the system's capability, but the developed system is still in the research stage.

The tested 3D laser system in this research project employs high-speed cameras, custom optics, and laser line projectors to acquire 2D images and high-resolution 3D profiles of road surfaces that allow for automatic detection of cracks and the evaluation of macro-texture and other road surface features. Designed for both daytime and nighttime operation in all types of lighting conditions, the system is immune to sun and shadows and is capable of measuring pavement types ranging from concrete to dark asphalt. The 3D laser can be operated at a speed of up to 100 km/h and cover pavement widths as wide as 4 meter on a travel lane. The 3D laser can achieve 0.5mm crack depth resolution, collect 5,600 profiles per second, and operate at highway speed (100 km/h for collecting transverse profiles at an interval less than 5mm). Collected data is processed with the 3D-line-laser's automated analysis software. Distress analysis results can then be used in association with a PMS to take appropriate pavement rehabilitative action.

This system can produce data with much better granularity and, thus, has great potential to better detect pavement distress. This chapter will comprehensively evaluate the capability of the 3D

laser to conduct pavement surface condition surveys, including both 3D laser profiles data and the automatic crack detection algorithm provided in the 3D laser software platform.

3. Advantages of 3D laser Data

Since 3D laser data uses the range (elevation) information to describe pavement surface, it has several advantages over traditional techniques. Unlike 2D digital images, the range data is hardly influenced by different lighting conditions. Noise, like oil stains and poor intensity contrast, will not interfere with the segmentation result using the acquired range data. This section will demonstrate these advantages.

3.1 Pavements under Different Lighting Conditions and Low Contrast Conditions

Experimental tests were conducted to evaluate the feasibility of using 3D laser technology to detect pavement cracks under different lighting conditions and low contrast conditions. Two key components of the tests were designed to consistently and quantitatively evaluate the 3D laser data. First, the dynamic optimization-based crack segmentation method was employed to evaluate the quality of the 3D laser data. Second, the automated detection results were quantitatively evaluated by comparing them with the ground truth using a linear-buffered Hausdorff scoring method proposed by Kaul et al. (2010). The ground truth was manually digitalized and extracted from the 3D laser data, as suggested by other researchers (Lee & Kim, 2006; Raman et al., 2004).

To perform the study, two series of tests were used. One performed controlled laboratory tests on simulated cracks with known crack widths and depths, and the other performed field tests on roadways. In the controlled tests, the objective was to assess the capability of the 3D laser technology to detect cracks of different widths under different lighting conditions. Four crack widths (1mm, 2mm, 3mm, and 5mm) under two extreme lighting conditions (daytime and nighttime) were tested. The crack depth was about 19mm. The test procedure is briefly described. First, a controlled gap between two solid wood boards was used to simulate a pavement crack on the road. The width of the gap was measured before and after the test with a caliper, as shown in Figure 8.1. Second, an operator drove the integrated sensing vehicle to collect the 3D laser data from two wood boards. Third, with the 3D laser data, the dynamic optimization was employed to segment the simulated cracks. Meanwhile, the ground truth was

manually digitized and extracted from the 3D laser data. The objective crack segment scoring method was applied to quantitatively assess the performance of the crack segmentation results by comparing the segmented outcomes with the ground truth. The tests were conducted during daytime and nighttime, as shown in Figure 8.2. The test results are summarized in Figure 8.3 and Table 8.1.

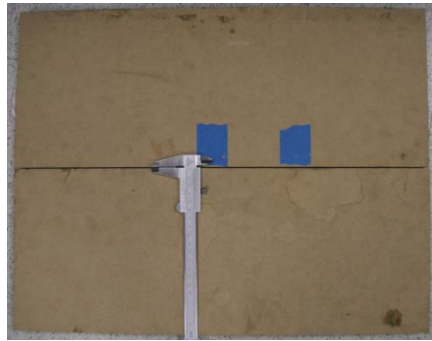


Figure 8.1 A Gap between Two Solid Wood Boards to Create the Simulated Known Crack Widths



(a) Daytime



(b) Nighttime

Figure 8.2 Two Lighting Conditions

Figure 8.3 presents part of the controlled laboratory test results. It includes four subsets of figures. Each subset shows the 3D raw data on the left and the segmented crack map image produced using a dynamic optimization algorithm on the right. As shown in Figure 8.3, the 1mm cracks are partially captured, and the 2mm cracks are fully detected. Although Figure 8.3 shows only the results of 1mm and 2mm, the entire laboratory test results are shown in Table 8.1. As shown in Table 8.1, 2mm, 3mm, and 5mm cracks can be fully detected by the 3D laser.

Table 8.1 Scores for the Controlled Tests

Score	Crack width			
	1mm	2mm	3mm	5mm
Day-time	63.9	93.6	93.1	93.3
Night-time	64.1	93.4	93.0	93.1

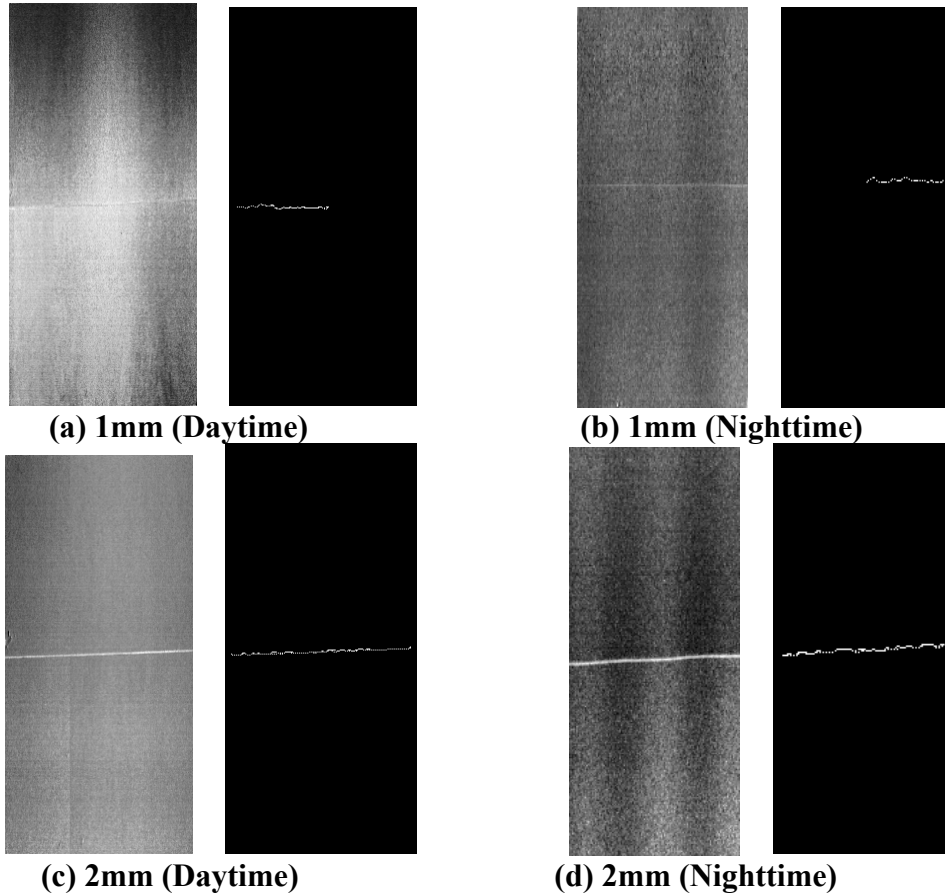


Figure 8.3 Crack Segmentation Results on Simulated Cracks: the One on the Left is Raw 3D Data, and the One on the Right is the Crack-Segmented Results (Tsai, 2010)

Table 8.1 lists the quantitative scores derived from the linear buffered Hausdorff scoring method for the cracks of different widths under two lighting conditions. Cracks with widths of 1mm, as shown in Figure 8.3, are detected partially. The scores are approximately 64. For cracks with widths equal to or greater than 2mm, the scores are better, about 93. Daytime and nighttime tests result in similar scores. The maximum score difference is 0.2. The controlled laboratory test results, shown in Table 8.1, demonstrate that the 3D laser system is capable of detecting cracks whose widths are equal to or wider than 2mm.

Besides the controlled laboratory test conducted above, two field tests on actual roadways were also conducted. The first field tests evaluated the capability of the 3D laser system to detect cracks under low-intensity contrast conditions. The second field test evaluated the capability of the 3D laser system to detect cracks under different lighting conditions, including nighttime, daytime with shadow, and daytime without shadow.

Figure 8.4 (a) shows a roadway image with low-intensity contrast between a crack (approximately 1mm to 6mm wide) and its pavement background. The low-intensity contrast makes the crack difficult to detect, even with the human eye, on an intensity-based digital image. However, the same image collected by 3D laser technology shows a more distinct contrast between the crack and the pavement background. This is illustrated by Figure 8.4 (b) and (d), collected during the day and at night, respectively, and Figure 8.4 (c) and (e), which represent the corresponding crack segmentation results. The high scores from this first test, 98.3 for daytime and 98.0 for nighttime, demonstrate the potential of 3D laser technology to detect cracks under low intensity contrast conditions.

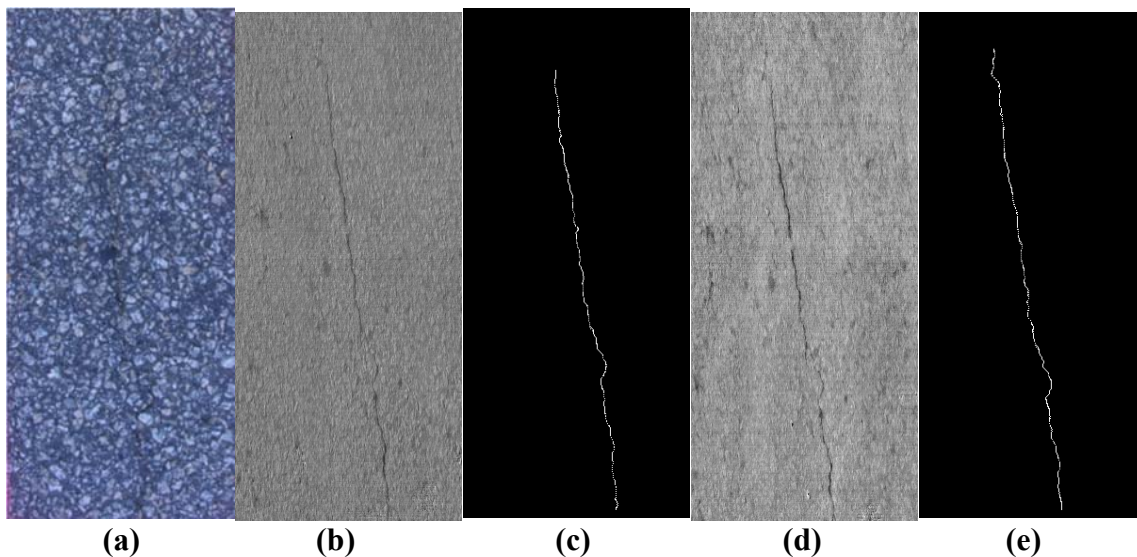


Figure 8.4 Test Results on Crack with Low-Intensity Contrast: (a) Roadway Image; (b) 3D Laser Data Collected during the Daytime; (c) Crack Segmentation Result (Daytime; Score = 98.3); (d) 3D Laser Data Collected during the Nighttime; (e) Crack Segmentation Result (Nighttime; Score = 98.0) (Tsai, 2010)

The second field test was conducted on SR 80 to evaluate the consistency of using the 3D laser system to detect cracks under three different lighting conditions: nighttime, daytime with shadows, and daytime without shadows. Eleven test segments, including ten longitudinal cracks (cracks A to J) and a transverse crack (crack T), were labeled in the field. Examples of the three lighting conditions are shown in Figure 8.5. All eleven crack segments were analyzed using the dynamic optimization-based crack segmentation algorithm. Figure 8.6 shows the example of 3D raw data collected under three lighting conditions and the corresponding crack segmentation results for the crack J. Each sub-figure contains the 3D raw data on the left and the segmented crack on the right. Visual observation shows that the crack can be clearly captured by the 3D laser system and well segmented using the dynamic optimization-based method.

Then, the detected cracks were compared with the ground truth using the linear buffered Hausdorff scoring method to obtain the score; the ground truth was established by observing the cracks in the field and digitizing them manually on the crack images. The scores for each 3D raw data image captured under three lighting conditions are listed in Table 5.2. As observed, the three scores for each crack are very close to each other. The score range was calculated for each crack and is shown in Table 5.2. The average score difference for those eleven cracks is 1.9. This difference is very small and may easily be caused by a tiny deviation, e.g. a 2-pixel deviation, from the actual crack pixels when digitizing the ground truth. Therefore, the preliminary results demonstrate that the proposed 3D laser system can perform consistently under different lighting conditions in the field.



Figure 8.5 Examples of Three Lighting Conditions

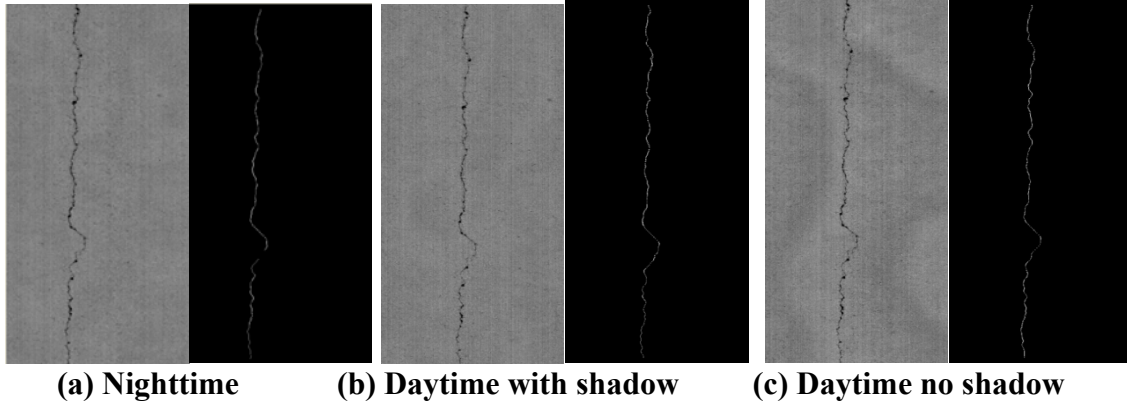


Figure 8.6 3D Laser Data and Corresponding Crack Segmentation Results on the Crack J for Three Lighting Conditions

Table 8.2 Scores for the Second Field Tests

Crack Name	Score			Score Difference
	Night-time	Day-time with Shadow	Day-time no Shadow	
A	95.8	97.4	97.2	1.6
B	95.5	96.1	95.4	0.7
C	93.6	96.8	97.2	3.6
D	95.0	97.2	96.9	2.2
E	96.5	97.8	97.3	1.3
F	96.5	98.0	97.5	1.5
G	95.1	97.7	97.5	2.6
H	95.4	96.6	97.6	2.2
I	96.3	96.3	97.4	1.1
J	95.6	97.6	97.7	2.1
T	95.9	96.9	97.6	1.7
Average score difference				1.9

In summary, both field tests demonstrated the feasibility of using the 3D laser technology to detect pavement cracks under different lighting and low-intensity contrast conditions. For three lighting conditions, the average quantitative score difference is less than 2%.

3.2 Pavements with Oil Stains

Oil stains usually appear to be darker than surrounding areas on a pavement surface. In traditional 2D digital images, crack pixels have similar characteristics. Therefore, it is difficult to differentiate pavement cracking from noise produced by such elements as oil stains. However,

when roadway data is captured by a 3D laser, oil stains are not a more distinctive feature in range data.

This experimental test used pavement samples with oil stains and other noise to show the advantages of the 3D laser technique. The data used in this test were collected on SR 275 between Milepost 0 and Milepost 1. There is an intersection and a gas station in this section of the roadway. Because the road has very little traffic, it is relatively good condition. Nevertheless, the pavement surface is usually not clean, so the roadway images are affected by noise caused by various road conditions. Figure 8.7 and Figure 8.8 demonstrate two representative samples in which noise from various conditions, such as oil stains, influence the pavement appearances. The intensity image, range, range image, and crack-detection results for these samples are presented in Figure 8.7.

Figure 8.7 (a) shows the intensity image of the first pavement sample. From the image, we can see that there is a large oil stain near the bottom left corner and some small noise indications distributed over the image. These noise indications (including the oil stain) appear to be darker than the surrounding areas. On the other hand, the pavement cracking (which is on the left side of the sample) is hard to differentiate because of an image discoloration issue caused by the camera. Figure 8.7 (b) shows the range image of this sample based on the 3D laser data. The range image is generated from the elevation of the pavement surface. Noise indications, such as oil stains, have a darker intensity and do not have a distinctive elevation change on the surface. However, cracking can be clearly observed on range images, since a crack usually has a sharp elevation drop compared to the surrounding area. Based on this 3D range data, the crack detection was conducted, and the results are shown in Figure 8.7 (c). The crack detection algorithm gives good performance, even if the cracks are hard to observe on intensity pavement images.

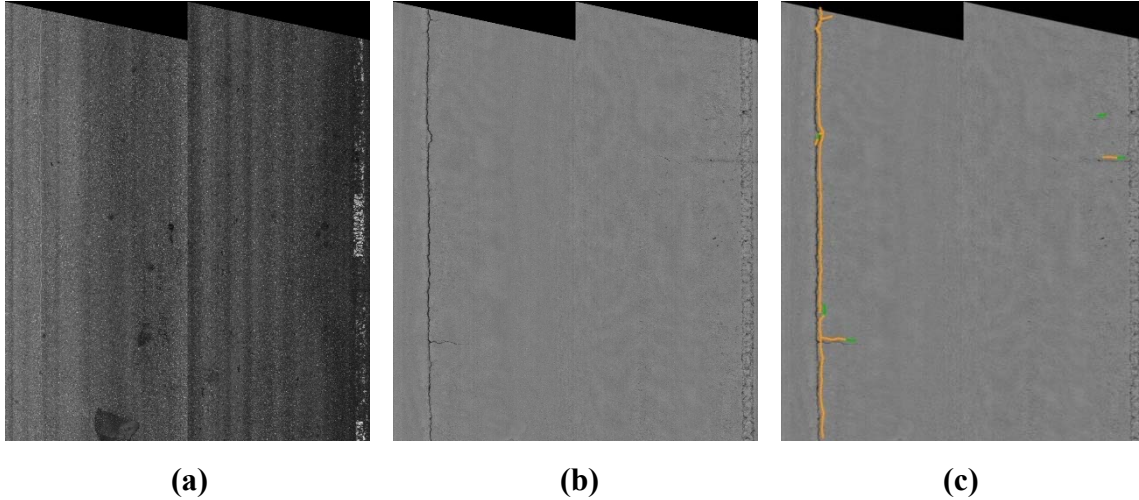


Figure 8.7 Pavement Images with Oil Stain:
(a) Intensity image; (b) Range image; (c) Crack detection results

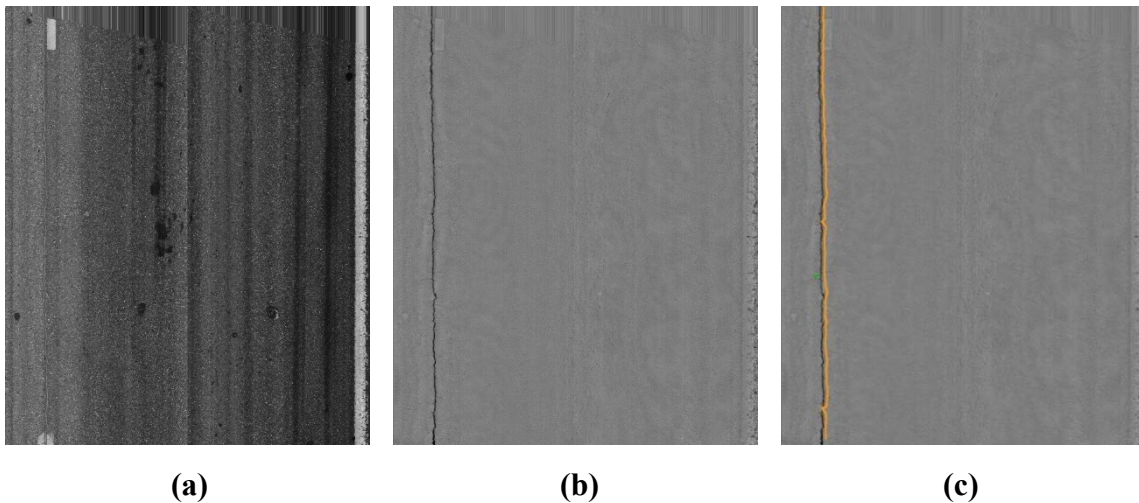


Figure 8.8 Pavement Images with Oil Stain and Other Noises:
(a) Intensity Image; (b) Range Image; (c) Crack Detection Results

Similarly, Figure 8.8 presents another sample of pavement with noise indications. Besides the oil stains in the middle of Figure 8.8 (a), there are also some long, dark strips caused by tire marks and camera discoloration. From Figure 8.8 (b) and (c), we can observe that these noise indications were effectively removed in the range image, and the crack detection results were good. It is also noticed from this experiment that besides pavement noise, such as oil stains, image discoloration caused by the camera lens and, even, pavement markings, can be removed or faded using the 3D laser data.

4. Evaluation of Automatic Crack Map Generation

The 3D laser software platform provides a crack-detection algorithm based on 3D laser data. The corresponding crack map will be automatically generated as an output of the algorithm. This section will quantitatively evaluate the accuracy of the detected crack map compared to the ground truth. Since the performance of the 3D laser crack detection algorithm is related to the selection of parameters, data collection format, and characteristics of collected data, this section will not present a large-scale performance validation; instead, the framework of evaluating the performance of the 3D laser crack detection will be demonstrated so that future users of this system can optimize its performance on the unique data they collect. Also, representative result samples will be presented to reveal the potential issue of 3D laser data collection and crack detection.

The following procedures were conducted to quantitatively evaluate the performance of the 3D laser crack-detection algorithm:

- First, the ground truth was manually digitized and extracted from the 3D laser data. The 3D laser data was presented in the form of range image (Figure 8.9 (a)). Based on the visual inspection of range image, the cracking position was manually digitized and converted to a binary ground truth crack map.
- Then, the crack map results were generated using the 3D laser crack-detection algorithm. The crack map was presented and overlaid on the intensity image or range image (Figure 8.9 (b)), and different colors of the detected crack line represented different crack width ranges. There are two typical ways to convert it into binary crack map:
 - o The first way is to manually digitize the intensity or range image with the crack map overlay (similar to establishing ground truth).
 - o The second way is to interpret the XML file as the results of distress detection and reconstruct a binary crack map.

The binary crack map is displayed in Figure 8.9 (c).

- Finally, the two binary crack maps' ground truth and detection results were compared quantitatively. The buffered Hausdorff scoring method was employed to conduct an objective evaluation.

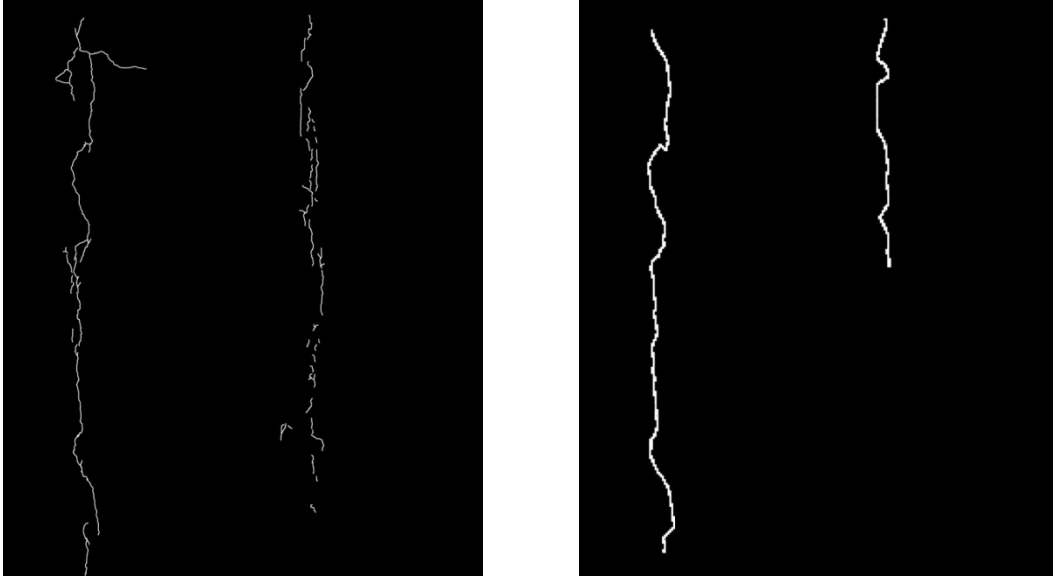


Figure 8.10 Ground Truth Image (Left) and Result Image (Right) for Sample 1 Collection on SR275

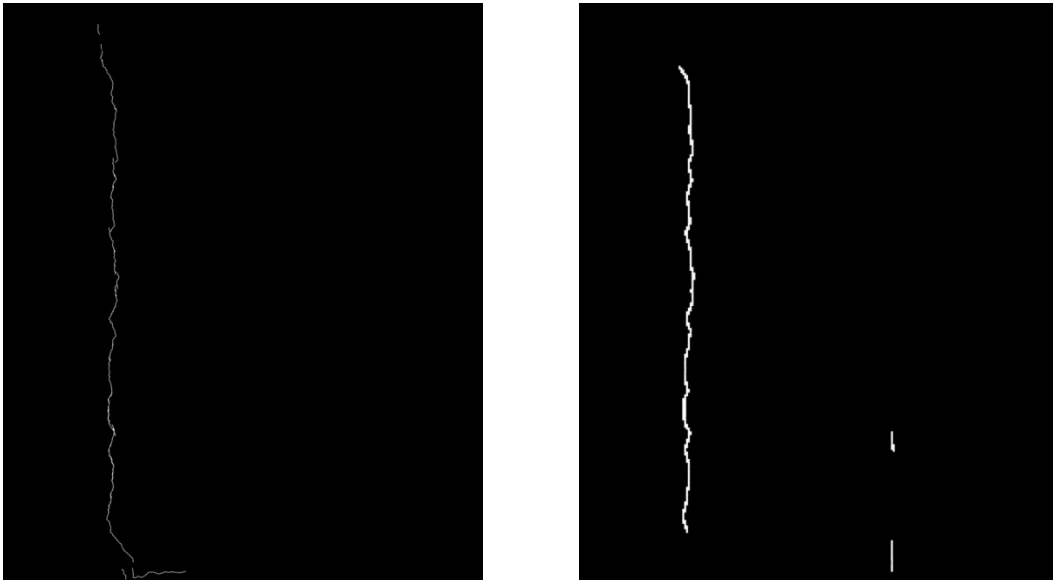


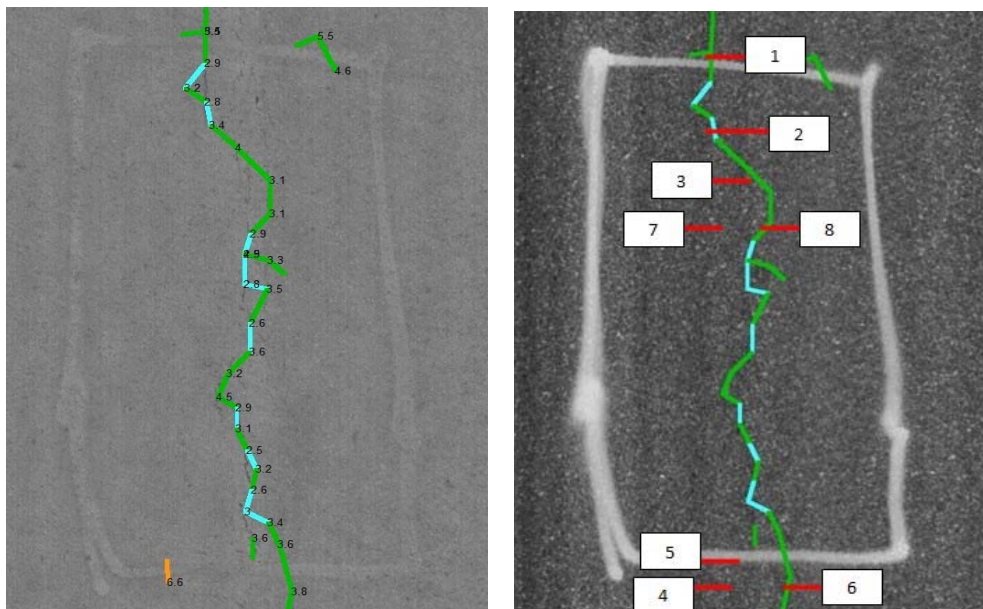
Figure 8.11 Ground Truth Image (Left) and Result Image (Right) for Sample 2 Collected on SR275

5. Evaluation of Crack Width Measurement

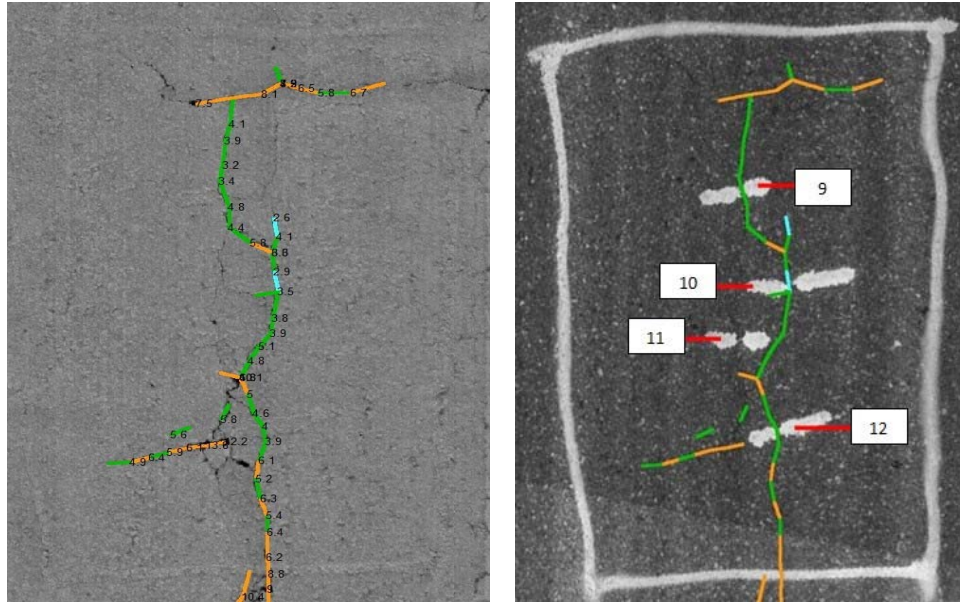
Almost all the existing automatic crack evaluation studies focus on using 2D intensity-based digital pavement images as the input. Compared to the traditional 2D digital image technique, the emerging 3D laser technology can provide a more accurate width measurement and additional

crack depth information. Crack width is a common and important crack classification factor in most DOTs' pavement surface condition survey protocols, especially when differentiating severity levels. It is also crucial information for determining pavement maintenance operations, such as crack sealing/filling. However, crack width has rarely been used in the past crack classification studies. Considering the properties of 2D digital images, the accuracy of crack width measurement (measured pixel by pixel) is limited; even for high resolution images, crack width measurement is still influenced by other factors, such as lighting conditions and pavement noise (e.g. oil stain). . The 3D laser technology provides a better opportunity to measure crack width more accurately.

In this experimental test, a total of 12 spots are selected from SR 275 Mile 1-2 for crack width measurement validation (as shown in Figure 8.12 (a) and (b)). The left image is the range image (based on elevation information of the pavement surface) with a detected crack map overlaid, and the automatically measured crack width information using 3D laser data is labeled beside the corresponding crack elements. The right image is the intensity image with the crack map overlaid, and the selected 12 locations are marked for reference.



(a) Eight Locations for Crack Width Measurement Validation



(b) Another Four Locations for Crack Width Measurement Validation
Figure 8.12 Twelve Locations Selected for Crack Width Measurement

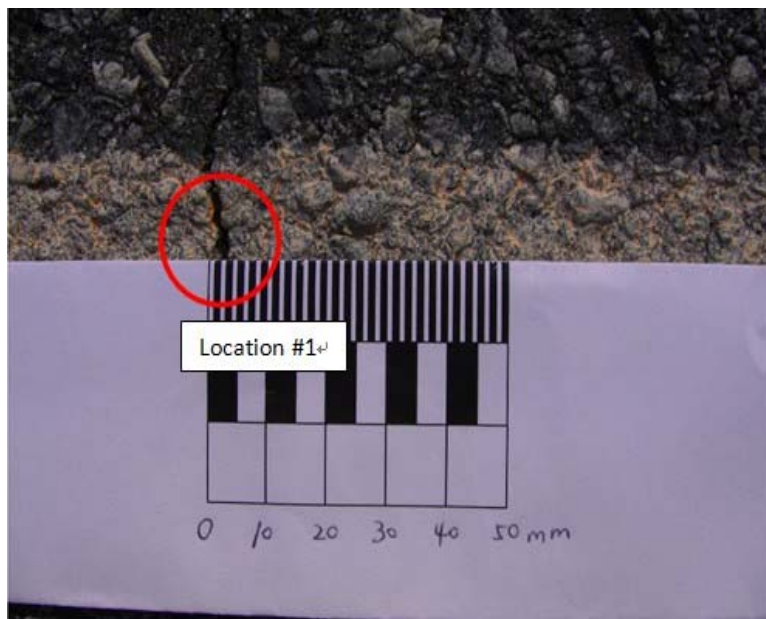


Figure 8.13 Field Crack Width Measurement for Establishing Ground Truth

In order to validate the automatic crack width measurement accuracy for the 12 selected spots, the ground truth crack width in the field (as shown in Figure 8.13) was manually measured. The validation results are shown in Table 8.3. From the results, we can see that, based on the 3D laser pavement data, it is difficult to detect hairline cracks with a width of about 1 mm. This is

reasonable, considering the properties of the laser technique and, also, the resolution of the 3D laser system. Hairline cracks are also difficult to detect using traditional digital intensity image. Actually, based on GDOT pavement survey practices, hairline cracks, which usually occur in low-severity level load cracking, do not have significant influence on the deduct value computation; in other words, although hairline cracks are, also, a pavement distress issue, they do not have a large influence on the current pavement condition survey results. For the detected cracks, the automatically measured width information is relatively consistent with field-measured ground truth. The maximum absolute difference is 1mm, and the average absolute difference is 0.4mm. The results show the capability of using the accurate crack width information for further crack classification tasks.

Table 8.3 Crack Width Measurement Validation Results for 12 Locations

Location No.	Computed Crack Width (mm)	Manually Measured Crack Width (mm)	Absolute Difference (mm)
1	3.5	3.5	0
2	2.8	3.0	0.2
3	4	3.5	0.5
4	Not detected	1.5	N/A
5	Not detected	1	N/A
6	3.8	3	0.8
7	Not detected	1	N/A
8	3.1	3	0.1
9	4.8	4	0.8
10	2.9	3	0.1
11	Not detected	1	N/A
12	4	5	1
Avg. (detected)	3.6	3.5	0.4

The above validation results show good accuracy for measuring longitudinal crack width. To further assess the measurement accuracy for transverse crack, 12 spots on three transverse cracks on SR 275 were selected. The manually measured crack width, which is considered as ground truth, varies from 1 mm to 7 mm. Figure 8.14 shows an example for transverse crack spot AT1. Roughly, the manually measured crack width for AT1 is 1 mm as shown in Figure 8.14 (b) while the 3D-line-laser-measured result is around 5 mm as shown in Figure 8.14 (c). Table 8.4 lists the comparison results for all 12 spots. It can be seen that all three transverse cracks can be detected by using 3D laser, but the crack width measurement is very inaccurate for fine cracks, e.g., AT1 and AT2. This type of inaccuracy is caused by the coarser resolution of 3D laser data in the driving direction, which is about 5mm.

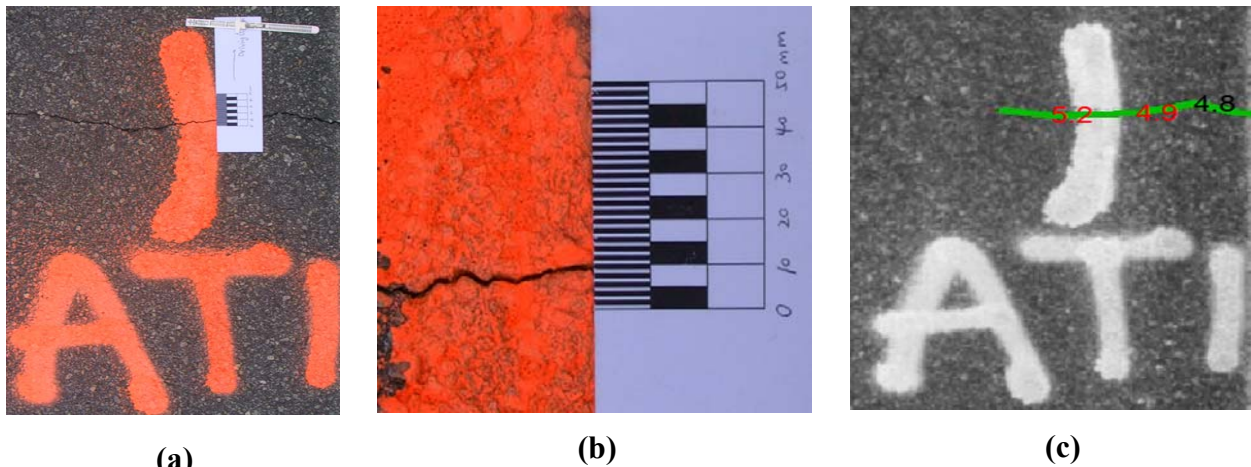


Figure 8.14 Measurement of Transverse Crack Width

6. Summary

The validation study in this chapter shows that the 3D laser is insensitive to different lighting conditions, low intensity contrast, and pavement oil marks, unlike the traditional line scan camera. Laboratory tests on fabricated crack samples show consistent detection results in daytime and nighttime. Cracks with widths greater than 1mm can be detected easily. However, a hairline crack with a width of approximately 1mm is hard to detect due to the current resolution of the integrated 3D laser. Field tests on Georgia SR 80 were conducted under three different lighting conditions, daytime with shadow, daytime without shadow, and night. The crack detection results show very good consistency and the average difference of performance scores is less than 2% (out of 100). Though low intensity contrast is a challenge for the traditional line

scan camera for crack detection, the test result shows no difficulty for the integrated 3D laser as long as the crack is distinct on surface depth change. Similarly, oil stains can be effectively removed from a possible false detected crack because of indistinguishable depth change.

Table 8.4 Crack Width Measurement Validation Results for Transverse Crack

Location No.	Computed Crack Width (mm)	Manually Measured Crack Width (mm)	Absolute Difference (mm)
AT1	5.1	1	4.1
BT1	6.2	2	4.2
CT1	5.4	3	2.4
DT1	5.1	4	1.1
T1	4.8	3	1.8
T2	4.8	3	1.8
T3	5.5	3	2.5
T4	5.1	3	2.1
T5	5.5	3-4	1.5-2.5
T6	5.3	6	0.8
T7	4.9	7	2.1
T8	5.4	6	0.6

To validate the crack width measurement accuracy, 12 spots were selected on SR 275 with manually measured crack width as the ground truth. Cracks with widths greater than 2mm can be detected correctly. However, cracks equal to and less than 1 mm cannot be detected correctly. Compared to the manually measured results, crack widths were captured well by the automatic method. The maximum absolute difference of crack width was 1 mm, and the average absolute difference was 0.4 mm. This result shows a promising potential to measure crack width for further crack classification tasks. While the 3D-line-laser-provided software can effectively detect the longitudinal crack widths, the transverse crack width cannot be reliably detected because the current data resolution in the driving direction is about 5 mm. This issue can be solved by improving the resolution of 3D laser system, especially at longitudinal direction.

Actually, it has been claimed that 1 mm resolution at both transverse and longitudinal direction can be acquired at highway speed using the newest 3D laser system (Li, et al., 2014).

References

- Ahmed, M. F. M., and Haas. C. T. (2010). "The Potential of Low Cost Close Range Photogrammetry Towards Unified Automatic Pavement Distress Surveying." *Transportation Research Board Annual Meeting*, Washington, D. C.
- Alekseychuk, O. (2006). "Detection of Crack-Like Indications in Digital Radiography by Global Optimisation of a Probabilistic Estimation Function." PhD Thesis, BAM-Dissertationsreihe, Band 18.
- EI-Korchi, T., Gennert, M. A., Ward M. O., Wittels. N. (1991). "Lighting Design for Automated Pavement Surface Distress Evaluation." *Transportation Research Record: Journal of the Transportation Research Board*, 1311, 144-148.
- Hou, Z., Wang K. C. P., Gong. W. (2007). "Experimentation of 3d Pavement Imaging through Stereovision." *Proc., International Conference on Transportation Engineering*, 376-381.
- Kaul, V., Tsai Y., Mersereau. R. M. (2010). "A Quantitative Performance Evaluation of Pavement Distress Segmentation Algorithms." *Transportation Research Record: Journal of the Transportation Research Board*, 2153, 106-113.
- Laurent, J., Lefebvre D., Samson. E. (2008). "Development of a New 3D Transverse Laser Profiling System for the Automatic Measurement of Road Cracks." *SURF 2008*.
- Lee, H., and Kim. J. (2006). "Analysis of Errors in Ground Truth Indicators for Evaluating the Accuracy of Automated Pavement Surface Image Collection and Analysis System for Asset Management." *Journal of ASTM International*, 3(5), 1-15.
- Li, Q., Yao, M., Yao X., Xu. B. (2010). "A Real-Time 3d Scanning System for Pavement Distortion Inspection." *Measurement Science and Technology*, 21(1), 1-8.
- Li, Q., Wang, K. C. P., Yang, G. and Li, L. (2014). "One-mm 3D Laser Imaging Survey for Comprehensive Runway Evaluation." 2014 FAA Worldwide Airport Technology Transfer Conference, Galloway, New Jersey.

- McGhee, K. H. (2004). "Automated Pavement Distress Collection Techniques: A Synthesis of Highway Practice." *NCHRP Synthesis 334*, Washington, D.C.
- Nazef, A., Mraz, A., Gunaratne M., Choubane. B. (2006). "Experimental Evaluation of a Pavement Imaging System: Florida Department of Transportation's Multipurpose Survey Vehicle." *Transportation Research Record: Journal of the Transportation Research Board*, 1974, 97-106.
- Raman, M., Hossain, M., Miller, R., Cumberledge, G., Lee, H., Kang. K., (2004). "Assessment of Image-Based data Collection and the AASHTO Provisional Standard for Cracking on Asphalt-Surfaced Pavements." *Transportation Research Record: Journal of Transportation Research Board*, 1889, 166-125.
- Tsai, Y., Kaul, V., Mersereau, R. M. (2010). "A Critical Assessment of Pavement Distress Segmentation Methods Performance Evaluation of Pavement Distress Segmentation Methods." *Journal of Transportation Engineering*, 136 (1), 11-19.
- Wang, K. C. P. (2000). "Designs and Implementations of Automated Systems for Pavement Surface Distress Survey." *Journal of Infrastructure Systems*, 6(1), 24-32.
- Wang, K. C. P., and Gong. W. (2002). "Real-Time Automated Survey of Pavement Surface Distress." *Proc., International Conference on Applications of Advanced Technologies in Transportation Engineering*, 465-472.
- Wang, K. C. P., and Tee. W. (2002). "Understanding of Pavement Profiling and Validation of an Implementation." *Proc., International Conference on Traffic and Transportation Studies*, 817-824.
- Wang, K. C. P. (2004). "Challenges and Feasibility for Comprehensive Automated Survey of Pavement Conditions." *Proc., International Conference on Applications of Advanced Technologies in Transportation Engineering*, 531-536.
- Wang, K. C. P., and Gong. W. (2005). "Real-Time Automated Survey System of Pavement Cracking in Parallel Environment." *Journal of Infrastructure Systems*, 11(3), 154-164.
- Wang, K. C. P., Gong W., Hou. Z. (2008). "Automated Cracking Survey". *Proc., RILEM International Conference on Cracking in Pavements*, 881-889.

Xu, B. (2005). "Artificial Lighting for the Automated Pavement Distress Rating System."
Austin, TX.

Xu, B. (2007). "Summary of Implementation of an Artificial Lighting System for Automated
Visual Distress Rating System." Austin, TX.

Chapter 9 Feasibility Study of Crack Deterioration Behavior Using 3D Laser Data

Cracking is one of the predominant types of pavement distresses, mainly caused by repetitive vehicle loads and weathering. Pavement crack characteristics, including location (in the wheel path or the non-wheel path), orientation (transverse or longitudinal), length, width, density, pattern, and crack deterioration behavior (e.g. crack growth in length and width) are essential for determining an adequate treatment method, timing, and the corresponding quantity of materials, such as crack filling/sealing materials. It is also crucial to study the detailed pavement cracking deterioration behavior with respect to length, width, density, branch pattern, and/or growth rate to validate the Mechanistic-Empirical Pavement Design Guide (MEPDG).

Although a tremendous amount of effort has been made in labs to simulate the actual pavement crack deterioration behavior, it is still difficult to use lab tests to fully determine the actual pavement crack deterioration behavior due to complicated roadway conditions and traffic loads in the real-world environment. Therefore, to obtain detailed in-field pavement cracking data, it is still essential to study crack characteristics and deterioration behavior, which are indispensable for validating/calibrating the MEPDG, forecasting pavement performance, and determining treatment method and timing. However, it is very challenging to accurately and reliably collect detailed pavement crack data in field using either visual inspection or videolog-based method. Visual inspection requires tremendous effort to measure cracks in field, which is not even feasible on high-traffic-volume interstate highways. The accuracy is also hard to maintain by using visual inspection. Videolog-based methods require manual crack identification or automatic crack detection. Due to the impact of lighting conditions and the complicated pavement surface textures, the crack detection using videolog images is still a challenge.

The advancement of 3D laser technology provides a great opportunity to use 3D laser data to automatically collect detailed crack data in the field. In addition, the 3D laser technology has been proven to be robust in crack detection; it enables the extraction of detailed crack characteristics, including location, orientation, length, and width, which makes it feasible to study the pavement characteristics and crack deterioration behavior in the real-world environment, and it provides valuable information for determining cost-effective pavement crack

treatments. Though the data resolution at longitudinal direction is 5 mm using our current 3D laser system, which makes it difficult to accurately detect and measure fine, transverse cracks, this issue can be solved by improving the resolution of 3D laser system, especially at longitudinal direction. Actually, it has been claimed that 1 mm resolution at both transverse and longitudinal direction can be acquired at highway speed using the newest 3D laser system

Detailed crack characteristics, including location, orientation, length, width, density, and pattern, derived from 3D laser data, could be used to support a) fundamental study of pavement mechanics and deterioration behavior, b) validation of current pavement design methods and development of new design concepts and methods, c) determination of adequate treatment methods and timing, d) development of accurate and reliable pavement deterioration models, and e) development of cost-effective pavement maintenance programming, such as intelligent crack sealing planning.

This study focuses on evaluating the feasibility of using the detailed crack data derived from field-collected 3D laser data and will support the study of multi-scale crack deterioration behavior, such as an individual crack or pavement sections of different lengths (e.g. 100 feet, 0.1 mile, 1 mile, etc.); it will, also, identify the vulnerable and/or robust pavement sections/spots with high and/or low deterioration rates. Development of a method/tool to identify these sections/spots of interest is important for a) development of resilient and sustainable infrastructure system (to study why infrastructures behave differently), and b) application of localized treatments to isolated spots to save precious pavement maintenance and rehabilitation money. Ultimately, it should be able to be used to support the development of a long-term performance forecasting model in the future.

1. Research Objectives

The following are the objectives of the study presented in this chapter:

- 1) to identify the potential issues related to the crack deterioration study using long-term monitoring data derived from 3D laser data

- 2) to study the variability, caused by 3D data acquisition and automatic crack detection method so the changes resulting from crack growth instead of data variability can be better quantified
- 3) to discuss the potential utilization of the long-term monitoring data

Based on above objectives, field tests were conducted to collect the 3D laser data at different sites and at different times to study crack growth and deterioration.

2. Analysis of Crack Growth

This section presents an analysis of crack growth using long-term monitoring data. The long-term monitoring data was collected using 3D laser technology at different times. To study crack deterioration behavior, it is a logical, first step to explore the feasibility of using crack data collected at different times using multi-scales, such as an individual crack or pavement sections of different lengths (e.g. 100 feet, 0.1 mile, 1 mile, etc.); this will identify the vulnerable and/or robust sections/spots based on their high and/or low deterioration rates.

A series of field experimental tests were conducted at different times to collect 3D laser data on a one-mile asphalt pavement section located on Pooler Parkway in Pooler, Georgia, as shown in Figure 9.1. The test site is on a one-mile asphalt pavement section with a total of 4 lanes (two lanes in each direction). The data were collected on the outside lanes in both directions. Pooler Parkway has a moderate traffic volume, shown in Table 9.1. The AADT has remained around 18,000, although there is a slight variation over the past seven years.

The 3D data was collected seven times, as shown in Table 9.2, from the outside lanes of both direction since July 2011, using the GTSV. Table 9.2 shows the sensor angle configurations and the corresponding resolutions in longitudinal and transverse directions at seven time stamps.

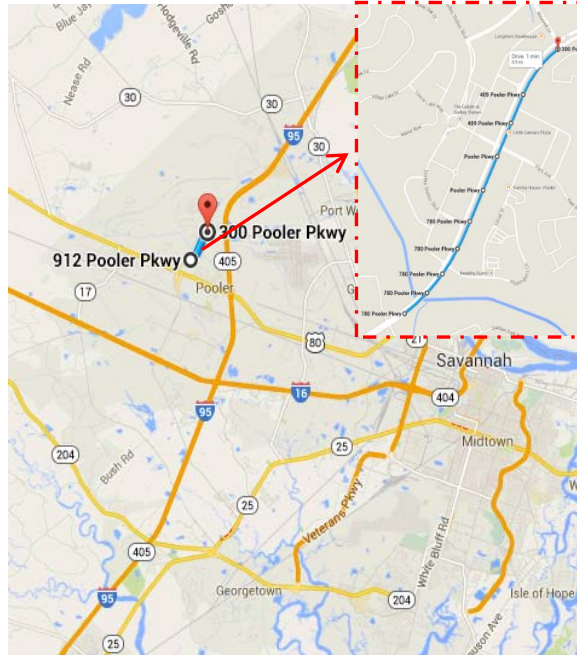


Figure 9.1 Test Site on Pooler Parkway, Pooler near Savannah, Georgia

Table 9.1 Pooler Parkway Traffic Volume

Year	AADT
2007	17530
2008	17440
2009	17090
2010	19190
2011	18730
2012	18410

Table 9.2 General Information of Data Collection

Date and Time	Configuration	Transverse Resolution	Longitudinal Resolution
07/29/2011 4pm	-15 degrees	1 mm	5 mm
09/29/2011 3pm	-15 degrees	1 mm	5 mm
10/21/2011 11am	-15 degrees	1 mm	5 mm
12/08/2011 1pm	-15 degrees	1 mm	5 mm
03/21/2012 12am	15 degrees	1 mm	5 mm
03/20/2013 4pm	15 degrees	1 mm	5 mm
12/07/2013 9am	15 degrees	1 mm	5 mm

Two experimental studies were conducted to explore the feasibility of studying crack deterioration behavior using 3D laser data and identify the potential issues that are useful for transportation agencies and vendors in their data collection. One study explored the growth of individual cracks over time; another study explored the clustered crack deterioration behavior of a 0.1 mile roadway section.

2.1 Individual Crack Analysis

This sub-section presents the data processing and analyses of the 3D laser data and crack data collected and extracted from different times in the long-term monitoring program to explore the behavior of individual crack growth and the corresponding issues. This will be crucial when 3D laser data is used to analyze individual crack propagation in the future.

2.1.1 Data Processing

Figure 9.2 shows a roadway image collected on 07/29/2011 with a labeled crack, C1, on the pavement. The detected crack has an offset to the original one for the purpose of visibility. 3D laser data have been collected seven times, as shown in Table 9.2, to analyze the crack growth in these individual cracks. The following steps were applied:

- Step 1: The 3D laser data, collected at 7 times, were analyzed using the same crack detection algorithms for the purpose of being consistent.
- Step 2: The extracted crack pieces were statistically analyzed. Each crack piece contains the properties of length, width, orientation (transverse/longitudinal), location (wheel path or non-wheel path), depth, etc. Instead of precisely registering the individual cracks extracted at two different times to analyze the crack growth topologically, this study analyzed each individual crack by clustering the crack pieces for each labeled crack and analyzed them statistically in terms of the crack width, length, orientation, etc.
- Step 3: Compared the change of each individual crack in terms of its property at different times.
- Step 4: The deterioration rate was then computed in terms of the growth of length, width, density, etc.
- Step 5: The deterioration (e.g. crack length growth) for different individual cracks were then compared to understand the typical crack length and width growth per year, length

and width growth at different times of the pavement life, and the crack deterioration rates among the different cracks.

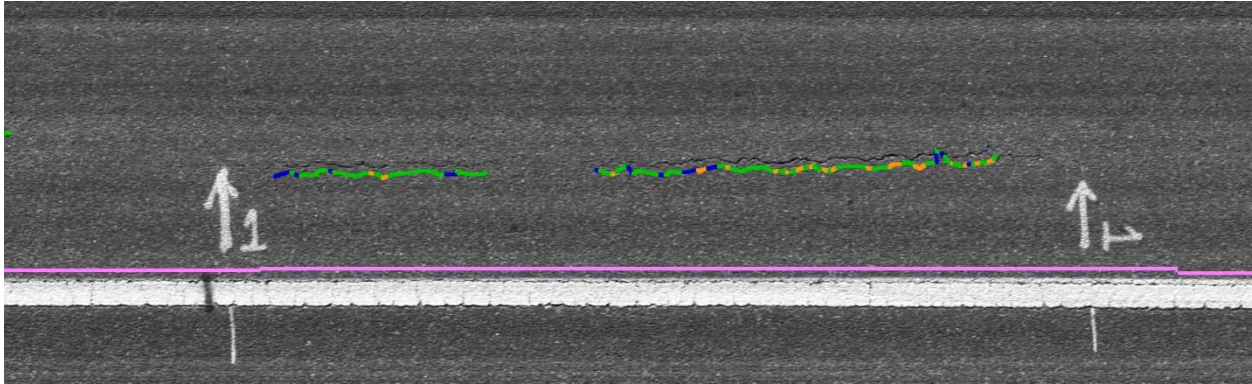


Figure 9.2 Labeled Crack

2.1.2 Data Analysis

The crack width measured using 3D laser data is more accurate for longitudinal cracks than for transverse cracks because the data resolution in the transverse direction (1 mm) is higher than the longitudinal direction (5 mm). Therefore, two longitudinal cracks were selected for evaluation of their crack growth. Figure 9.3 shows the locations of the cracks (C1 and C2) monitored on Pooler Parkway. These extracted cracks (C1 and C2) were collected at different times and are shown in Figure 9.4. Table 9.3 lists the crack lengths and the corresponding crack widths (weighted average width, standard deviation, and median value) at different times.

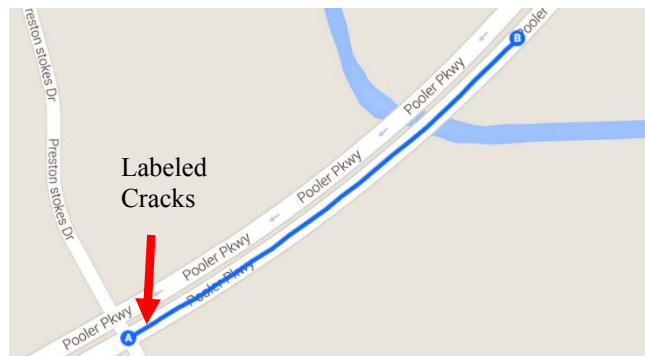


Figure 9.3 Locations of Labeled Cracks

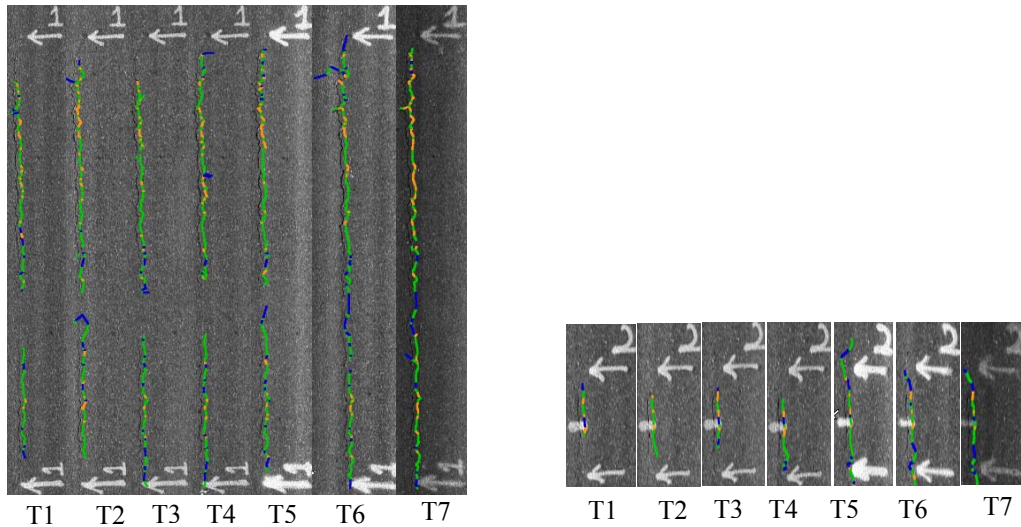


Figure 9.4 Crack Maps of Cracks C1 and C2 at Different Times

Table 9.3 Crack Length and Width of Cracks C1 and C2 at Different Times

Date	C1				C2			
	Length (m)	Width (mm)			Length (m)	Width (mm)		
		Average	Std. Dev.	Median		Average	Std. Dev.	Median
07/29/2011	3.69	4.8	1.4	4.6	0.35	5.5	1.7	5.8
09/29/2011	3.95	5.1	1.7	4.9	0.39	5.1	1.2	4.7
10/21/2011	4.35	4.6	1.4	4.4	0.38	5.0	1.7	4.6
12/08/2011	4.98	4.7	1.7	4.5	0.51	4.6	1.7	4.2
03/21/2012	4.42	4.9	1.6	4.8	1.27	4.3	1.6	3.8
03/20/2013	5.61	4.4	1.5	4.2	0.97	4.2	1.5	3.6
12/07/2013	5.26	5.3	1.8	5.1	1.05	4.2	1.4	3.9

As shown in Figure 9.4, the two selected cracks vary over time; the total length has increased, except for certain times when the crack detection algorithm did not successfully capture all the fine parts of the crack because of the following:

- The detection of fine cracks is still a challenge due to the limited data resolution (1 mm in the transverse direction and 5 mm in the longitudinal direction). The detected fine cracks might change from time to time when sensor configuration has minor changes or the data collection vehicle wanders. The changed fine part of a detected crack contributes most of crack length variation.

- Falsely detected cracks are another reason for crack length variation. For example, there are several small branches detected for C1 at T2, T4, and T6 as shown in Figure 9.4. These falsely detected cracks could be caused by data noise or the algorithms used.
- The length variation could also be caused by fines that fill the cracks, leading to the inaccurate detection of cracks. Cracks filled with fines will show less contrast on 3D laser data, which is a disadvantage to automatic crack detection.

To better evaluate the propagation of the selected cracks, the whole lengths of the selected cracks have been extracted and presented in Figure 9.5; the average widths and median widths of the selected cracks are presented in Figure 9.6. We can see that the lengths of these two cracks are increasing at different speeds. Slight variations can be observed from time to time, which can be mostly attributed to the variation of the crack detection results. On the other hand, the crack width does not show a clear increasing trend; instead, the average width varies significantly. Since median crack width is more robust to outliers than the average one, it was drawn in Figure 9.6 side by side with the average values (which are also listed in Table 9.3). It can be seen that the trends of the average values and median values are similar for these two cracks. For C1, the difference between the average width and the median value is about 0.2 mm; the difference is fairly stable over time. Thus, the two lines (the blue solid and dotted lines) in Figure 9.6 are almost parallel. The difference for C2 is between 0.3 mm and 0.6 mm with slight variation (red solid and dotted lines) as shown in Figure 9.6. These comparison might indicate that there is no apparent outlier in width measurements for these two cracks; either average value or median value can be used as a measure for the overall crack width. However, since crack length changes over time and a new crack might be tight at its early stage, it will lower the average crack width of the entire crack over time, which is hard to be used for modeling pavement deterioration. An ideal way is to select a crack with a fixed length and location; then, its average width being changed over time could be used to observe its deterioration, which requires a good registration (i.e. alignment) of the same crack over time. In addition, temperature is another important factor that could affect the change of crack width. For thermal cracks, they often close and open when temperature increases and decreases, which are caused by the expansion and contraction of asphalt concrete, respectively. Though C1 and C2 are more likely longitudinal, loading-induced cracks, their crack widths might also be affected by the change of temperature. It is suggested in

the future to measure a crack width at different times and different temperatures to more accurately assess the impact of temperature change.

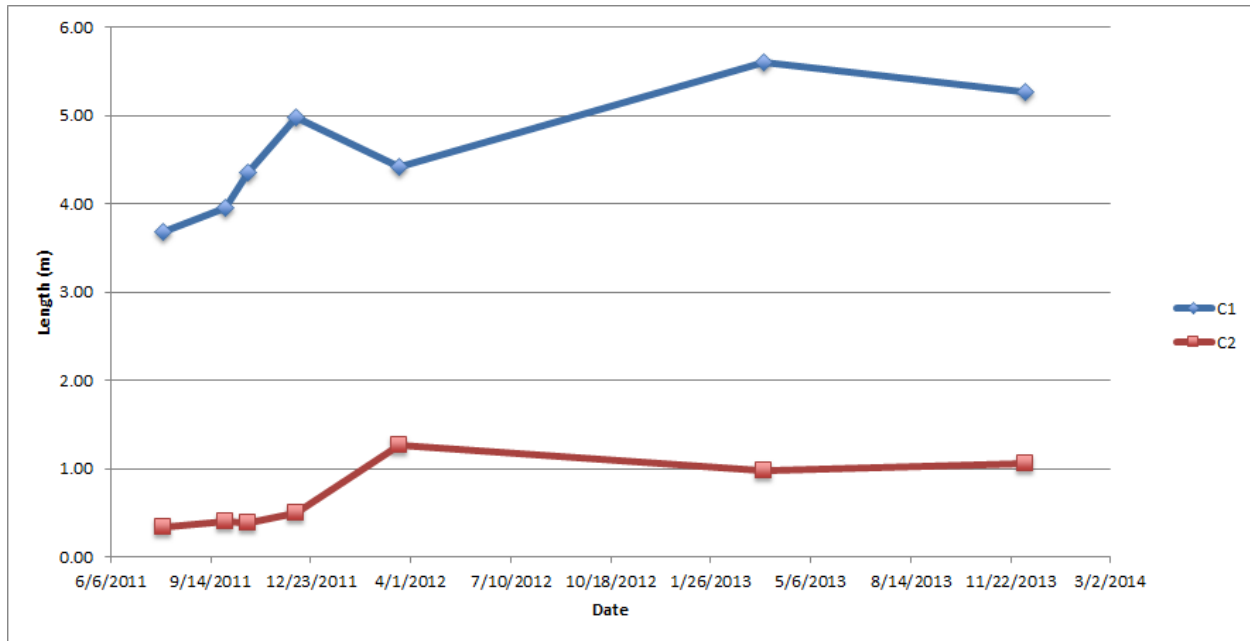


Figure 9.5 Trend of Total Length of Selected Cracks

Since a crack normally has no uniform crack width during the automatic crack detection, it is divided into smaller segments, each of which has the same crack width. Thus, a histogram of crack distribution can better describe a crack than the average crack width. Figure 9.7 shows the crack distributions of Cracks 1 and 2 over time. In general, when crack length increases over time, the length of the crack with the smaller crack width also increases. For C2 because the total length increased from 0.35 m to 1.05 m (see Table 9.3), the histogram changes more significantly than the one for C1 (the total length increased from 4.8 m to 5.3 m). It should be noted that, for C2 at T4 and T5, there is a small portion of cracks with width between 8 mm and 9 mm. However, at T6 and T7, the total length between 8 mm and 9 mm decrease. This phenomena might be caused by temperature. However, in considering the small total length (only about 40 mm) and the available data resolution (greater than 1 mm), it can be considered as normal measurement variation.

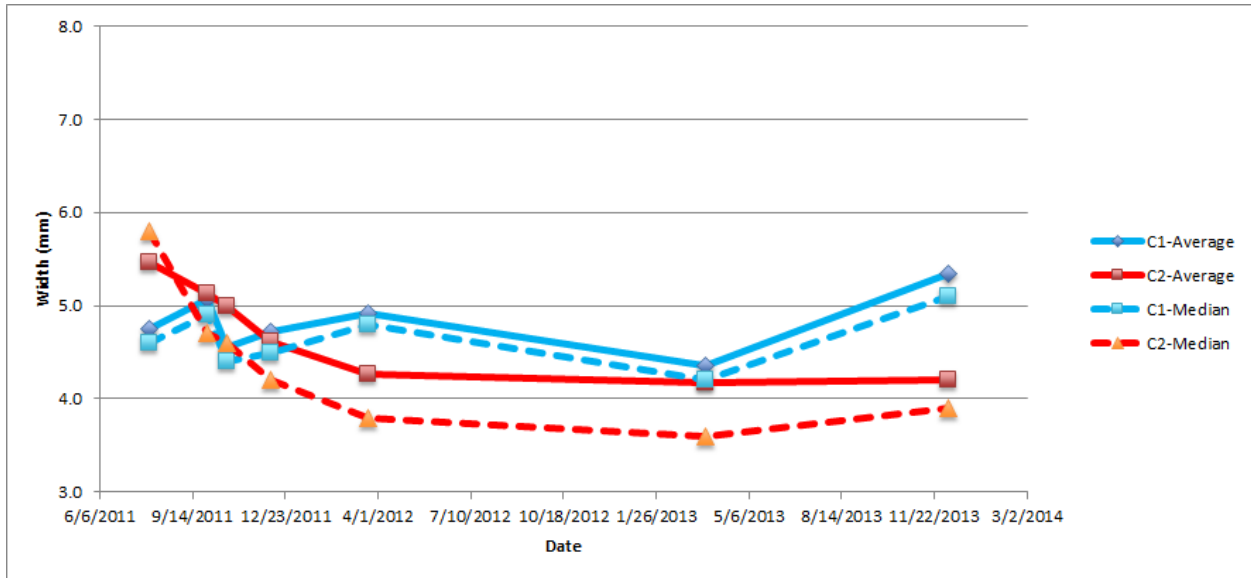
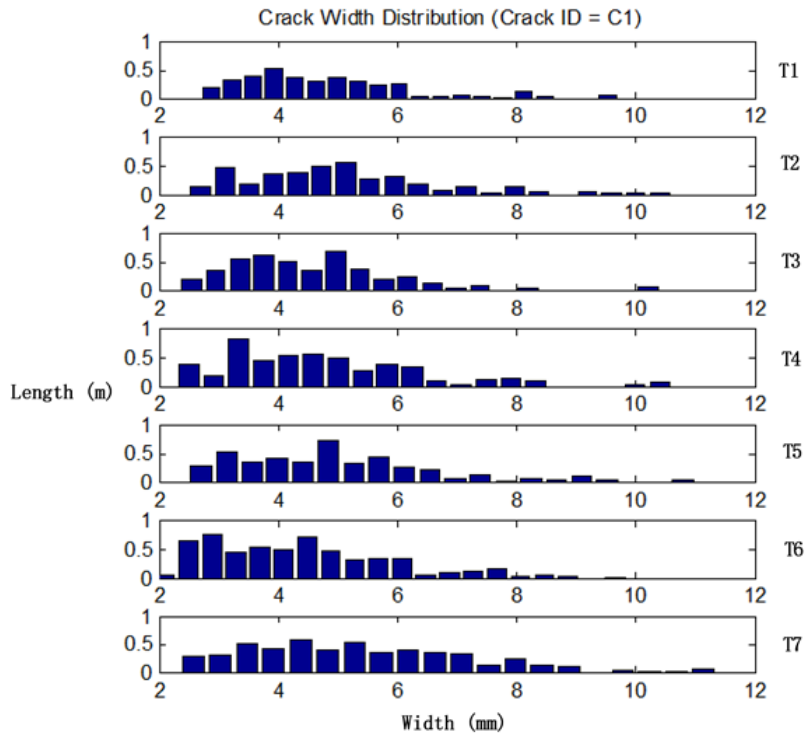


Figure 9.6 Trend of Average Width and Median Width of Selected Cracks



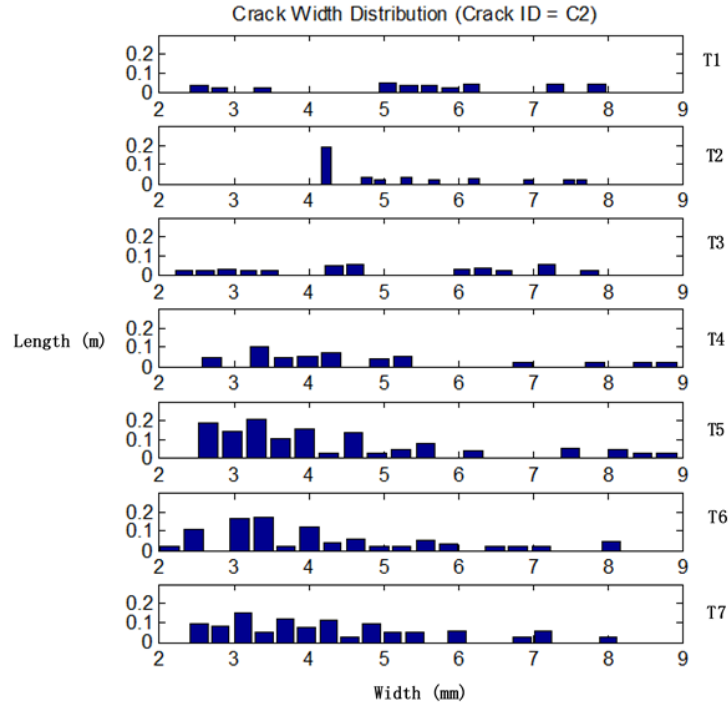


Figure 9.7 Crack Width Distributions of Selected Cracks

2.2 Clustered Crack Analysis

The study of individual crack growth is useful for revealing the behavior of crack propagation in length and width. This section will consider a section of pavement as a whole and analyze the overall growth of the clustered cracks, which can be used to study the pavement performance related to pavement structure, traffic load, and environment.

2.2.1 Data Processing

To consider the variation of pavement structure and pavement conditions, the 1-mile test section on Pooler Parkway was divided into 10 subsections, each of which was 0.1 mile long. Then, statistical analyses were performed on each subsection to study the growth of the clustered cracks in terms of length and length-weighted average width. The following steps were applied:

- Step 1: For consistency, the 3D laser data, collected at 7 different times were analyzed using the same crack detection algorithms.
- Step 2: The 1-mile test section was divided into 10 subsections, each of which was 0.1 mile. The total crack length was calculated for each subsection at each timestamp. Then, a linear regression was performed for each subsection to determine the crack's increasing

rate in length. Different crack increase rates in different subsections might indicate different structural conditions, which can be used for engineering investigation.

- Step 3: To study the crack width growth, a length-weighted average width was used to study the crack's change over time. The *Length-Weighted Average Width* can be defined as

$$Average_Width = \frac{\sum L_i W_i}{\sum L_i}$$

where L_i is the length of crack i in a subsection and W_i is the width of crack i in the subsection. To trace the crack width growth of a specific group of cracks, e.g. the initial cracks, the new cracks should be excluded. An ideal method is to register the detected cracks at different times, then choose only the cracks that align with the initial ones.

However, doing this is still a challenge. We used a simplified method based on the crack width histogram and disregarded the cracks that were tight. Then, the length-weighted average width was computed for each subsection at each times. Linear regression was performed to determine the crack width increase rate.

2.2.2 Data Analysis

- **Crack Length in Clustered Sections**

We computed the total crack length for each 0.1-mile subsection and evaluated the crack growth quantitatively by examining the propagation rate of the total crack length in each subsection at different times. Figure 9.8 shows the overall trend of the total crack length in each 0.1-mile subsection for the outside lanes in both directions of Pooler Parkway. In general, the total crack length in each subsection shows an increasing trend in the quantity of cracks. However, some variations can be observed, which could have been caused by the GSTV's wandering during data collection. The quantity of the cracks in the westbound lane is apparently greater than in the eastbound lane. The total crack length in the eastbound subsections ranged from 10 m to 74 m at the beginning of the study and has developed to be between 20 m to 150 m; the westbound subsections developed from between 80 m and 230 m to be between 100 m and 270 m. In Figure 9.8, different colors of the trend lines are used to indicate the magnitude of the propagation or increasing rates: green lines show increasing rates less than 0.02 m/day (7.3 m/year); red lines

show increasing rates greater than 0.04 m/day (14.6 m/year); and blue lines show increasing rates in between.

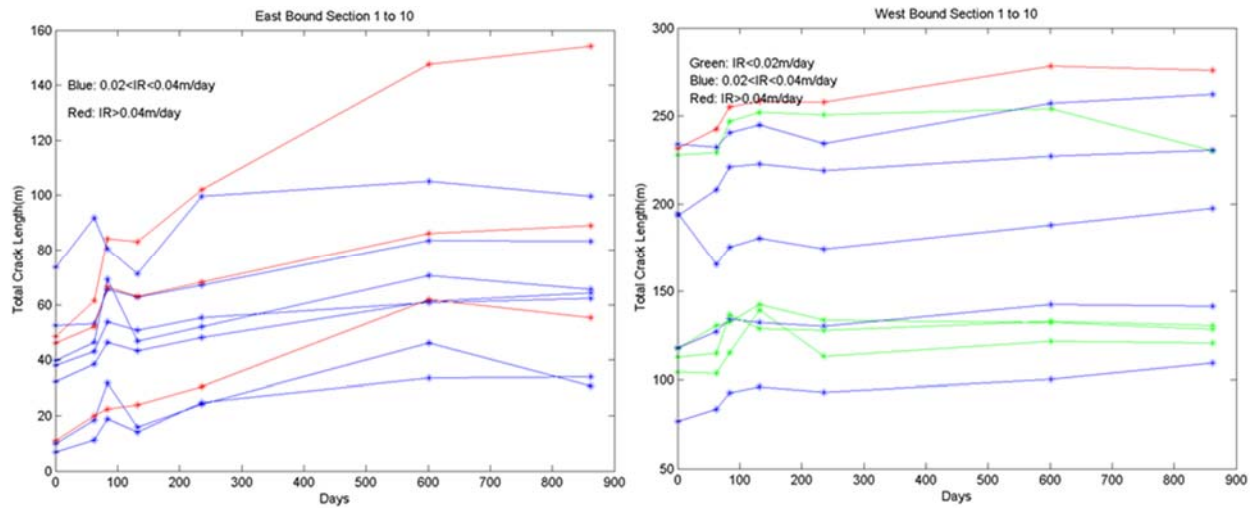


Figure 9.8 Eastbound and Westbound Subsections Total Crack Length Trends

The propagation rate for the total crack length for each subsection was obtained through linear regression of total crack length against time, which can be represented as follows:

$$Total\ Crack\ Length = \beta_1 t + \beta_0$$

where t represents time and β_1 indicates the crack length propagation rate.

Univariate linear regression was conducted between total crack length of all timestamps for each subsection and time. The detailed results are listed in Table 9.4 and

Table 9.5.

Table 9.4 Eastbound Subsections Total Crack Length Regression

Section No	Total Length (m)	Increasing rate (β_1) (m/day / (m/year))	R ²
1	53-83	0.04 (14.6)	0.856
2	46-89	0.05 (18.3)	0.856
3	38-62	0.02 (7.3)	0.691
4	32-64	0.03 (11.0)	0.888
5	7-34	0.03 (11.0)	0.829

6	49-154	0.12 (43.8)	0.914
7	74-105	0.03 (11.0)	0.510
8	10-46	0.03 (11.0)	0.454
9	40-71	0.03 (11.0)	0.426
10	11-62	0.06 (21.9)	0.881

Table 9.5 Westbound Subsections Total Crack Length Regression

Section No	Total Length (m)	Increasing rate (β_1) (m/day (m/year))	R²
1	104-122	0.01 (3.7)	0.097
2	76-109	0.03 (11.0)	0.761
3	230-278	0.05 (18.3)	0.757
4	227-254	0.0 (0.0)	0.002
5	117-135	0.0 (0.0)	0.002
6	118-142	0.02 (7.3)	0.669
7	113-133	0.01 (3.7)	0.233
8	194-197	0.02 (7.3)	0.315
9	233-262	0.03 (11.0)	0.841
10	193-230	0.03 (11.0)	0.521

The regression results of the eastbound subsections are better than the ones of the westbound subsections. The goodness of fit (R^2) of eastbound subsections is at least 0.42. However, Subsections 7 to 9 in the eastbound test section have fairly low R^2 values, which could be caused by the variations at the earlier timestamps. The length of the cracks for all the eastbound subsections increases by the rate of 0.02-0.06 m/day (7.3-21.9 m/year), except for the sixth subsection, which increases by 0.12 m/day (43.8 m/year). Visual inspection reveals that a significant amount of load cracking has developed since the pavement performance monitoring. The westbound subsections have a higher quantity of cracks; however, the cracks' increase rates are slightly lower than those of the eastbound subsections. The westbound crack increase rates ranges from 0 to 0.05 m/day (0 to 18.3 m/year). With larger condition variations, some regressions of the westbound subsections are of poor quality with R-Square as low as 0.002.

In general, the total crack length of the test site on Pooler Parkway is increasing with considerable variations. Such variations could be caused by non-uniform pavement structural

quality or by the data variations. As a result, further studies are needed to analyze the true causes of such variations.

- **Crack Width in Clustered Sections**

Similar to the total crack length, we evaluated the length-weighted average crack width by taking all the cracks into consideration. However, the average width generally shows little increments, which could be because new cracks generate over time and these new cracks are tight in width at their early stages. As a result, the length-weighted average crack width by taking all the cracks, including the old cracks and new cracks, cannot be used to reveal the real trend of crack width growth over time. To study the propagation rate of the crack width of old cracks, we assumed that new cracks fall into the tightest crack categories. This assumption can be further illustrated in Figure 9.9. The red bars represent new cracks, and the blue bars represent old cracks.

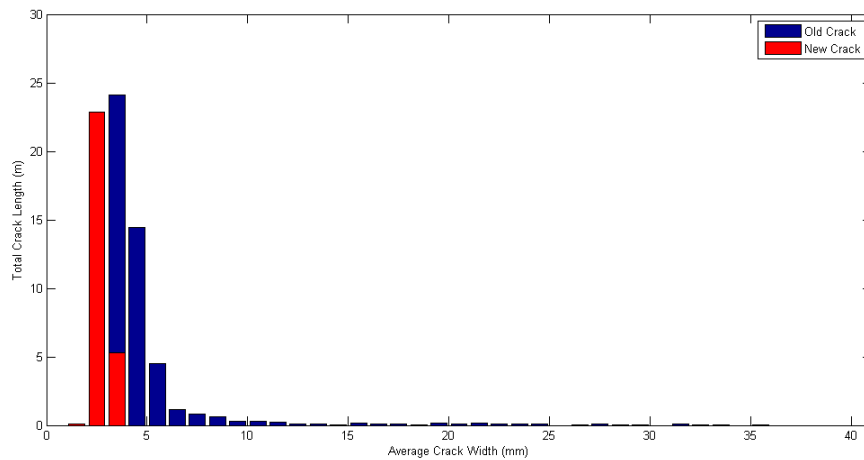


Figure 9.9 Assumption of Average Crack Width Analysis

Based on this assumption, we can evaluate the propagation rate of crack width by first disregarding these new cracks from the data at each timestamp. Then, we conduct linear regression based on the cracks that have been adjusted. The entire process can be described as follows:

- Step 1: Define quantity of cracks in each subsection for initial timestamp T_0 as L_0 ;

- Step 2: For each timestamp i , remove the tightest cracks by a total length of $(L_i - L_0)$ in each subsection;
- Step 3: Conduct linear regressions based on the average width of the remaining cracks (i.e. old cracks) for each subsection.

Following these three steps, we have evaluated the 20 0.1-mile subsections on Pooler Parkway and the results are presented in Figure 9.10 and Figure 9.11. As shown in Figure 9.10, most subsections (subsection 1 to 6, and 10) in the eastbound test section show an average increasing rate of crack width around 0.0015 mm/day (0.55 mm/year) (two subsections show an increasing rate slightly lower than 0.0015 mm/day (0.55 mm/year), and four subsections show a higher increase rate), indicating that the average width of the cracks increases more than 0.5 mm per year in the eastbound test section under the current moderate traffic volume and weathering. The eastbound test section also contains three subsections (section 7, 8, and 9) that show unclear trends with large variations, as shown in the right figure in Figure 9.10. Careful examination showed that such variation could be attributed to the absence of pavement markings in the collected 3D laser data, which caused a significant number of false positives during automatic crack detection. Besides the false positive cracks, the classification of regions of lanes also failed because of the lack of lane markings, which further contributed to the variation of the trends by including extra cracks lying on the edges of the lane.

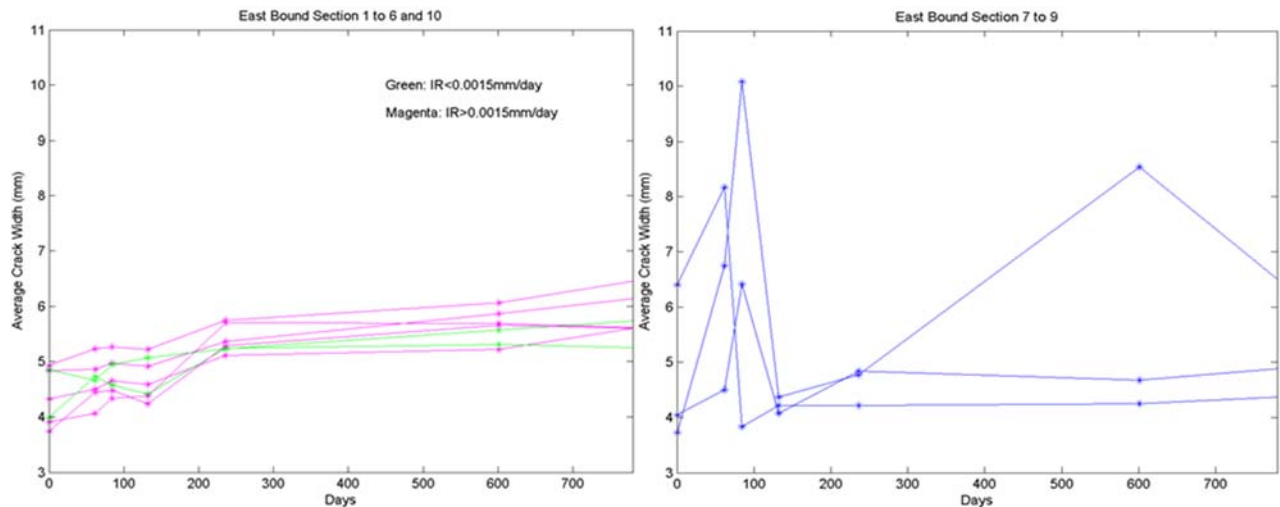


Figure 9.10 Eastbound Subsections Average Crack Width Trend

The detailed regression results are listed in Table 9.6. Accordingly, the data of the three subsections (7, 8, and 9) in red are problematic because of the lack of pavement markings. Regressions will not produce meaningful results and, thus, are omitted. The R² values of all valid regressions are above 0.6, indicating a strong linear correlation.

The length-weighted average width of all ten subsections in the westbound direction shows overall good trends with minor variations (Figure 9.11). Two out of the ten subsections have a propagation rate greater than 0.0025mm/day (0.91 mm/year), and three are below 0.0015mm/day (0.55 mm/year), leaving half the number of subsections in between.

Table 9.7 lists the detailed regression results. The R² values of most regressions are above 0.7, indicating good correlations. Sections 1 and 2 have the highest propagation rate in terms of average width, while sections 4, 6, and 7 have the lowest propagation rates. Looking further into the causes to the different propagation rates among these subsections (Sections 4, 6, and 7 at specific times) is recommended.

Table 9.6 Eastbound Average Crack Width Increasing Ratio Regression

Section No	Increasing ratio (mm/day (mm/year))	R ²
1	0.0018 (0.66)	0.886
2	0.0018 (0.66)	0.955
3	0.0013 (0.47)	0.852
4	0.0014 (0.51)	0.778
5	0.0018 (0.66)	0.636
6	0.0031 (1.13)	0.712
7	--	--
8	--	--
9	--	--
10	0.0019 (0.69)	0.740

Note: -- indicates problematic data set

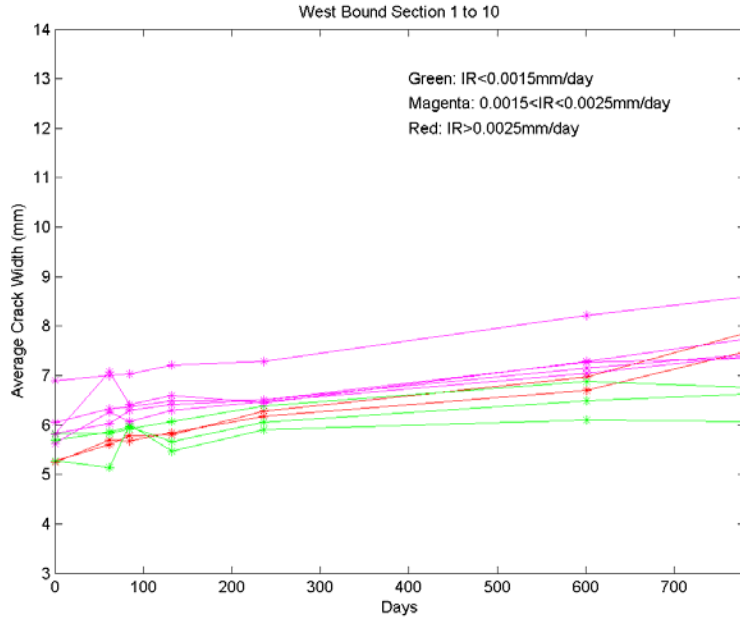


Figure 9.11 Westbound Subsections Average Crack Width Trend

Table 9.7 Westbound Average Crack Width Increasing Ratio Regression

Section No	Increasing ratio (mm/day (mm/year))	R ²
1	0.0031 (1.13)	0.972
2	0.0026 (0.95)	0.960
3	0.0018 (0.66)	0.959
4	0.0012 (0.44)	0.818
5	0.0018 (0.66)	0.730
6	0.0011 (0.40)	0.912
7	0.0009 (0.33)	0.476
8	0.0019 (0.69)	0.933
9	0.0022 (0.80)	0.994
10	0.0015 (0.55)	0.949

3. Issues of Long-term Monitoring Data

This section identifies the issues of using long-term monitoring data to study the crack deterioration behavior, which might be the source of data variation.

It is important to collect data at the same sampling area/region at different timestamps so they can be compared consistently to evaluate the crack growth. In addition, the temperatures when data is collected should also be comparable, thus, the growth of crack width can be consistently evaluated. The following are the factors that could lead to inconsistent sampling area/region at different timestamps:

- **Vehicle lateral wandering**

It is difficult to collect the data along the same path at different times because vehicle wandering always happens. The sensor coverage at different times could vary with a lateral displacement of a sensing vehicle. A vehicle's lateral wandering would not be an issue when the entire lane is covered, including both left and right pavement markings, because a consistent sampling area/region can be identified with the left and right pavement markings. Although the sensors are able to cover an area slightly wider than an entire pavement width (e.g. 4 meters), a vehicle's wandering that is large due to changing lanes, avoiding obstructions, etc. could lead to inconsistent sampling area/region because the left and right pavement markings are not included. Below are some examples.

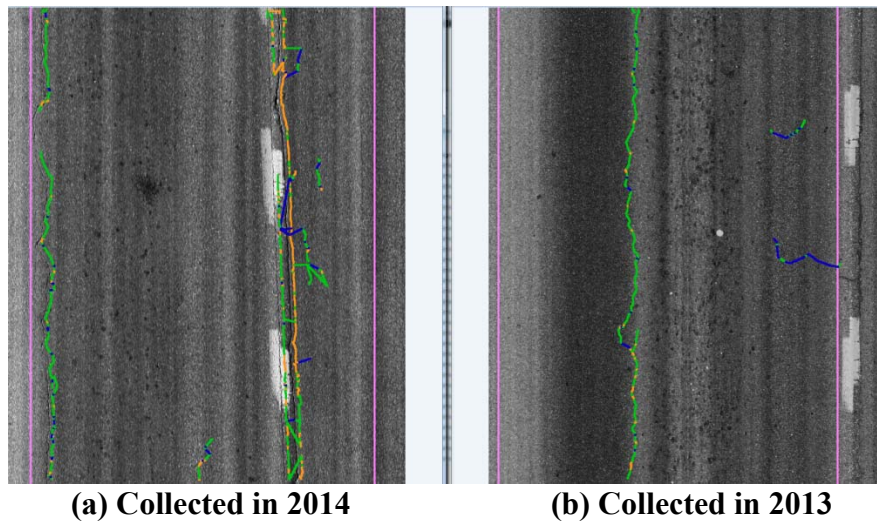
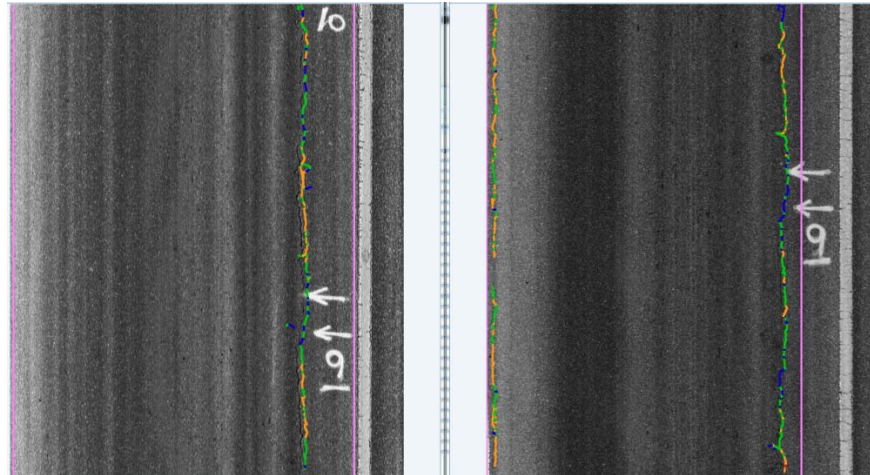


Figure 9.12 Inconsistent Sampling Area/Region Caused by Vehicle Wandering

The sampling areas/regions in Figure 9.12 are different. Thus, the computations of crack growth by comparing these two images are incorrect.

- **Inconsistent pavement marking detection or eroded pavement marking**

The left and right pavement markings are often used to identify and define a consistent sampling area/region in lateral/transverse directions. If the detection of pavement marking is incorrect at different timestamps, the sampling area/region could be defined incorrectly. Figure 9.13 shows an example.



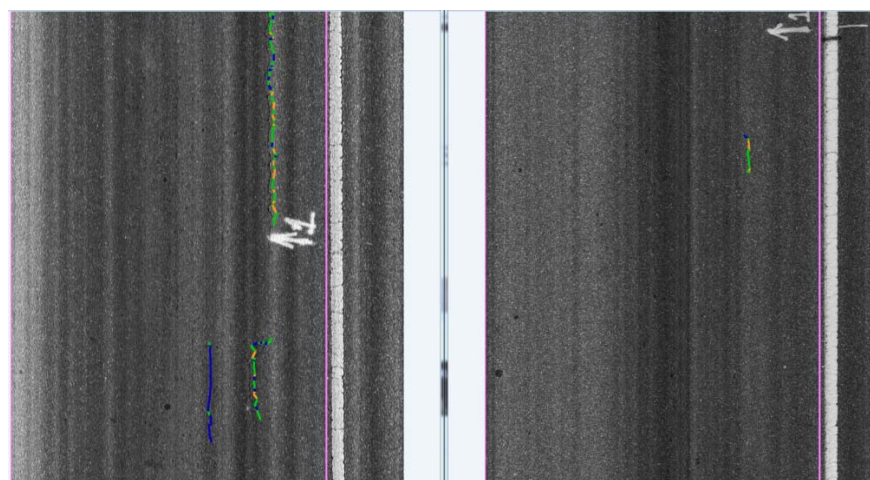
(a) Collected in 2014

(b) Collected in 2013

Figure 9.13 Inconsistent Sampling Area/Region Caused by Incorrect Pavement Marking Detection

- **Lack of consistent longitudinal references**

Longitudinal reference is crucial for establishing a consistent sampling area/region. The possible longitudinal reference candidates are the milepost markers (one mile sample) or other manual pavement markers. It is typically more challenging when the sample area or region is small (say 5 meters) because there could be a longitudinal shift in data collection. Figure 9.14 shows an example in which a longitudinal shift happened in two consecutive data collections; consequently, the cracks in these two images cannot be registered and directly compared.



(a) Collected in 2014

(b) Collected in 2013

Figure 9.14 Inconsistent Sampling Area/Region Caused by Shift of Data Collection in Longitudinal Direction

Other than the inconsistent sampling area/region, the accuracy of crack detection and crack width measurement is another source of data variation. Due to the limitation of 3D laser data resolution (the transverse resolution is 1 mm and the longitudinal resolution is 5 mm), fine cracks with crack widths less than 2 mm cannot be completely detected. As for crack width, the theoretical accuracy for a longitudinal crack is 1 mm; it is 5 mm for a transverse crack. Thus, it is still difficult to measure the width of a fine crack. However, with the advancement of sensing technology, it is believed that the data resolution can be further improved.

4. Summary

The chapter presents a feasibility study of asphalt pavement crack deterioration behavior using long-term monitoring 3D laser data that has been collected since 2011 on a one-mile test site on Pooler Parkway near Savannah, Georgia. Two types of studies were performed. The first studied the crack growth in length and width for two selected individual cracks; the second studied the crack growth of clustered cracks in 0.1-mile subsections. These two studies demonstrated the use of long-term monitoring 3D laser data to explore the detailed crack deterioration behavior at the levels of individual cracks and clustered cracks, which can be used to support a) fundamental study of pavement mechanics and deterioration behavior, b) validation of current pavement design methods and development of new design concepts and methods, c) determination of adequate treatment methods and timing, d) development of accurate and reliable pavement deterioration models, and e) development of cost-effective pavement maintenance programming, for example an intelligent crack sealing planning.

3D laser technology is still an emerging technology that is being applied to support highway agencies' research and engineering practice. Before it can be fully implemented in agencies' various applications, sufficient calibration/validation is invaluable and indispensable. The study presented in this chapter fulfills this purpose. Other than the feasibility study of crack deterioration behavior, the potential issues were also discussed and uncovered, which are useful for researchers and industries for further improving the technology. The following are suggested for future study:

- Data collection vehicle lateral wandering causes the variation of data sampling area/region. To mitigate the impact of this issue, more robust algorithms are needed for

pavement marking detection, even in the case when a pavement marking is missed, and crack detection. Furthermore, a mechanism is needed to facilitate a vehicle driver's ability to conveniently maintain the vehicle in the middle of a lane while sensing data is being collected.

- The evaluation of crack width increasing rate was based on an assumption that new cracks fall into the category of the tightest cracks without further checking whether the excluded cracks were actually new cracks or not. This assumption could create some data variation because the tight, old cracks could, also, be excluded. Thus, developing a crack registration method to spatially align cracks that are collected at different timestamps is recommended; then, the behavior of crack width changing can be studied for spatially registered individual cracks or clustered cracks.
- The current 3D laser technology is capable of collecting project-level and network-level pavement distress data for purpose of pavement management and maintenance. However, studying detailed pavement crack deterioration behavior requires higher resolution of 3D laser data to detect finer cracks. The 3D laser system used in this study has a resolution of 5 mm at longitudinal direction, which limits the capability to detect and measure the width of fine transverse cracks. Thus, there is still a need to enhance the resolution of 3D laser system. Fortunately, some manufacturers started to develop the new 3D laser system with 1 mm resolutions.
- In current study, length-weighted average and median (50th percentile) crack widths are used to analyze the crack-width-related crack propagation. To provide more informative statistics that can be more relevant to pavement maintenance, rehabilitation, and reconstruction (MR&R), other factors, e.g. 75th, 90th, or 95th percentiles, can be used to represent the overall crack width. Further discussion with pavement engineers and experts will be needed.

Chapter 10 Conclusions and Recommendations

Thanks to the support of USDOT and GDOT, this research project scientifically and comprehensively validated the use of CRS&SI technologies to improve the inventory, condition assessment, and management of traffic sign and pavement asset. Using the sensing data, including the 3D laser data, video log images, and mobile LiDAR, collected by the GTSV, the scientific validation approaches include 1) laboratory tests in a well-controlled environment; 2) field tests on carefully selected test road sections; 3) acquisition of data from other transportation agencies; 4) development of algorithms and applications; 5) statistical analysis; and 6) extensive discussion with TAC members and other participating transportation agencies. The following list the major conclusions and recommendations.

1. Conclusions

The following conclusions are categorized based on the research focuses for sign asset and pavement asset.

- **Sign Asset - Develop and validate an enhanced sign inventory procedure using image-processing-based method and mobile LiDAR**

To improve the efficiency of traffic sign data collection, the automatic traffic sign detection and recognition algorithms using video log images and mobile LiDAR were tested using real data acquired from different transportation agencies and the GTSV. The results demonstrate the potential for applying these automatic algorithms for establishing a cost effective sign inventory method.

For the automatic traffic sign detection algorithm using video log images provided by LaDOTD and the city of Nashville, more than 75% of the traffic signs were correctly detected. For the automatic traffic sign recognition algorithm using video log images collected by the GTSV, 81% of the stop signs and 96% of the speed limit signs were correctly recognized. For the automatic traffic sign detection algorithm using mobile LiDAR, more than 94% of the traffic signs were correctly detected based on 17.5 miles of the LiDAR data collected by the GTSV on I-95 near Savannah, Georgia. The LiDAR technology is very promising for sign data collection.

While the current algorithms cannot achieve a satisfactory detection and recognition accuracy for a fully automatic data collection purpose, an enhanced procedure was proposed. The procedure enables the incorporation of these developed algorithms and technologies into the manual process method. The efficiency of the proposed procedure can be further enhanced by improving the detection and recognition algorithms. The ultimate goal of a full automation can be achieved when the accuracy of the algorithms reach a satisfactory level. The preliminary assessment results, based on 47 traffic signs on I-95, demonstrate a 40% improvement over the manual data collection process (i.e. the frame-by-frame manual review).

- **Sign Asset – A real-world large-scale case study on traffic sign inventory and condition assessment**

A real-world large-scale case study was conducted on I-285 to practice the enhanced procedure for traffic sign inventory and condition assessment. Other than the data collection productivity, the enhanced procedure greatly reduces the danger to engineers by enabling them to take inventory of signs without being exposed to roadway hazards, especially on interstate highways and near overhead signs. Based on the case study, there are total 2,969 signs on I-285. The majority of the installed traffic signs on interstate highways are messages signs that convey direction, destination, and service information (2,321 signs, 78.17%). Only limited number of warning signs and regulatory signs are installed to indicate hazardous conditions or regulate drivers' behavior. A large percentage of installed traffic signs are mounted on overhead structures on interstate highways (643 signs, 21.66%). There are 252 signs in poor condition that require sign maintenance action based on the sign condition assessment.

Visual inspection on the high-resolution video log images reveals the possible reasons for damaged signs. The most frequently occurring sign damage type is surface failure on milepost signs due to truck gusts. They are located on the concrete barriers, on roadsides, or on medians. These signs are damaged by the strong truck gusts that are created by fast moving trucks. Another sign type suffering frequent damage is made up of exit signs that are damaged due to the instability of their dual posts. They are located at the interstate exits. The

inspection shows that the signs are damaged by the unbalanced vibration and twisting of the dual posts. In addition, post failures also frequently occur due to direct crash impact or soft bases. The only type of overhead sign that is damaged is D3-1 (i.e. street name sign) mounted on bridges. The majority of D3-1 signs are damaged due to surface failure (i.e. color fading and erosion).

- **Sign Asset - Feasibility study of using mobile LiDAR for sign condition assessment**

To validate the use of mobile LiDAR for sign retroreflectivity condition assessment, ten Type I stop signs collected in a community in Savannah, Georgia, have been tested to demonstrate the feasibility of the tested LiDAR-based method. The ground truths were established using both nighttime visual inspection and retroreflectometer measurement. The retroreflectivity condition assessment results using the proposed method are consistent with all of the nighttime visual inspection results; they match 90% of the retroreflectometer measurement results in differentiating good and bad sign retroreflectivity conditions. Using the developed mobile-LiDAR based method, coupled with the integrated GTSV, the traffic sign retroreflectivity condition assessment can potentially be conducted cost-effectively at highway speed.

- **Sign Asset - Develop a prototype GIS-based sign management system**

A prototype GIS-based sign management system was developed in this study. The objective is to demonstrate the capability of a GIS platform for integrating different data sources, including traffic sign data, video log images, and GIS maps, managing important traffic sign data, and supporting various sign maintenance practices. Though this prototype is not a comprehensive, final product, it is the foundation for full implementation in the future.

- **Pavement Asset - Network-level rut depth measurement using the 3D laser**

Rutting is one of the important pavement performance measures required by HPMS, and every state DOT is required to submit the data to FHWA annually. However, the point-based laser measurement methods (e.g. 3 points) commonly used by state DOTs may not be reliable due to vehicle wandering, variation of rut locations, and rut shapes. Preliminary test results show that 3-point and 5-point rut bar systems significantly underestimate the rut depth, and

the average relative measurement errors for 3-point and 5-point rut bar systems are about 63% and 44%. If the number of sensors is more than 25, the relative measurement error drops constantly with a value below 10%. With a 39-point equally-spaced rut bar system, the relative measurement error is about 8%.

Compared to the traditionally used manual and rut-bar measurement methods, the 3D laser has virtually 100% coverage in a travel lane width. It provides a more accurate and reliable method to measure rut depth than the traditional rut-bar method. According to laboratory and field tests, the 3D laser can provide rut depth measurements with satisfactory accuracy. The measurement error is within ± 3 mm and satisfies the accuracy requirements of many state transportation agencies. It is capable of performing project-level and network-level rutting condition assessment.

Besides providing the information needed for network-level rutting condition assessment, the integrated 3D laser provides much denser rutting data. In cooperation with GDOT liaison engineers, case studies were performed on several state and non-state routes using the integrated 3D laser. A systematic approach was developed to aggregate the raw, continuous rut depth measurements on each pavement segment and to generate different statistical indicators that can provide added value to engineers of state DOTs. In comparison with GDOT's past rutting survey results, the 3D laser can provide more useful network-level rutting data and better support the network-level maintenance decision making. It was suggested by GDOT liaison engineers that the 60th percentile rut depth is a good rutting indicator on each pavement segment.

- **Pavement Asset - Identify isolated ruts using the 3D laser in support of effective localized treatment**

The accurate and dense rutting information acquired from the 3D laser provides an opportunity to further identify the isolated ruts, which has never been done in the past due to the lack of continuous and accurate rutting measurements in longitudinal direction. The identification of isolated ruts can better support effective, low-cost localized pavement treatments, and the efficient use of the currently stringent pavement preservation funds. After discussing these issues with GDOT liaison engineers, four sets of criteria were proposed to

define an isolated rut: rut depth requirement, rut length requirement, rut division criterion, and rut termini determination criterion. Case studies on two selected roadway sections show the developed approach is applicable to and promising for use in transportation agencies' pavement preservation practice.

- **Pavement Asset - Develop and validate a quantitative method to scientifically evaluate the performance of different automatic pavement crack detection algorithms**

Pavement distress segmentation is identified as a crucial step for automatic distress detection and classification. Researchers have developed many segmentation algorithms, but it is difficult to compare the performance of different algorithms efficiently without an accurate quantitative method. Also, it is hard for a transportation agency to perform a quality check when automatic pavement crack detection is applied in its data collection. To address these issues, a novel quantification method based on the buffered Hausdorff distance was developed to evaluate the performance of distress segmentation algorithms.

The proposed method was compared with four other common quantification methods (MSE, SC, ROC, and Hausdorff distance) on both real data (raw downward pavement images acquired from GDOT) and synthetic data. It was found that the proposed buffered Hausdorff scoring measure accurately reflected the observed performance of the segmentation techniques and outperformed the other three quantification methods. Both MSE and SC are not sensitive to the relative proximity of the crack pixels between the segmented image and the ground truth image. The Hausdorff distance measure is very sensitive to outliers and is heavily influenced by isolated noise pixels that are far away from crack pixels. Thus, it does not accurately reflect the overall performance of a segmentation method. ROC is a useful scoring measure, but it suffers due to the fact that across a certain boundary, all crack pixels are either detected as true defects or false alarms. The proposed buffered Hausdorff distance measure gave evaluation results consistent with the visual performance inspection of different segmentation techniques. It also achieved good score separation to distinguish between the performance of different methods.

Two potential applications of the proposed buffered Hausdorff distance measure were also explored, including the selection of proper distress segmentation algorithms and the

optimization of algorithm parameter settings. Because the distress classifier definitions vary among states and regions, the testing of segmentation precision is of critical importance in assessing the reliability of pavement distress segmentation algorithms. The proposed method provides a solution for transportation agencies to choose the proper pavement distress segmentation algorithm based on their own survey requirements and data format. Also, the proposed method provides an opportunity to optimize the parameter setting for each segmentation algorithm, since it gives sortable scoring measures for the algorithm performance under each parameter setting. Therefore, the proposed method is expected to help transportation agencies determine their automated pavement distress survey strategies.

- **Pavement Asset - Validate the asphalt pavement crack detection using the 3D laser**

The 3D laser is insensitive to different lighting conditions, low intensity contrast, and pavement oil marks, unlike the traditional line scan camera. Laboratory tests on fabricated crack samples show consistent detection results in daytime and nighttime. Cracks with widths greater than 2mm can be detected easily. However, a hairline crack with a width of approximately 1mm is hard to detect due to the current resolution of the integrated 3D laser. Field tests on Georgia SR 80 were conducted under three different lighting conditions, daytime with shadow, daytime without shadow, and nighttime. The crack detection results show very good consistency and the average difference of performance scores is less than 2%. Though low intensity contrast is a challenge for the traditional line scan camera for crack detection, the test result shows no difficulty for the integrated 3D laser as long as the crack is distinct on surface depth change. Similarly, oil stains can be effectively removed from a possible falsely detected crack because of indistinguishable depth change.

To validate the crack width measurement accuracy, 12 spots on two longitudinal cracks were selected on Georgia SR 275 with manually measured crack width as the ground truth. Cracks with widths greater than 2mm can be detected correctly. However, cracks equal to and less than 1mm cannot be detected correctly. Compared to the manually measured results, crack widths were captured well by the automatic method. The maximum absolute difference of crack width was 1mm, and the average absolute difference was 0.4mm. This result shows a promising potential to measure crack width for further crack classification tasks. While the

3D-line-laser-provided software can effectively detect the longitudinal crack widths, the transverse crack width cannot be reliably detected because the current data resolution in the driving direction is about 5mm. Improvement is needed in this area.

- **Pavement Asset - Feasibility Study of Crack Deterioration Behavior Using 3D Laser Data**

A feasibility study of asphalt pavement crack deterioration behavior was performed using long-term monitoring 3D laser data that has been collected since 2011 on a one-mile test site on Pooler Parkway near Savannah, Georgia. First, the crack growth in length and width for two selected individual cracks was analyzed; second, the crack growth of clustered cracks in 0.1-mile subsections was studied. These two studies demonstrated the use of long-term monitoring 3D laser data to explore the detailed crack deterioration behavior at the levels of individual cracks and clustered cracks, which can be used to support a) fundamental study of pavement mechanics and deterioration behavior, b) validation of current pavement design methods and development of new design concepts and methods, c) determination of adequate treatment methods and timing, d) development of accurate and reliable pavement deterioration models, and e) development of cost-effective pavement maintenance programming, for example an intelligent crack sealing planning.

2. Recommendations

The performance of the above research focuses aimed at bridging the gap between the state-of-the-practice CRS&SI technologies and GDOT and other state agencies' practices; it also aimed at validating and promoting the use of technologies to improve the transportation asset data collection, condition assessment, and management. The research results show that using the automatic image-processing-based sign detection and recognition algorithms and the LiDAR-based sign detection can improve the current time-consuming image-based traffic sign data collection process. It also shows that the 3D laser is promising for producing an accurate and reliable rutting measurement that can be used as a standard rut measurement for HPMS. In addition, the validated 3D laser technology has the potential to advance automatic crack detection by better addressing low intensity contrast and poor lighting conditions. The following suggest the future research and implementation:

- The large-scale case study on I-285 traffic sign inventory and condition assessment shows that the proposed enhanced sign inventory procedure using video log images and mobile LiDAR is very promising and can greatly reduce the effort of manual sign data collection especially on interstate highways. It is suggested that, using the proposed and validated method, a comprehensive sign inventory could be done for the entire 2,500-centerline-mile interstate highways in Georgia.
- Sign retroreflectivity condition assessment is of great concern in GDOT and other state agencies. The current preliminary study on engineer grade STOP signs show that mobile LiDAR could be a promising alternative to the time-consuming manual method for sign retroreflectivity condition assessment. However, further tests on more engineer grade STOP signs with different retroreflectivity conditions are still needed. Also, tests on other types of traffic signs, e.g. speed limit signs, warning signs, etc., with different sheeting materials are needed to study the sensitivity of the proposed method on different colors and sheeting materials.
- The currently developed prototype of the GIS-based sign management system has demonstrated the capability to integrate different spatial and non-spatial data sources, such as GIS maps, roadway images, and sign data, and improve sign management and maintenance practice. Next, a pilot study is suggested to further materialize the functionalities by using a large-scale dataset and introducing the GDOT's practice on sign management and maintenance.
- The comprehensive validation of network-level rutting measurement and isolated rutting detection shows that the 3D laser technology can be used to conduct the statewide rutting data collection. In considering the difficulty for measuring rut depth on interstate highways, especially on the high-traffic-volume highways like I-285, it is suggested to firstly conduct rutting data collection for the entire 2,500-centerline-mile interstate highways. The collected data can be used for two purpose. First, the data can be fed into COPACES database. Thus, the current manual rutting data collection on interstate highway can be replaced by the automatic method. Second, the full-coverage rutting data can further be used to identify isolated spots where rutting is a problem and local treatment can be done.

- The validated crack detection using 3D laser data shows that this technology is capable of collecting cracking data. Along with the validation of crack classification that is under development in an on-going research project (RS-GAMS Phase 2), the results can be fed into COPACES, which is very useful for high-traffic-volume interstate highways. After the validation of crack classification is done, it is suggested to conduct a cracking survey for the entire interstate highways in Georgia.
- Data collection vehicle lateral wandering causes the variation of data sampling area/region. To mitigate the impact of this issue, more robust algorithms are needed for pavement marking detection, even in the case when a pavement marking is missed, and crack detection. Furthermore, a mechanism is needed to facilitate a vehicle driver's ability to conveniently maintain the vehicle in the middle of a lane while sensing data is being collected.
- The evaluation of crack width increasing rate was based an assumption that new cracks fall into the category of the tightest cracks without further checking whether the excluded cracks were actually new cracks or not. This assumption could create some data variation because the tight, old cracks could, also, be excluded. Thus, developing a crack registration method to spatially align cracks that are collected at different timestamps is recommended; then, the behavior of crack width changing can be studied for spatially registered individual cracks or clustered cracks.
- The current 3D laser technology is capable of collecting project-level and network-level pavement distress data for purpose of pavement management and maintenance. However, studying detailed pavement crack deterioration behavior requires higher resolution of 3D laser data to detect finer cracks. The 3D laser system used in this study has a resolution of 5 mm at longitudinal direction, which limits the capability to detect and measure the width of fine transverse cracks. Thus, there is still a need to enhance the resolution of 3D laser system. Fortunately, some manufacturers started to develop the new 3D laser system with 1 mm resolutions.

- In current study, length-weighted average and median (50th percentile) crack widths are used to analyze the crack-width-related crack propagation. To provide more informative statistics that can be more relevant to pavement maintenance, rehabilitation, and reconstruction (MR&R), other factors, e.g. 75th, 90th, or 95th percentiles, can be used to represent the overall crack width. Further discussion with pavement engineers and experts will be needed.

Appendix I: List of Poor Condition Signs on I-285

RCLINK	Milepoint	MUTCD	Visual Condition
0891040700	8.357	W8-13	Surface/Post Failure
1211040700	24.365	I13	Surface/Post Failure
1211040700	3.244	D10-3	Surface/Post Failure
0891040700	25.407	W4-1	Surface Failure
0891040700	25.443	W4-1	Surface Failure
1211040700	25.989	Unknown	Surface Failure
0891040700	3.584	Unknown	Surface Failure
1211040700	10.720	R2-4	Surface Failure
1211040700	2.538	R2-1	Surface Failure
0671040700	6.620	Missing	Surface Failure
0891040700	22.925	I-3	Surface Failure
0891040700	22.013	I-3	Surface Failure
1211040700	24.926	E5-1A	Surface Failure
1211040700	21.896	E5-1A	Surface Failure
0671040700	2.796	E5-1A	Surface Failure
0891040700	25.609	E5-1A	Surface Failure
0891040700	23.813	E5-1A	Surface Failure
0891040700	19.226	E5-1A	Surface Failure
0891040700	11.323	E5-1A	Surface Failure
0891040700	12.447	E5-1A	Surface Failure
0891040700	14.546	E5-1A	Surface Failure
0891040700	6.062	E5-1A	Surface Failure
0891040700	6.712	E5-1A	Surface Failure
1211040700	26.332	E5-1a	Surface Failure
0891040700	15.956	E5-1a	Surface Failure
1211040700	54.252	E5-1a	Surface Failure
0891040700	24.394	E5-1a	Surface Failure
0891040700	18.456	E5-1a	Surface Failure
1211040700	12.420	E5-1	Surface Failure
0891040700	12.166	E5-1	Surface Failure
0891040700	13.710	E5-1	Surface Failure
0891040700	3.854	E5-1	Surface Failure
1211040700	21.420	E5-1	Surface Failure
0631040700	0.505	D9-18E	Surface Failure
0891040700	12.743	D9-18E	Surface Failure
0671040700	5.294	D3-1	Surface Failure
0671040700	2.608	D3-1	Surface Failure
0671040700	2.624	D3-1	Surface Failure
0671040700	1.341	Dc3-1	Surface Failure

RCLINK	Milepoint	MUTCD	Visual Condition
0671040700	1.333	D3-1	Surface Failure
0671040700	2.635	D3-1	Surface Failure
0671040700	5.241	D3-1	Surface Failure
1211040700	23.073	D10-3	Surface Failure
1211040700	23.075	D10-3	Surface Failure
1211040700	25.797	D10-3	Surface Failure
0891040700	1.672	D10-3	Surface Failure
0891040700	13.946	D10-3	Surface Failure
0891040700	9.784	D10-3	Surface Failure
0891040700	9.388	D10-3	Surface Failure
0891040700	8.597	D10-3	Surface Failure
0891040700	5.628	D10-3	Surface Failure
0891040700	5.430	D10-3	Surface Failure
0891040700	5.037	D10-3	Surface Failure
0891040700	4.240	D10-3	Surface Failure
0891040700	4.837	D10-3	Surface Failure
0891040700	9.586	D10-3	Surface Failure
0891040700	19.686	D10-3	Surface Failure
0891040700	18.893	D10-3	Surface Failure
0891040700	18.101	D10-3	Surface Failure
0891040700	17.111	D10-3	Surface Failure
0891040700	17.704	D10-3	Surface Failure
0891040700	21.865	D10-3	Surface Failure
0891040700	22.658	D10-3	Surface Failure
1211040700	21.313	D10-3	Surface Failure
0891040700	0.091	D10-3	Surface Failure
0891040700	17.507	D10-3	Surface Failure
1211040700	61.679	D10-3	Surface Failure
1211040700	60.984	D10-3	Surface Failure
0631040700	5.340	D10-3	Surface Failure
0631040700	2.761	D10-3	Surface Failure
0631040700	1.965	D10-3	Surface Failure
0631040700	0.983	D10-3	Surface Failure
0631040700	0.193	D10-3	Surface Failure
1211040700	3.244	D10-3	Surface Failure
1211040700	6.249	D10-3	Surface Failure
1211040700	8.224	D10-3	Surface Failure
1211040700	23.623	D10-3	Surface Failure
0671040700	7.133	D10-3	Surface Failure
1211040700	21.101	D10-3	Surface Failure
1211040700	21.101	D10-3	Surface Failure
1211040700	24.062	D10-3	Surface Failure

RCLINK	Milepoint	MUTCD	Visual Condition
0631040700	1.380	D10-3	Surface Failure
0631040700	1.182	D10-3	Surface Failure
0891040700	17.112	D10-3	Surface Failure
0891040700	11.231	D10-3	Surface Failure
0891040700	6.195	D10-3	Surface Failure
0891040700	5.431	D10-3	Surface Failure
0891040700	5.629	D10-3	Surface Failure
0891040700	5.233	D10-3	Surface Failure
1211040700	25.798	D10-3	Surface Failure
0891040700	1.672	D10-3	Surface Failure
0891040700	4.241	D10-3	Surface Failure
0891040700	4.439	D10-3	Surface Failure
0891040700	5.431	D10-3	Surface Failure
0891040700	5.629	D10-3	Surface Failure
0891040700	8.599	D10-3	Surface Failure
0891040700	9.587	D10-3	Surface Failure
0891040700	11.966	D10-3	Surface Failure
0891040700	13.947	D10-3	Surface Failure
0891040700	17.112	D10-3	Surface Failure
0891040700	17.705	D10-3	Surface Failure
0891040700	18.498	D10-3	Surface Failure
0891040700	18.894	D10-3	Surface Failure
0891040700	19.687	D10-3	Surface Failure
0891040700	21.865	D10-3	Surface Failure
0891040700	22.656	D10-3	Surface Failure
0891040700	24.736	D10-3	Surface Failure
1211040700	53.093	D10-3	Surface Failure
0631040700	0.193	D10-3	Surface Failure
0631040700	0.983	D10-3	Surface Failure
0631040700	1.964	D10-3	Surface Failure
0631040700	2.760	D10-3	Surface Failure
0631040700	5.339	D10-3	Surface Failure
0631040700	5.337	D10-3	Surface Failure
1211040700	8.224	D10-3	Surface Failure
1211040700	8.627	D10-3	Surface Failure
1211040700	11.716	D10-3	Surface Failure
1211040700	13.195	D10-3	Surface Failure
0671040700	4.508	D10-3	Surface Failure
1211040700	23.076	D10-3	Surface Failure
1211040700	6.644	D10-3	Surface Failure
0891040700	4.839	D10-3	Surface Failure
1211040700	61.473	D10-3	Surface Failure

RCLINK	Milepoint	MUTCD	Visual Condition
0891040700	6.816	D10-3	Surface Failure
0671040700	2.380	D10-3	Surface Failure
1211040700	8.426	D10-3	Surface Failure
0671040700	6.736	D10-3	Surface Failure
1211040700	20.888	D10-3	Surface Failure
1211040700	11.716	D10-3	Surface Failure
0671040700	4.509	D10-3	Surface Failure
0891040700	6.913	D10-2	Surface Failure
0891040700	22.756	D10-2	Surface Failure
0891040700	14.839	D10-2	Surface Failure
1211040700	53.403	D10-2	Surface Failure
1211040700	22.805	D10-2	Surface Failure
0671040700	1.647	D10-2	Surface Failure
0631040700	1.670	D10-2	Surface Failure
0891040700	10.875	D10-2	Surface Failure
0891040700	1.969	D10-2	Surface Failure
0891040700	22.755	D10-2	Surface Failure
1211040700	53.403	D10-2	Surface Failure
1211040700	61.170	D10-2	Surface Failure
1211040700	61.436	D10-2	Surface Failure
0891040700	14.838	D10-2	Surface Failure
1211040700	62.188	D10-2	Surface Failure
1211040700	60.877	D10-2	Surface Failure
1211040700	8.929	D10-1	Surface Failure
1211040700	6.931	D10-1	Surface Failure
1211040700	9.210	ClickIt	Surface Failure
0891040700	3.552	BuckleUp	Surface Failure
0891040700	18.639	W9-1	Post Failure
0891040700	17.978	W8-13	Post Failure
0891040700	24.919	W8-13	Post Failure
0631040700	2.551	W8-13	Post Failure
1211040700	25.996	W4-3	Post Failure
0891040700	19.366	W4-3	Post Failure
0891040700	23.797	W4-3	Post Failure
1211040700	62.348	W4-3	Post Failure
0891040700	5.060	W4-2	Post Failure
1211040700	26.227	W4-1	Post Failure
0891040700	16.160	W4-1	Post Failure
1211040700	6.813	W4-1	Post Failure
0891040700	3.669	W1-1	Post Failure
1211040700	13.131	ThrowingTrash	Post Failure
0891040700	6.057	ThrowingTrash	Post Failure

RCLINK	Milepoint	MUTCD	Visual Condition
0891040700	20.411	ThrowingTrash	Post Failure
1211040700	54.620	ThrowingTrash	Post Failure
1211040700	53.453	ThrowingTrash	Post Failure
1211040700	25.725	RightLaneExitOnly	Post Failure
1211040700	9.670	RightLaneExitOnly	Post Failure
1211040700	6.245	R2-4	Post Failure
0671040700	6.361	R2-4	Post Failure
1211040700	0.459	R2-1	Post Failure
1211040700	1.013	R2-1	Post Failure
1211040700	2.958	R2-1	Post Failure
1211040700	5.710	R2-1	Post Failure
1211040700	7.674	R2-1	Post Failure
1211040700	25.290	R2-1	Post Failure
0891040700	22.878	NoDUI	Post Failure
1211040700	8.616	M3-3	Post Failure
0891040700	23.230	M3-2	Post Failure
1211040700	8.616	M1-1	Post Failure
0891040700	16.679	M1-1	Post Failure
1211040700	11.204	I13-A	Post Failure
0631040700	0.686	GAHero	Post Failure
1211040700	9.489	E5-1a	Post Failure
1211040700	22.994	E5-1	Post Failure
0891040700	11.163	E5-1	Post Failure
1211040700	11.329	E5-1	Post Failure
0891040700	13.223	D12-5	Post Failure
0891040700	23.264	D12-5	Post Failure
1211040700	22.803	D10-3	Post Failure
1211040700	12.221	D10-3	Post Failure
1211040700	22.912	D10-3	Post Failure
1211040700	26.000	D10-3	Post Failure
0891040700	8.004	D10-3	Post Failure
0891040700	10.179	D10-3	Post Failure
0891040700	13.349	D10-3	Post Failure
0891040700	21.666	D10-3	Post Failure
0891040700	22.458	D10-3	Post Failure
0891040700	24.440	D10-3	Post Failure
1211040700	3.872	D10-3	Post Failure
1211040700	8.984	D10-3	Post Failure
1211040700	11.260	D10-3	Post Failure
1211040700	5.849	D10-3	Post Failure
1211040700	2.614	D10-3	Post Failure
0631040700	4.748	D10-3	Post Failure

RCLINK	Milepoint	MUTCD	Visual Condition
0631040700	2.958	D10-3	Post Failure
1211040700	54.489	D10-3	Post Failure
1211040700	53.710	D10-3	Post Failure
0891040700	17.706	D10-3	Post Failure
0891040700	11.967	D10-3	Post Failure
0891040700	10.774	D10-3	Post Failure
1211040700	21.506	D10-3	Post Failure
1211040700	6.050	D10-3	Post Failure
1211040700	9.875	D10-2	Post Failure
1211040700	1.987	D10-1	Post Failure
1211040700	25.969	ClickIt	Post Failure
1211040700	10.538	BuckleUp	Post Failure
1211040700	8.780	BuckleUp	Post Failure
0631040700	2.124	W8-13	Obstructed
0671040700	6.690	W8-13	Obstructed
0891040700	18.712	W4-1	Obstructed
0891040700	3.759	W13-3	Obstructed
0891040700	18.948	W13-2	Obstructed
0891040700	19.026	ThrowingTrash	Obstructed
0891040700	4.804	R2-1	Obstructed
0891040700	17.907	R2-1	Obstructed
0891040700	5.695	NoDUI	Obstructed
0891040700	18.052	M3-1	Obstructed
0891040700	18.052	M1-1	Obstructed
0891040700	18.840	I-3	Obstructed
0891040700	0.836	I-3	Obstructed
0891040700	4.744	GAHero	Obstructed
0891040700	18.816	E5-1A	Obstructed
1211040700	4.616	D3-1	Obstructed
0891040700	1.136	D2-1	Obstructed
0891040700	3.008	D10-3	Obstructed
1211040700	5.250	D10-3	Obstructed
0891040700	2.463	D10-3	Obstructed
1211040700	10.151	D10-2	Obstructed
0891040700	13.343	W8-13	Dirty
0891040700	25.812	W4-1	Dirty
0891040700	2.242	SlowerTraffic	Dirty
0891040700	14.824	R7-201a	Dirty
1211040700	53.256	R2-1	Dirty
0891040700	20.402	I-3	Dirty
1211040700	60.870	D10-3	Dirty
0891040700	9.785	D10-3	Dirty

RCLINK	Milepoint	MUTCD	Visual Condition
0891040700	3.644	D10-3	Dirty
1211040700	54.311	D10-3	Dirty
0631040700	0.585	D10-3	Dirty

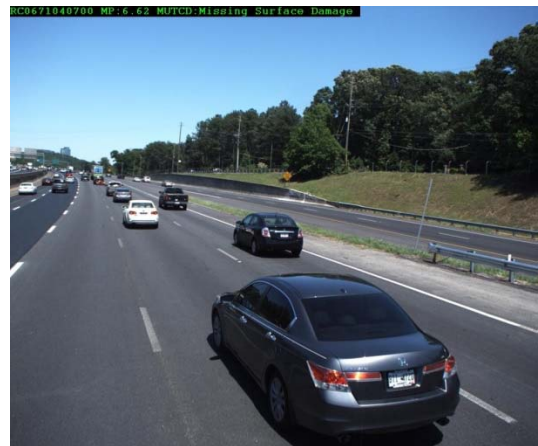
Surface Failure (150 Cases)













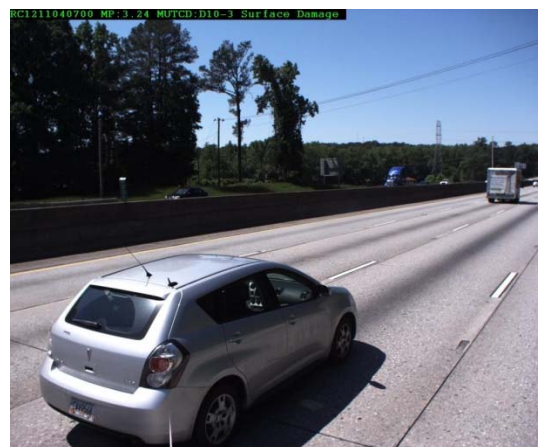
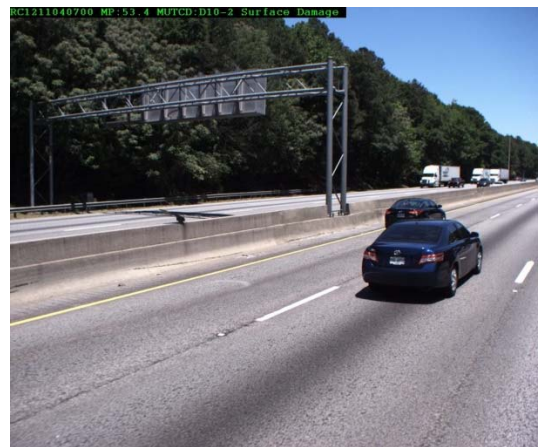


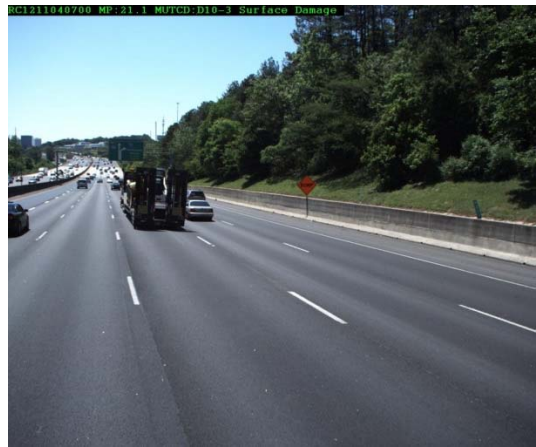


















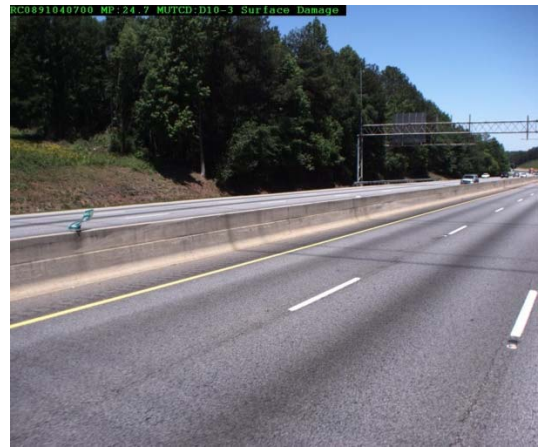


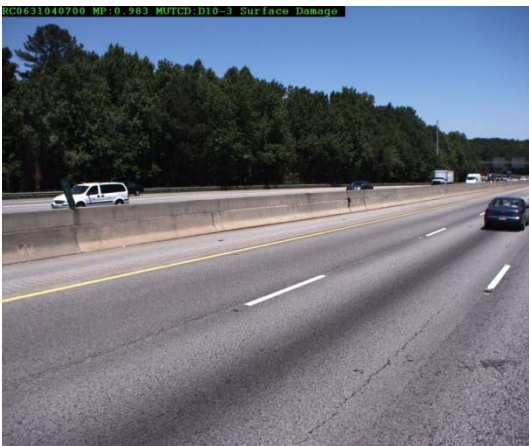
















Post Failure (73 Cases)













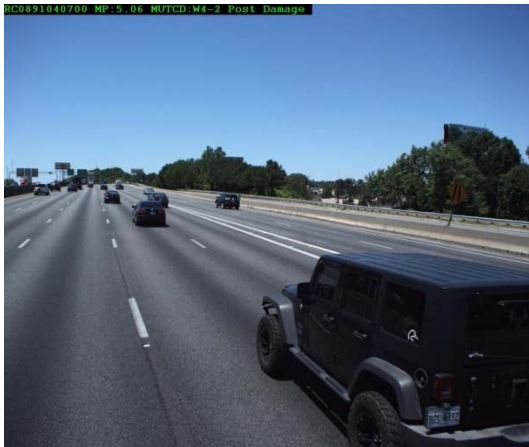






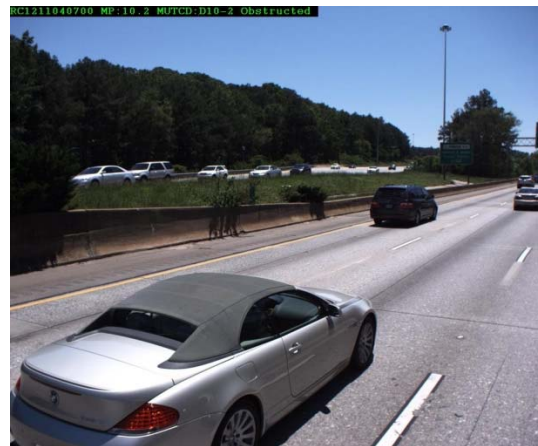






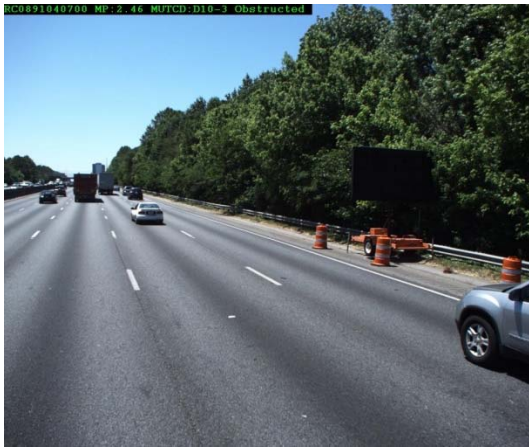


Obstructed (21 Cases)

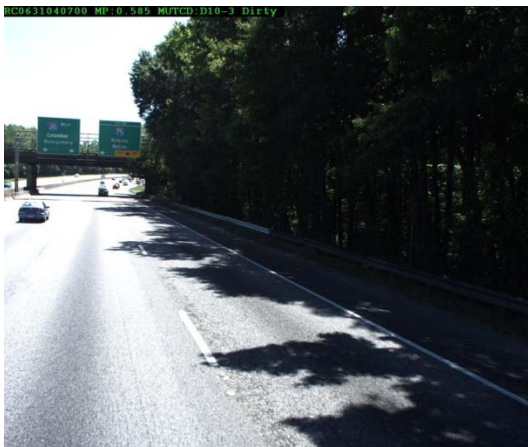








Dirty (11 Cases)





Appendix II: List of Overhead Signs on I-285

RCLINK	Milepoint	MUTCD	Overhead Type
1211040700	0.044	E1-1	Sign Bridge
1211040700	0.045	E6-2A	Sign Bridge
0631040700	0.114	E6-2A	Sign Bridge
0631040700	0.114	NoTrucks	Sign Bridge
0631040700	0.114	E11-1	Sign Bridge
1211040700	0.314	E6-2A	Sign Bridge
1211040700	0.315	E11-1	Sign Bridge
0631040700	0.621	E6-2A	Sign Bridge
0631040700	0.626	E11-1	Sign Bridge
0631040700	0.627	E6-2A	Sign Bridge
1211040700	0.796	E6-2A	Sign Bridge
1211040700	0.802	E1-1	Sign Bridge
1211040700	0.802	NoTrucks	Sign Bridge
0631040700	0.802	E11-1	Sign Bridge
0631040700	0.803	E6-2A	Sign Bridge
0631040700	0.803	E6-2A	Sign Bridge
1211040700	0.902	E1-1	Sign Bridge
1211040700	0.906	E1-1	Sign Bridge
1211040700	1.009	E6-2	Sign Bridge
0631040700	1.228	E11-2	Sign Bridge
0631040700	1.229	E6-2A	Sign Bridge
0631040700	1.230	E11-1D	Sign Bridge
0631040700	1.230	E6-2A	Sign Bridge
0631040700	1.501	E11-1	Sign Bridge
0631040700	1.502	E6-2A	Sign Bridge
0631040700	1.502	E6-2A	Sign Bridge
0631040700	1.502	E6-2A	Sign Bridge
0631040700	1.502	E11-1	Sign Bridge
0671040700	1.560	E1-1	Sign Bridge
0631040700	1.687	E6-2A	Sign Bridge
0631040700	1.687	E6-2A	Sign Bridge
1211040700	1.892	E1-1	Sign Bridge
1211040700	1.892	E1-1	Sign Bridge
0891040700	1.969	NoTrucks	Sign Bridge
0891040700	1.970	E1-1	Sign Bridge
0891040700	1.971	E1-1	Sign Bridge
0631040700	2.057	E11-1E	Sign Bridge
0631040700	2.065	E11-2	Sign Bridge

RCLINK	Milepoint	MUTCD	Overhead Type
0631040700	2.066	E11-1	Sign Bridge
1211040700	2.087	E6-2A	Sign Bridge
0671040700	2.412	MoveAccident	Sign Bridge
0671040700	2.414	E6-2	Sign Bridge
1211040700	2.472	E6-2	Sign Bridge
0631040700	2.628	E6-2A	Sign Bridge
0671040700	2.862	StateLaw	Sign Bridge
0671040700	2.862	E6-2	Sign Bridge
0631040700	2.891	E6-2A	Sign Bridge
0631040700	2.891	E6-2A	Sign Bridge
0631040700	3.001	E6-2A	Sign Bridge
0631040700	3.001	E6-2A	Sign Bridge
0891040700	3.003	E1-1	Sign Bridge
0891040700	3.005	E1-1	Sign Bridge
0891040700	3.007	StateLaw	Sign Bridge
0891040700	3.372	E6-2	Sign Bridge
0891040700	3.374	D2-3	Sign Bridge
0631040700	3.507	E1-1	Sign Bridge
0631040700	3.511	E1-1	Sign Bridge
0631040700	3.524	E6-2A	Sign Bridge
0631040700	3.525	E6-2A	Sign Bridge
0631040700	3.525	E11-1	Sign Bridge
0891040700	3.573	E6-2	Sign Bridge
0891040700	3.573	NoTrucks	Sign Bridge
0891040700	3.573	E6-2	Sign Bridge
0891040700	3.574	MoveAccident	Sign Bridge
0891040700	3.744	E1-1	Sign Bridge
0891040700	3.744	E6-2	Sign Bridge
0891040700	3.744	E6-2	Sign Bridge
0891040700	3.808	E1-1	Sign Bridge
0891040700	3.808	E6-2A	Sign Bridge
0891040700	3.808	NoTrucks	Sign Bridge
0631040700	3.822	E11-1	Sign Bridge
0631040700	3.822	E6-2A	Sign Bridge
0631040700	3.822	E6-2A	Sign Bridge
0631040700	3.823	E6-2A	Sign Bridge
0671040700	3.881	NoTrucks	Sign Bridge
0671040700	3.883	E6-2	Sign Bridge
0891040700	3.905	E5-1A	Sign Bridge
0631040700	3.977	E1-1	Sign Bridge
0631040700	3.977	E1-1	Sign Bridge
0891040700	4.003	E1-1	Sign Bridge

RCLINK	Milepoint	MUTCD	Overhead Type
0891040700	4.004	E6-2A	Sign Bridge
0891040700	4.004	E11-1	Sign Bridge
0891040700	4.004	MoveAccident	Sign Bridge
0671040700	4.117	E1-1	Sign Bridge
0891040700	4.348	E1-1	Sign Bridge
0891040700	4.351	E1-1	Sign Bridge
0891040700	4.351	E1-1	Sign Bridge
1211040700	4.390	E6-2A	Sign Bridge
1211040700	4.391	E1-1	Sign Bridge
0631040700	4.430	E1-1	Sign Bridge
0631040700	4.430	E1-1	Sign Bridge
0631040700	4.515	E6-2A	Sign Bridge
0671040700	4.549	E6-2	Sign Bridge
0891040700	4.607	E11-1	Sign Bridge
0891040700	4.608	E1-1	Sign Bridge
0891040700	4.608	E6-2A	Sign Bridge
0671040700	4.779	E1-1	Sign Bridge
0671040700	4.785	E1-1	Sign Bridge
0891040700	4.813	NoTrucks	Sign Bridge
1211040700	4.814	E1-1	Sign Bridge
1211040700	4.814	E6-2	Sign Bridge
0891040700	4.814	E6-2	Sign Bridge
0891040700	4.817	E6-2	Sign Bridge
0891040700	4.821	E6-2	Sign Bridge
0891040700	4.830	StateLaw	Sign Bridge
0891040700	4.830	E1-1	Sign Bridge
0891040700	4.831	E6-2A	Sign Bridge
0631040700	5.068	E6-2A	Sign Bridge
0891040700	5.071	E6-2	Sign Bridge
0891040700	5.081	E6-2	Sign Bridge
0891040700	5.082	E6-2	Sign Bridge
0631040700	5.221	E6-2A	Sign Bridge
0631040700	5.231	E6-2A	Sign Bridge
0631040700	5.232	E11-1	Sign Bridge
0891040700	5.273	E11-1	Sign Bridge
0891040700	5.274	E6-2A	Sign Bridge
0891040700	5.274	E6-2A	Sign Bridge
0891040700	5.299	E6-2	Sign Bridge
0891040700	5.299	E6-2	Sign Bridge
0891040700	5.300	E6-2	Sign Bridge
0891040700	5.414	E6-2	Sign Bridge
0891040700	5.414	E6-2	Sign Bridge

RCLINK	Milepoint	MUTCD	Overhead Type
0891040700	5.432	E6-2	Sign Bridge
0891040700	5.432	E6-2	Sign Bridge
0891040700	5.444	E11-1	Sign Bridge
0891040700	5.444	E6-2A	Sign Bridge
0891040700	5.444	E6-2A	Sign Bridge
0671040700	5.452	E1-1	Sign Bridge
0671040700	5.453	NoTrucks	Sign Bridge
0671040700	5.455	E1-1	Sign Bridge
0631040700	5.528	E6-2A	Sign Bridge
0631040700	5.528	E11-1	Sign Bridge
0631040700	5.529	E6-2A	Sign Bridge
0631040700	5.719	E6-2A	Sign Bridge
0631040700	5.720	E6-2A	Sign Bridge
0671040700	5.803	E6-2	Sign Bridge
0671040700	5.810	E6-2	Sign Bridge
0631040700	5.837	E1-1	Sign Bridge
0631040700	5.838	E1-1	Sign Bridge
0671040700	5.977	E6-2	Sign Bridge
0671040700	5.980	E6-2	Sign Bridge
0671040700	5.989	E6-2	Sign Bridge
0891040700	6.149	E6-2	Sign Bridge
0891040700	6.151	E6-2	Sign Bridge
0891040700	6.164	E11-1	Sign Bridge
0891040700	6.164	E6-2A	Sign Bridge
0891040700	6.226	E6-2A	Sign Bridge
0891040700	6.226	E6-2A	Sign Bridge
0891040700	6.277	E6-2	Sign Bridge
0891040700	6.279	E6-2	Sign Bridge
1211040000	6.722	E6-2	Sign Bridge
1211040000	6.722	E6-2A	Sign Bridge
1211040700	6.757	NoTrucks	Sign Bridge
1211040700	6.758	E6-2A	Sign Bridge
0891040700	6.815	E1-1	Sign Bridge
0891040700	6.815	E11-1	Sign Bridge
0891040700	6.815	E6-2A	Sign Bridge
1211040000	6.898	E6-2A	Sign Bridge
1211040000	6.899	E6-2A	Sign Bridge
1211040000	6.899	E6-2	Sign Bridge
0671040700	6.934	E6-2	Sign Bridge
0671040700	6.934	E6-2A	Sign Bridge
0671040700	6.934	E11-1	Sign Bridge
0671040700	6.937	E11-1	Sign Bridge

RCLINK	Milepoint	MUTCD	Overhead Type
0671040700	6.939	E6-2	Sign Bridge
0671040700	6.945	NoTrucks	Sign Bridge
0671040700	6.945	E1-1	Sign Bridge
0891040700	6.996	E6-2A	Sign Bridge
0891040700	6.998	E6-2A	Sign Bridge
0891040700	6.998	E6-2A	Sign Bridge
0891040700	6.999	E11-1	Sign Bridge
1211040700	7.165	E6-2	Sign Bridge
0671040700	7.303	E6-2A	Sign Bridge
0671040700	7.306	E6-2	Sign Bridge
0671040700	7.307	E11-1	Sign Bridge
0671040700	7.308	E11-1	Sign Bridge
0891040700	7.395	E11-1	Sign Bridge
0891040700	7.395	E6-2A	Sign Bridge
0891040700	7.396	E1-1	Sign Bridge
0891040700	8.229	E1-1	Sign Bridge
0891040700	8.230	E1-1	Sign Bridge
1211040700	8.394	E1-1	Sign Bridge
1211040700	8.400	E1-1	Sign Bridge
1211040700	8.646	TrucksAllowed	Sign Bridge
1211040700	8.648	DIAG	Sign Bridge
0891040700	8.716	E6-2	Sign Bridge
1211040700	8.896	E6-2A	Sign Bridge
1211040700	9.419	E6-2A	Sign Bridge
1211040700	9.421	TrucksAllowed	Sign Bridge
1211040700	9.421	E11-1	Sign Bridge
1211040700	9.421	E6-2A	Sign Bridge
0891040700	9.947	E6-2	Sign Bridge
1211040700	9.967	E6-2	Sign Bridge
1211040700	10.095	E6-2	Sign Bridge
1211040700	10.097	E11-1	Sign Bridge
1211040700	10.328	E11-1C	Sign Bridge
1211040700	10.332	DIAG	Sign Bridge
0891040700	10.423	E6-2	Sign Bridge
0891040700	10.427	E1-1	Sign Bridge
0891040700	10.827	E1-1	Sign Bridge
0891040700	10.827	E1-1	Sign Bridge
0891040700	10.829	StateLaw	Sign Bridge
1211040700	10.912	E11-1C	Sign Bridge
1211040700	10.913	DIAG	Sign Bridge
0891040700	11.049	E6-2	Sign Bridge
0891040700	11.050	E6-2	Sign Bridge

RCLINK	Milepoint	MUTCD	Overhead Type
0891040700	11.050	E6-2	Sign Bridge
1211040700	11.267	E6-2	Sign Bridge
0891040700	11.323	E6-2	Sign Bridge
0891040700	11.374	D10-3	Sign Bridge
0891040700	11.374	E6-2A	Sign Bridge
0891040700	11.630	E1-1	Sign Bridge
0891040700	11.633	E6-2A	Sign Bridge
0891040700	11.633	E11-1	Sign Bridge
1211040700	11.662	TrucksAllowed	Sign Bridge
1211040700	11.662	E6-2	Sign Bridge
0891040700	11.805	E1-1	Sign Bridge
0891040700	11.806	E11-1	Sign Bridge
0891040700	11.806	E6-2A	Sign Bridge
0891040700	11.808	E1-1	Sign Bridge
0891040700	12.084	E1-1	Sign Bridge
0891040700	12.084	MoveAccident	Sign Bridge
1211040700	12.379	StateLaw	Sign Bridge
1211040700	12.379	E6-2	Sign Bridge
0891040700	12.513	E1-1	Sign Bridge
0891040700	12.514	E6-2A	Sign Bridge
0891040700	12.514	E1-1	Sign Bridge
0891040700	12.590	E1-1	Sign Bridge
0891040700	12.932	E1-1	Sign Bridge
0891040700	12.936	E1-1	Sign Bridge
0891040700	13.085	E1-1	Sign Bridge
0891040700	13.429	MoveAccident	Sign Bridge
0891040700	13.432	E1-1	Sign Bridge
0891040700	13.582	E1-1	Sign Bridge
0891040700	14.672	E6-2A	Sign Bridge
0891040700	14.805	E6-2A	Sign Bridge
0891040700	14.816	E1-1	Sign Bridge
0891040700	15.157	E1-1	Sign Bridge
0891040700	16.316	E6-2A	Sign Bridge
0891040700	16.317	E6-2A	Sign Bridge
0891040700	16.553	E1-1	Sign Bridge
0891040700	16.563	E1-1	Sign Bridge
0891040700	17.362	StateLaw	Sign Bridge
0891040700	17.364	E6-2A	Sign Bridge
0891040700	17.516	DIAG	Sign Bridge
0891040700	17.844	E1-1	Sign Bridge
0891040700	17.999	DIAG	Sign Bridge
0891040700	18.243	NoTrucks	Sign Bridge

RCLINK	Milepoint	MUTCD	Overhead Type
0891040700	18.245	E1-1	Sign Bridge
0891040700	18.383	E6-2A	Sign Bridge
0891040700	18.384	E1-11F	Sign Bridge
0891040700	18.386	E6-2A	Sign Bridge
0891040700	18.921	E6-2A	Sign Bridge
0891040700	19.376	E11-1	Sign Bridge
0891040700	19.378	E6-2A	Sign Bridge
0891040700	19.378	E1-1	Sign Bridge
0891040700	19.749	E1-1	Sign Bridge
0891040700	19.751	E6-2A	Sign Bridge
0891040700	20.217	E11-1	Sign Bridge
0891040700	20.217	E1-1	Sign Bridge
0891040700	20.218	E6-2A	Sign Bridge
0891040700	20.602	E6-2A	Sign Bridge
1211040700	21.017	E11-1	Sign Bridge
1211040700	21.017	NoTrucks	Sign Bridge
0891040700	21.458	E6-2A	Sign Bridge
0891040700	21.458	E6-2A	Sign Bridge
1211040700	21.754	DIAG	Sign Bridge
0891040700	23.492	E6-2A	Sign Bridge
0891040700	23.492	E1-1	Sign Bridge
1211040700	23.899	E1-1	Sign Bridge
1211040700	23.902	E1-1	Sign Bridge
0891040700	24.000	E6-2A	Sign Bridge
0891040700	24.000	E11-1	Sign Bridge
0891040700	24.003	E1-1	Sign Bridge
0891040700	24.299	E6-2A	Sign Bridge
0891040700	24.299	E11-1	Sign Bridge
0891040700	24.299	E6-2A	Sign Bridge
0891040700	24.693	E1-1	Sign Bridge
0891040700	24.695	E1-1	Sign Bridge
1211040700	24.836	E1-1	Sign Bridge
0891040700	25.073	E6-2A	Sign Bridge
1211040700	25.520	E6-2	Sign Bridge
1211040700	25.520	E6-2	Sign Bridge
1211040700	25.522	E6-2	Sign Bridge
1211040700	25.523	E6-2A	Sign Bridge
0891040700	25.676	E6-2A	Sign Bridge
0891040700	25.676	E6-2A	Sign Bridge
1211040700	26.628	E11-1	Sign Bridge
1211040700	26.654	E6-2A	Sign Bridge
1211040700	26.655	E6-2	Sign Bridge

RCLINK	Milepoint	MUTCD	Overhead Type
1211040700	26.660	E6-2A	Sign Bridge
1211040700	26.661	E6-2A	Sign Bridge
1211040700	53.776	E1-1	Sign Bridge
1211040700	53.777	E1-1	Sign Bridge
1211040700	53.779	NoTrucks	Sign Bridge
1211040700	54.578	E6-2A	Sign Bridge
1211040700	60.786	E11-1C	Sign Bridge
1211040700	60.790	E6-2A	Sign Bridge
1211040700	61.042	E6-2A	Sign Bridge
1211040700	61.042	E11-2	Sign Bridge
1211040700	61.042	E11-1E	Sign Bridge
1211040700	61.087	E6-2A	Sign Bridge
1211040700	61.175	E6-2A	Sign Bridge
1211040700	61.175	E6-2A	Sign Bridge
1211040700	61.175	E11-2	Sign Bridge
1211040700	61.182	E6-2A	Sign Bridge
1211040700	61.184	E6-2A	Sign Bridge
1211040700	61.636	E6-2A	Sign Bridge
1211040700	61.636	E6-2A	Sign Bridge
1211040700	61.679	E6-2A	Sign Bridge
1211040700	61.681	E6-2A	Sign Bridge
1211040700	61.898	E6-2A	Sign Bridge
1211040700	61.898	E6-2A	Sign Bridge
1211040700	62.043	E6-2A	Sign Bridge
1211040700	62.323	E6-2A	Sign Bridge
1211040700	62.323	E6-2A	Sign Bridge
1211040700	62.484	E6-2A	Sign Bridge
1211040700	62.484	E11-1	Sign Bridge
1211040700	62.486	E6-2A	Sign Bridge
1211040700	62.636	E6-2A	Sign Bridge
1211040700	62.636	E6-2A	Sign Bridge
1211040700	62.637	E6-2A	Sign Bridge
1211040700	62.637	E11-1	Sign Bridge
0671040700	0.139	E1-1	Cantilever
0891040700	0.159	D2-1	Cantilever
0891040700	0.299	E6-2	Cantilever
0631040700	0.496	D2-2	Cantilever
0671040700	0.690	E1-1	Cantilever
0891040700	0.845	E6-2A	Cantilever
0891040700	0.845	E11-1	Cantilever
0671040700	1.112	E1-1	Cantilever
0891040700	1.144	E6-2	Cantilever

RCLINK	Milepoint	MUTCD	Overhead Type
0891040700	1.210	E11-1	Cantilever
0891040700	1.212	E6-2A	Cantilever
0891040700	1.586	E6-2	Cantilever
0671040700	1.978	E1-1	Cantilever
0891040700	2.533	E1-1	Cantilever
0891040700	3.252	E11-1	Cantilever
0891040700	3.252	E6-2A	Cantilever
1211040700	3.390	E1-1	Cantilever
0891040700	3.503	E6-2A	Cantilever
0891040700	3.503	E11-1	Cantilever
0631040700	3.726	E6-2A	Cantilever
1211040700	3.854	E1-1	Cantilever
0891040700	5.253	E6-2	Cantilever
1211040700	5.307	E1-1	Cantilever
0631040700	5.754	E6-2A	Cantilever
0631040700	5.757	E11-1	Cantilever
1211040700	5.885	E1-1	Cantilever
0671040700	7.077	D2-1	Cantilever
0671040700	7.495	E6-2	Cantilever
0891040700	9.057	E6-2	Cantilever
1211040700	9.484	E6-2A	Cantilever
1211040700	9.485	E11-1	Cantilever
0891040700	9.572	E6-2A	Cantilever
1211040700	9.625	E11-1	Cantilever
1211040700	9.625	E6-2A	Cantilever
1211040700	9.729	E6-2A	Cantilever
1211040700	9.729	E11-1C	Cantilever
0891040700	10.201	E1-1	Cantilever
1211040700	10.319	E1-1	Cantilever
1211040700	10.603	E6-2A	Cantilever
1211040700	10.603	E11-1	Cantilever
0891040700	10.677	E1-1	Cantilever
1211040700	10.747	E1-1	Cantilever
1211040700	11.176	E6-2A	Cantilever
1211040700	11.179	E11-1	Cantilever
0891040700	11.232	E6-2A	Cantilever
1211040700	12.217	E1-1	Cantilever
1211040700	12.677	E1-1	Cantilever
0891040700	15.901	E6-2A	Cantilever
0891040700	16.158	E1-1	Cantilever
0891040700	16.785	E1-1	Cantilever
0891040700	17.023	E6-2A	Cantilever

RCLINK	Milepoint	MUTCD	Overhead Type
1211040700	21.017	DIAG	Cantilever
1211040700	21.321	E6-2	Cantilever
1211040700	21.698	E1-1	Cantilever
0891040700	21.897	E1-1	Cantilever
1211040700	21.982	E6-2	Cantilever
1211040700	22.429	E1-1	Cantilever
1211040700	22.451	E1-1	Cantilever
1211040700	23.356	E6-2	Cantilever
0891040700	23.885	E11-1D	Cantilever
0891040700	23.886	E6-2A	Cantilever
1211040700	23.890	E1-1	Cantilever
0891040700	24.152	E11-1	Cantilever
0891040700	24.152	E6-2A	Cantilever
1211040700	24.339	E1-1	Cantilever
1211040700	24.656	E6-2	Cantilever
1211040700	25.005	E6-2A	Cantilever
1211040700	25.005	E11-1	Cantilever
1211040700	25.124	E1-1	Cantilever
1211040700	25.313	E6-2	Cantilever
1211040700	25.315	E11-1	Cantilever
1211040700	25.315	E6-2A	Cantilever
1211040700	25.790	E6-2	Cantilever
0891040700	25.830	E1-1	Cantilever
0891040700	26.051	E6-2A	Cantilever
1211040700	26.141	E6-2	Cantilever
1211040700	26.434	E6-2A	Cantilever
1211040700	26.434	E11-1	Cantilever
1211040700	26.434	D10-3	Cantilever
1211040700	53.092	E1-1	Cantilever
1211040700	54.181	E1-1	Cantilever
1211040700	54.181	E6-2A	Cantilever
1211040700	54.350	D2-2	Cantilever
1211040700	54.419	E1-1	Cantilever
0891040700	0.015	E6-2	Other Overhead
0891040700	0.129	D2-3	Other Overhead
0891040700	0.129	D2-3	Other Overhead
0891040700	0.256	MARTA	Other Overhead
0891040700	0.261	MARTA	Other Overhead
0631040700	0.341	E1-1	Other Overhead
1211040700	0.491	E1-1	Other Overhead
0891040700	0.573	E1-1	Other Overhead
0891040700	0.574	NoTrucks	Other Overhead

RCLINK	Milepoint	MUTCD	Overhead Type
0891040700	0.575	D3-1	Other Overhead
0891040700	0.593	E1-1	Other Overhead
0891040700	0.593	D3-1	Other Overhead
0891040700	0.594	E1-1	Other Overhead
0631040700	0.632	D3-1	Other Overhead
0631040700	0.638	D3-1	Other Overhead
0631040700	0.639	NoTrucks	Other Overhead
0631040700	0.827	E1-1	Other Overhead
1211040700	0.862	D3-1	Other Overhead
0891040700	1.267	D2-3	Other Overhead
0891040700	1.268	D2-3	Other Overhead
1211040700	1.315	D2-2	Other Overhead
0671040700	1.333	D3-1	Other Overhead
0671040700	1.334	NoTrucks	Other Overhead
0671040700	1.334	D3-1	Other Overhead
0671040700	1.335	E1-2	Other Overhead
0671040700	1.337	NoTrucks	Other Overhead
0671040700	1.341	D3-1	Other Overhead
1211040700	1.418	E1-1	Other Overhead
0631040700	1.523	NoTrucks	Other Overhead
0631040700	1.525	D3-1	Other Overhead
1211040700	1.533	E1-1	Other Overhead
0631040700	1.543	D3-1	Other Overhead
0631040700	1.578	E11-1	Other Overhead
0631040700	1.578	D3-1	Other Overhead
0631040700	1.579	E6-2A	Other Overhead
0631040700	1.579	E6-2A	Other Overhead
0631040700	1.579	NoTrucks	Other Overhead
0891040700	1.944	D3-1	Other Overhead
0891040700	1.944	NoTrucks	Other Overhead
0891040700	1.966	D3-1	Other Overhead
1211040700	2.250	NoTrucks	Other Overhead
1211040700	2.250	D3-1	Other Overhead
1211040700	2.266	D3-1	Other Overhead
1211040700	2.267	NoTrucks	Other Overhead
1211040700	2.487	D3-1	Other Overhead
1211040700	2.488	NoTrucks	Other Overhead
1211040700	2.494	D3-1	Other Overhead
0671040700	2.592	SlowerTraffic	Other Overhead
0671040700	2.604	D3-1	Other Overhead
0671040700	2.608	D3-1	Other Overhead
0671040700	2.624	D3-1	Other Overhead

RCLINK	Milepoint	MUTCD	Overhead Type
0671040700	2.635	D3-1	Other Overhead
0671040700	2.643	E1-1	Other Overhead
1211040700	2.841	E1-1	Other Overhead
0631040700	2.866	D3-1	Other Overhead
0671040700	2.933	E1-1	Other Overhead
0631040700	3.162	NoTrucks	Other Overhead
0631040700	3.170	D3-1	Other Overhead
0631040700	3.170	D3-1	Other Overhead
0631040700	3.170	NoTrucks	Other Overhead
0891040700	3.374	D2-3	Other Overhead
0671040700	3.396	NoTrucks	Other Overhead
0671040700	3.403	E1-1	Other Overhead
1211040700	3.459	E1-1	Other Overhead
0671040700	3.460	E1-1	Other Overhead
0631040700	3.713	D3-1	Other Overhead
0891040700	4.189	D2-3	Other Overhead
0891040700	4.191	D2-3	Other Overhead
0891040700	4.538	MARTA	Other Overhead
1211040700	4.573	NoTrucks	Other Overhead
1211040700	4.574	E6-2A	Other Overhead
1211040700	4.575	D3-1	Other Overhead
0891040700	4.585	D3-1	Other Overhead
0891040700	4.597	D3-1	Other Overhead
1211040700	4.616	D3-1	Other Overhead
1211040700	4.617	NoTrucks	Other Overhead
1211040700	4.618	E6-2	Other Overhead
0631040700	4.664	D2-1	Other Overhead
0631040700	4.794	E1-1	Other Overhead
0631040700	4.795	D10-3	Other Overhead
1211040700	4.814	E6-2	Other Overhead
0631040700	4.825	NoTrucks	Other Overhead
0631040700	4.828	D3-1	Other Overhead
0631040700	4.828	E1-1	Other Overhead
0891040700	4.940	D2-3	Other Overhead
0671040700	5.197	DIAG	Other Overhead
0671040700	5.241	D3-1	Other Overhead
0671040700	5.293	NoTrucks	Other Overhead
0671040700	5.294	D3-1	Other Overhead
0891040700	5.329	D2-3	Other Overhead
0631040700	5.377	E1-1	Other Overhead
1211040700	5.809	E1-1	Other Overhead
1211040700	6.284	E1-1	Other Overhead

RCLINK	Milepoint	MUTCD	Overhead Type
0891040700	6.485	D3-1	Other Overhead
0891040700	6.491	NoTrucks	Other Overhead
0891040700	6.557	NoTrucks	Other Overhead
0891040700	6.560	D3-1	Other Overhead
0671040700	7.313	D2-3	Other Overhead
0671040700	7.313	D2-3	Other Overhead
1211040700	7.609	E1-1	Other Overhead
0891040700	7.776	E1-1	Other Overhead
0891040700	7.778	D3-1	Other Overhead
0891040700	7.780	NoTrucks	Other Overhead
0891040700	7.791	D3-1	Other Overhead
0891040700	7.791	E1-1	Other Overhead
0891040700	7.791	E1-1	Other Overhead
1211040700	7.970	E1-1	Other Overhead
1211040700	7.972	D3-1	Other Overhead
1211040700	7.972	E1-1	Other Overhead
1211040700	7.979	D3-1	Other Overhead
1211040700	7.980	NoTrucks	Other Overhead
1211040700	7.980	E1-1	Other Overhead
1211040700	8.901	D3-1	Other Overhead
1211040700	8.902	D3-1	Other Overhead
0891040700	8.938	D3-1	Other Overhead
0891040700	8.942	NoTrucks	Other Overhead
0891040700	8.942	E1-1	Other Overhead
0891040700	8.954	D3-1	Other Overhead
0891040700	8.955	E1-1	Other Overhead
0891040700	8.956	E1-1	Other Overhead
1211040700	9.033	DIAG	Other Overhead
1211040700	9.036	D3-1	Other Overhead
1211040700	9.050	D3-1	Other Overhead
0891040700	9.265	E1-1	Other Overhead
0891040700	9.269	NoTrucks	Other Overhead
0891040700	9.269	D3-1	Other Overhead
0891040700	9.271	E1-1	Other Overhead
0891040700	9.285	D3-1	Other Overhead
0891040700	9.286	NoTrucks	Other Overhead
1211040700	9.902	D3-1	Other Overhead
1211040700	10.097	E6-2A	Other Overhead
0891040700	10.596	E1-1	Other Overhead
0891040700	11.317	E1-1	Other Overhead
1211040700	11.479	D3-1	Other Overhead
1211040700	11.492	D3-1	Other Overhead

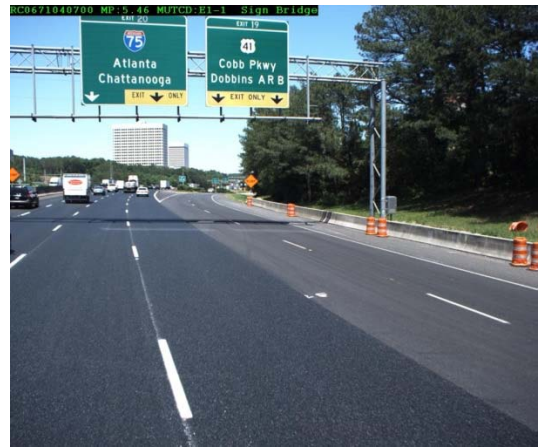
RCLINK	Milepoint	MUTCD	Overhead Type
1211040700	11.890	E1-1	Other Overhead
0891040700	12.310	NoTrucks	Other Overhead
0891040700	12.313	D3-1	Other Overhead
0891040700	12.351	D3-1	Other Overhead
0891040700	12.352	E1-1	Other Overhead
0891040700	12.353	NoTrucks	Other Overhead
1211040700	12.512	D3-1	Other Overhead
1211040700	12.516	NoTrucks	Other Overhead
1211040700	12.520	D3-1	Other Overhead
0891040700	13.724	NoTrucks	Other Overhead
0891040700	13.725	D3-1	Other Overhead
0891040700	13.744	D3-1	Other Overhead
0891040700	14.954	marta	Other Overhead
0891040700	14.963	MARTA	Other Overhead
0891040700	15.348	E1-1	Other Overhead
0891040700	15.349	NoTrucks	Other Overhead
0891040700	15.350	D3-1	Other Overhead
0891040700	15.356	D3-1	Other Overhead
0891040700	15.357	NoTrucks	Other Overhead
0891040700	15.357	E1-1	Other Overhead
0891040700	16.117	D3-1	Other Overhead
0891040700	16.144	D3-1	Other Overhead
0891040700	16.250	E1-1	Other Overhead
0891040700	16.252	D3-1	Other Overhead
0891040700	16.252	NoTrucks	Other Overhead
0891040700	16.260	NoTrucks	Other Overhead
0891040700	16.262	D3-1	Other Overhead
0891040700	17.183	NoTrucks	Other Overhead
0891040700	17.184	D3-1	Other Overhead
0891040700	17.196	D3-1	Other Overhead
0891040700	17.197	NoTrucks	Other Overhead
0891040700	17.197	E1-1	Other Overhead
0891040700	19.067	D3-1	Other Overhead
0891040700	19.069	D3-1	Other Overhead
0891040700	19.347	D3-1	Other Overhead
0891040700	19.349	D3-1	Other Overhead
0891040700	19.674	E1-1	Other Overhead
0891040700	19.979	NoTrucks	Other Overhead
0891040700	19.979	D3-1	Other Overhead
0891040700	19.992	NoTrucks	Other Overhead
0891040700	19.993	D3-1	Other Overhead
0891040700	20.143	E1-1	Other Overhead

RCLINK	Milepoint	MUTCD	Overhead Type
0891040700	20.834	D3-1	Other Overhead
0891040700	20.844	D3-1	Other Overhead
0891040700	21.114	NoTrucks	Other Overhead
0891040700	21.114	D3-1	Other Overhead
0891040700	21.128	NoTrucks	Other Overhead
0891040700	21.130	D3-1	Other Overhead
1211040700	21.546	NoTrucks	Other Overhead
1211040700	21.560	NoTrucks	Other Overhead
1211040700	22.252	D2-3	Other Overhead
0891040700	22.515	E1-1	Other Overhead
0891040700	22.515	D3-1	Other Overhead
0891040700	22.515	NoTrucks	Other Overhead
0891040700	22.515	E1-1	Other Overhead
0891040700	22.516	D3-1	Other Overhead
0891040700	22.520	NoTrucks	Other Overhead
1211040700	22.627	D2-3	Other Overhead
1211040700	22.830	E6-2	Other Overhead
1211040700	22.834	E1-1	Other Overhead
0891040700	23.043	E1-1	Other Overhead
1211040700	23.199	E1-1	Other Overhead
0891040700	23.656	E1-1	Other Overhead
0891040700	23.657	D3-1	Other Overhead
0891040700	23.658	NoTrucks	Other Overhead
0891040700	23.675	NoTrucks	Other Overhead
0891040700	23.676	D3-1	Other Overhead
1211040700	24.110	D2-3	Other Overhead
0891040700	24.828	NoTrucks	Other Overhead
0891040700	24.831	D3-1	Other Overhead
1211040700	24.835	NoTrucks	Other Overhead
1211040700	24.835	E1-1	Other Overhead
0891040700	24.987	D3-1	Other Overhead
1211040700	25.230	D2-3	Other Overhead
0891040700	25.734	D3-1	Other Overhead
0891040700	25.736	NoTrucks	Other Overhead
0891040700	25.764	NoTrucks	Other Overhead
0891040700	25.766	D3-1	Other Overhead
1211040700	26.068	E6-2	Other Overhead
1211040700	26.075	NoTrucks	Other Overhead
1211040700	26.100	E1-1	Other Overhead
1211040700	26.137	E11-1	Other Overhead
1211040700	53.200	E1-1	Other Overhead
1211040700	53.424	D3-1	Other Overhead

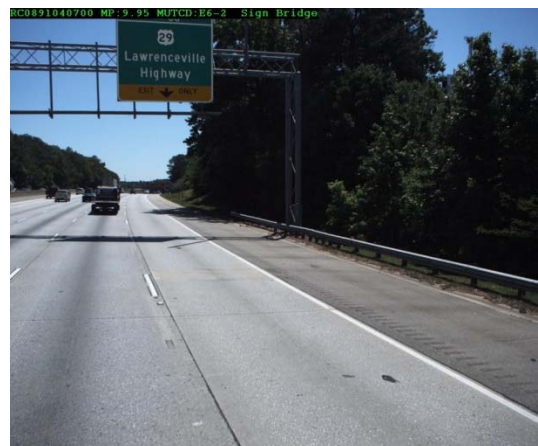
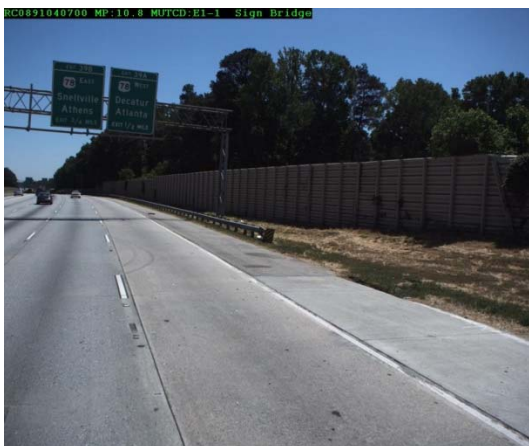
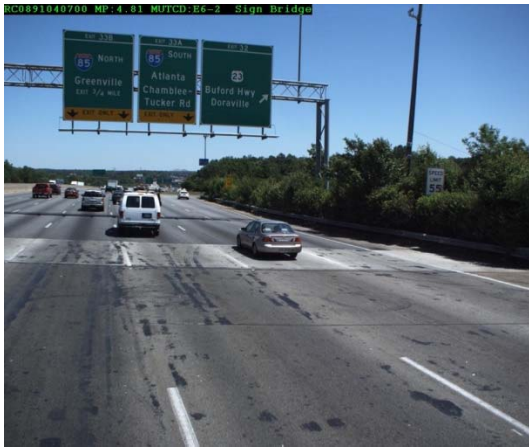
RCLINK	Milepoint	MUTCD	Overhead Type
1211040700	53.437	NoTrucks	Other Overhead
1211040700	53.438	E1-1	Other Overhead
1211040700	53.438	D3-1	Other Overhead
1211040700	53.439	E1-1	Other Overhead
1211040700	54.368	D3-1	Other Overhead
1211040700	54.397	NoTrucks	Other Overhead
1211040700	54.400	D3-1	Other Overhead
1211040700	61.414	D3-1	Other Overhead
1211040700	61.414	E6-2A	Other Overhead
1211040700	61.416	NoTrucks	Other Overhead
1211040700	61.417	E6-2A	Other Overhead
1211040700	61.417	D10-2	Other Overhead
1211040700	61.420	NoTrucks	Other Overhead
1211040700	61.423	D3-1	Other Overhead
1211040700	61.431	D10-3	Other Overhead
1211040700	61.432	E6-2A	Other Overhead
1211040700	61.435	D3-1	Other Overhead

Sign Bridge (323 Cases)

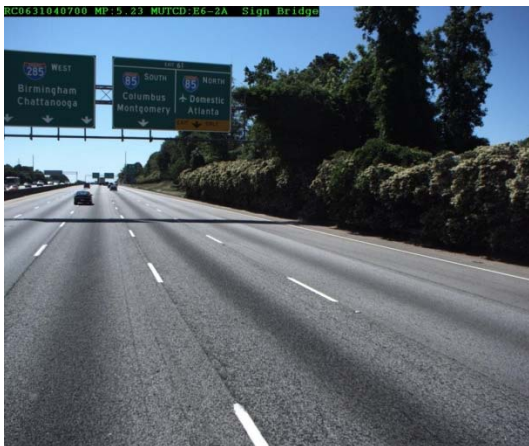


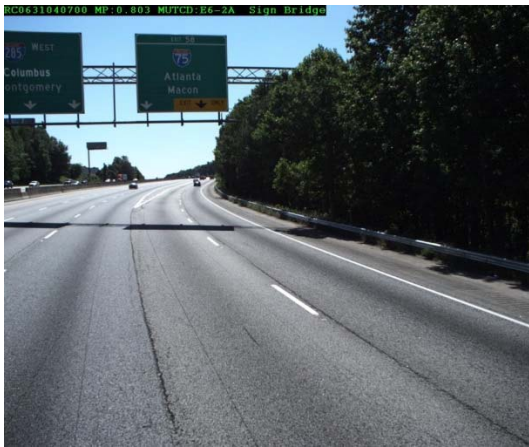








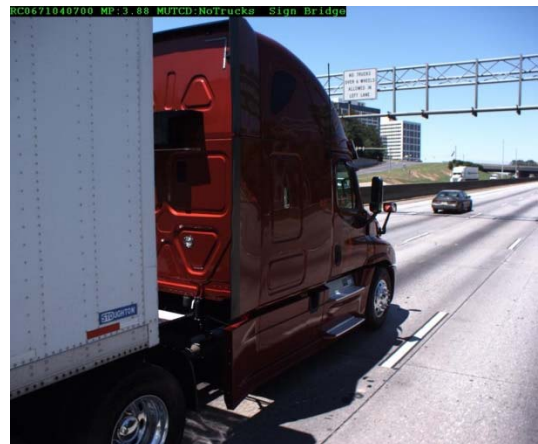
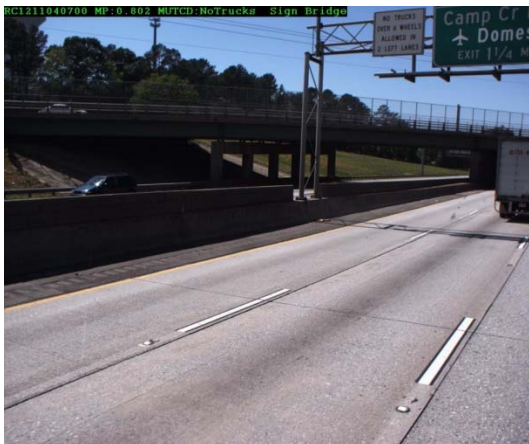
















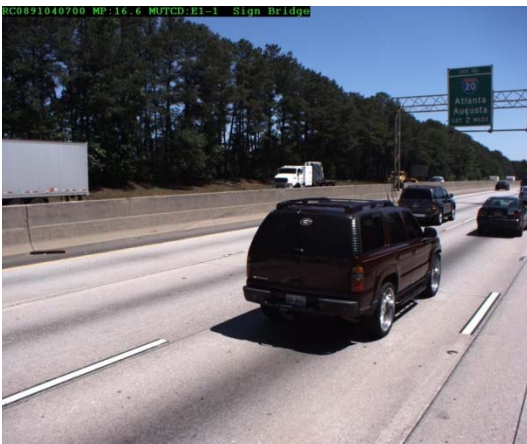


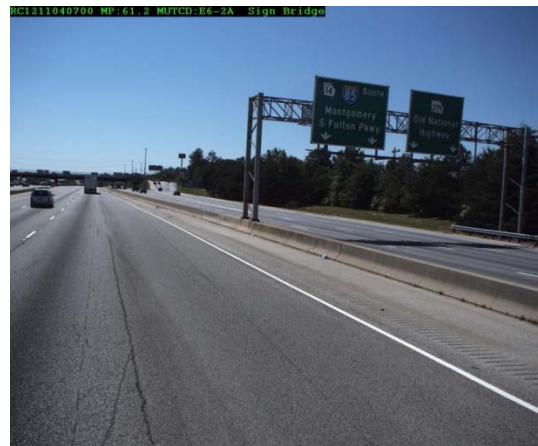
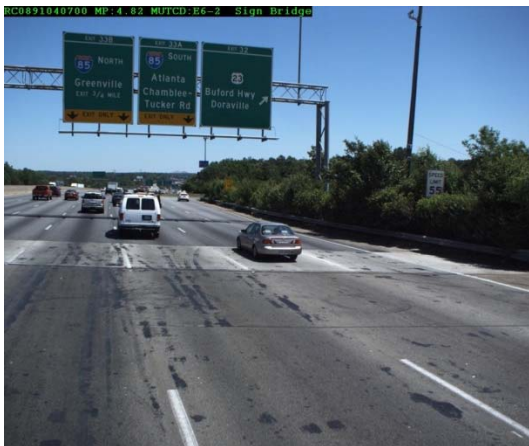








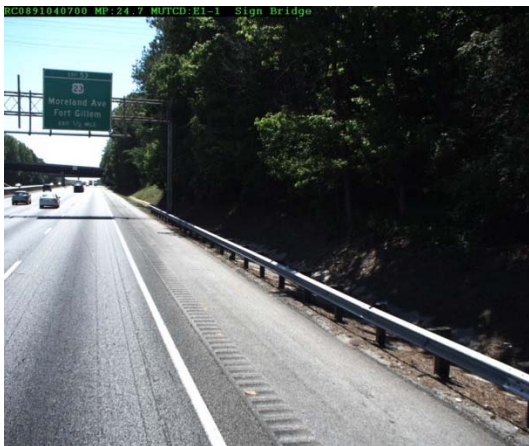
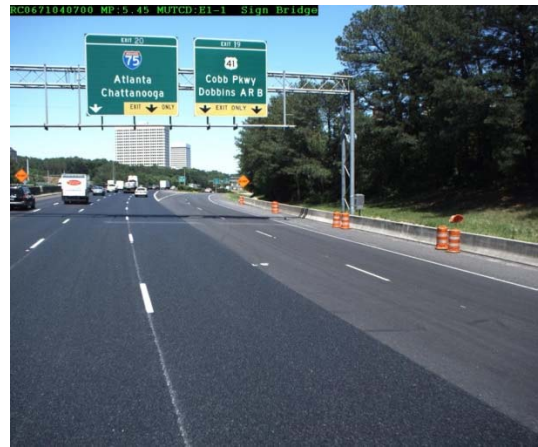






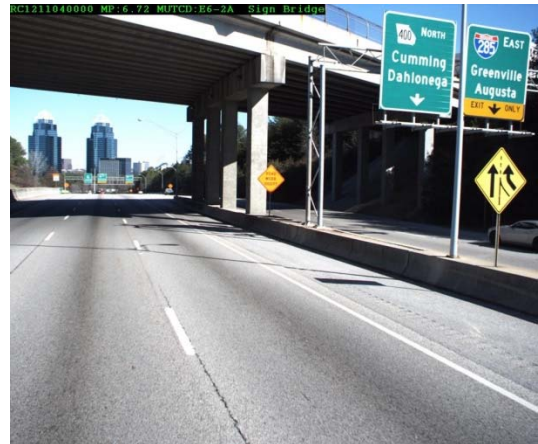
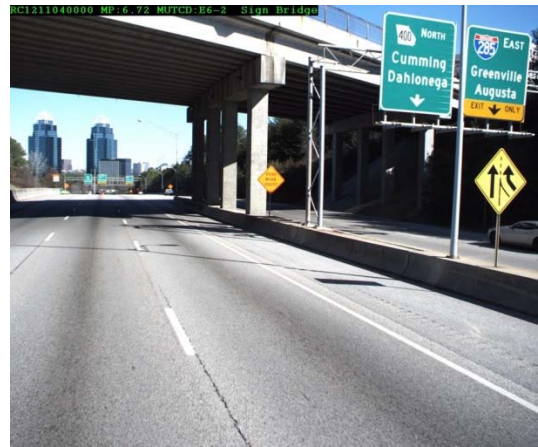


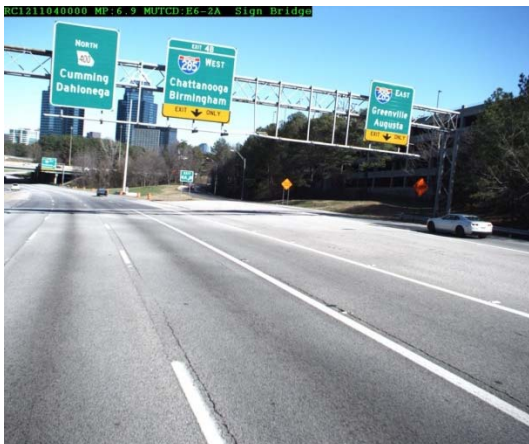












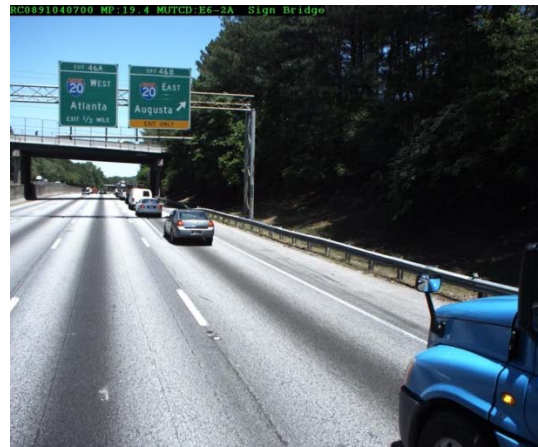


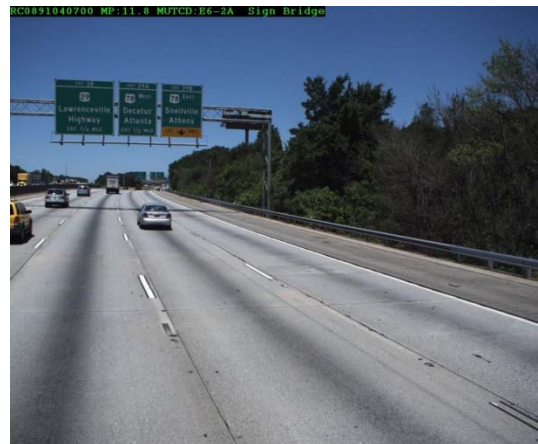






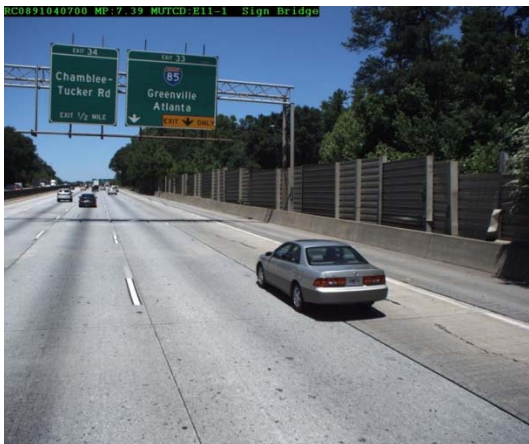
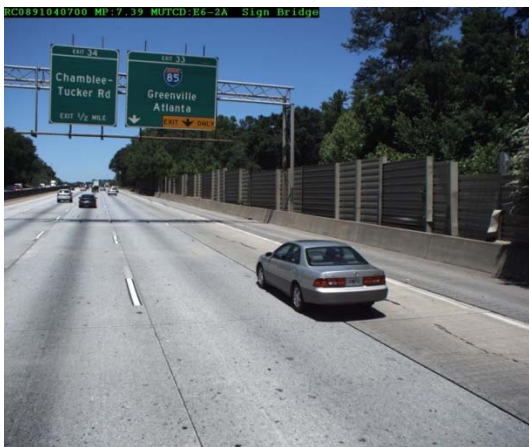
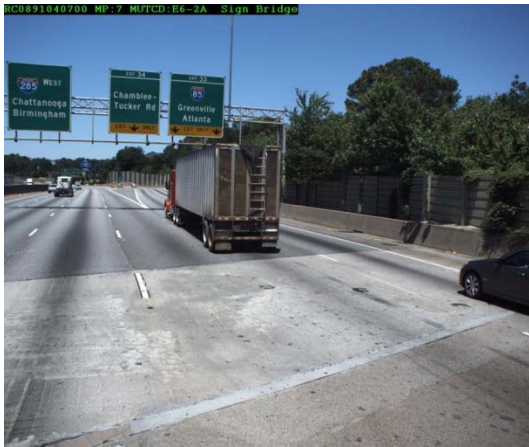




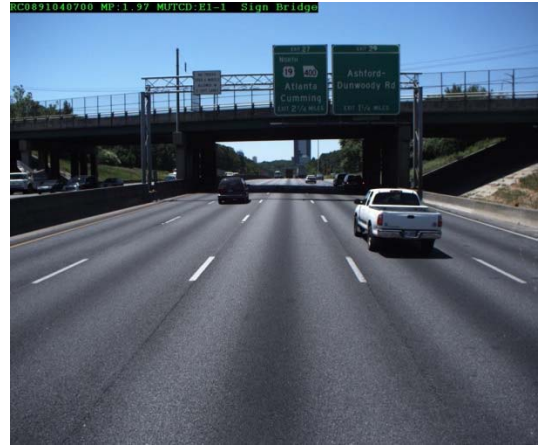




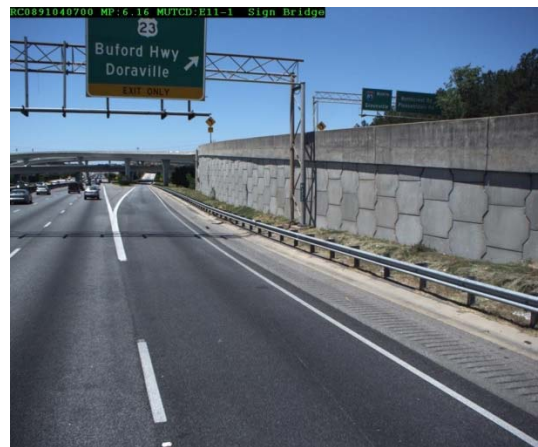








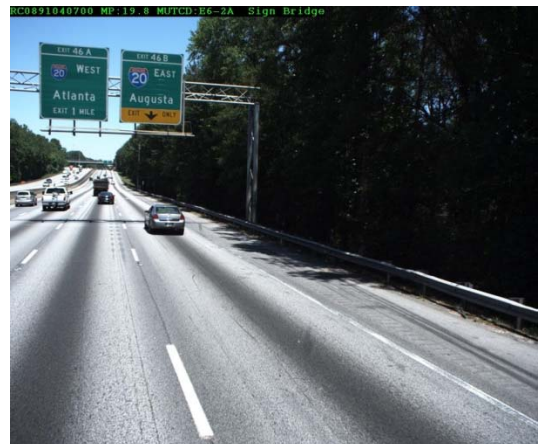
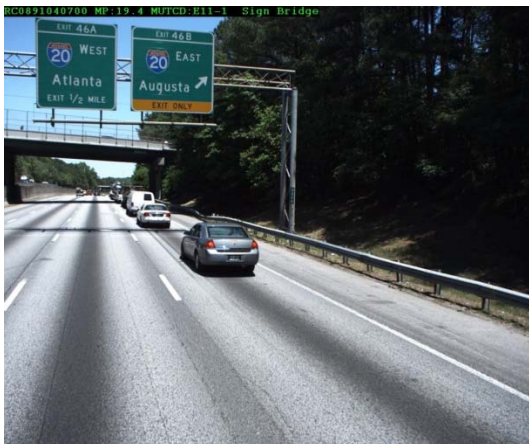
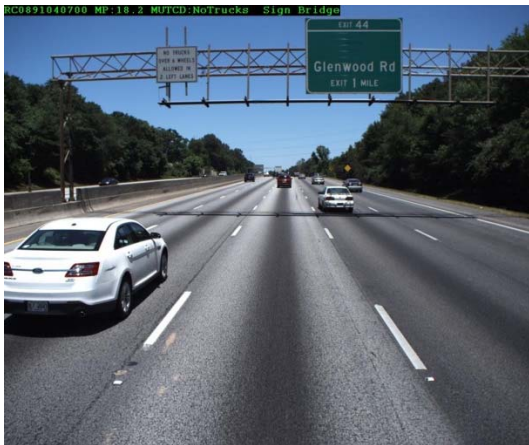




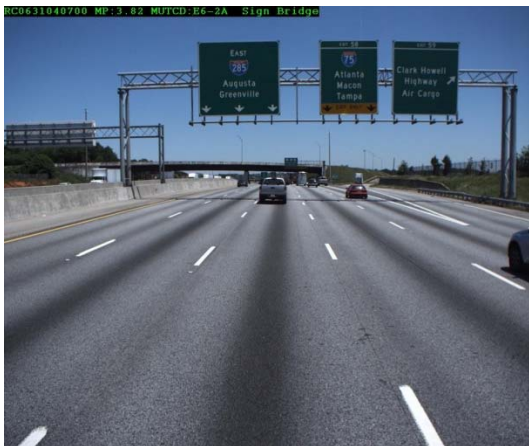




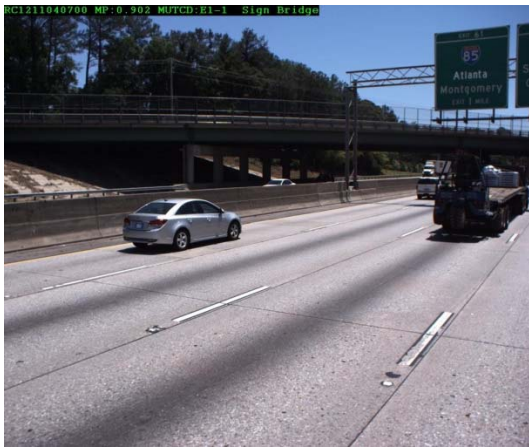














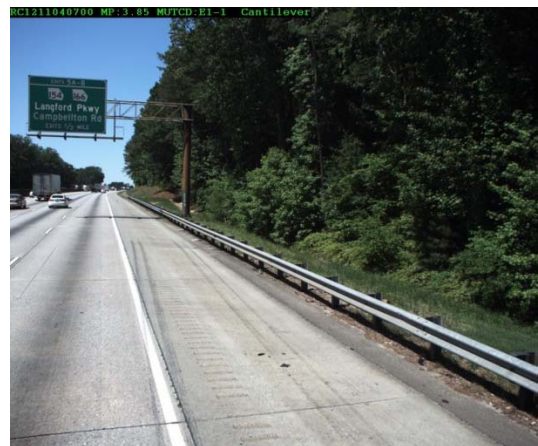




Cantilever (84 Cases)



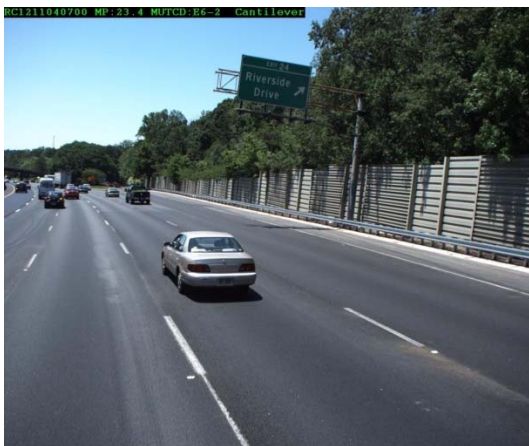
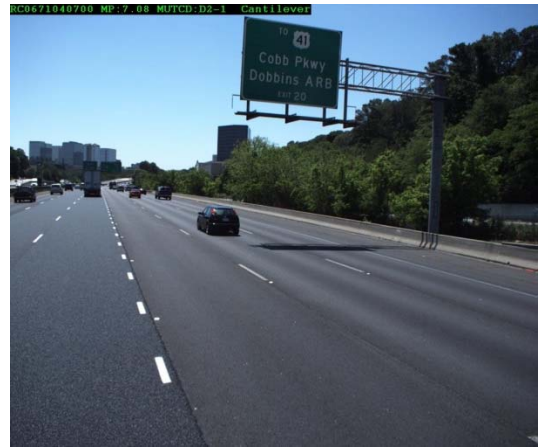


























Other Overhead (236 Cases)

